UNIVERSITY OF CAMBRIDGE

DEPARTMENT OF ENGINEERING

ELASTOHYDRODYNAMIC LUBRICATION OF SMOOTH AND ROUGH SURFACES

GUILLERMO ENRIQUE MORALES ESPEJEL

CHURCHILL COLLEGE

April 1993

Dissertation submitted to the University of Cambridge

for the Degree of Doctor of Philosophy

" TLALTICPAC TOQUICHTIN TIEZ "

" LA TIERRA SERA COMO SEAN LOS HOMBRES "

' THE LAND WILL BE LIKE ITS MEN '

DECLARATION

This dissertation is the result of the author's own work and includes nothing which is the outcome of work done in collaboration. The results presented are, to the best of the author's knowledge, original except where reference and commonly accepted ideas are made. No part of this dissertation has been submitted for any degree, diploma or qualification at any other university or institution.

Guillermo E. Morales Espejel
Engineering Department
University of Cambridge
April 1993

ACKNOWLEDGEMENTS

I am deeply grateful to my supervisor, Dr. J.A. Greenwood, for his enthusiasm, advice and encouragements throughout the course of this research programme. I am very indebted to Dr. Greenwood for carefully proof-reading this dissertation, for his multiple suggestions and for his enormous patience with my language limitations especially just after my arrival to Cambridge. I am also grateful to Professor K.L. Johnson F. R. S. for his valuable suggestions in the several meetings we had to discuss my work; I am especially indebted to him for his encouragement and advice in the transient micro-EHL chapter of this thesis.

I would like to thank the Instituto Tecnológico y de Estudios Superiores de Monterrey (ITESM) México, who financially supported me during the first year of the research and the Mexican council for science and technology (CONACyT) who, together with the British Council, sponsored me during the remaining two years and a half.

I am deeply grateful to my family, who have encouraged and supported me during the period of my study. I am also grateful to Dr. Eugenio García Gardea and Dr. Eduardo López Soriano from the ITESM because without their encouragement and help I would have never come to Cambridge. I would like to thank my friends who made the difficult periods less difficult and the good ones even better: the Mexican community in the Engineering Department. I am especially grateful to José Echeverría, Rafael Chávez and 'mi tocayo' Guillermo Aguirre for their multiple and constant advice on my studies and personal life.

Finally, I would like to say thanks to Wai Khee Yap for his reliable help in everything related to computing and contact mechanics. Thanks to the computer operators of the D.P.O. for their valuable help. And thanks to all those many people who, in one way or another, have contributed to the development of this work.

Thanks Nathalie for your full support.

Dedicated
to
my parents

ABSTRACT

Different aspects of Elastohydrodynamic Lubrication (EHL) are studied. For smooth surfaces, a novel approach which solves separately the inlet and outlet regions by using the fracture mechanics equations, is proposed to solve EHL line contacts for shape and pressure. For rough surfaces, the full EHL geometry is reduced to an infinitely long contact with known mean film thickness and pressure; so real-roughness steady state analyses are carried out by considering the separate Fourier components of roughness and pressures, transient analysis by applying general finite difference methods. The subsurface stresses under micro-EHL are also calculated and given in form of a probability rather than a specific value and location.

Initially, full-geometry EHL line contacts of smooth surfaces are studied. The spike of pressures is assumed to be singular and the idea is to start with an original Hertzian pressure distribution, then the edges of this pressure are truncated and the effects calculated via linear fracture mechanics; after this, the removed pressures are replaced by the converged inlet and outlet pressures, previously obtained by iterating the Reynolds and fracture mechanics equations.

It is found that the outlet pressures follow a modified logarithmic function and therefore the exit bump in the shape joins the parallel film zone with a finite value of slope, unlike the Greenwood extension of Grubin's theory. From a set of solutions, the behaviour of the pressure spike as a function of two dimensionless numbers is followed. Comparisons with results from full numerical solutions are shown, giving good agreement. The scheme is later extended to consider compressibility and the Roelands viscosity law.

After reducing full EHL geometry, the effects of real and wavy roughness in micro-EHL of Newtonian and Eyring fluids with or without compressibility are studied. Steady state analyses of real roughness show that only the high frequency components remain after deformation. By linearizing the Reynolds-Eyring equation an analytical solution is obtained and a criterion for the deformation of the roughness in EHL is given; from this, it is shown that the deformation is very much dependent on the ratio $\lambda/\bar{h}$, obtaining little deformation for low values of it.

Transient analyses of roughness in lubrication are also carried out considering the infinitely long contact. It is found that the transient pressure and film distributions are made of two parts: a) the well known steady state solution, plus b) a complementary function depending only on the modulation of film and pressures from the inlet. It is shown that the conclusions outlined for some authors (e.g. Venner and Lubrecht) about pressures travelling with the velocity of the roughness but shape with the average velocity of the lubricant, are only a particular case of a more general understanding. It is now believed that there is no a real physical damping in the transient shape.

NOTATION

a	deformed roughness amplitude; half width of a Hertzian flat (in Ch. 3 and 4)
$\hat{A}$	$2\lambda/\pi E'$
$A_n,\ B_n$	pressure Fourier coefficients
b	half width of a Hertzian contact
$\bar{B}$	$12\eta\bar{u}/h$
$\hat{B}$	$rDh^2/12\eta$
B	logarithmic constant
B_f	logarithmic dimensionless constant
C	$(\gamma-\beta)/[(1+\beta\ p_o)(1+\gamma\ p_o)]$
C_o	C/α
$\hat{C}$	$1/(\bar{h}\alpha C_o\bar{p}_m)$
C_1	dimensionless constant, $C_1 = h^*/(2\tau_o\alpha L)$
C_T	dimensionless constant, $C_T = \hat{B}\hat{C}/(1+\hat{C}\hat{A}\bar{p}_m)$
C_3	dimensionless constant, $C_3 = \alpha h^* E'/L$
c	spike location
D	Eyring correction factor
DM	$(M_h)_R - M_R^R$
E'	$2\left[\frac{1-\nu_1^2}{E_1}+\frac{1-\nu_2^2}{E_2}\right]^{-1}$
$E_1,\ E_2$	Young's modulus, bodies 1 and 2
f	non-linear term in the Reynolds equation; density function (in Ch. 7)
G	vector of known values in the transient equations
h	film thickness
h_1	amplitude of a sinusoidal film thickness
$\bar{h}$	mean film thickness
h^*	nominal film thickness, central region
h_G	$h(p_{max})\rho(p_{max})/\rho(p_o)$
H	dimensionless film thickness $H = h/\bar{h}$; $H = \frac{2R}{a^2}h$ (in Ch.3 and 4)
I	integrals
$k_1,\ k_2$	Greenwood and Johnson factors for sinusoidal roughness
$K_1,\ K$	dimensionless constants (in Ch. 3 and 4)
L	length of the analysed contact length; length of the outlet region (in Ch. 3)
$L_1,\ L_2$	lengths of the outlet and inlet regions
M	stress intensity factor; even number of points taken along x (in Ch. 5)
M_1	stress intensity factor
N	$M/2$ (in Ch. 5)
n	frequency number in the Fourier analysis
p	pressure
p_1	amplitude of the sinusoidal pressures
p_n	Fourier component of pressures
p_o	mean pressure; maximum Hertzian pressure (in Ch. 3 and 4)
p_a^*	maximum Hertzian pressure of a contact width $2a$

P	dimensionless pressure $P = \alpha p$; $P = \frac{4R}{aE'}p = p_a^* p$ (in Ch.3 and 4)
P_h	dimensionless max. pressure of the equivalent dry contact case $P_h = \sqrt{\frac{2\hat{W}}{\pi}}$
$\mathcal{P}$	dimensionless pressure used in the maps, $\mathcal{P} = \alpha p_h$ (in Ch.4)
Q	$Q = p_o/b$, $Q = p_o/a$
Q_g	Greenwood equivalent load
Q_m	mass flow
q	reduced pressure
R	radius of roller; square root term in the Reynolds-Eyring eq. (in Ch. 5)
r	numerical error amplification factor per iteration (in Ch. 5); $r = \bar{\rho}h$ (in Ch. 8)
s	slide-roll ratio; $s = (u_2 - u_1)/\bar{u}$
S	standard deviation of dimensionless stresses (in Ch. 7)
S_p	standard deviation of dimensionless pressures (in Ch. 7)
$\mathcal{S}$	dimensionless velocity used in the maps, $\mathcal{S} = \alpha E'[(\eta_o \bar{u})/(E'R)]^{1/4}$ (in Ch.4)
t	time
t_p, t_v	dimensionless constants; $t_p = (h/2\tau_o)\frac{dp}{dx}$, $t_v = (\eta\bar{u}/(h\tau_o)$
T	dimensionless time, $T = t\bar{u}/b$
u_1, u_2	surface velocities, body 1 and body 2
$\bar{u}$	mean velocity of the lubricant, $\bar{u} = (u_1 + u_2)/2$
v	elastic displacements
v_f	final shape
V	dimensionless elastic displacements, $V = v/\bar{h}$; $V = (2R/a^2)v$ (in Ch. 3 and 4)
w	load per unit of width
$\hat{W}$	dimensionless load, $\hat{W} = w/ap_a^*$ (integral of pressures P)
x	abscissa
X	dimensionless abscissa, $X = x/\lambda$; $X = x/a$ (in Ch. 3 and 4)
z	initial roughness amplitude; depth below the surface (in Ch. 7); Roelands constant (in Ch. 2, 3, 4)
α	viscosity-pressure coefficient
β	density equation constant, $\beta = 1.683 \times 10^{-9}$ m^2/N
η	lubricant viscosity
η_o	viscosity at atmospheric pressure
ϕ	deformed roughness shift of phase angle; internal angle of the film crease
γ	density equation constant, $\gamma = 2.266 \times 10^{-9}$ m^2/N
λ	wavelength of the roughness
ν	Poisson ratio
ρ	lubricant density
ρ_o	density at atmospheric pressure
$\bar{\rho}$	ρ/ρ_o
ρ_m	density at mean pressure
σ	normal stress
τ	shear stress
τ_o	Eyring stress of the lubricant
θ	stability constant, $0 \leq \theta \leq 1$ (in Ch. 8)

CONTENTS

CHAPTER ONE

INTRODUCTION

Lubrication has been part of human knowledge even since the early days. It is known that in almost all the ancients cultures, e.g. Egyptians, Romans, Greeks and Mayans, some sort of primitive lubrication procedures were used to facilitate daily mechanical activities such as milling, transporting and even the manufacture of weapons. But it was not until 1886 when the actual physical and mathematical understanding of the phenomenon began with the work of O. Reynolds, and in this way the science of hydrodynamic lubrication was born.

By the beginning of this century engineers observed some odd behaviour in heavily loaded lubricated contacts such as gears, where hydrodynamics predicted extremely small film thicknesses and still those contacts seemed to work properly. In 1949 with the work attributed to Grubin, the reason turned out to be that the elastic deformation of the contacting bodies was of much bigger order than the film thickness and therefore it had to be taken into account in the calculations. So Elastohydrodynamic Lubrication (EHL) theory was initiated.

1.1 Elastohydrodynamic Lubrication

Elastohydrodynamic lubrication is a branch of hydrodynamic lubrication which deals with the interaction between the elastic deformation of the contacting moving elements and the fluid film formation between them. The placement of EHL within the conventional lubrication regimes is shown in Fig. 1.1, which has been taken from Shieh and Hamrock [72] 1991.

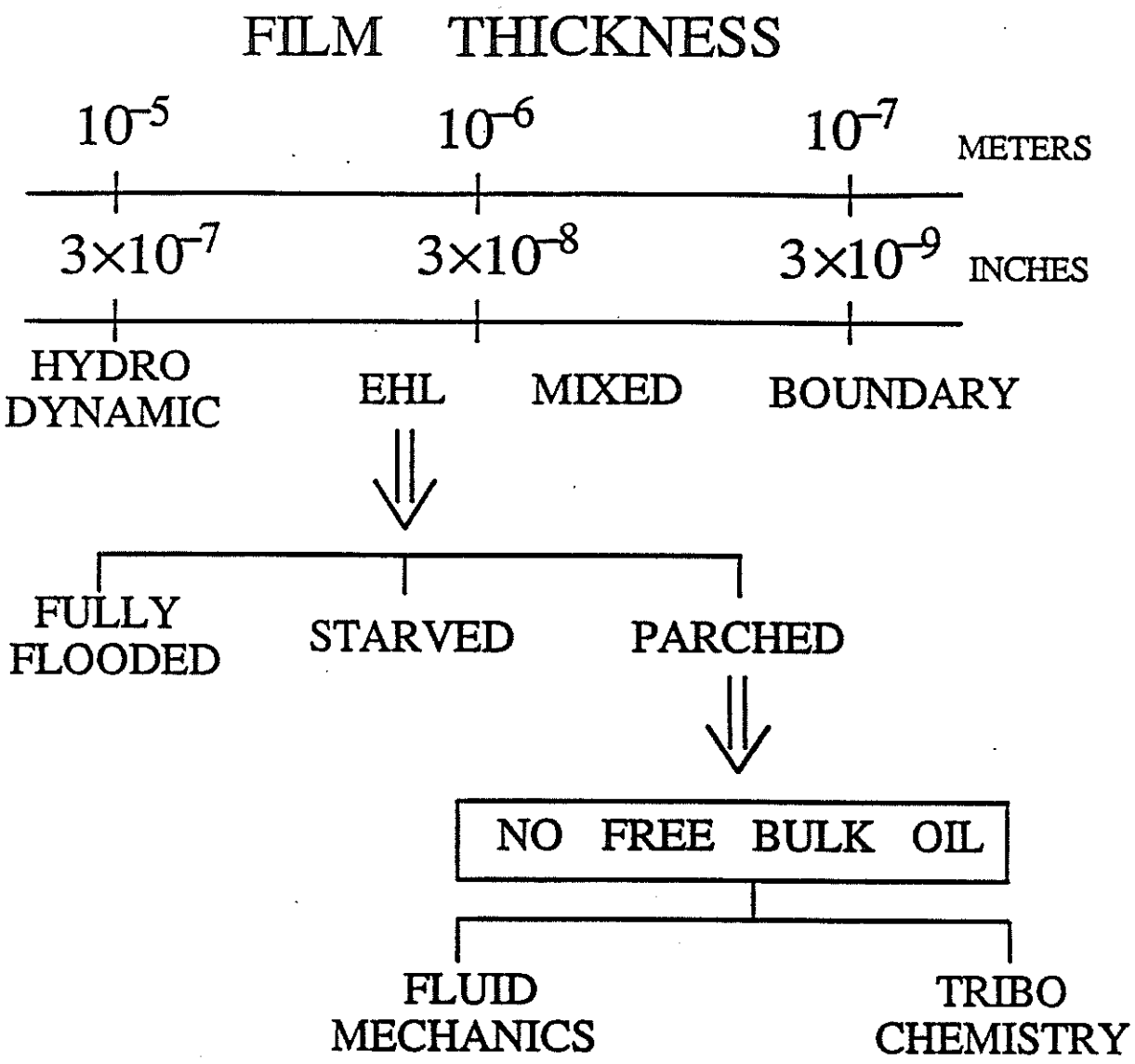

Figure 1.1: Placement of EHL within the lubrication regimes

Typical applications of EHL are gears, cams, bearings, etc, it applies to all situations where the stiffness of one or both of the involved surfaces is small compared to the pressure in the lubricant.

In the application of EHL theory, several aspects play a major role and they have to be considered:

a).- The geometry of the contacting bodies.

In lubrication theory contacts are classified in two branches: conformal and non-conformal contacts.

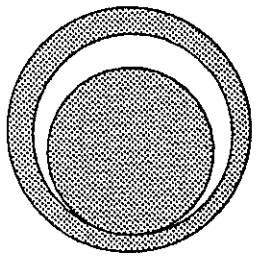

Figure 1.2: Example of conformal contact

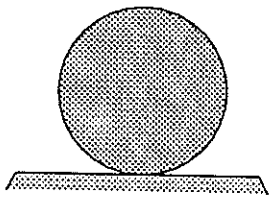

Figure 1.3: Example of non-conformal contact

The first ones involve a large proportion of the area of the bodies in contact, e.g. one concave and one convex surface, like journal bearings (Fig. 1.2). The second ones (non-conformal) involve in the contact a very small part of their area, e.g. one convex surface in contact with a flat or with a convex surface (Fig. 1.3), such are the cases of gear teeth and most cams and followers. It also includes most ball bearing designs, since the radius of the balls is in general very small in comparison to the radius of the path where they

run.

The contacts more likely to suffer elastic distortion are the non-conformal contacts. Since their contact area is small, the overall geometry of the bodies in general can be ignored from the elastic point of view.

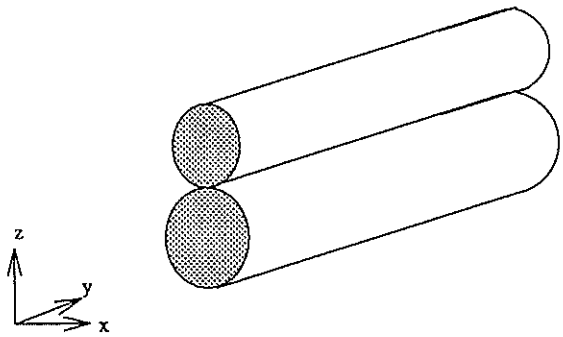

Figure 1.4: Line contact situation

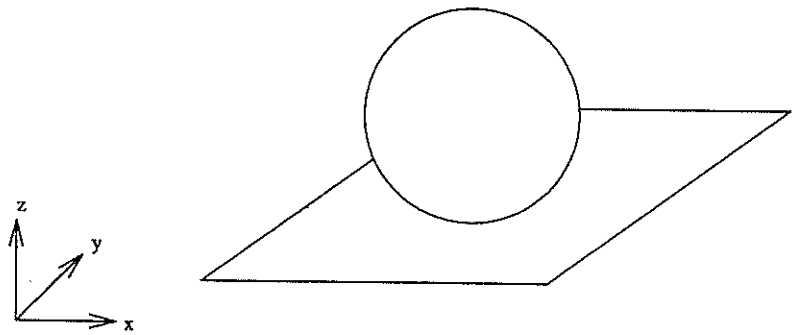

Figure 1.5: Point contact situation

Non-conformal contacts are also classified according to the load distribution in the contact area into point and line contacts.

In the case of line contacts the bodies are assumed to be infinitely long in one of the principal directions, so that in the unloaded dry contact situation the surfaces touch along a straight line and the case can be modelled using only two dimensions x and z (see Fig. 1.4), good examples of line contacts are most gear teeth.

Point contacts are a more general situation and involve the three geometrical directions

x, y and z. A good example of point contacts are ball bearings, see Fig. 1.5.

In elasticity theory, point and line contacts can be considered as situations where applied pressures act on a half-space: the geometry of the bodies is not involved directly in the calculation of the elastic deformation.

b).- Roughness of the surfaces.

In many EHL situations typical lubricant film thicknesses are of the same order as the roughness or surface distortions of the contacting bodies, so that it can no longer be assumed that the surfaces are smooth. The situation is even worse if there is sliding as well as rolling in the movement since the roughness of one surface is changing its position at every instant of time with respect to the roughness of the other surface. Only since the 80's has a new division of EHL been taking form: micro-Elastohydrodynamic Lubrication (micro-EHL), which analyses the effects and behaviour of the surface roughness (including elastic deformation) in the lubrication process.

c).- Lubricant properties.

In EHL, as important as the elastic deformation of the bodies is the behaviour of the lubricant in the process; its rheology, viscosity and compressibility are basic properties which play a major role in lubrication.

Lubricant rheology provides the relationship between the internal shear stress of the lubricant, its velocity distribution across the film thickness and its viscosity. In general a lubricant is said to be Newtonian if this relationship is linear and non-Newtonian if non-linear.

The lubricant viscosity is one of the most important properties and it is essential practice in EHL calculations to consider its variation with pressure and in some cases with temperature.

The high pressures involved in most of EHL situations make it difficult to neglect lubricant compressibility in the analysis.

1.2 Development of EHL and Related Problems

In 1886 O. Reynolds [66] derived the basic differential equation which relates the pressure in the lubricant film with its geometry and the velocities of the moving surfaces , now known as the 'Reynolds Equation'. This work marked the beginning of the theoretical understanding of the lubrication mechanism.

Martin [54] 1916 found the solution of the Reynolds equation for the case of a rigid cylinder and a flat surface, considering an isoviscous and incompressible lubricant. Using this geometrical model, Martin applied his results to the lubrication problem in gears. But the results predicted by his calculations gave very small film thicknesses compared with the known surface roughness.

For the years to come the contradictions between theory and practice remained unresolved and successful operation of gears was attributed to many other reasons but not to a continuous lubricant film between the teeth.

Meldahl [55] 1941 was one of the first to examine the elastic distortion of the surfaces interacting with the Reynolds equation. But without the help of computers in those days, the labour required was so great that he only produced one solution, suggesting that elasticity could play a major role in gear lubrication.

But it was not until 1949 when in Russia the first successful theoretical analysis of the interaction of the Reynolds equation and elasticity was to be produced by Grubin [31] (however, some people attribute the work to Ertel, see Cameron [9]). Grubin divided the heavily loaded contact geometry in two regions: the inlet with low pressures; and a parallel film thickness region with a Hertzian pressure distribution on it. With these considerations he was able to examine the generation of pressures and film thickness in the contact; he applied Hertz theory for dry contacts (Hertz [38]) to calculate the pressures in the parallel film zone and the shape in the inlet (which was then substituted in the Reynolds equation to calculate the pressures). The analysis allowed for the effect of pressure upon viscosity. Grubin's results predicted film thicknesses of several orders of magnitude larger than the surface roughness and the lubrication in gears could finally be explained.

Grubin also speculated about the distribution of pressure in the outlet and concluded that the pressures should present two maxima: the known maximum in the middle of the parallel film section and a second maximum near the end of it. Grubin's speculations were later confirmed by Petrusevich [63] 1951 who obtained numerical solutions of the combined Reynolds and elasticity equations which for the first time showed the outlet spike of pressures.

After this, many other important theoretical and experimental contributions came out. In the theoretical ground, of great importance are the works of Dowson and Higginson

[20] 1959 in obtaining reliable numerical solutions, the results and data collection of Blok [7] 1959 and the analytical extension of the Grubin's work by Greenwood [28] 1972 to account for the outlet zone. Equally important in the experimental field are the earlier measurements of the film thickness reported by Crook [19] 1963 and by Gohar and Cameron [27] 1963, and the pressure measurements of Hamilton and Moore [34] 1971.

Other important aspects were considered in the theoretical solutions. In 1962 Dowson, Higginson and Whitaker [22] first included the effects of the lubricant compressibility. Sternlicht, Lewis and Flynn [73] 1961 accounted for the temperature in highly loaded contacts by introducing the energy equation. Bell [5] 1961 contributed with an important analysis of the effects of non-Newtonian behaviour of rolling surfaces.

After the 70's decade with the arrival of powerful computers, the effort was addressed mainly to the development of robust and sophisticated numerical techniques to deal with the convergence difficulties and to include in the simulation more aspects of the physical reality.

In general, the numerical techniques to solve the EHL problem are classified in two main groups: direct and inverse methods.

Direct methods involve the solution of the Reynolds equation for pressures with known film thickness (it is the most natural way to do it) therefore, an iterative scheme between this equation and the elasticity equations has to be produced to satisfy both equations with a solution. Among these iterative schemes, it is possible to find: Gauss-Seidel relaxation approaches, e.g. Hamrock and Dowson [36] 1976, Chittenden et al. [13] 1985, Hamrock and Jacobson [37] 1984. Newton-Raphson approaches,e.g. Okamura [61] 1982, Sadeghi and Sui [70] 1989, etc.

The main problems with the direct approaches are their convergence difficulties in the high pressure zone. However, very recently multigrid techniques are helping to overcome the difficulties and with great success, e.g. Lubrecht [51] 1987 and Venner [75] 1991.

Inverse methods involve the solution of the Reynolds equation for film thickness with known pressures. One of these approaches was used by Dowson and Higginson [20] 1959 to overcome the convergence difficulties. However, although the techniques are highly convergent in the high pressure zone, they do not work equally well with low pressures. Therefore Dowson and Higginson only used an inverse method in the Hertzian zone of the EHL contact and they applied a direct method in the inlet.

Nowadays, another important source of research in EHL is the role of surface roughness in lubrication. First, relatively simple averaging techniques appeared e.g. Christensen [16] 1971 , Tønder [60] 1984 followed by the flow-factor method introduced by Patir and Cheng [62] 1978. In neither of them was the effect of roughness deformation considered. However, Cheng made also one of the earliest analyses of an asperity passing through an EHL contact (Lee and Cheng [47]) and proved that it certainly did not pass through unchanged.

Goglia, Cusano and Conry [25] 1984 produced one of the first complete numerical solutions of the micro-EHL problem for single asperities and wavy surfaces, their results suggested that in general the asperities are flattened by the elastic deformation, later on the same conclusions were obtained by Kweh et al. [48] 1989, Lubrecht et al. [52] 1988 and Venner at al. [77] 1991. Venner and ten Napel [78] 1992 go beyond this and are able to give numerical solutions of not only wavy surfaces but also real roughness, showing as well the flattening of the roughness. Greenwood and Johnson [30] 1992 published an analytical solution of the micro-EHL problem for sinusoidal transverse roughness in line contacts with interesting conclusions for Newtonian fluids.

The latest studies in micro-EHL are addressed to the understanding of the kinematic behaviour of the roughness in the lubrication process; specially when sliding is involved, e.g. Chang et al. [10] 1989, Chang and Webster [11] 1992, Venner and Lubrecht [76] 1992 and Lubrecht and Venner [53] 1992. This thesis includes also a contribution on this aspect.

Another area of interest is the investigation of the conditions which govern the flattening of the roughness. Chang and Webster [11] 1992, Sadeghi [69] 1991 have shown odd examples of micro-EHL contacts where the initial roughness is barely changed even with very high pressures, which seem to be in contradiction with previous results where the original roughness was always flattened. The present thesis also studies this aspect and a simple criterion to describe the flattening of the roughness as a function of its wavelength is presented.

1.3 Structure of the Thesis

Chapter 2 outlines the basic lubrication and elasticity theory which establish the basis to study the phenomenon of Elastohydrodynamic Lubrication. It starts by explaining the

derivation of the basic equations: Reynolds, elasticity and lubricant properties.

In Chapter 3 a novel method to solve the outlet and central zones of an EHL line contact of smooth surfaces is presented, the scheme is based on a fracture mechanics approach developed by Greenwood and Johnson [29] 1989 to replace pressures in truncated dry Hertzian contacts. The method follows the pattern set by Grubin and makes use of the similarity between the central zone of a heavily loaded EHL contact and a dry contact. It first considers an original Hertzian flat and pressures which are then truncated and replaced by imposing outlet EHL pressures (previously found by solving iteratively the Reynolds and fracture mechanics equations); after this, the internal stresses are added to modify the original Hertzian pressures. Incompressible outlet solutions are obtained and compared with the Greenwood's extension of the Grubin theory. Hall's ideas about the logarithmic nature of the outlet EHL pressures are also discussed. Finally it is shown that these pressures actually behave as a modified logarithmic function, which changes the traditional idea of a purely square root shape and inverse square root pressures surrounding the spike.

In Chapter 4 the previous approach is extended to the inlet and the two are put together to build a complete EHL approach. Several examples are solved and compared with literature results; in general good agreement is found for film thickness and shape. The spike location is also investigated, however, disagreement among different authors is still found. Later the approach is modified to include compressible fluids and the Roelands law for viscosity. In the compressible solutions the characteristic behaviour is observed (the spike is shifted towards the outlet and the central film thickness is reduced). The effect of changing to the Roelands viscosity law is very small in film thickness and pressures. In this chapter also some collected results for the central film thickness, spike location and spike height are shown. Some thoughts about the behaviour of the spike singularity within the dimensionless pressure and velocity map are presented.

In Chapter 5 the study of the behaviour of steady state rough surfaces is introduced. An analysis of wavy and real roughness is made for which an interesting approach is developed; the method isolates a small length of the EHL contact and assumes it to be infinitely long, then the Fourier components of the surface roughness can be calculated, and the simple analysis made by Greenwood and Johnson [30] 1992 for sinusoidal roughness can be applied for real roughness. Solutions for Newtonian and Eyring fluids, with and without

compressibility, with sinusoidal and real roughness are shown demonstrating that in most of the cases the roughness after deformation is almost completely flattened especially the low frequency components.

Chapter 6 shows an analysis of short wavelength wavy surfaces in EHL. Since with the scheme of Chapter 5 the solution of these cases becomes numerically unstable, it is necessary to develop different approaches. By linearising the Reynolds-Eyring equation an analytical expression for the deformed amplitude is obtained, from which an important criterion to determine the importance of the wavelength of the original roughness on the deformation is derived. It is shown that for short wavelengths the roughness is likely to persist even in extreme conditions of load.

Chapter 7 introduces an analysis of subsurface stresses in micro-EHL again considering the length of the contact to be infinitely long. Basically the idea is to present the results for maximum stress and its location as a probability rather than a precise value, since the stresses are proved to be Gaussian variables.

Chapter 8 brings to light a clearer understanding of the transient micro-EHL physical phenomenon. It describes a transient analysis in micro-EHL which is applicable to sliding-rolling contacts. The idea of the infinitely long contact is retained, but a general implicit finite difference method is now used for the solution of the Reynolds equation. The complete transient solution of a micro-EHL contact is found to consist of two components: the moving steady state pressure and shape and a complementary function induced by the entrance of every surface ripple in the inlet. The scheme does not allow for the calculation of the final shape amplitude, since the inlet is not included in the geometry and therefore the amplitude of the excitation is unknown. However, several solutions for Newtonian and Eyring fluids are obtained and compared with results from the literature.

Finally Chapter 9 describes the basic conclusions along the work and outlines the topics of future research in the area.

CHAPTER TWO

ELASTOHYDRODYNAMIC LUBRICATION THEORY

In this chapter the mathematical background which governs the behaviour of an elastohydrodynamically lubricated contact will be described.

The problem of sustaining a lubricant film between two moving, elastically deformable surfaces is described in general by three equations: a) the Reynolds equation which explains the relationship between the lubricant flow and the building up of a distribution of pressure against the containing walls; b) the film thickness equation to relate the geometry of the walls and the elastic deformation with the thickness of the lubricant film; c) finally the load balance equation which requires the integrated pressures to be equal to the applied load in order to sustain the equilibrium of the system.

The equations are then solved by either numerical methods or approximated by analytical schemes. The solution provides the pressure distribution and the film thickness variation along the contact region. From those results the minimum film thickness and maximum pressure are easily obtained, since in machine design these last are the most important parameters.

In general, it is accepted that for an incompressible lubricant the maximum pressure and minimum film thickness in a EHL contact are a function of only two dimensionless quantities, the definition of which varies according to the author, but in general, one of them is a sort of dimensionless load and the other some kind of dimensionless velocity.

Since the pressures involved in a EHL contact in general are very high, the compressibility of the lubricant and the variation of viscosity with pressure become important and must be taken into account. Some experimental relationships of these parameters will be

also described.

An important aspect of sliding EHL contacts is that the lubricant is subjected to large shear rates and pressures, so that its rheology is a major factor to be considered. Some important aspects of Newtonian and non-Newtonian lubricants will be seen herein.

It is well known that the heat produced by the viscosity shear in EHL contacts changes the properties of the lubricant, especially its viscosity, however, in this analysis and throughout the thesis this will not be considered.

2.1 The Reynolds Equation

The differential equation governing the pressure distribution in a Newtonian lubricant film, was first obtained by Reynolds in 1886 from the more general Navier-Stokes equations by making the appropriate simplifications in the analysis; the same method described for example by Dowson and Higginson [21].

However, in this section the derivation of the Reynolds equation will be explained by following a rather simpler approach of balance of forces and mass, used for example by Cameron [8].

The following assumptions will be considered:

1).- Body forces are neglected: There are no extra forces acting on the body (e.g. magnetic fields)

2).- Pressure is constant across the lubricant film (z direction): Since the thickness is only one or two microns it is always true.

3).- The radius of curvature of the surfaces is large compared with the film thickness: There is no need to consider the surface velocities as varying in direction.

4).- There is no slip at the boundary: The velocity of the oil layer at the boundaries is the same as the velocity of the boundary itself.

The following assumptions are included for simplification, they are not necessarily always true.

5).- The lubricant is Newtonian: The stress on it is proportional to the rate of shear. Modifications to the final Reynolds equation will be shown below when this assumption is removed in non-Newtonian fluids.

6).- Laminar flow: In EHL no turbulent flow arises since the film thickness is always

small.

7).- Fluid inertia is neglected: Even when the Reynolds number is 1000 the pressures are only modified in a very small proportion, e.g. Cameron [8].

8).- The lubricant viscosity is constant across the film (z direction): This would not be true if the generated heat were taken into account.

2.1.1 Equilibrium of Forces on a Lubricant Element

Consider a lubricant element passing through a channel of moving boundaries as shown in Fig. 2.1

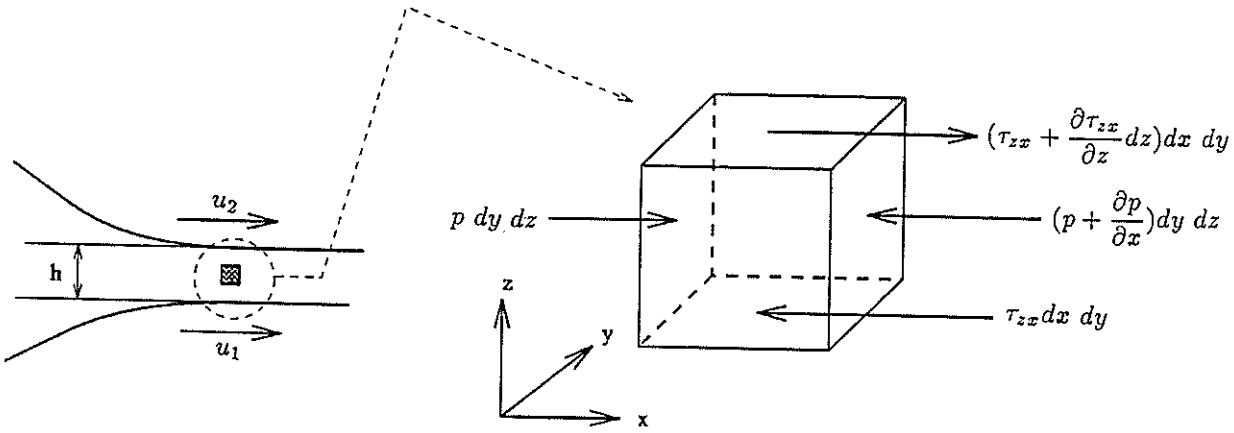

Figure 2.1: Equilibrium of an element showing forces in x direction

By making $\Sigma F_x = 0$ and $\Sigma F_y = 0$ it is possible to obtain:

$$\begin{aligned} \frac{\partial \tau_{zx}}{\partial z} &= \frac{\partial p}{\partial x} \\ \frac{\partial \tau_{zy}}{\partial z} &= \frac{\partial p}{\partial y} \end{aligned} \tag{2.1}$$

with τ_{zx} representing the shear stress acting along x.

For a Newtonian fluid the relation between shear and velocity is given by:

$$\begin{aligned} \tau_{zx} &= \eta \frac{\partial u_x}{\partial z} \\ \tau_{zy} &= \eta \frac{\partial u_y}{\partial z} \end{aligned} \tag{2.2}$$

where η is the lubricant viscosity (constant along z), and u_x , u_y are the velocities of the lubricant element in x and y directions.

The substitution of equations 2.2 into equations 2.1 leads to:

$$\begin{aligned} \frac{\partial}{\partial z}[\eta \frac{\partial u_x}{\partial z}] &= \frac{\partial p}{\partial x} \\ \frac{\partial}{\partial z}[\eta \frac{\partial u_y}{\partial z}] &= \frac{\partial p}{\partial y} \end{aligned} \tag{2.3}$$

2.1.2 Velocity Distribution

Equations 2.3 can be integrated twice respect to z with the substitution of the following boundary conditions, to find the velocity distribution of the lubricant in both directions x and y at any point of z.

Boundary conditions:

$$\begin{array}{l} \text{when } z = h, \text{ then } u_x = u_2 \\ \text{when } z = 0, \text{ then } u_x = u_1 \\ \text{when } z = h, \text{ then } u_y = v_2 \\ \text{when } z = 0, \text{ then } u_y = v_1 \end{array}$$

leading to:

$$\begin{aligned} u_x &= \frac{1}{2\eta}\frac{\partial p}{\partial x}(z^2 - zh) + \frac{z}{h}(u_2 - u_1) + u_1 \\ u_y &= \frac{1}{2\eta}\frac{\partial p}{\partial y}(z^2 - zh) + \frac{z}{h}(v_2 - v_1) + v_1 \end{aligned} \tag{2.4}$$

2.1.3 Mass Continuity

Consider a column of compressible lubricant of height h and base dx, dy as shown in Fig. 2.2. By performing a balance of mass in the column it is easy to obtain:

$$\frac{\partial m_y}{\partial y} + \frac{\partial m_x}{\partial x} + \frac{\partial}{\partial t}(\rho h) = 0 \tag{2.5}$$

where the term $\frac{\partial}{\partial t}(\rho h)$ has been obtained by replacing the difference of the boundary velocities in z direction (w_2 and w_1) by the change of the column height with time.

The mass flows can be obtained by integrating the velocities:

$$\begin{aligned} m_x &= \rho \int_0^h u_x dz = -\frac{\rho h^3}{12\eta}[\frac{\partial p}{\partial x}] + (u_2 + u_1)[\frac{\rho h}{2}] \\ m_y &= \rho \int_0^h u_y dz = -\frac{\rho h^3}{12\eta}[\frac{\partial p}{\partial y}] + (v_2 + v_1)[\frac{\rho h}{2}] \end{aligned} \tag{2.6}$$

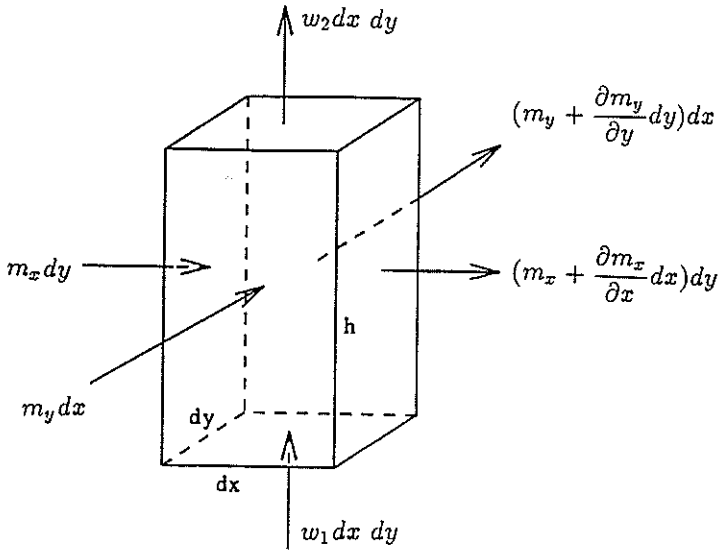

Figure 2.2: Continuity of flow in a column of lubricant

2.1.4 The Full Reynolds Equation

Substituting equations 2.6 into equation 2.5 it is possible to obtain the full Reynolds equation for a compressible Newtonian fluid:

$$\frac{\partial}{\partial x}(\frac{\rho h^3}{12\eta}\frac{\partial p}{\partial x}) + \frac{\partial}{\partial y}(\frac{\rho h^3}{12\eta}\frac{\partial p}{\partial y}) = \left[\bar{u}\frac{\partial(\rho h)}{\partial x} + \bar{v}\frac{\partial(\rho h)}{\partial y} + \frac{\partial}{\partial t}(\rho h)\right] \tag{2.7}$$

where $\bar{u}$ and $\bar{v}$ are the average velocities of the surfaces in x and y direction and are defined by:

$$\bar{u} = \frac{u_1 + u_2}{2}\ ,\quad \bar{v} = \frac{v_1 + v_2}{2}$$

2.1.5 Infinitely Long Bearing

In some cases it is possible to treat bearings as infinitely long in the y direction, for example, most gears. Then the variation of pressures in the y direction becomes negligible. And the flow in the same direction too. For those cases the Reynolds equation becomes one-dimensional and equation 2.7 can be reduced to:

$$\frac{\partial}{\partial x}(\frac{\rho h^3}{\eta}\frac{\partial p}{\partial x}) = 12\bar{u}\frac{\partial(\rho h)}{\partial x} + 12\frac{\partial(\rho h)}{\partial t} \tag{2.8}$$

2.1.6 No Squeeze Film Term

The term $\frac{\partial(\rho h)}{\partial t}$ in equation 2.8 represents the movement of the boundaries in z direction and it is called the squeeze term. This term can be taken as zero in the cases when the external load is stationary in time and the boundary surfaces are smooth (no roughness involved) or if only one of the surfaces is rough but has zero velocity, such that the bearing runs in a steady state condition. For such cases the Reynolds equation 2.8 becomes:

$$\frac{\partial}{\partial x}(\frac{\rho h^3}{\eta}\frac{\partial p}{\partial x}) = 12\bar{u}\frac{\partial(\rho h)}{\partial x} \tag{2.9}$$

which can be integrated with respect to x and the integration constant taken in a convenient form using boundary condition such as $\rho h = \rho^* h^*$ when $\frac{dp}{dx} = 0$; obtaining:

$$\frac{dp}{dx} = 12\bar{u}\eta\frac{h - h^*(\rho^*/\rho)}{h^3} \tag{2.10}$$

Equation 2.10 is one of the most used forms of the Reynolds equation for Newtonian compressible lubricants in hydrodynamics.

2.1.7 Non-Newtonian Lubricants

There is no yet a clear agreement on what should be the rheological model for a non-Newtonian lubricant relating shear stress with velocity. Fig. 2.3 shows a comparison of the behaviour of several rheological models (taken from Rong-Tsong and Hamrock [50] 1990).

However, it is known that the Eyring model suggested by Eyring [24] 1936 and later used by Johnson and Tevaarwerk [43] 1977 agrees well with experimental results and is mathematically simpler than some others. The rheological Eyring model reads:

$$\dot{\gamma} = \frac{du}{dz} = \frac{\tau_o}{\eta}\sinh(\frac{\tau}{\tau_o}) \tag{2.11}$$

where τ_o is the Eyring stress of the lubricant which varies slightly with pressure but is normally taken as constant. τ is the shear stress in the lubricant τ_{xz} or τ_{yz}.

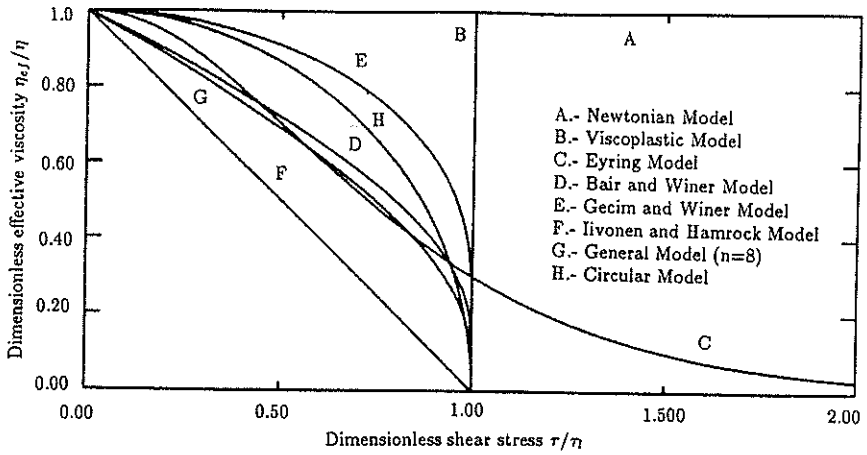

Figure 2.3: Rheological models, where $\tau_o = \tau_l/3$ for the Eyring model ($\eta_{ef} = \tau/\dot{\gamma}$). Taken from Rong-Tsong and Hamrock.

By using equation 2.11 instead of equations 2.2 in the deduction of the Reynolds equation and following the procedure already described, it is possible to obtain the so-called Reynolds-Eyring equation, which according to Conry et al. [17] 1987 is:

$$\frac{\partial}{\partial x}\left(\frac{\rho h^3}{\eta} D \frac{\partial p}{\partial x}\right) = 12\bar{u}\frac{\partial(\rho h)}{\partial x} + 12\frac{\partial(\rho h)}{\partial t} \tag{2.12}$$

where:

$$D = \frac{3t_v}{t_p}(\coth t_p - 1/t_p)\sqrt{s^2 + \left[\frac{\sinh t_p}{t_p t_v}\right]^2}$$

and:

$$s = \frac{u_2 - u_1}{\bar{u}}\ , \quad t_p = \frac{h}{2\tau_o}\frac{dp}{dx}\ , \quad t_v = \frac{\eta\bar{u}}{h\tau_o}$$

s is known as the slide-roll ratio.

In equation 2.12 it is easy to see that when $\tau_o \to \infty$ then $D \to 1$ (Newtonian fluid) and the equation becomes the Reynolds equation 2.8.

For steady state, equation 2.12 can be written as:

$$\frac{dp}{dx} = \frac{12\bar{u}\eta}{D}\left[\frac{h - h^*(\rho^*/\rho)}{h^3}\right] \tag{2.13}$$

2.2 Viscosity-Pressure Relationships

The increase of the lubricant viscosity with pressure is a very important aspect in the lubrication of heavily loaded contacts and it must be considered in the calculations.

In general, there are two very well known relationships between lubricant viscosity and pressure: the Barus' law (Barus [4] 1893) and the Roelands's equation (Roelands [68] 1966).

a).- Barus Law:

The relation between pressure and viscosity is given by the simple exponential equation:

$$\eta(p) = \eta_o e^{\alpha p} \tag{2.14}$$

where η_o is the viscosity at gauge pressure $p = 0$ and α is an experimental constant depending on the lubricant and called the pressure-viscosity coefficient with units Pa^{-1}.

It is said (e.g. Gohar [26]) that equation 2.14 becomes inaccurate above 0.5 GPa since it predicts much bigger viscosities than those observed experimentally. However, the equation is still adequate when solving the Reynolds equation for film thickness, since either way the term $\frac{\rho h^3}{\eta}$ in equation 2.8 is very small; using equation 2.14 to calculate tractions gives incorrect answers.

b).- Roelands Equation:

A recent more realistic equation is:

$$\eta(p) = \eta_o \exp\left\{[9.67 + \ln \eta_o][(1 + \frac{p}{p_o^*})^z - 1]\right\} \tag{2.15}$$

Where z is the pressure viscosity index, which is a feature of the lubricant (typically $0.5 \leq z \leq 0.7$), and p_o^* is a constant $p_o^* = 1.98 \times 10^8$ Pa.

For low pressures equation 2.15 reduces to :

$$\eta = \eta_o \exp(\alpha^* p)$$

where: $\alpha^* = \frac{z}{p_o^*}[9.67 + \ln \eta_o]$

2.3 The Density-Pressure Equation

In EHL contacts generally the compressibility of the lubricant becomes important due to the high pressures involved , therefore in most of the cases it has to be considered in the

calculations of the film thickness. The following relationship suggested by Dowson and Higginson [21] is used throughout the thesis:

$$\bar{\rho} = \frac{\rho(p)}{\rho_o} = \frac{1+\gamma p}{1+\beta p} \tag{2.16}$$

Where $\bar{\rho}$ = density ratio, $\rho(p)$ = density of the lubricant as function of pressure, ρ_o = density of the lubricant at ambient pressure, $\gamma = 2.266 \times 10^{-9}$ Pa, $\beta = 1.683 \times 10^{-9}$ Pa.

Equation 2.16 limits the compressibility of the lubricant to approximately 30 percent.

2.4 The Lubricant Film Geometry Equation

Throughout this work the interest is focused only on non-conformal line contacts, e.g. gear teeth, cams, roller bearings, etc. Therefore the film geometry equation will be deduced only for such cases.

2.4.1 Rigid Cylinders

In non-conformal contacts the area of contact is very small in comparison with the dimensions of the bodies, this facilitates an important simplification of the geometry: the contacting surface of a cylinder (or indeed any non-conformal surface) can be approximated to a mathematically simpler curve, a parabola, see Fig. 2.4.

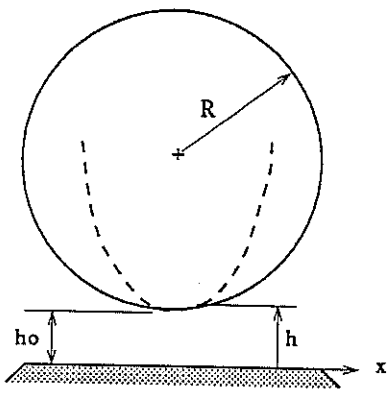

Figure 2.4: Approximation of the contact geometry by a parabola

Therefore the film thickness equation for a rigid cylinder against a flat surface can be written as:

$$h(x) \approx h_o + \frac{x^2}{2R} \tag{2.17}$$

2.4.2 Equivalent Cylinders

The contact between two cylinders can adequately be reduced, from the mathematical point of view, to the simpler geometry of an equivalent cylinder and a flat surface, as shown in Fig. 2.5.

From equation 2.17:

$$h \approx h_o + \frac{x^2}{2R_1} + \frac{x^2}{2R_2}$$

and for the equivalent cylinder:

$$h \approx h_o + \frac{x^2}{2R}$$

The separation of the bodies at any given x will be equal if:

$$\frac{1}{R} = \frac{1}{R_1} + \frac{1}{R_2}$$

for instance the equivalent cylinder has a radius:

$$R = \frac{R_1 R_2}{R_1 + R_2} \tag{2.18}$$

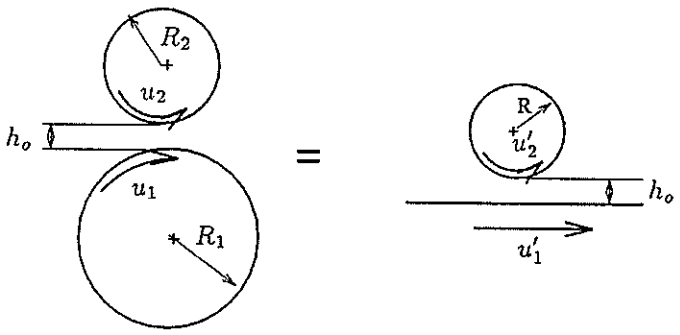

Figure 2.5: Equivalent cylinders

2.4.3 Elastic Deformation

If equation 2.17 has to be used with elastically deformable bodies, then the elastic displacements have to be added.

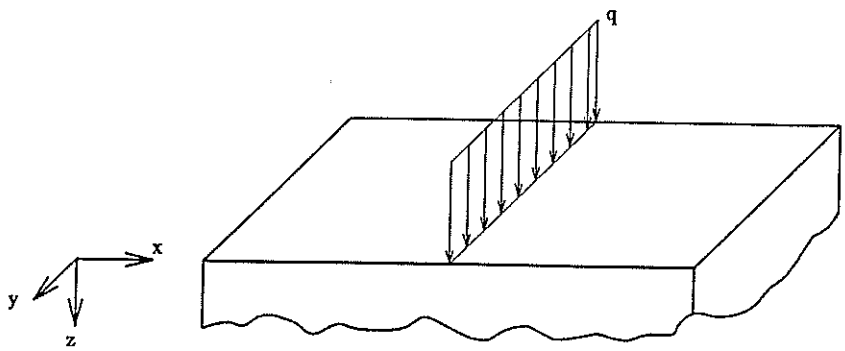

Figure 2.6: Line load on an elastic half-space

In non-conformal line contacts, the geometry of the body can be neglected in the elastic analysis and the contact can be treated as an elastic half-space with an assembly of line loads on its surface. Fig. 2.6 shows a half-space loaded with a line load on its surface.

Following Johnson [41] under plane strain conditions (no deformation in y direction) the elastic displacements $v(x)$ in z direction are given by:

$$v(x) = -\frac{2(1-\nu^2)}{\pi E} q \ln|\frac{x}{x_o}| \tag{2.19}$$

where: q = load per unit width, x_o = distance where $v = 0$, E = Young's modulus, ν = Poisson's ratio.

The displacements produced by a distributed load $p(x)$ are obtained by integrating equation 2.19

$$v(x) = -\frac{2(1-\nu^2)}{\pi E} \int_{-\infty}^{+\infty} \ln|\frac{x-x'}{x_o}| \, p(x')dx' + c \tag{2.20}$$

therefore the combined elastic deformation of upper and lower bodies is:

$$v(x) = -\frac{2}{\pi}\left\{\frac{(1-\nu_1^2)}{E_1} + \frac{(1-\nu_2^2)}{E_2}\right\} \int_{-\infty}^{+\infty} \ln|\frac{x-x'}{x_o}| \, p(x')dx' + c \tag{2.21}$$

and the film thickness geometry would be:

$$h \approx h_o + \frac{x^2}{2R} + v(x) \tag{2.22}$$

with $v(x)$ given by equation 2.21.

From equation 2.22 the 'plane strain' modulus E' is written:

$$\frac{2}{E'} = \frac{(1-\nu_1^2)}{E_1} + \frac{(1-\nu_2^2)}{E_2} \tag{2.23}$$

2.5 The Force Balance Equation

The entire external load pushing together the contacting surfaces has to be equal to the integral of the pressures in the film over the contact width. This condition guarantees the balance of forces. For line contacts it can be written as:

$$\int_{-\infty}^{+\infty} p(x)dx = w \tag{2.24}$$

where w is the external load per unit of width.

CHAPTER THREE

TRUNCATED HERTZIAN CONTACTS AND ITS APPLICATION TO EHL LINE CONTACTS. CENTRAL AND EXIT SOLUTION

Numerical solutions of heavily loaded EHL contacts have always been a challenge for computational techniques due to the difficulties to reach convergence.

Since the first robust numerical EHL solutions given by Dowson and Higginson [20], the search for more stable techniques to deal with even more complex models has not ended. Many approaches have been used: direct, inverse and variational methods, and recently multigrid techniques have been introduced to accelerate convergence.

However, the first successful EHL solution was not only numerical: in 1949 A.N. Grubin [31] suggested an important idealization of the contact geometry by considering the central zone having parallel film thickness, the value of which could be calculated by solving only the Reynolds equation at the inlet. The central zone was assumed to behave like a dry contact problem, so that in this zone no solution of the Reynolds equation was required since the pressures could be calculated by simple Hertzian theory. However, the Grubin approach by itself is not capable of predicting either film shape or pressures at the outlet of the contact.

In the 60's the importance of the outlet in providing the minimum film thickness had been understood due to the theoretical works of Petrusevich [63] 1951, Blok [7] 1959, Dowson and Higginson [20] 1959 and the measurements of Crook [19]. And now more convincingly by using optical EHL.

In 1972 Greenwood [28] extended the Grubin's theory by simply moving the flat region upstream, which produces an exit constriction in the shape and a pressure spike similar

to that exhibited by numerical solutions: approximations for the minimum film thickness then became possible.

The Greenwood's pressure distribution and shape may be considered analogous to the obtained from a partial indentation problem, e.g. Fig. 3.1; despite the fact that Greenwood did not use this idea to develop his work. However, the concept was first mentioned by Grubin himself and much later practically used by Christensen [15], 1979 and Prakash and Christensen [64], 1981.

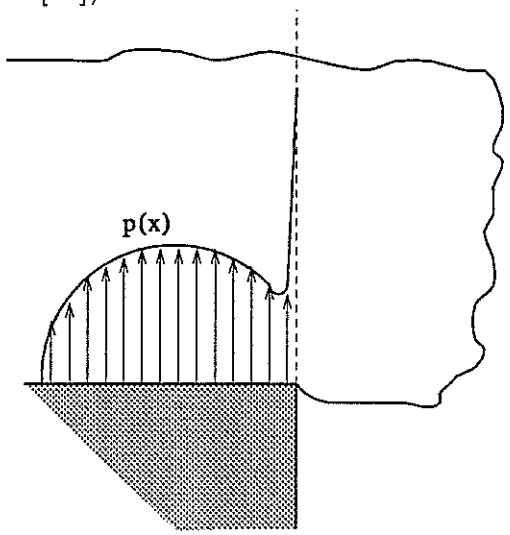

Figure 3.1: Partial indentation geometry

One of the major source of numerical difficulties in full EHL solutions is the large gradients of pressure surrounding the spike, the heavier the contact is the larger the pressure gradients are and the more difficult the numerical solution becomes. The main simplicity of the Grubin and Greenwood idealizations is that the solution of the Reynolds equation at the spike location is avoided. However, the main drawback is that both treatments neglect the inlet and outlet pressures as a cause of elastic deformations. The Grubin analysis does not account for the pressure spike at all and in the case of the Greenwood's extension the pressure spike is always one-sided, lying on the side of the flat region, so if the spike moves upstream the proportion of neglected pressures increases. Therefore Greenwood's treatment should only be used for contacts where the spike is close to the exit.

Clearly the next refinement of the Grubin and Greenwood analyses should be the generation of the inlet and outlet pressures by solving simultaneously the Reynolds and elasticity equations.

In this chapter an EHL analysis for Newtonian incompressible fluids which involves only the elastic deformation and pressures in the central and outlet zones is described. The work is based on a novel theoretical background developed by Greenwood and Johnson [29] 1989 which uses linear fracture mechanics theory to study the deformation and pressure distribution of truncated Hertzian dry contacts.

It will be shown that the outlet pressures can be closely described by a modified logarithmic function determined completely by two constants. As a consequence of this, the outlet shape joins the parallel film zone with an angle different from that (90°) predicted by the Greenwood scheme.

The described theory will be extended in Chapter 4 to produce a complete EHL solution method which includes the inlet.

3.1 Truncated Hertzian Contacts and Fracture Mechanics

Heavily loaded contacts in EHL have pressure distributions very similar to dry contact Hertzian pressures, these pressures are related to the nearly parallel film thickness also common in EHL. In the inlet and outlet the film ceases to be parallel and the pressures from being Hertzian. However, it looks reasonable to think of an analytical approach to generate EHL pressures which first considers a full Hertzian pressure distribution and then chops its edges off to replace them with the proper inlet and outlet EHL pressures while suitably modifying the central pressures.

Greenwood and Johnson [29] 1989 have solved the problem of replacing part of a Hertzian pressure distribution while maintaining a Hertzian flat over the remainder by using linear fracture mechanics theory.

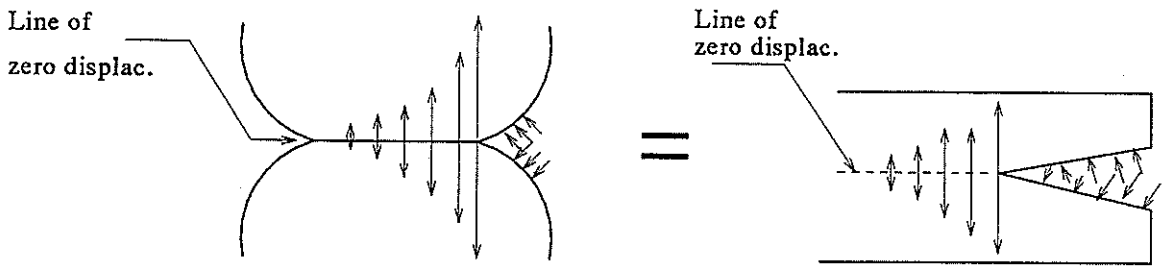

Figure 3.2: Geometrical similarity between a Hertzian contact and a crack

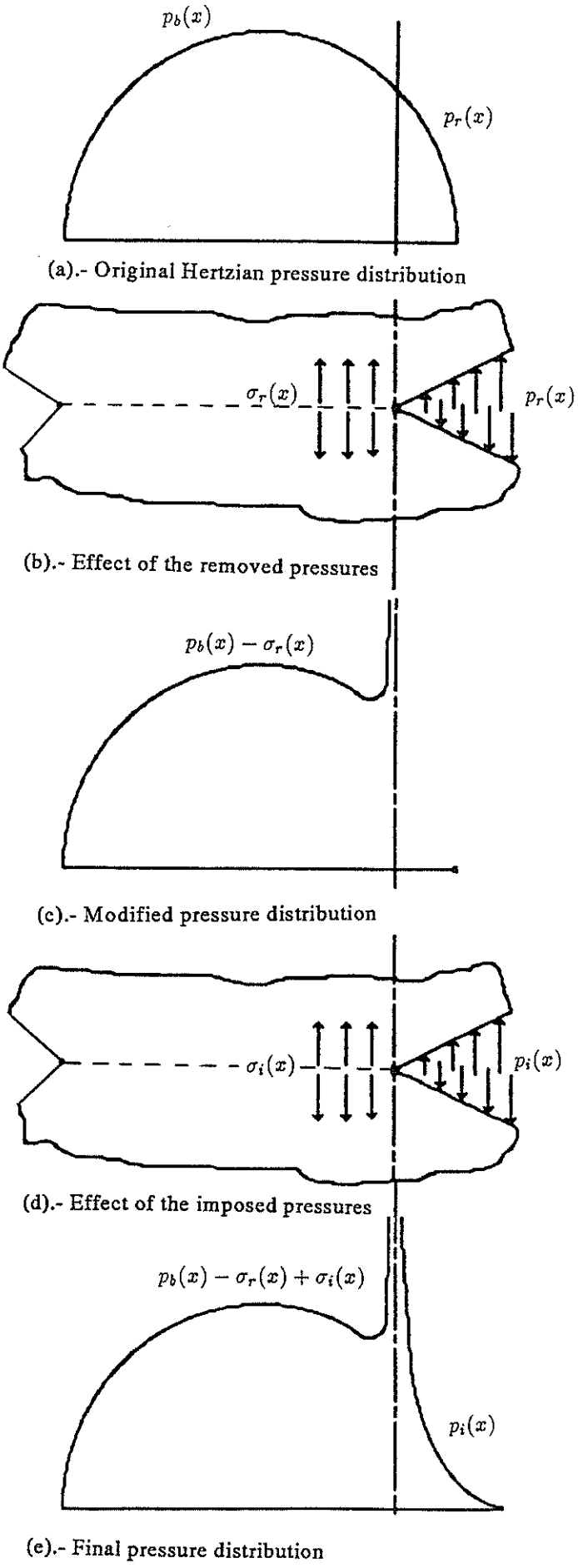

Figure 3.3: Replacement stresses scheme

It is well known that the only restriction for the application of elastic fracture mechanics equations is that in the cracked body the displacements on the line beyond the crack tip should be zero. So by considering the geometry of a dry Hertzian contact it is possible to see that after the initial Hertzian deformation has taken place, any external traction applied outside the contact (e.g. Fig. 3.2) would not produce displacements along the contact line, therefore the geometries are identical. So there is no reason which inhibits the use of elastic fracture mechanics theory to calculate the displacements and internal stresses due to external tractions in a Hertzian contact.

An EHL contact can be better represented by a doubly cracked body with tractions on both cracks, but for simplicity at the moment consider only tractions on the right hand side crack, representing the outlet region of the contact. Considering Fig. 3.3 it is possible to obtain a Hertzian flat by taking the original Hertzian pressure distribution (p_b); then a portion of these pressures is removed (p_r). Using fracture mechanics the effects on the remaining pressures can be calculated from the internal stresses (σ_r) and a modified Hertzian pressures are obtained ($p_b - \sigma_r$). After this, an external pressure distribution (p_i) can be imposed; again via internal stresses from fracture mechanics (σ_i) the effect on the modified Hertzian pressures can be calculated and added to obtain the final pressure distribution ($p_b - \sigma_r + \sigma_i$). The deformation is also obtained from fracture mechanics theory.

In EHL contacts, this concept can be applied to obtain pressure distributions and shapes from an original Hertzian flat.

3.2 Fracture Mechanics Theory

In a double cracked body with coplanar cracks and pressure distribution applied on one of them ($x_1 > a$), i.e. Fig. 3.4, along the line $y = 0$ and for $-a < x < a$, Greenwood and Johnson [29] found the internal stresses following the method introduced by Westergaard [81] 1939, as:

$$\sigma(x) = \frac{1}{\pi}\sqrt{\frac{a+x}{a-x}} \int_{x_1=a}^{\infty} p(x_1)\sqrt{\frac{x_1-a}{x_1+a}}\,\frac{dx_1}{x_1-x} \tag{3.1}$$

since $p(x_1) \to 0$ as $x_1 \to \infty$, a finite length L can be chosen for the integration. When $x \to a$, equation 3.1 tends to:

$$\sigma(x) \approx M\sqrt{\frac{a+x}{a-x}} \tag{3.2}$$

where M is a stress intensity factor, related to the more usual K_I by: $K_I = M\sqrt{4a\pi}$ (e.g. Barenblatt [3] 1962 and Schapery [71] 1975).

$$M = \frac{1}{\pi}\int_{x_1=a}^{L} \frac{p(x_1)}{\sqrt{x_1^2 - a^2}}\, dx_1 \tag{3.3}$$

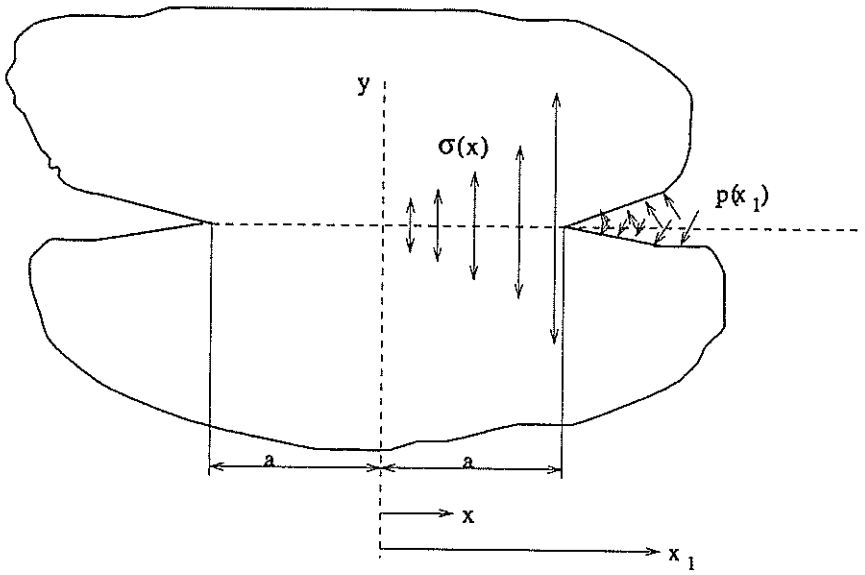

Figure 3.4: Double cracked body

Now, following Greenwood and Johnson [29] 1989 it is possible to rewrite equation 3.1 in its separate *singular* and *non-singular* terms:

$$\sigma(x) = \frac{1}{\pi}\sqrt{\frac{a+x}{a-x}}\int_{x_1=a}^{L} \frac{p(x_1)\, dx_1}{\sqrt{x_1^2 - a^2}} - \frac{\sqrt{a^2 - x^2}}{\pi}\int_{x_1=a}^{L} \frac{p(x_1)\, dx_1}{(x_1 - x)\sqrt{x_1^2 - a^2}} \tag{3.4}$$

where the first term of the RHS of equation 3.4 represents the square-root singular part and the second one is either finite or at most a weaker singularity.

Substituting equation 3.3 into the first term of the RHS of equation 3.4:

$$\sigma(x) = M\sqrt{\frac{a+x}{a-x}} - \frac{\sqrt{a^2 - x^2}}{\pi}\int_{x_1=a}^{L} \frac{p(x_1)}{(x_1 - x)\sqrt{x_1^2 - a^2}}\, dx_1 \tag{3.5}$$

Greenwood and Johnson have also shown that:

$$\sigma(x) = M\sqrt{\frac{a+x}{a-x}} - p(a)$$

$$-\frac{2}{\pi}\left[\int_{x_1=a}^{L} p'(x_1)\arctan\sqrt{\frac{x_1+a}{x_1-a}\,\frac{a-x}{a+x}}\,dx_1 - p(L)\arctan\sqrt{\frac{L+a}{L-a}\,\frac{a-x}{a+x}}\right] \tag{3.6}$$

where $p'(x_1)$ is the pressure gradient. And as $x \to a$, then by series:

$$\sigma(x) \approx M\sqrt{\frac{a+x}{a-x}} - p(a) + M_1\sqrt{\frac{a-x}{a+x}} \tag{3.7}$$

and M is defined by equation 3.3 and:

$$M_1 = \frac{2}{\pi}\left[-\int_{x_1=a}^{L} p'(x_1)\sqrt{\frac{x_1+a}{x_1-a}}\,dx_1 + p(L)\sqrt{\frac{L+a}{L-a}}\right] \tag{3.8}$$

where M_1 is also an stress intensity factor.

In order to obtain the slopes of the elastic displacements for the region $a < x < L$ corresponding to the pressures of equation 3.1, Greenwood and Johnson followed Westergaard's method to obtain:

$$\frac{E'}{2}\frac{\partial v}{\partial x} = \frac{1}{\pi}\sqrt{\frac{x+a}{x-a}}\int_{x_1=a}^{L} p(x_1)\sqrt{\frac{x_1-a}{x_1+a}}\,\frac{dx_1}{x_1-x} \tag{3.9}$$

or alternatively separating out the singular term:

$$\frac{E'}{2}\frac{\partial v}{\partial x} = M\sqrt{\frac{x+a}{x-a}} + \frac{1}{\pi}\sqrt{x^2-a^2}\int_{x_1=a}^{L}\frac{p(x_1)}{(x_1-x)\sqrt{x_1^2-a^2}}\,dx_1 \tag{3.10}$$

Either equation 3.9 or 3.10 can be integrated to obtain the elastic displacements.

3.3 Single Truncation

In this section the original Hertzian pressure distribution will be modified according to the ideas above described. Firstly the right hand side pressures will be removed and then replaced by the outlet EHL pressures, as shown in Fig. 3.6. From now on the term 'pressures' will be used for tractions applied beyond the Hertzian flat, and the term 'internal stresses' for tractions within the Hertzian flat $-a \leq x \leq a$, this convention is adopted for clarity and in accordance with fracture mechanics applications, though obviously in the EHL contact both are hydrodynamic pressures in the lubricant film.

3.3.1 Convention of Signs

At this point it is convenient to introduce the convention of signs used in the derivation of the equations.

a).- Compressive pressures applied:

A compressive pressure distribution $(-p)$ applied on the right hand side of the crack tip will produce tensile internal stresses $(+\sigma)$, see Fig. 3.5.

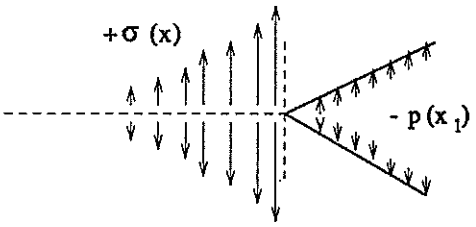

Figure 3.5: Convention of signs for compressive pressures

b).- Tensile pressures applied:

On the contrary, a tensile pressure distribution $(+p)$ applied on the right hand side of the crack tip will produce compressive internal stresses $(-\sigma)$.

3.3.2 The Removed Pressures

For a Hertzian flat extending from $x_1 = -a$ to $x_1 = 2b - a$ (i.e. Fig. 3.6) it is well known that the Hertzian pressures with the origin at the centre of the flat are given by:

$$p_b(x_1) = \frac{p_o}{b}\sqrt{(x_1 + a)(2b - a - x_1)} \tag{3.11}$$

with: p_o = maximum value.

In order to remove the Hertzian pressures for $a < x_1 < 2b - a$ a positive equal pressure distribution must be imposed. Substituting equation 3.11 into 3.3 and integrating from a to $2b - a$ the stress intensity factor due to the removed Hertzian pressures is:

$$M_h = Q(a - c) \tag{3.12}$$

where: $Q = p_o/b$. According to Fig. 3.6: $2a = b + c$, therefore:

$$M_h = \frac{Q}{2}(b-c) \tag{3.13}$$

The effect of removing this portion of pressures on the remaining Hertzian internal stresses $(-a < x < a)$ can be calculated by equation 3.5 which becomes:

$$\sigma_r(x) = M_h\sqrt{\frac{a+x}{a-x}} - \frac{\sqrt{a^2-x^2}}{\pi}\int_{x_1=a}^{2b-a}\frac{p_b(x_1)\,dx_1}{(x_1-x)\sqrt{x_1^2-a^2}} \tag{3.14}$$

and with $p_b(x_1)$ given by equation 3.11.

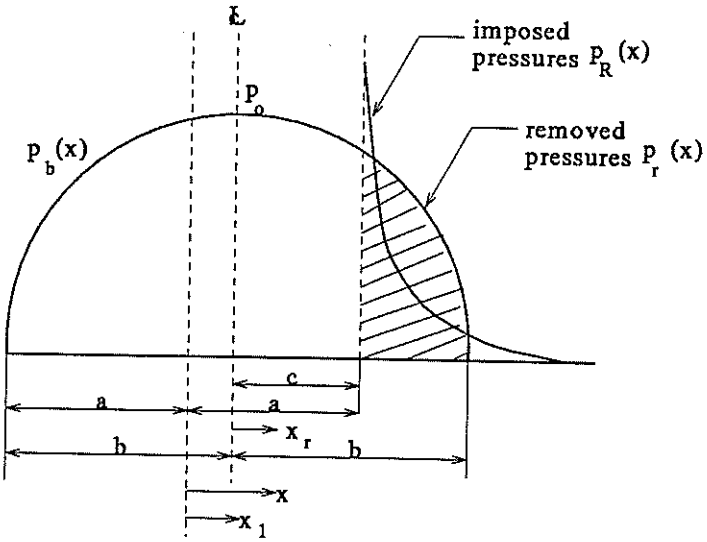

Figure 3.6: Replacement of pressures in a singly truncated Hertzian contact

The final modified internal stresses $(-a < x < a)$ are given by:

$$\sigma_t(x) = -p_b(x) - \sigma_r(x) = -Q\sqrt{(x+a)(2b-a-x)} - \sigma_r(x) \tag{3.15}$$

Solving the integral of equation 3.14 one obtains:

$$\sigma_t(x) = -Q\sqrt{a^2-x^2} - M_h\sqrt{\frac{a+x}{a-x}} \tag{3.16}$$

note that $\sigma_r(x)$ becomes ∞ as $x \to a$. $\sigma_t(x)$ is the pressure distribution found by Greenwood [28] by a different method and taken by him as the final pressures; however, here they will be modified to include the effect of the pressures applied on the outlet.

3.3.3 Hall's Thoughts About the Pressures Surrounding the Spike

Before introducing the imposed EHL outlet pressure distribution it is convenient to describe some important thoughts about its nature.

Kostreva [46] 1984, and later on Hall [32] 1989 have given arguments to suggest that the spike of pressures behaves as a logarithmic singularity, this concept is important in order to understand the nature of the outlet pressures in EHL.

Hall suggested that the exit bump of an EHL contact shape can be represented as shown in Fig. 3.7, where it can be seen that the bump joins the parallel film (h^*) smoothly with an angle ϕ. Three transition points can be identified at x_s^-, x_s and x_s^+ which for severe conditions of load: $x_s^+ \rightarrow x_s^-$ and $h(x_s^-) \rightarrow h(x_s^+) \rightarrow h^*$.

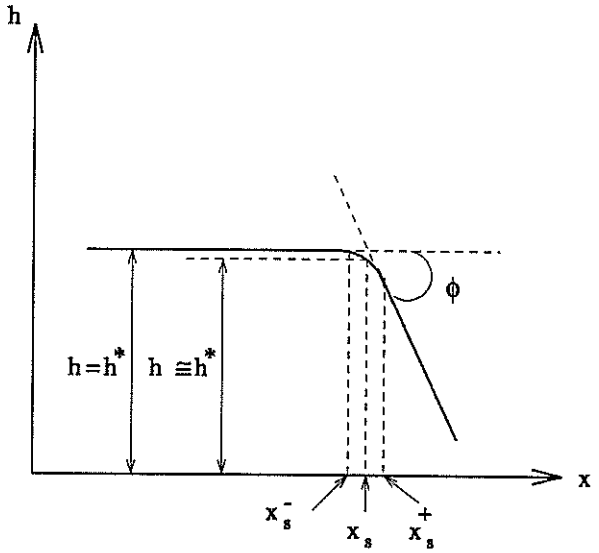

Figure 3.7: Hall's representation of the exit bump for an EHL contact shape

Integrating the Reynolds equation 3.30 between the limits x_s^+ and x ($x > x_s^+$):

$$-\frac{1}{\alpha}\left[e^{-\alpha p(x)} - e^{-\alpha p(x_s^+)}\right] = 12\eta_o\bar{u}\int_{x=x_s^+}^{x}\frac{h-h^*}{h^3}\,dx$$

and by approximating the integrand by its Taylor series in the region near x_s^+, one obtains:

$$-\frac{1}{\alpha}\left[e^{-\alpha p(x)} - e^{-\alpha p(x_s^+)}\right] \approx (x-x_s^+)^2\,\frac{6\eta_o\bar{u}}{(h^*)^3}\left[\frac{dh}{dx}(x_s^+)\right]$$

Observe that $p(x_s^+)$ is of the same order but larger than the pressure in the middle of the parallel zone p_o. Besides, $p(x_s^+) > p(x)$; and for typical values: $e^{-\alpha p_o} \approx 0$, so it is

possible to neglect the term $e^{-\alpha p(x_s^+)}$ and the equation is reduced to:

$$p(x) \approx (-2/\alpha)\ln(x - x_s^+) + constant \tag{3.17}$$

Similarly, on the left hand side of the spike:

$$p(x) \approx (-2/\alpha)\ln(x_s^- - x) + constant \tag{3.18}$$

Notice that equations 3.17 and 3.18 show singularities in both sides of the spike, at $x = x_s^+$ and $x = x_s^-$.

The first conclusion obtained by Hall from this analysis is that the pressure distribution is *closely logarithmic* and *singular* on both sides of the spike. This conclusion has certain elastic implications: according to Hall, by using integral transform methods for frictionless indentation problems, it can be shown that:

$$p(x) \approx \frac{\Delta h' E'}{4\pi} \ln|x - x_s| \tag{3.19}$$

where:

$$\Delta h' = \frac{dh}{dx}(x_s^+) - \frac{dh}{dx}(x_s^-)$$

But see Section 3.5.4 to check the coefficient of the RHS of equation 3.19.

By comparing equations 3.17 and 3.18 with equation 3.19 it seems that:

$$\Delta h' = \frac{-8\pi}{E'\alpha} \tag{3.20}$$

finally:

$$\phi = \arctan[\Delta h'] \tag{3.21}$$

The second conclusion obtained by Hall is that the internal angle of the film crease ϕ is not a right angle any more, contrary to the earlier finding by Greenwood.

In this thesis, once the theoretical background is explained, a contribution on the analysis of the exit shape and pressures will be described in Sections 3.5.2, 3.5.3 and 3.5.4. Also some thoughts about the behaviour of the pressure spike will be given in Chapter 4 (Section 4.5).

3.3.4 The Imposed Pressures

Once the Reynolds and elasticity equations have been solved for the outlet, a pressure distribution (nearly logarithmic and imposed on the right hand side) $p_R(x_1)$ for $a < x_1 \leq L$

is obtained. These pressures partially replace the portion previously removed. The effects of these imposed pressures are given again by equation 3.5 which becomes:

$$\sigma_i(x) = M_R\sqrt{\frac{a+x}{a-x}} - \frac{\sqrt{a^2-x^2}}{\pi}\int_{x_1=a}^{L}\frac{p_R(x_1)\,dx_1}{(x_1-x)\sqrt{x_1^2-a^2}} \tag{3.22}$$

where M_R is the corresponding intensity factor M for the pressures p_R, and is given by equation 3.3 with $p_R(x_1)$ for $p(x_1)$.

3.3.5 The Final Internal Stress Distribution

The final internal stress distribution for $-a \leq x < a$ is given by: $\sigma_f(x) = \sigma_t(x) + \sigma_i(x)$, it is to say:

$$\sigma_f(x) = -Q\sqrt{a^2-x^2} - (M_h - M_R)\sqrt{\frac{a+x}{a-x}} - \frac{\sqrt{a^2-x^2}}{\pi}\int_{x_1=a}^{L}\frac{p_R(x_1)\,dx_1}{(x_1-x)\sqrt{x_1^2-a^2}} \tag{3.23}$$

Note that if $M_h = M_R$, the square root singular term of $\sigma_f(x)$ vanishes giving a stress distribution with only a weaker singularity in the integrand due to the nearly logarithmic pressures $p_R(x_1)$.

At this point of the theory it will be convenient to remove the square root singularity, so the condition $M_h = M_R$ will be adopted and equation 3.23 becomes:

$$\sigma_f(x) = -Q\sqrt{a^2-x^2} - \frac{\sqrt{a^2-x^2}}{\pi}\int_{x_1=a}^{L}\frac{p_R(x_1)\,dx_1}{(x_1-x)\sqrt{x_1^2-a^2}} \tag{3.24}$$

3.3.6 The Final Shape

According to the basic condition for applying fracture mechanics to this problem: there are no displacements along the contact line ($-a \leq x < a$) due to the imposed pressures, therefore the only displacements to be calculated are the precise ones occurring on the external zone where the pressures are applied: $a < x \leq L$. The deformation slopes resulting after replacing the pressures are given according to equation 3.10 and the above procedure by:

$$\frac{E'}{2}\frac{\partial v}{\partial x} = (M_R - M_h)\sqrt{\frac{a+x}{x-a}} + \frac{1}{\pi}\sqrt{x^2-a^2}\int_{x_1=a}^{L}\frac{p_R(x_1)\,dx_1}{(x_1-x)\sqrt{x_1^2-a^2}} \tag{3.25}$$

provided $M_h = M_R$, this is:

$$\frac{E'}{2}\frac{\partial v}{\partial x} = \frac{1}{\pi}\sqrt{x^2 - a^2}\int_{x_1=a}^{L} \frac{p_R(x_1)\, dx_1}{(x_1 - x)\sqrt{x_1^2 - a^2}} \tag{3.26}$$

Once equation 3.25 is integrated the elastic displacements v can be obtained and in order to calculate the final deformed shape v_f, the original Hertzian shape $v_h(x)$ has to be added:

$$v_f(x) = v(x) + v_h(x) \tag{3.27}$$

Under the condition $M_h = M_R$ one can take the initial shape as Hertzian.:

$$v_h(x) = \frac{a^2}{2R}\left\{\frac{x}{a}\left[(\frac{x}{a})^2 - 1\right]^{1/2} - \ln\left(\frac{x}{a} + \left[(\frac{x}{a})^2 - 1\right]^{1/2}\right)\right\} \tag{3.28}$$

for $a < x \leq \infty$.

Notice that if in equation 3.25 only the square root singular term is integrated from a to x, the corresponding elastic displacements v_s are:

$$\frac{E'}{2}v_s = (M_R - M_h)\left\{\sqrt{(\frac{x}{a})^2 - 1} + 2\ln\left[\sqrt{\frac{x}{a} - 1} + \sqrt{\frac{x}{a} + 1}\right] - \ln 2\right\} \tag{3.29}$$

which is the basic function obtained by Greenwood [28] 1972 to describe the outlet displacements in his extension to the Grubin theory. In his solution the exit bump joined the flat forming a 90^o angle as expected from a square root singular pressure distribution.

3.4 Outlet Integration of the Reynolds Equation

Consider a Newtonian incompressible lubricant, from Chapter 2, the Reynolds equation is:

$$\frac{dp}{dx} = \frac{12\bar{u}\eta}{h^3}(h - h^*) \tag{3.30}$$

Using the substitution attributed to Grubin [31] 1949 but earlier used by Muskat and Evinger [58] 1940:

$$p = -\frac{1}{\alpha}\ln(1 - \alpha q) \tag{3.31}$$

where q is the so-called reduced pressure; α is the pressure-viscosity index of the lubricant according to the Barus's law (e.g. Section 2.2).

The final displacements are:

$$v_f(x) = h(x) - h^* \tag{3.32}$$

therefore substituting equations 3.31 and 3.32 into equation 3.30 the Reynolds equation can be reduced to:

$$\frac{dq}{dx} = 12\bar{u}\eta_o \frac{v_f(x)}{[h^* + v_f(x)]^3} \tag{3.33}$$

where the coefficient $12\bar{u}\eta_o$ is a constant.

The boundary conditions of equation 3.33 for the outlet can be calculated by firstly considering that at $x = a$, $p_R = \infty$ (pressure spike) so that from equation 3.31: $q(a) = 1/\alpha$. Integrating equation 3.33:

$$q(x) = q(a) - 12\bar{u}\eta_o I(x)$$

therefore:

$$q(x) = \frac{1}{\alpha} - 12\bar{u}\eta_o I(x) \tag{3.34}$$

where:

$$I(x) = \int_{x=a}^{x} \frac{v_f(x)}{[h^* + v_f(x)]^3}\, dx \tag{3.35}$$

Secondly, at $x = L$ (end of the outlet) $p_R = 0$, so $q(L) = 0$, hence from equation 3.34:

$$q(L) = 0 = \frac{1}{\alpha} - 12\eta_o \bar{u} I(L)$$

where:

$$I(L) = \int_{x=a}^{L} \frac{v_f(x)}{[h^* + v_f(x)]^3}\, dx \tag{3.36}$$

thus:

$$12\eta_o \bar{u} I(L) = \frac{1}{\alpha} \tag{3.37}$$

Substituting equation 3.34 into equation 3.31 and then substituting equation 3.37 into the result it is possible to obtain:

$$p(x) = -\frac{1}{\alpha} \ln \left[\frac{I(x)}{I(L)} \right] \tag{3.38}$$

Equations 3.35, 3.36 and 3.38 give the outlet pressure distribution which satisfies the Reynolds equation 3.30 and its boundary conditions.

3.4.1 Non-Dimensionalisation

Consider the following definitions:

$$X = x/a,\ V(X) = \frac{2R}{a^2} v(x),\ P = \frac{4R}{aE'} p = p/p_a^*,\ \hat{M} = M/p_a^*$$

where p_a^* is the maximum Hertzian pressure corresponding to a dry contact of length $2a$ and it is only a convenient constant, since the fracture mechanics equations are simpler in terms of a. The non-dimensional forms for the elastic equations 3.12, 3.24, 3.26 and 3.28 are:

$$\hat{M}_h = 1 - c/a \tag{3.39}$$

$$P_f(X) = \sqrt{1 - X^2} + \frac{1}{\pi} \sqrt{1 - X^2} \int_{X_1=1}^{L/a} \frac{P_R(X_1)\, dX_1}{(X_1 - X)\sqrt{X_1^2 - 1}} \tag{3.40}$$

$$\left(\frac{\partial V}{\partial X}\right) = +\frac{1}{\pi} \sqrt{X^2 - 1} \int_{X_1=1}^{L/a} \frac{P_R(X_1)\, dX_1}{(X_1 - X)\sqrt{X_1^2 - 1}} \tag{3.41}$$

$$V_h(X) = X[X^2 - 1]^{1/2} - \ln[X + (X^2 - 1)^{1/2}] \tag{3.42}$$

For the hydrodynamic equations consider the definitions already made and now include the following ones:

$$\hat{q} = \frac{4R}{aE'} q = q/p_a^*,\quad H = \frac{2R}{a^2} h$$

$$K_1 = \frac{\alpha E' a}{4R} = \alpha p_a^*, \quad K = \frac{E' a^4}{192 R^3 \eta_o \bar{u}}$$

Therefore equations 3.38, 3.35, 3.36 and 3.37 become:

$$P(X) = -\frac{1}{K_1} \ln[\frac{I(X)}{I(L/a)}] \tag{3.43}$$

$$I(X) = \int_{X=1}^{X} \frac{V_f(X)}{[H^* + V_f(X)]^3} \, dX \tag{3.44}$$

$$I(L/a) = \int_{X=1}^{L/a} \frac{V_f(X)}{[H^* + V_f(X)]^3} \, dX \tag{3.45}$$

$$K = K_1 I(L/a) \tag{3.46}$$

3.4.2 Outlet Computational Procedure

a).- Suggest an initial logarithmic pressure distribution (as implied by Hall):

$$P = B \ln(\frac{X-1}{L-1})$$

for $1 < X \leq L/a$. Enter the values of: K_1, H^*.

b).- Solve equation 3.41 to obtain the slopes for the elastic displacements. Then integrate them to obtain the displacements $V(X)$.

c).- Add the Hertzian shape from equation 3.42 to obtain the final shape $V_f(X)$.

d).- Integrate the Reynolds equation 3.43 to calculate the new pressures $P(X)$. Solve equation 3.46 to find the corresponding K.

e).- Go back to (b) until convergence in pressures and shape is reached.

f).- At this point the central region stresses can be calculated with equation 3.40.

The integrals of the final pressure and slope equations can be solved numerically by following the schemes given in Appendix A.

Note that at this point in the process there is no way to calculate the central film thickness, the procedure requires it as an input parameter.

3.5 Outlet Solutions

3.5.1 Comparison with Greenwood's Scheme

In order to investigate the behaviour of the present scheme, it is easier to start by isolating and solving the EHL outlet region. Then comparisons of results with the Greenwood's scheme are possible. An interesting comparison is obtained by matching in both theories the values of the integral $I(L)$ and the central film thickness h^*. Since the only difference between the two schemes is the inclusion of the outlet pressures by the present theory, then the minimum film thickness calculated with the present scheme is expected to be larger than its Greenwood equivalent, and therefore the outlet length in the present theory must be larger.

The exit shape according to Greenwood [28] is obtained by considering only the elastic effect of the central region pressures and it is given in dimensionless form by:

$$V_f(X) = X\sqrt{X^2-1} - \cosh^{-1} X - 2\mu\left\{\sqrt{X^2-1} + \cosh^{-1} X\right\} \tag{3.47}$$

where: $\mu = 1 - c/a$.

Greenwood defined the total load (which excludes the inlet) as:

$$Q_g = \left\{\frac{\pi b_h^3}{8\alpha\eta_o\bar{u}R^2}\right\}^{1/2}$$

and it is related to the dimensionless constants K and K_1 by:

$$Q_g = \left\{6\pi^3(1+2\mu)^{3/2}(\frac{K}{K_1})\right\}^{1/2} \tag{3.48}$$

The integral $I(L)$ for the present scheme, in dimensionless form, is given by equation 3.45, and it is related to the variables K_1 and K by equation 3.46, from which:

$$I(L/a) = K/K_1$$

and substituting into equation 3.48, this leads to:

$$(6\pi^3)I(L/a) = \frac{Q_g^2}{(1+2\mu)^{3/2}} \tag{3.49}$$

which relates the Greenwood's parameters Q_g and μ with $I(L/a)$. Note that $\mu = \hat{M}_h$ since both are equal to $1 - c/a$.

							central+outlet
Example	K_1	K	H^*	L/a	B_f	K/K_1	$\hat{W}$
1	6.900	67.328	0.050	1.082	-0.257	9.758	1.757
2	5.580	19.650	0.100	1.127	-0.317	3.521	1.857
3	4.100	4.014	0.250	1.228	-0.432	0.979	2.096
4	3.250	1.251	0.500	1.358	-0.546	0.385	2.410
5	2.600	0.357	1.000	1.544	-0.682	0.137	2.878
6	1.900	0.076	2.500	1.973	-0.936	0.040	4.038
with B_f defined in Section 3.5.2							

Table 3.1: Present theory parameters

Present Theory						
Example	$6\pi^3 I(L/a)$	H_o	h_{min}/h^*	$\hat{M}_R$	H	c/b_h
1	1815.300	0.100	0.766	0.059	0.089	0.890
2	655.128	0.200	0.776	0.091	0.169	0.836
3	182.124	0.500	0.780	0.165	0.375	0.723
4	71.596	1.000	0.790	0.261	0.652	0.597
5	25.570	2.000	0.790	0.400	1.091	0.443
6	7.471	5.000	0.791	0.731	1.945	0.168
Greenwood's Theory						
Example	$6\pi^3 I(L/a)$	H_o	h_{min}/h^*	μ	H	c/b_h
1	1714.630	0.100	0.751	0.022	0.096	0.957
2	668.390	0.200	0.753	0.035	0.187	0.933
3	190.166	0.500	0.765	0.064	0.443	0.881
4	72.675	1.000	0.758	0.100	0.833	0.821
5	27.462	2.000	0.763	0.157	1.521	0.735
6	7.443	5.000	0.769	0.284	3.190	0.572

Table 3.2: Outlet results comparisons

The dimensionless central film thickness used by Greenwood is defined as:

$$H_o = \frac{4Rh^*}{a^2}$$

which also can be written as:

$$H_o = 2H^* \tag{3.50}$$

another dimensionless film thickness given by Greenwood as a function of an equivalent dry contact Hertzian width is:

$$H = \frac{4Rh^*}{b_h^2}$$

And b_h represents the half width of the equivalent Hertzian contact with the same total load (excluding the inlet and outlet) as the EHL contact under consideration.

Now, using Hertz theory it can be proved (Section 4.3.3) that:

$$\frac{a^2}{b_h^2} = \frac{\pi}{2\hat{W}}$$

where $\hat{W}$ is the dimensionless total load (in this case excluding only the inlet) and it is calculated by integrating the pressures p/p_a^*, so $\hat{W} = w/ap_a^*$; therefore H, for the present scheme, can be written as:

$$H = \frac{\pi H^*}{2\hat{W}} \tag{3.51}$$

The spike location corresponding to the Greenwood scheme is given by:

$$\frac{c}{b_h} = \frac{1-\mu}{\sqrt{1+2\mu}} \tag{3.52}$$

in the present theory, from equation 3.39: $c/a = 1 - \hat{M}_h$ and changing from a to b_h (see also Section 4.3.3) it gives:

$$\frac{c}{b_h} = \frac{1-\hat{M}_R}{\sqrt{2\hat{W}/\pi}} \tag{3.53}$$

Table 3.1 gives the parameters of several solutions obtained with the present theory which are compared with the Greenwood's results in Table 3.2. It is possible to see that in general the two theories agree better for large values of $I(L/a)$ where the effect from the outlet pressures is small.

The shapes corresponding to examples 2, 4 and 6 are shown in Fig. 3.8, Fig. 3.9 and Fig. 3.10; where the depth of the exit bump from the present scheme, is always smaller (larger h_{min}) than that predicted by the Greenwood's scheme; for accurate values compare the columns h_{min}/h^* in table 3.2. Note that under these circumstances and with equal $I(L/a)$ and H_o the length of the outlet zone L in the present theory, is expected to be always larger than the Greenwood's value; and according to the figures it is indeed larger. The corresponding outlet pressure distributions for the shapes are shown in Fig. 3.11.

Table 3.2 also shows that the spike location by the Greenwood's scheme gives always larger values than the present theory; the reason is because the load for the present theory includes also the outlet pressures. It also can be seen that the disagreement on c/b_h is worse for large values of L; when the difference in load is larger.

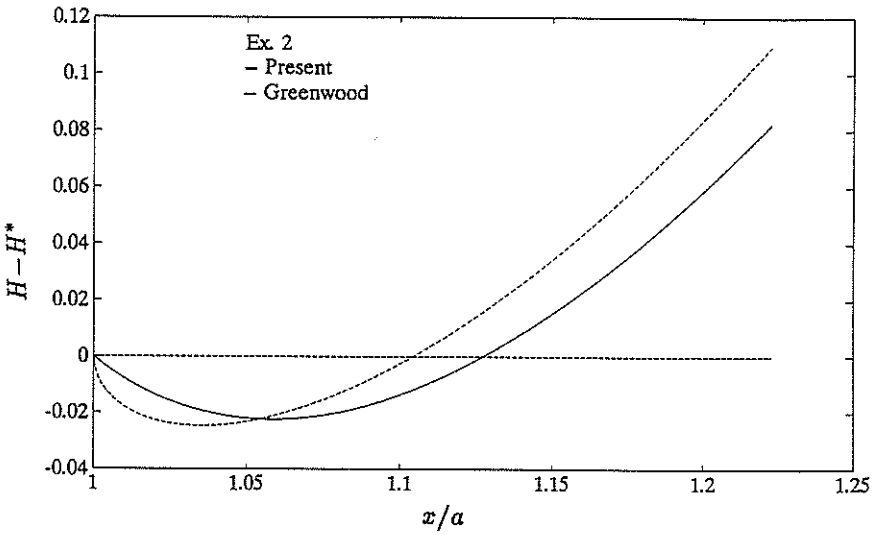

Figure 3.8: Exit shape comparison, matching $I(L/a)$ and H_o. Example 2

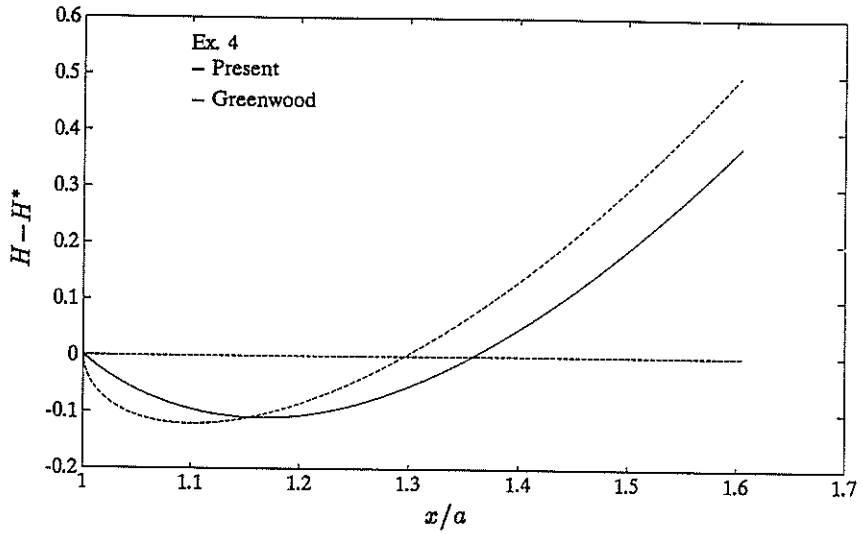

Figure 3.9: Exit shape comparison, matching $I(L/a)$ and H_o. Example 4

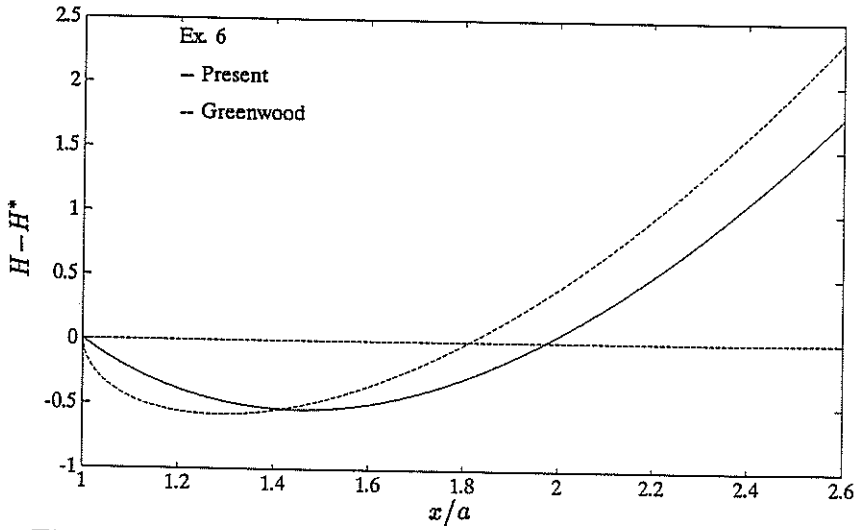

Figure 3.10: Exit shape comparison, matching $I(L/a)$ and H_o. Example 6

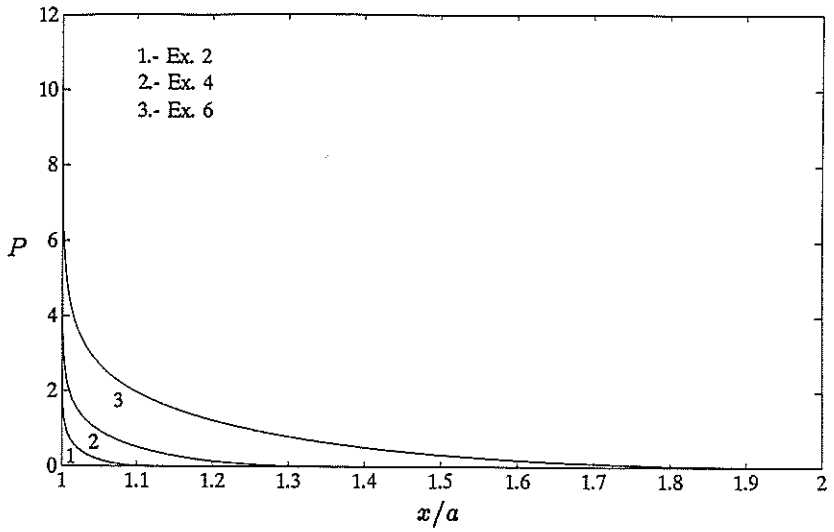

Figure 3.11: Exit pressures, present theory

3.5.2 The Outlet Pressure Distribution

Several investigations have been addressed towards the nature of the pressure spike in EHL contacts and there are major analytical attempts to relate the outlet pressures to a known mathematical function. Both Kostreva [46] 1984 and Hall [32] 1989 have shown that the pressures closely behave as a logarithmic singularity in the region neighbouring the spike. According to the analysis of Hall (i.e. Section 3.3.3), this logarithmic singularity results in the slopes of the final shape at the beginning of the exit bump becoming finite with a known value, unlike Greenwood's theory which predicts infinite slopes at that point, see Fig. 3.12.

By looking at Figs. 3.8 to 3.10 it is possible to see that the shapes obtained by the present theory look more similar to the Hall's prediction than the Greenwood one.

Then, performing a simple curve fitting analysis it was found that the outlet pressures are very well described by the function:

$$p = B\left[\frac{L-x}{L-a}\right]\ln\left(\frac{x-a}{L-a}\right) \tag{3.54}$$

or in dimensionless form:

$$P = B_f\left[\frac{L/a-X}{L/a-1}\right]\ln\left(\frac{X-1}{L/a-1}\right) \tag{3.55}$$

where $B_f = B/p_a^*$ and L/a are the two constants which fully define the outlet pressure

distribution. In a converged solution their values can be calculated by choosing two values of X and solving equation 3.55.

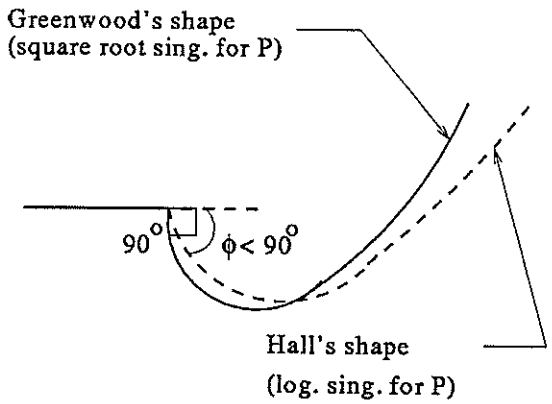

Figure 3.12: The exit shape bump according to two theories

Using the values of Table 3.1 the pressures of the same three examples of Fig. 3.11 have been compared with the approximation of equation 3.55 in Figs. 3.13 to 3.15, the agreement is always good. The same comparison was carried out with many other solutions giving always good agreement.

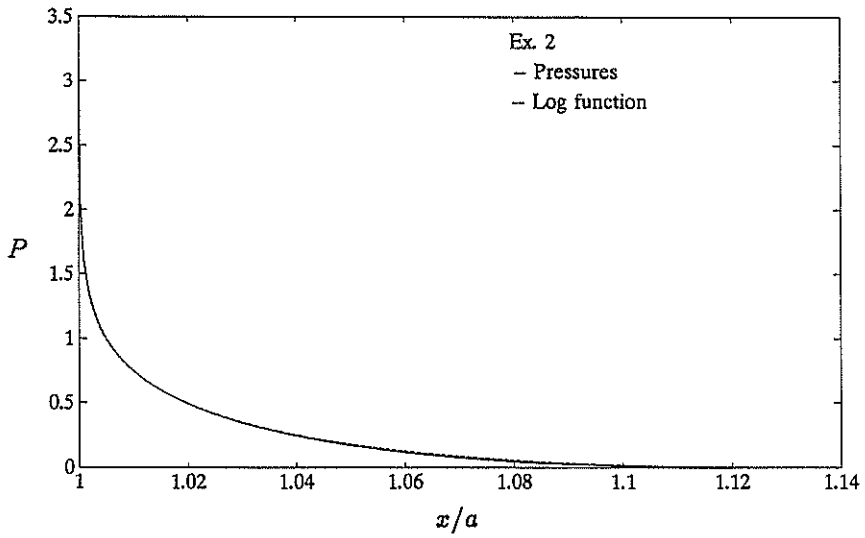

Figure 3.13: Outlet pressures comparison, example 2

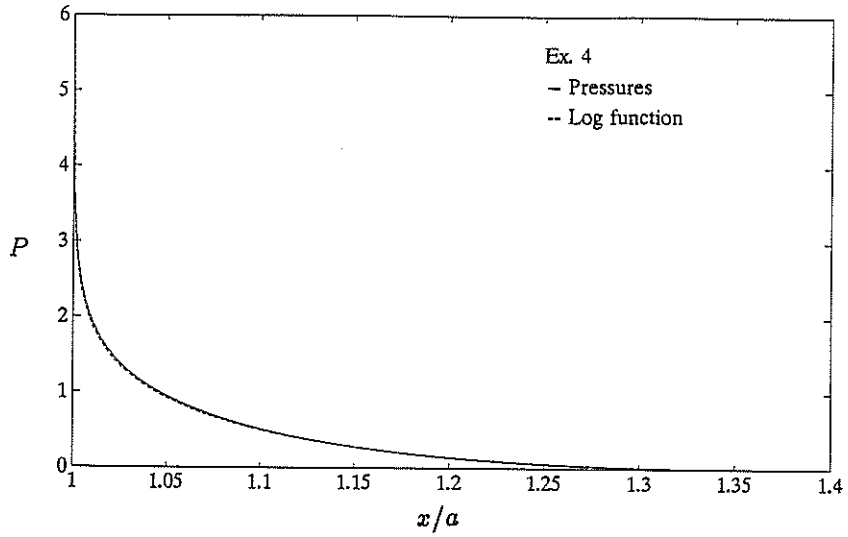

Figure 3.14: Outlet pressures comparison, example 4

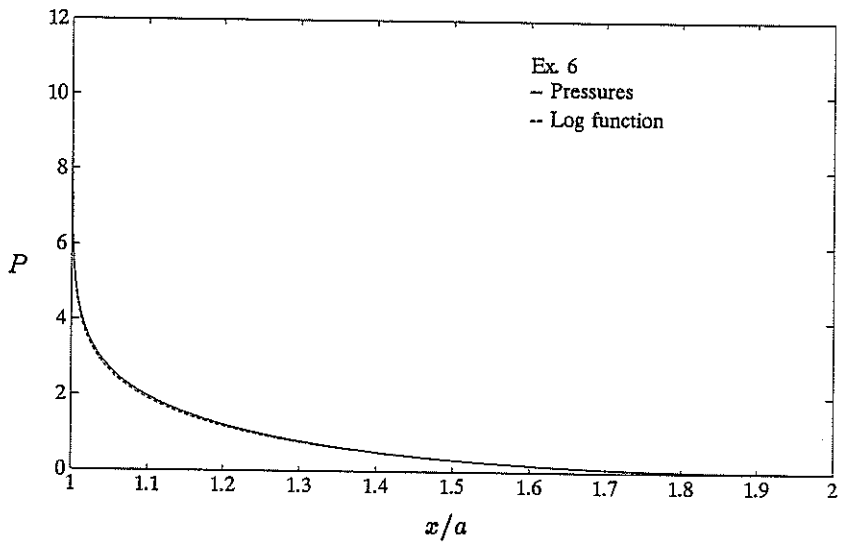

Figure 3.15: Outlet pressures comparison, example 6

3.5.3 Relation $B_f - K_1$

Assuming that near to the beginning of the outlet, the displacements V_f vary linearly along X (i.e. Fig. 3.16) hence, the displacements are given by:

$$V_f(X) = -(\tan\phi)(X-1) \tag{3.56}$$

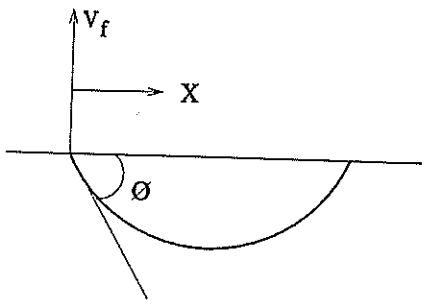

Figure 3.16: Linear shape variation at the beginning of the exit bump

with:

$$\tan\phi = \frac{V_f}{X-1}$$

substituting equation 3.56 into the dimensionless Reynolds equation:

$$\frac{d\hat{q}}{dX} = \frac{1}{K}\frac{V_f}{(H^* + V_f)^3}$$

and applying the boundary conditions of Section 3.4 then:

$$\hat{q} = \frac{1}{K_1} - \frac{\tan\phi}{K(H^*)^3}\left[\frac{(X-1)^2}{2}\right] \tag{3.57}$$

according to equation 3.31 the relationship of P and $\hat{q}$ is given by:

$$K_1 P = -\ln(1 - K_1\hat{q})$$

substituting equation 3.57, and solving:

$$K_1 P = -2\ln(X-1) - ln[\frac{K_1\tan\phi}{2K(H^*)^3}] \tag{3.58}$$

Notice that the approximated pressures (equation 3.55) as $X \to 1$ behave as:

$$P \approx B_f \ln(X-1) - B_f \ln(L/a - 1) \tag{3.59}$$

multiplying equation 3.59 by K_1 and comparing the result with equation 3.58 it is easy to find that:

$$K_1 B_f \approx -2 \tag{3.60}$$

$$(L/a-1)^{-2} \approx \frac{K_1 \tan\phi}{2|K|(H^*)^3} \tag{3.61}$$

3.5.4 Analytical Expression for the Shape Slope and its Limiting Value

If the length of the contact is not very small, the outlet region can be elastically independent from the inlet, so the slopes of the elastic displacements are given by equation 3.25 and with $M_h = M_R$ it is:

$$\frac{E'}{2}\frac{\partial v}{\partial x} = \frac{\sqrt{x^2-a^2}}{\pi}\int_{x_1=a}^{L} \frac{P_R(x_1)}{(x_1-x)\sqrt{x_1^2-a^2}}\,dx_1 \tag{3.62}$$

substituting the approximated outlet pressures equation 3.54:

$$\frac{E'}{2}\frac{\partial v}{\partial x} = \frac{\sqrt{x^2-a^2}}{\pi}\int_{x_1=a}^{L} \frac{B\frac{L-x_1}{L-a}\ln(\frac{x_1-a}{L-a})}{(x_1-x)\sqrt{x_1^2-a^2}}\,dx_1 \tag{3.63}$$

writing: $\varepsilon = x-a$, $L' = L-a$, $t = \sqrt{(x_1-a)/(\varepsilon)}$ and $l = \sqrt{L'/(x-a)}$, equation 3.63 becomes:

$$\frac{E'}{2}\frac{\partial v}{\partial x} = \frac{2B}{\pi L'}\sqrt{\varepsilon+2a}\,[2L'I_1 + L'\ln(\varepsilon/L')I_2 - 2\varepsilon I_3 - \varepsilon\ln(\varepsilon/L')I_4] \tag{3.64}$$

where:

$$I_1 = \int_{t=0}^{l} \frac{\ln t}{(t^2-1)\sqrt{\varepsilon t^2+2a}}\,dt \tag{3.65}$$

$$I_2 = \int_{t=0}^{l} \frac{dt}{(t^2-1)\sqrt{\varepsilon t^2+2a}} \tag{3.66}$$

$$I_3 = \int_{t=0}^{l} \frac{t^2\ln t}{(t^2-1)\sqrt{\varepsilon t^2+2a}}\,dt \tag{3.67}$$

$$I_4 = \int_{t=0}^{l} \frac{t^2}{(t^2-1)\sqrt{\varepsilon t^2+2a}}\,dt \tag{3.68}$$

In the solutions of the integrals I_1 and I_3 it is possible to approximate by series:

$$\frac{1}{\sqrt{2a+\varepsilon t^2}} \approx \frac{1}{\sqrt{2a}[1+(\varepsilon t^2)/4a]}$$

for $\varepsilon \to 0$. So the solution can be proved to be:

$$I_1 = \frac{1}{(4a+\varepsilon)}\left[4aI_o - \sqrt{4a\varepsilon}\ln l \tan^{-1}(l\sqrt{\varepsilon/4a}) + \sqrt{4a\varepsilon}I_p\right] \tag{3.69}$$

$$I_2 = \frac{1}{2\sqrt{2a+\varepsilon}}\ln\left|\frac{l\sqrt{2a+\varepsilon} - \sqrt{2a+\varepsilon l^2}}{l\sqrt{2a+\varepsilon} + \sqrt{2a+\varepsilon l^2}}\right| \tag{3.70}$$

$$I_3 = \frac{2\sqrt{2a}}{\varepsilon+4a}\left[\sqrt{4a/\varepsilon}\ln l \tan^{-1}(l\sqrt{\varepsilon/4a}) - \sqrt{4a/\varepsilon}I_p + I_o\right] \tag{3.71}$$

$$I_4 = \frac{1}{\sqrt{\varepsilon}}\left[\ln(l\sqrt{\varepsilon} + \sqrt{\varepsilon l^2 + 2a}) - \ln\sqrt{2a}\right] + I_2 \tag{3.72}$$

With:

$$I_o = \int_{t=0}^{l} \frac{\ln t}{t^2-1}\,dt = \frac{\pi^2}{8} + f(m) - \frac{1}{4}f(m^2) \tag{3.73}$$

$$I_p = l\sqrt{\varepsilon/(4a)} - \frac{(l\sqrt{\varepsilon/(4a)})^3}{3^2} + \frac{(l\sqrt{\varepsilon/(4a)})^5}{5^2} - \frac{(l\sqrt{\varepsilon/(4a)})^7}{7^2} + ... \tag{3.74}$$

$$f(z) = -\ln z \ln(1-z) + \frac{\pi^2}{6} - \sum_{k=1}^{\infty}(-1)^k\frac{(-z)^k}{k^2} \tag{3.75}$$

for $1 \geq z \geq 0$.

The dimensionless form of equations 3.64 to 3.75 are given by the same relations but substituting L' by $L/a-1$; ε by $X-1$; l by $\sqrt{\frac{L/a-1}{X}}$; m by $1/l$; B by B_f and a by 1.

The limiting value of equation 3.64 as $x \to a$ ($\varepsilon \to 0$) is given by:

$$\lim_{x\to a}\left(\frac{E'}{2}\frac{\partial v}{\partial x}\right) = \frac{2B}{\pi L'}\sqrt{2a}\left[\frac{2L'}{\sqrt{2a}}\left(\lim_{\varepsilon\to 0} I_o\right)\right]$$

and:

$$\lim_{\varepsilon\to 0} I_o = \frac{1}{4}\pi^2$$

since the Hertzian displacements for the outlet (i.e. equation 3.28) have zero slopes at $x = a$, then:

$$\lim_{x\to a}\left(\frac{\partial v_f}{\partial x}\right) = \frac{2\pi B}{E'} \tag{3.76}$$

and in dimensionless form:

$$\lim_{X\to 1}(\frac{\partial V_f}{\partial X}) = B_f \pi \tag{3.77}$$

By using the approximation of equation 3.60: $B = B_f p_a^* \approx -2/\alpha$, and therefore:

$$\lim_{x\to a}(\frac{\partial v_f}{\partial x}) = \frac{-4\pi}{\alpha E'} \tag{3.78}$$

Finally the angle ϕ of Fig. 3.7 is:

$$\phi = \arctan \frac{-4\pi}{\alpha E'} \tag{3.79}$$

which is exactly a half of the value obtained by Hall in Section 3.3.3. Despite the disagreement in shapes, the pressures agree very well; equation 3.54 for $x \approx a$ becomes a pure logarithmic function, and from equation 3.60, in dimensional form: $B = -2/\alpha$ which is the same value predicted by Hall for the coefficient of his logarithmic pressure (equations 3.17 and 3.18). Besides all this, in an earlier article, Hall and Savage [33] 1988 solve a rigid punch example (example 2) with contact length $2a$ which for $x \approx a$ exhibit pressures:

$$p \approx B \ln |x|$$

and with:

$$B = \frac{E'}{2\pi} \tan \phi$$

for $B = -2/\alpha$ one obtains: $\tan \phi = -4\pi/\alpha E'$ which is the result predicted by the present theory. So it is now believed that the coefficient of the RHS of Hall's equation 3.19 must indeed be:

$$\frac{\Delta h' E'}{2\pi}$$

Numerical example:

Consider the following outlet solution:

$$\begin{array}{ll} B_f = -0.385 & h_{min}/h^* = 0.864 \\ L/a = 1.177 & K_1 = 4.5 \\ H^* = 0.200 & K = 1.367 \end{array}$$

Example	K	H^*	K_1	B_f	$K_1 B_f$	$\lvert\tan\phi\rvert$	L/a	L/a eq. 3.61
1	0.002	19.546	1.0	-1.879	-1.879	5.904	4.111	3.073
2	0.079	2.279	2.0	-0.918	-1.836	2.883	1.880	1.568
3	54.314	0.068	6.0	-0.312	-1.872	0.980	1.110	1.077
4	117.863	0.043	7.0	-0.267	-1.873	0.839	1.081	1.057
5	529.486	0.019	9.0	-0.212	-1.904	0.665	1.050	1.036
6	895.880	0.014	10.0	-0.190	-1.902	0.597	1.041	1.029
7	1439.289	0.011	11.0	-0.173	-1.905	0.544	1.034	1.024

Table 3.3: Outlet solutions, testing equations 3.60 and 3.61

Fig. 3.17 shows the converged pressure distribution, Fig. 3.18 shows the comparison between the converged slopes and the result from the analytical solution (i.e. equation 3.64 and equations 3.69 to 3.75), finally Fig. 3.19 shows the corresponding final shapes (including the Hertzian displacements).

Fig. 3.17 shows the good agreement for the elastic slopes between the two methods. The curves slightly diverge for high values of X due to the increment of error in the approximation by series used in the solution of the integrals I_1 and I_3, however, the difference is still small and this is in general typical for any other solution. Equation 3.77 also agrees well with the numerically calculated limit.

Now a set of outlet solutions is shown in Table 3.3 where equations 3.60 and 3.61 are tested, for which it has been taken $\tan\phi \approx B_f\pi$:

It can be seen that the values given by equation 3.60 are more or less similar to the ones obtained from the numerical solution ($K_1 B_f \approx -2$). The results for L/a from equation 3.61 are not so close to the numerical solution but at least they follow the same pattern. And for an initial guess the solution is good enough if the value of K is known.

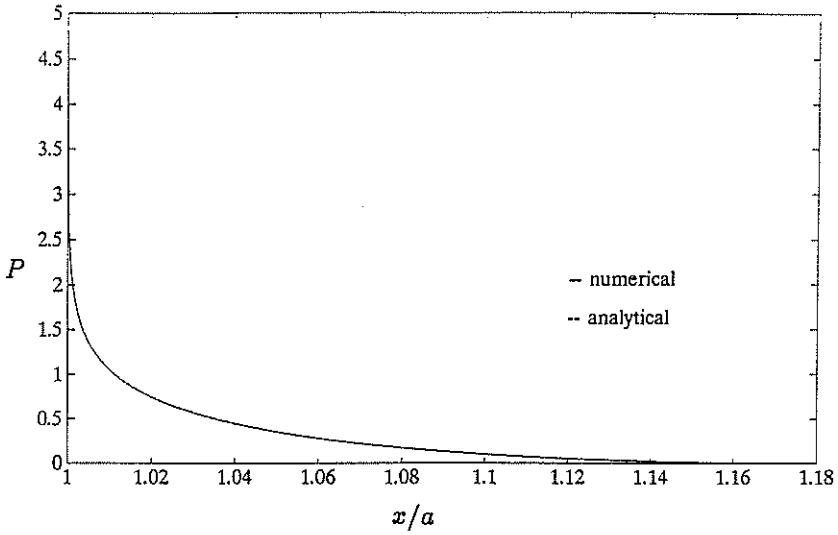

Figure 3.17: Converged outlet pressures

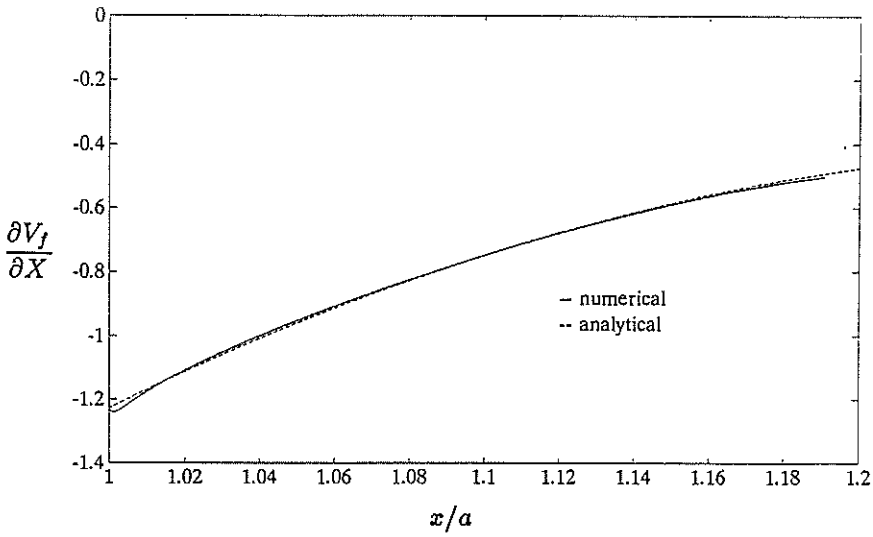

Figure 3.18: Comparison of numerical and analytical slopes

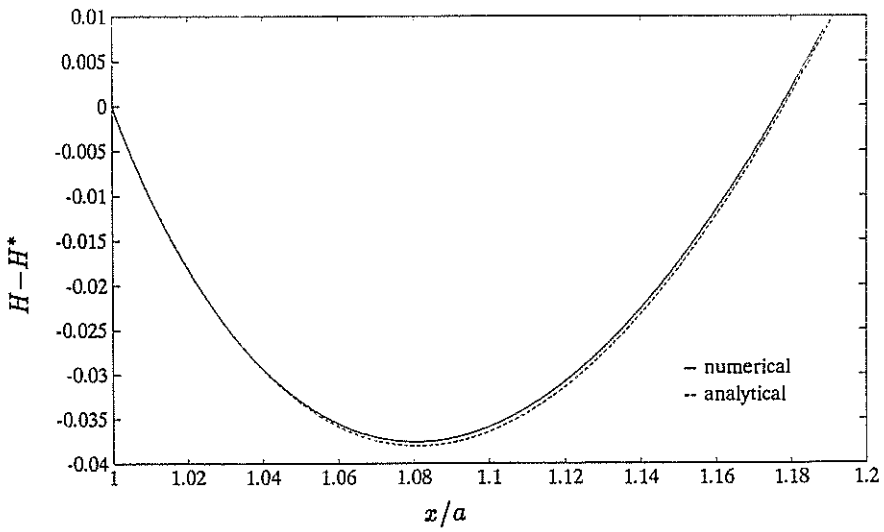

Figure 3.19: Comparison of numerical and analytical final shapes

3.6 Conclusions

A novel approach for the solution of the outlet and central regions of heavily loaded EHL line contacts problems has been described. The method is based on the Modified Hertzian Contacts theory developed by Greenwood and Johnson which applies linear fracture mechanics to find pressures and deformations in dry Hertzian contacts.

The scheme solves iteratively the Reynolds and fracture mechanics equations for the outlet pressures and shape. With these pressures and once again applying fracture mechanics, it is possible to calculate the central zone pressures assuming that this region behaves like a dry contact problem with a known central film thickness.

With the present scheme and cancelling out the square root singular terms in the elastic equations by equating the stress intensity factors, converged outlet solutions have been obtained from which the following conclusions can be observed:

a).- The outlet pressure distribution is accurately described by the function:

$$p = \frac{B}{\alpha}\left[\frac{L-x}{L-a}\right]\ln\left(\frac{x-a}{L-a}\right)$$

where: B and L are the only two constants which fully define the outlet pressures: $B \approx -2/\alpha$ but L unknown a priori.

b).- As a consequence of (a) the exit bump joins the parallel film shape with an internal angle of the film crease:

$$\phi = \arctan(\frac{-2\pi B}{E'}) \approx \arctan(\frac{-4\pi}{\alpha E'})$$

Which is a different result from the one predicted by the Greenwood scheme where the square root central pressures make $\phi = 90°$. The result is a half of the value predicted by Hall's second conclusion. However, Hall in an earlier article solves a rigid punch contact with also logarithmic pressures near $x = a$ and finds an slope for the shape at that point with the same result as the one given by the present theory.

c).- Outlet solutions calculated with the present scheme show a more deformed exit bump (giving higher h_{min}) compared with the Greenwood scheme for equal values of $I(L/a)$ and H^* and resulting in larger outlet lengths L. This is due to the Greenwood assumption of no outlet pressures.

CHAPTER FOUR

TRUNCATED HERTZIAN CONTACTS AND ITS APPLICATION TO EHL LINE CONTACTS. THE FULL SOLUTION

Herein the concepts explained in Chapter 3 are used and extended to develop a complete scheme for the solution of the entire EHL geometry and are applied in practical cases. Full EHL solutions are compared with other authors' results; compressibility and the Roelands viscosity law are included in the analysis. Three different maps of collected solutions are also presented showing several authors' results for: central film thickness, location of the spike and the spike height as function of two dimensionless parameters, $\mathcal{P}$ and $\mathcal{S}$.

It is shown that a heavily loaded EHL contact can be separated for its solution in three parts: inlet, central (parallel film zone) and outlet. The replacement stresses theory described in Chapter 3 is now extended to include the elastic interactions outlet-inlet, continuity requirements and smooth join condition for the inlet-central pressures are also considered. In the outlet of the full EHL solution the square root singular term of the elasticity equations in the RH side of the contact is no longer completely removed ($M_h \neq M_R$) and the elastic consequences of this are also analysed. The inlet and outlet are solved for pressure and shape, then they are joined to the central region, including their corresponding effects on internal stresses, via fracture mechanics. The analysis still assumes the pressure spike to be singular but its strength will depend on the load and velocity parameters. Only Newtonian lubricants are considered.

In Chapter 3 it was found that for the special case of $M_h = M_R$ the outlet pressure distribution behaves as a logarithmic function determined by two constants: the coefficient B_f and the length L_1 both approximately related to the given parameters K and H^*. Here

it is found that this relationship still describes accurately the outlet pressures even when $M_h \neq M_R$. However, the relationship is not so accurate for Roelands viscosity law cases.

In general, the final shape given by the present analysis is a combination of two pressure components related to the central region pressures: a square root singular term with coefficient $M_h - M_R$ and a logarithmic term related to the outlet pressures. Therefore the right hand side of the pressure spike will be closer to a square root singularity for large values of $M_h - M_R$.

The pressures and shapes obtained with the present scheme in general agree with reported solutions, however, for cases when the spike is located near the centre of the contact, the inaccuracy of the scheme increases and the spike location slightly diverges from reported results. This increase of error is due to the contradiction of the requirements between elasticity and hydrodynamics on the inlet-central pressures join, resulting in the removal of part of the inlet pressures to satisfy the continuity and smooth join conditions of elasticity. The analysis can be applied confidently for values of $\mathcal{P} > 7$ and $\mathcal{S} > 2$.

4.1 General Double Truncation

Following Greenwood and Johnson [29] 1989, the double truncation of a Hertzian contact to obtain a shorter Hertzian flat can be done easily by assuming an original flat from $-e$ to $+e$ (e.g. Fig. 4.1) the centre of which is on the line of the centres of the rollers, and from which the abscissa x_r is measured. The double truncation is made at the points $x_r = -b$ and $x_r = +c$ producing in this way the new flat of total length $2a$ with its centre located at a distance d from the centre of the rollers and the abscissa x is measured from here. Therefore the outlet truncation (right hand side) starts at the point $x = a$ with outlet pressures p_R imposed and the inlet truncation (left hand side) starts at the end of the flat $x = -a$ with imposed inlet pressures p_L.

Then from Fig. 4.1: $d + a = b$ and $a - d = c$, thus:

$$d = b - a \tag{4.1}$$

$$b + c = 2a \tag{4.2}$$

$$b - c = 2d \tag{4.3}$$

so that:

$$x_r = x - d \tag{4.4}$$

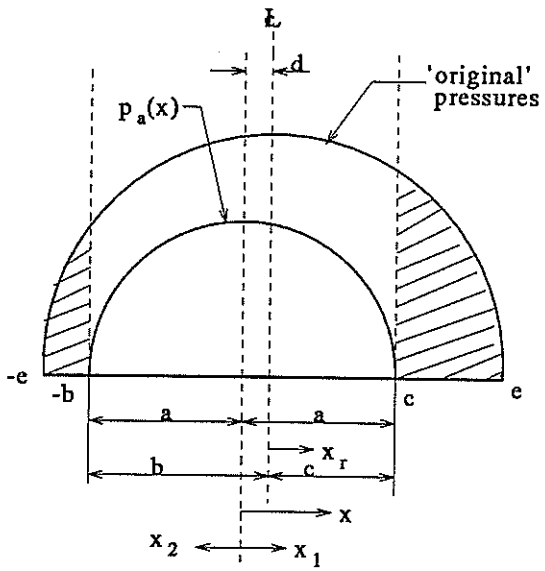

Figure 4.1: Hertzian flat generated from double truncation

Now following equation 3.16 the final internal stress distribution after the outlet and inlet pressures have been removed is:

$$\sigma_t(x) = -Q\sqrt{a^2 - x^2} - (M_h)_L\sqrt{\frac{a-x}{a+x}} - (M_h)_R\sqrt{\frac{a+x}{a-x}} \tag{4.5}$$

where $(M_h)_R$ and $(M_h)_L$ are the stress intensity factors M due to the removed right and left Hertzian portions of pressures.

From now on a convention for the stress intensity factors will be adopted: superscript denotes the location of the stress intensity factor and subscript denotes the cause of it (e.g. p_R or p_L).

With the first truncation on the right, at $x_r = c$ according to equation 3.13 the corresponding stress intensity factor is:

$$(M_h)_R = \frac{Q}{2}(e - c)$$

the second truncation on the left, at $x_r = -b$ the corresponding stress intensity factor is:

$$(M_h)_L = \frac{Q}{2}(e - b)$$

therefore:

$$(M_h)_R - (M_h)_L = \frac{Q}{2}(b-c) = Qd \tag{4.6}$$

Combining equation 4.6 with equation 4.1:

$$\frac{b}{a} = 1 + \frac{1}{aQ}[(M_h)_R - (M_h)_L] \tag{4.7}$$

and also:

$$\frac{c}{a} = 1 + \frac{1}{aQ}[(M_h)_L - (M_h)_R] \tag{4.8}$$

a).- Adding pressures on the right according to equation 3.7 gives internal stresses which near $x \approx a$ are:

$$\sigma_R^R(x) \approx M_R^R\sqrt{\frac{a+x}{a-x}} - p_R(a) + (M_1)_R^R\sqrt{\frac{a-x}{a+x}} \tag{4.9}$$

But near $x \approx -a$, these stresses are:

$$\sigma_R^L(x) \approx M_R^R\sqrt{\frac{a+x}{a-x}} - (M_1)_R^L\sqrt{\frac{a+x}{a-x}} \tag{4.10}$$

b).- Adding pressures on the left gives internal stresses which near $x \approx -a$ are:

$$\sigma_L^L(x) \approx M_L^L\sqrt{\frac{x-a}{-a-x}} - p_L(-a) + (M_1)_L^L\sqrt{\frac{-x-a}{x-a}} \tag{4.11}$$

But near $x \approx a$, these stresses are:

$$\sigma_L^R(x) \approx M_L^L\sqrt{\frac{x-a}{-x-a}} - (M_1)_L^R\sqrt{\frac{x-a}{-x-a}} \tag{4.12}$$

Therefore the total distribution of stresses after the replacement of pressures in the inlet and outlet when $x \approx a$ is:

$$\sigma_f(x \to a) = \sigma_t(x) + \sigma_R^R(x) + \sigma_L^R(x) \tag{4.13}$$

And the total distribution of stresses when $x \approx -a$ is:

$$\sigma_f(x \to -a) = \sigma_t(x) + \sigma_L^L(x) + \sigma_R^L(x) \tag{4.14}$$

it is to say:

$$\sigma(x \to -a) = -Q\sqrt{a^2 - x^2} - (M_h)_L\sqrt{\frac{a-x}{a+x}} - (M_h)_R\sqrt{\frac{a+x}{a-x}} + M_L^L\sqrt{\frac{x-a}{-x-a}}$$

$$- p_L(-a) + (M_1)_L^L\sqrt{\frac{-x-a}{x-a}} + M_R^R\sqrt{\frac{a+x}{a-x}} - (M_1)_R^L\sqrt{\frac{a+x}{a-x}} \qquad (4.15)$$

4.1.1 Continuity Conditions

In EHL only the inlet requires continuity conditions of pressure and smooth join, since at the outlet the 'spike' of infinite pressures is located. The conditions are obtained by analysing equation 4.15.

a).- Inlet finite pressures: This condition requires to remove all the square root singular terms in the internal stresses for $x \approx -a$, therefore from equation 4.15 it is necessary that:

$$M_L^L - (M_h)_L = 0 \qquad (4.16)$$

Therefore equation 4.15 is reduced to:

$$\sigma(x \to -a) = -Q\sqrt{a^2 - x^2} - p_L(-a) + (M_1)_L^L\sqrt{\frac{-x-a}{x-a}}$$

$$+ \left[-(M_1)_R^L - (M_h)_R + M_R^R\right]\sqrt{\frac{a+x}{a-x}} \qquad (4.17)$$

b).- Inlet-central smooth join of pressures: It requires equal derivatives at $x \approx -a$

$$\frac{d}{dx}\sigma_f(x \to -a) = \frac{d}{dx}p_L(x \to -a)$$

Now, for $x \approx -a$, x is negative and:

$$\sqrt{\frac{-a-x}{-a+x}} = \sqrt{\frac{a+x}{a-x}} = \sqrt{\frac{a-|x|}{a+|x|}} \approx \sqrt{\frac{a-|x|}{2a}}$$

and the term:

$$Q\sqrt{a^2 - x^2} = Q\sqrt{a+x}\,\sqrt{a-x} \approx Q\sqrt{a-|x|}\,\sqrt{2a}$$

Finally:

$$\sigma_f(x \to -a) \approx -\sqrt{a-|x|}\left\{Q\sqrt{2a} + \frac{1}{\sqrt{2a}}\left[-(M_1)_L^L + (M_1)_R^L + (M_h)_R - M_R^R\right]\right\} - p_L(-a) \tag{4.18}$$

Notice that for: $\sqrt{a-|x|} = 0$ then $|\sigma_f(x \to -a)| = |p_L(-a)|$

To have an inlet-central smooth join of pressures requires equal derivatives at $x \approx -a$, and from equation 4.18 it implies:

$$2aQ - (M_1)_L^L + (M_1)_R^L + (M_h)_R - M_R^R = 0 \tag{4.19}$$

Therefore it is possible to write:

$$(M_{1h})_L = (M_h)_R + 2aQ = (M_1)_L^L - (M_1)_R^L$$

which leads to:

$$(M_{1h})_L = (M_h)_R + 2aQ \tag{4.20}$$

$$-(M_{1h})_L + [(M_1)_L^L + (M_1)_R^L] = 0 \tag{4.21}$$

Finally after removing the singularities for the inlet, the final internal stress distribution for $-a \leq x \leq a$ can be written (see equation 3.23) as:

$$\sigma_f(x) \approx -Q\sqrt{a^2-x^2} - (M_1)_L^R\sqrt{\frac{a-x}{a+x}} - DM\sqrt{\frac{a+x}{a-x}} - \frac{\sqrt{a^2-x^2}}{\pi}\int_{x_1=a}^{L_1}\frac{p_R(x_1)dx_1}{(x_1-x)\sqrt{x_1^2-a^2}} \tag{4.22}$$

where $DM = (M_h)_R - M_R^R$.

4.1.2 Deflections

Applying pressures on both cracks the slopes of the elastic deflections on the outlet region are obtained by using equation 3.25:

$$\frac{E'}{2}(\frac{\partial v}{\partial x})^R = M_R^R\sqrt{\frac{x+a}{x-a}} + \frac{1}{\pi}\sqrt{x^2-a^2}\int_{x=a}^{L_1}\frac{p_R(x_1)\,dx_1}{(x_1-x)\sqrt{x_1^2-a^2}}$$

$$+M_L^L\sqrt{\frac{x-a}{x+a}} + \frac{1}{\pi}\sqrt{x^2-a^2}\int_{x_2=a}^{L_2}\frac{p_L(x_2)\,dx_2}{(x_2-x)\sqrt{x_2^2-a^2}}$$

Where for simplicity x_1 is measured positive from the centre of the flat ($x=0$) up to the outlet length L_1 and x_2 positive from $x=0$ to L_2, however, x is unchanged, see Fig. 4.1.

Adding the effect of the removed Hertzian pressures in both sides:

$$\frac{E'}{2}(\frac{\partial v}{\partial x})^R = -DM\sqrt{\frac{x+a}{x-a}} + [M_L^L - (M_h)_L]\sqrt{\frac{x-a}{x+a}}$$

$$+\frac{1}{\pi}\sqrt{x^2-a^2}\left[\int_{x_1=a}^{L_1}\frac{p_R(x_1)\,dx_1}{(x_1-x)\sqrt{x_1^2-a^2}} - \int_{x_2=a}^{L_2}\frac{p_L(x_2)\,dx_2}{(x_2+x)\sqrt{x_2^2-a^2}}\right]$$

but in order to avoid an inlet pressure spike, it was said in equation 4.16 that: $M_L^L - (M_h)_L = 0$, so:

$$\frac{E'}{2}(\frac{\partial v}{\partial x})^R = -DM\sqrt{\frac{x+a}{x-a}}$$

$$+\frac{1}{\pi}\sqrt{x^2-a^2}\left[\int_{x_1=a}^{L_1}\frac{p_R(x_1)\,dx_1}{(x_1-x)\sqrt{x_1^2-a^2}} - \int_{x_2=a}^{L_2}\frac{p_L(x_2)\,dx_2}{(x_2+x)\sqrt{x_2^2-a^2}}\right] \tag{4.23}$$

For the inlet, a changes to $-a$, x to $-x$ and L_1 to L_2 so, the elastic deflection slopes are:

$$\frac{E'}{2}(\frac{\partial v}{\partial x})^L = -DM\sqrt{\frac{-x-a}{-x+a}}$$

$$+\frac{1}{\pi}\sqrt{x^2-a^2}\left[\int_{x_2=a}^{L_2}\frac{p_L(x_2)\,dx_1}{(x_2+x)\sqrt{x_2^2-a^2}} - \int_{x_1=a}^{L_1}\frac{p_R(x_1)\,dx_1}{(x_1-x)\sqrt{x_1^2-a^2}}\right] \tag{4.24}$$

Note that in the inlet the numerical value of x is always negative therefore in equation 4.24 the terms $-x$ become in reality $|x|$.

After equations 4.23 and 4.24 are solved, the slopes are integrated to find the elastic displacements (i.e. Section 3.3.6). The constant term of equation 3.28: $a^2/2R$, can be written following Hertz theory as: $2a^2Q/E'$. For the inlet, the constant $Q = p_a^*/a$ can be arranged to satisfy the smooth join requirement of equation 4.20 for which:

$$Q = \frac{1}{2a}[(M_{1h})_L - (M_h)_R]$$

Finally it is important to point out that the integrals involved in the solution of pressures, stress intensity factors and slopes are solved numerically with different methods; all of them are discussed in Appendix A.

4.1.3 Non-Dimensionalisation

Consider the following definitions:

$$X = x/a,\ V(X) = \frac{2R}{a^2}v(x),\ P = \frac{4R}{aE'}p = p_a^*p,\ P' = p_a^*p'$$

$$\hat{\sigma} = p_a^*\sigma,\ \hat{M} = M/p_a^*,\ \hat{M}_1 = \frac{\pi}{2p_a^*}M_1,\ \Delta M = (\hat{M}_h)_R - \hat{M}_R^R = DM/p_a^*$$

where p_a^* is the maximum Hertzian pressure corresponding to a dry contact of length $2a$. The non-dimensional forms for the elasticity equations 4.22, 4.23 and 4.24 are:

$$\hat{\sigma}_f(X) = \sqrt{1-X^2} + (\hat{M}_1)_L^R\sqrt{\frac{1-X}{1+X}} + \Delta M\sqrt{\frac{1+X}{1-X}}$$
$$+ \frac{1}{\pi}\sqrt{1-X^2}\int_{X_1=1}^{L_1/a}\frac{P_R(X_1)\,dX_1}{(X_1-X)\sqrt{X_1^2-1}} \tag{4.25}$$

$$(\frac{\partial V}{\partial X})^R = -\Delta M\sqrt{\frac{X+1}{X-1}}$$
$$+\frac{1}{\pi}\sqrt{X^2-1}\left[\int_{X_1=1}^{L_1/a}\frac{P_R(X_1)\,dX_1}{(X_1-X)\sqrt{X_1^2-1}} - \int_{X_2=1}^{L_2/a}\frac{P_L(X_2)\,dX_2}{(X_2+|X|)}\sqrt{X_2^2-1}\right] \tag{4.26}$$

$$(\frac{\partial V}{\partial X})^L = -\Delta M\sqrt{\frac{X-1}{X+1}}$$
$$+\frac{1}{\pi}\sqrt{X^2-1}\left[\int_{X_2=1}^{L_2/a}\frac{P_L(X_2)\,dX_2}{(X_2-X)\sqrt{X_2^2-1}} - \int_{X_1=1}^{L_1/a}\frac{P_R(X_1)\,dX_1}{(X_1+X)}\sqrt{X_1^2-1}\right] \tag{4.27}$$

With the stress intensity factors given by:

$$\hat{M}_R^R = \frac{1}{\pi}\int_{X_1=1}^{L_1/a} \frac{P_R(X_1)}{\sqrt{X_1^2-1}}\, dX_1 \tag{4.28}$$

$$(\hat{M}_1)_L^L = -\int_{X_1=1}^{L_2/a} P_L'(X_1)\sqrt{\frac{X_1+1}{X_1-1}}\, dX_1 \tag{4.29}$$

$$(\hat{M}_1)_L^R = -\int_{X=-1}^{L_2/a} P_L'(X_1)\sqrt{\frac{X_1-1}{X_1+1}}\, dX_1 \tag{4.30}$$

$$(\hat{M}_1)_R^L = -\int_{X_1=1}^{L_1/a} P_R'(X_1)\sqrt{\frac{X_1-1}{X_1+1}}\, dX_1 \tag{4.31}$$

$$(\hat{M}_h)_R = \Delta M + \hat{M}_R^R \tag{4.32}$$

Finally from equation 4.20:

$$(\hat{M}_{1h})_L = \pi[\frac{1}{2}(\hat{M}_h)_R + 1] \tag{4.33}$$

and from equation 4.21:

$$(\hat{M}_{1h})_L = (\hat{M}_1)_L^L + (\hat{M}_1)_R^L \tag{4.34}$$

The Hertzian shapes from equation 3.28 and for the inlet also by substituting equation 4.21 they are:

for the outlet:

$$V_h(X) = X[X^2-1]^{1/2} - \ln[X + (X^2-1)^{1/2}]$$

for the inlet:

$$V_h(X) = \left\{\frac{1}{\pi}(\hat{M}_{1h})_L - \frac{1}{2}(\hat{M}_h)_R\right\}\left\{X[X^2-1]^{1/2} - \ln[X + (X^2-1)^{1/2}]\right\} \tag{4.35}$$

4.2 Inlet Integration of the Reynolds Equation

The inlet integration is very similar to the one carried out for the outlet (e.g. Section 3.4), but with the difference that in the inlet the pressures will always be considered finite. Hence the boundary condition for $x = -a$ is that the pressures reach a maximum finite value, say $p(-a) = p_f$. Therefore from equation 3.31, the reduced pressures become:

$$q_f = \frac{1}{\alpha}[1 - e^{-\alpha p_f}] \tag{4.36}$$

and equation 3.34 is now written as:

$$q(x) = q_f - 12\bar{u}\eta_o I(x) \tag{4.37}$$

Now at $x = L_2$ (beginning of the inlet) $p(L_2) = 0$, and $q(L_2) = 0$, hence from equation 4.37:

$$q_f = 12\eta_o \bar{u} I(L_2) \tag{4.38}$$

substituting equations 4.37 and 4.38 into 3.31 leads to:

$$p(x) = -\frac{1}{\alpha}\ln\left\{1 + \alpha q_f[\frac{I(x)}{I(L_2)} - 1]\right\} \tag{4.39}$$

where $I(x)$ and $I(L_2)$ are defined just like in the outlet but now integrating inlet pressures from $-a$ to L_2.

Notice in equation 4.39 that the maximum value that q_f can take is $1/\alpha$.

4.2.1 Non-Dimensionalisation

Following the outlet procedure of Section 3.4.1, equation 4.39 becomes:

$$P(X) = -\frac{1}{K_1}\ln\left\{1 + K_1\hat{q}_f[\frac{I(X)}{I(L_2/a)} - 1]\right\} \tag{4.40}$$

where:

$$I(X) = \int_{X=-1}^{X} \frac{V_f(X)}{[H^* + V_f(X)]^3}\, dX \tag{4.41}$$

$$I(L_2/a) = \int_{X=-1}^{L_2/a} \frac{V_f(X)}{[H^* + V_f(X)]^3}\, dX \tag{4.42}$$

equation 4.38 becomes:

$$K = \frac{I(L_2/a)}{\hat{q}_f} \tag{4.43}$$

finally equation 4.36 is written as:

$$\hat{q}_f = \frac{1}{K_1}[1 - e^{-K_1 P_f}] \tag{4.44}$$

with $\hat{q}_f \leq 1/K_1$.

4.2.2 Inlet Computational Procedure

In the computational sequence for the inlet the constant P_f has to be fixed in advance and the new pressures are given by equation 4.40. Then to start the process it is easier to guess an initial shape rather than an initial pressure distribution, since for the inlet the shape is known to behave approximately as: $V_f(X) = c_1 X^{3/2}$ (e.g. Crook [18] 1963) where c_1 is a given constant. So the inlet procedure is:

a).- Suggest an initial guess for the shape: $V_f = c_1 X^{3/2}$. Enter the values of: K_1, H^*, ΔM and P_f, then calculate $\hat{q}_f$ from equation 4.44.

b).- Solve equation 4.40 for the new pressures $P(X)$.

c).- Calculate the value of $(\hat{M}_1)_L^L$ from equation 4.29, then use equation 4.34 to calculate $(\hat{M}_{1h})_L$.

d).- Solve equation 4.27 to find the slopes. Integrate the slopes to find the elastic displacements $V(X)$.

e).- To calculate the final shape $V_f(X)$ add the proper Hertzian displacements from equation 4.35.

f).- Return to (b) until convergence for pressures and shape is reached.

4.3 The Central Region and the Full EHL Solution

Two inlet and outlet pressure distributions and shapes will be part of the same EHL contact only if their variables: K, K_1 and H^* are equal. If it is the case, the central pressure distribution and shape are completely defined; and by integration of pressures it is possible to calculate the total load per unit of with w.

So far, it has been shown how to obtain independently inlet and outlet pressure distributions and shapes. However, according to the elasticity equations, the inlet and outlet deformations are dependent one from the other, so an iterative scheme which relates both solutions has to be defined.

4.3.1 Computational Scheme for the Global Solution

Start from the outlet with the already given values for K_1, H^*, and ΔM, assume no inlet pressures. The procedure given in Section 3.4.2 then is followed to obtain the first outlet solution from which the factors $(\hat{M}_1)_R^L$ (equation 4.31), $\hat{M}_R^R$ (equation 4.28) and $(\hat{M}_h)_R$

(equation 4.32) are calculated and the constant K is obtained.

Then the inlet is solved following the procedure of Section 4.2.2 and using the same outlet constants K_1 and H^*. Here a value of $\hat{q}_f$ is required, it has to be chosen in order that the inlet constant K equals the outlet value. The factors $(M_1)_L^L$ and $(\hat{M}_{1h})_L$ are calculated, and the smooth join of pressures can be satisfied.

After this, the first outlet-inlet cycle has been performed and the process is started again until converged solutions in pressures and shape are obtained in both sides of the contact. Then the value of $(\hat{M}_{1h})_L$ from equation 4.33 is compared with the one of equation 4.34 if there is a substantial difference, the values of the initial parameters K_1, H^* and ΔM need to be changed and the whole process is started again.

Finally the final central pressure distribution (internal stresses $\hat{\sigma}_f(X)$) can be calculated by using equation 4.25 and the pressures and shape from the inlet and outlet can now be put together with a parallel film thickness of value equal to H^*. The complete procedure is shown in Fig. 4.2

4.3.2 The Inlet-Central Pressures Join

In Section 4.1.1 the conditions to obtain a smooth inlet-central pressures join were described. These conditions are related only to the elastic requirements. However, hydrodynamics have also to be satisfied.

Consider the inlet pressure distribution equation 4.39; then calculating by differentiation the pressure gradient one obtains:

$$p'(x) = -\frac{q_f v_f(x)}{I(L_2)[h^* + v_f(x)]^3[1 - \alpha q_f]} \tag{4.45}$$

At the end of the inlet ($x = -a$) it is required that $h = h^*$ and therefore $v_f(-a) = 0$, and equation 4.45 gives: $p'(-a) = 0$. It is to say that the inlet pressure distribution ends always with zero gradients.

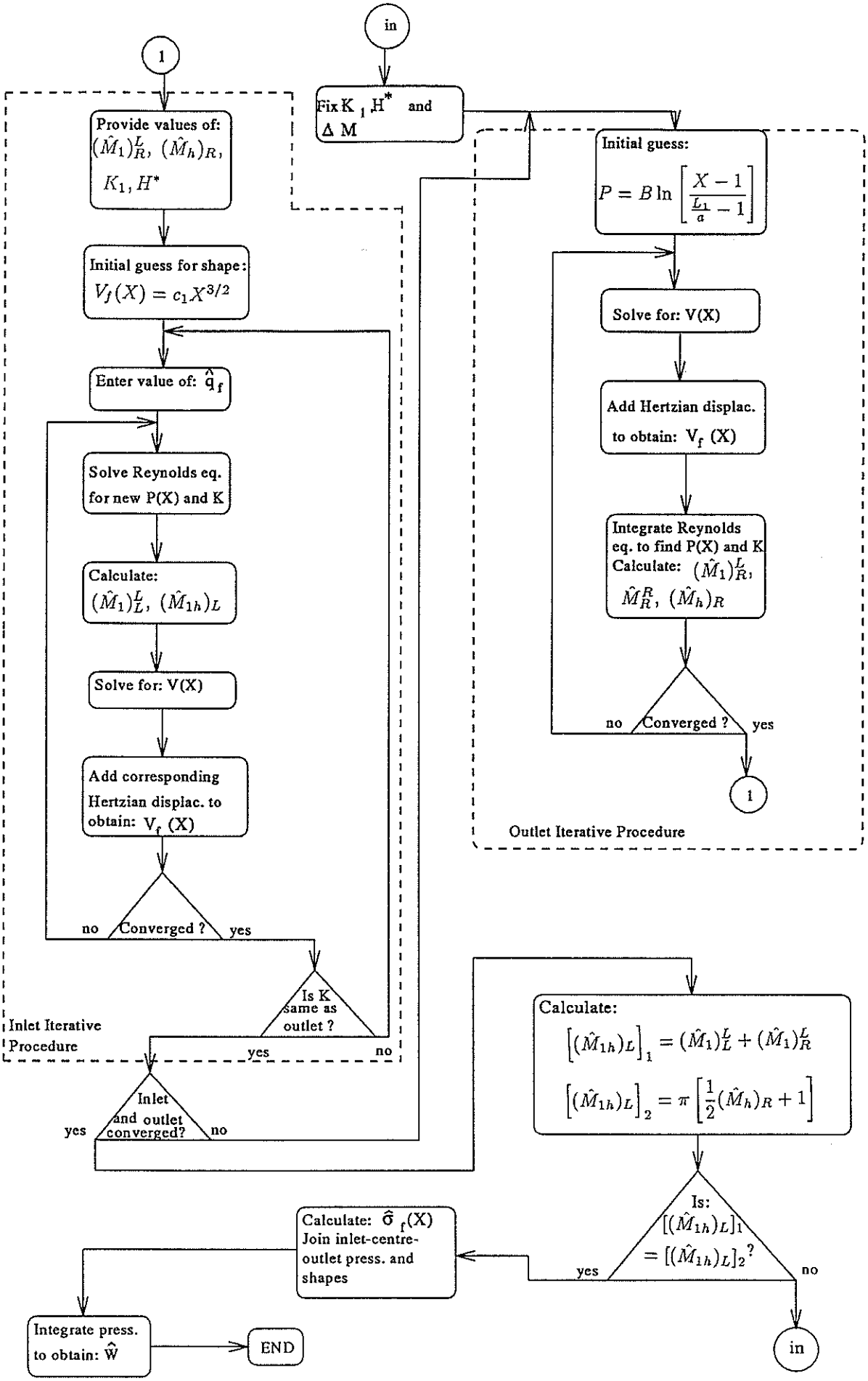

Figure 4.2: Complete scheme for the EHL solution

Note that to have a smooth join of pressures between the inlet and the central region, one would be forced to match the pressures at the first maximum value in the central region (at $x = 0$), where the gradient of the final internal stresses is also zero. However, there would be cases (when the spike is located near the centre of the contact) in which the central stresses would not exhibit such a point. Therefore it is more convenient to join the pressures before the centre line ($x = 0$); and with a non-zero pressure gradient.

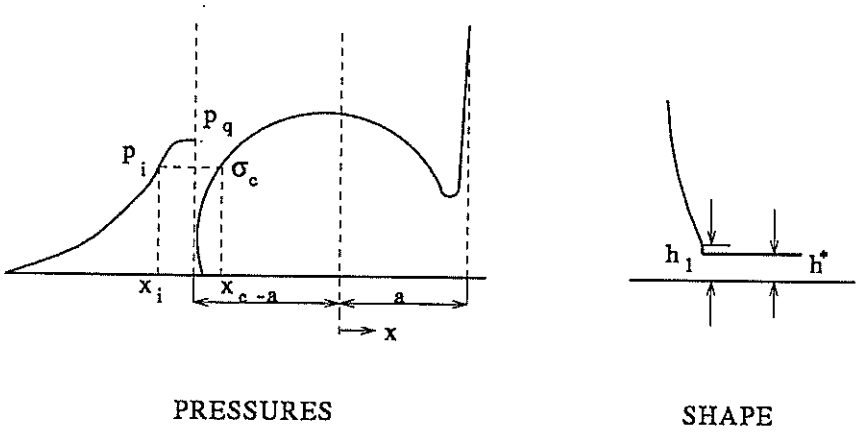

Figure 4.3: Inlet-central region join

In order to achieve this, a smooth join of pressures is obtained by finding the points where both the inlet (x_i) and the central (x_c) pressure distributions have the same value for pressures and gradients, then arbitrarily the excess of the inlet pressures is simply removed, see Fig. 4.3. This of course, is equivalent to choosing, at the pressures join, a slightly larger film thickness (h_1) than h^* which strictly means a non-parallel film in the central region, however, since the elasticity continuity conditions are always satisfied, the removed portion of the inlet pressures is small and $h_1 \approx h^*$.

4.3.3 Change of Axis

So far, the equations have been represented as functions of the abscissa x which is measured from the centre of the parallel zone, this is certainly convenient since the inlet ends at $x = -a$ so the outlet begins at $x = a$ and the equations are simpler. However, in practical cases it is more convenient to refer the location of the spike and other important points from the centre of the rollers (e.g. Fig. 4.1) and the convenient abscissa is x_r. This

variable and x are related by equation 4.4:

$$x_r = x - d$$

Substituting equation 4.1 it is possible to write:

$$x_r = x - a(\frac{b}{a} - 1) \tag{4.46}$$

where from equation 4.7 b/a is:

$$\frac{b}{a} = 1 + \frac{1}{aQ}[(M_h)_R - (M_h)_L]$$

which in dimensionless form is:

$$\frac{b}{a} = 1 + (\hat{M}_h)_R - (\hat{M}_h)_L$$

dividing equation 4.46 by a, the dimensionless form is obtained:

$$X_r = X - \frac{b}{a} + 1 \tag{4.47}$$

where: $X_r = x_r/a$.

Finally the location of the spike is given by equation 4.8:

$$\frac{c}{a} = 1 + \frac{1}{aQ}[(M_h)_L - (M_h)_R]$$

which in dimensionless form is:

$$\frac{c}{a} = 1 + (\hat{M}_h)_L - (\hat{M}_h)_R \tag{4.48}$$

where c is measured from the centre of the rollers, see Fig. 4.1.

One must remember that the variable a (i.e. Section 4.1) represents half the length of the obtained Hertzian flat. One must also realize that neither the pressure distribution of width $2a$ nor the one of width $b+e$, necessarily contain the total EHL load w, see Fig. 4.4.

However, in common practice the abscissa and spike location are often non-dimensionalised as a function of the half contact length (b_h) of the equivalent dry Hertzian contact with the same total load and with a maximum pressure p_h.

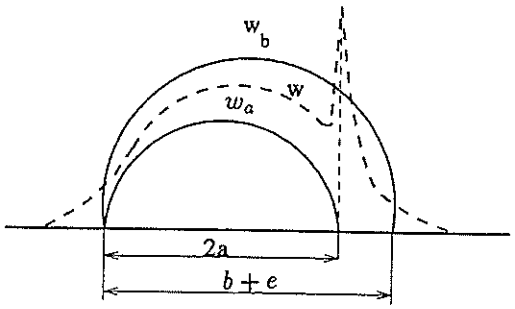

Figure 4.4: EHL pressures compared with the associate Hertzian distributions

Therefore, from Hertzian theory:

$$b_h = \sqrt{\frac{8Rw}{\pi E'}}; \quad a = \sqrt{\frac{8Rw_a}{\pi E'}}$$

thus:

$$\frac{b_h}{a} = \sqrt{\frac{w}{w_a}} \tag{4.49}$$

also from Hertzian theory:

$$p_h = \sqrt{\frac{wE'}{2R\pi}}; \quad p_a^* = \sqrt{\frac{w_a E'}{2R\pi}}$$

therefore:

$$\sqrt{\frac{w}{w_a}} = \frac{p_h}{p_a^*} \tag{4.50}$$

Non-dimensionalizing:

$$P_h = \frac{p_h}{p_a^*}, \quad \hat{W} = \frac{w}{ap_a^*}, \quad \hat{W}_a = \frac{w_a}{ap_a^*} = \frac{\pi}{2}$$

then substituting into equation 4.50:

$$P_h = \sqrt{\frac{2\hat{W}}{\pi}} \tag{4.51}$$

therefore equation 4.49 becomes:

$$\frac{b_h}{a} = \sqrt{\frac{2\hat{W}}{\pi}} = P_h \tag{4.52}$$

Finally, from equation 4.49 the new abscissa is:

$$\frac{x_r}{b_h} = \frac{1}{P_h}[X - \frac{b}{a} + 1] \tag{4.53}$$

and the spike location becomes:

$$\frac{c}{b_h} = \frac{1}{P_h}[1 + (\hat{M}_h)_L - (\hat{M}_h)_R] \tag{4.54}$$

4.4 Complete Solutions for Incompressible Lubricant

In this section, comparisons for complete solutions following the computational scheme of Fig. 4.2 with the results from other authors are shown. The first comparison is made with the examples 2 and 3 of Dowson and Higginson [21] 1977. The corresponding pressures and film thickness are shown in Figs. 4.5 and 4.6. The parameters of which are defined as:

$$W = \frac{w}{E'R} = \frac{4\hat{W}K_1^2}{G^2}; \quad G = \alpha E'; \quad U = \frac{\eta_o \bar{u}}{E'R} = \frac{4}{3}\frac{K_1^4}{KG^4}$$

$$H_D = \frac{h}{R} = \frac{8HK_1^2}{G^2}; \quad P_D = \frac{p}{E'} = \frac{K_1 P}{G}$$

The pressures and shapes from the present theory are shown in Figs. 4.7 and 4.8. And the corresponding parameters are given in Tables 4.1, 4.2 and 4.3. Table 4.2 gives the stress intensity factors involved in the calculation, notice that $(\hat{M}_{1h})_L$ has two values: the so-called numerical, which is given by equation 4.34 with $(\hat{M}_1)_L^L$ and $(\hat{M}_1)_R^L$ calculated numerically; and the other, given by equation 4.33. In a converged solution they must be equal (or nearly equal) in order to satisfy the inlet smooth join condition.

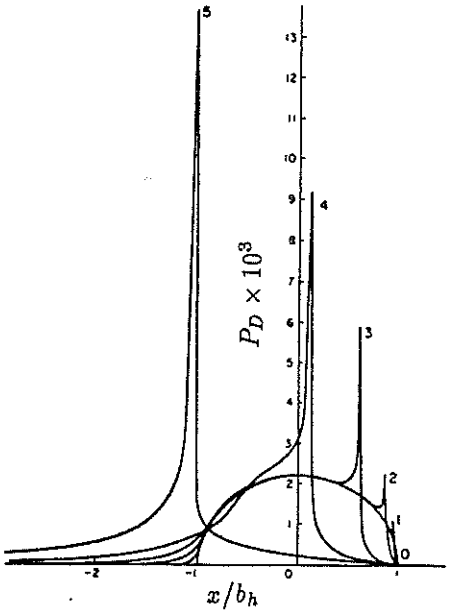

Figure 4.5: Dowson and Higginson pressures for: $W = 3 \times 10^{-5}$, $G = 5000$, U=0, 1) $U = 10^{-13}$, 2) $U = 10^{-12}$, 3) $U = 10^{-11}$, 4) $U = 10^{-10}$, 5) $U = 10^{-9}$

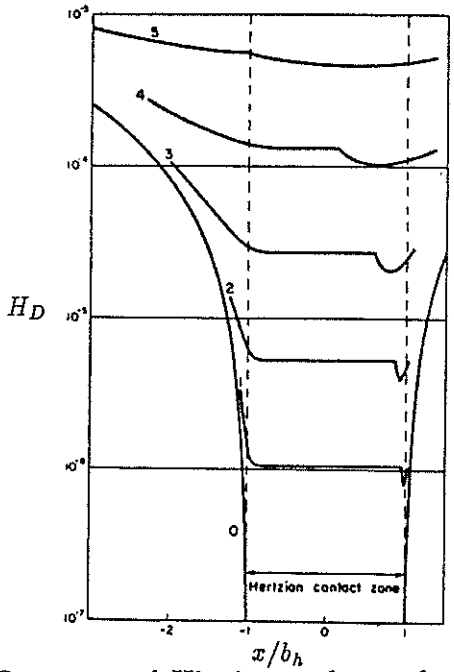

Figure 4.6: Dowson and Higginson shapes for: $W = 3 \times 10^{-5}$, $G = 5000$, U=0, 1) $U = 10^{-13}$, 2) $U = 10^{-12}$, 3) $U = 10^{-11}$, 4) $U = 10^{-10}$, 5) $U = 10^{-9}$

The pressures and film thickness distributions agree more or less well with the Dowson and Higginson solutions. The spike location obtained with the present theory is slightly shifted to the right hand side of the contact (i.e. Table 4.3).

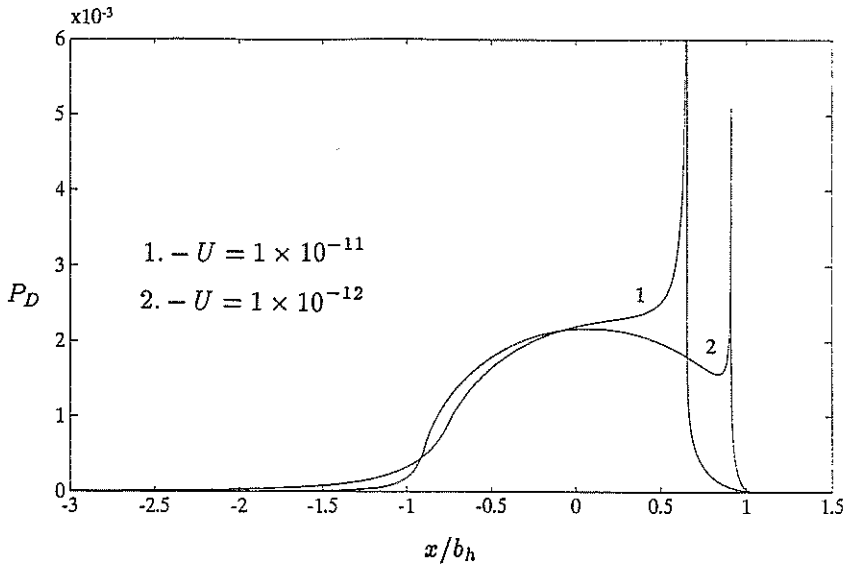

Figure 4.7: Present scheme pressures, examples 2 and 3

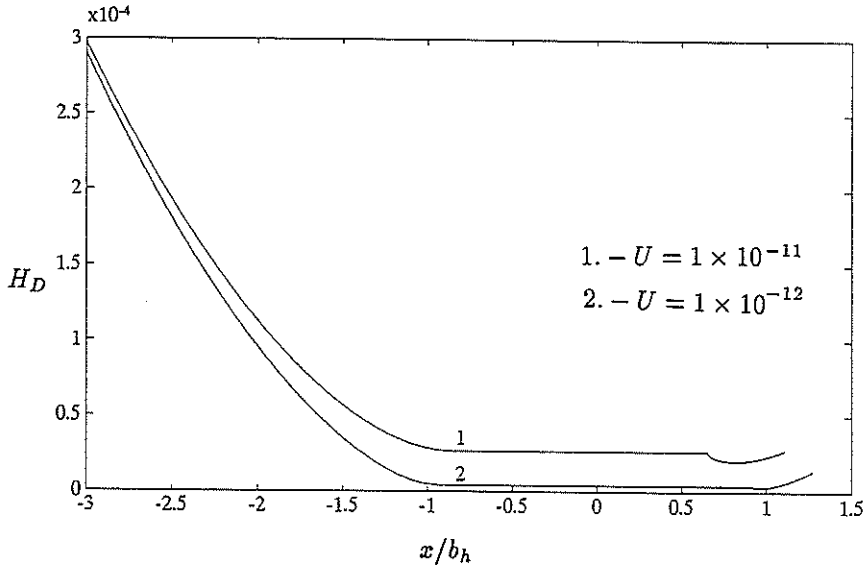

Figure 4.8: Present scheme shapes, examples 2 and 3

Differences in this parameter are common amongst authors, most of the times the reason is related to the numerical technique used or to the refinement of the mesh (e.g. Greenwood [28] 1972, Johnson [40] 1970), see also Section 4.5. However, specially for example 3, where the difference is about 11 %, the reason also could be that in the present theory the removed portion of inlet pressures begins to be important.

The second comparison is made with three examples taken from Bissett and Glander

[6] 1988 where the accuracy on the spike location and height is claimed to be very good. Their pressure and film thickness are defined as:

$$P_B = \frac{p}{p_h} = \frac{P}{P_h}; \quad H_B = \frac{2Rh}{b_h^2} = \frac{H}{P_h}$$

The pressures and film distributions from the reference are shown in Figs. 4.9, 4.10 and 4.11. The corresponding pressures and shapes calculated with the present scheme are shown in Figs. 4.12 and 4.13 and further data are given in Tables 4.1 and 4.2. Notice that example C has been compared with the solution of example 2 of Dowson and Higginson, the input data are not very different. Bissett and Glander in their article clearly show finite pressure spikes (i.e. Section 4.5); whilst in the present scheme the spikes are considered infinite, however, it is believed this difference makes no effect in the comparison.

Once again, the agreement in pressures and film thickness is good, but the values for the spike location from the present theory (e.g. Table 4.3) are slightly higher than the predictions by Bissett and Glander. In the worst of the cases, example A, the difference between the two results is about 35 %. However, Bissett and Glander report that for the same example Lubrecht [51] gives a value 30 % lower and Okamura [61] gives a value 33 % larger.

The central film thickness (e.g. Table 4.3) for example B agrees very well with the reference result. For example A the difference is about 10 % smaller in the present theory. For example C the difference is only 6.5 %.

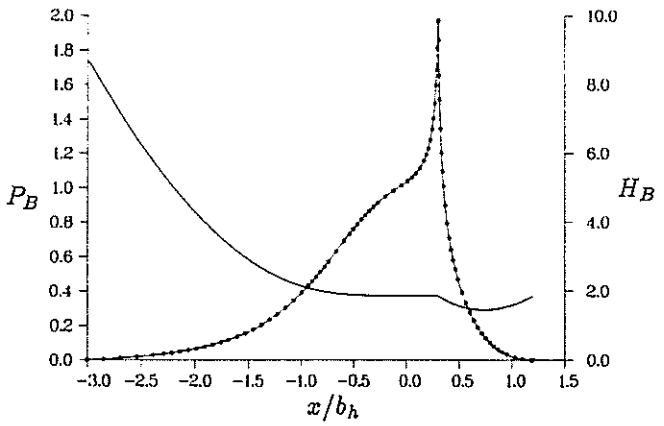

Figure 4.9: Bissett and Glander pressure and shape, example A, for: $W = 1 \times 10^{-5}$, $G = 4000$, $U = 10^{-11}$

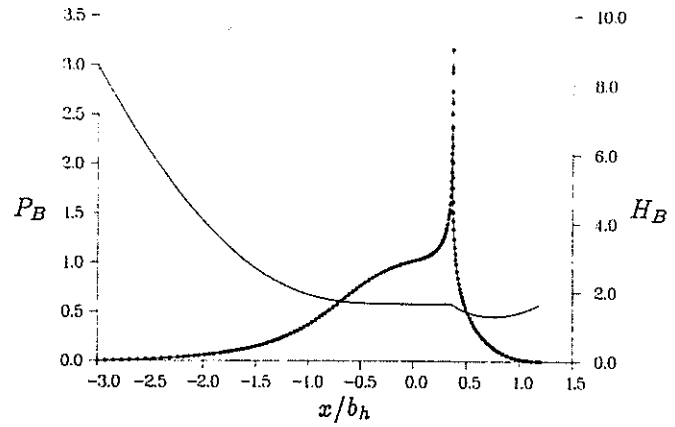

Figure 4.10: Bissett and Glander pressure and shape, example B, for: $W = 1.125 \times 10^{-5}$, $G = 4000$, $U = 10^{-11}$

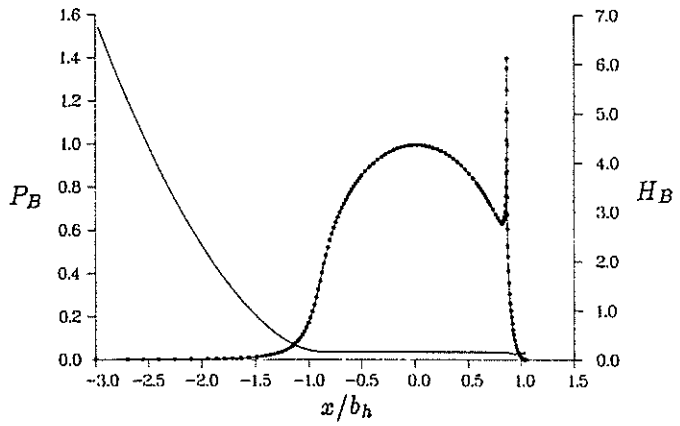

Figure 4.11: Bissett and Glander pressure and shape, example C, for: $W = 3.927 \times 10^{-5}$, $G = 4000$, $U = 2 \times 10^{-11}$

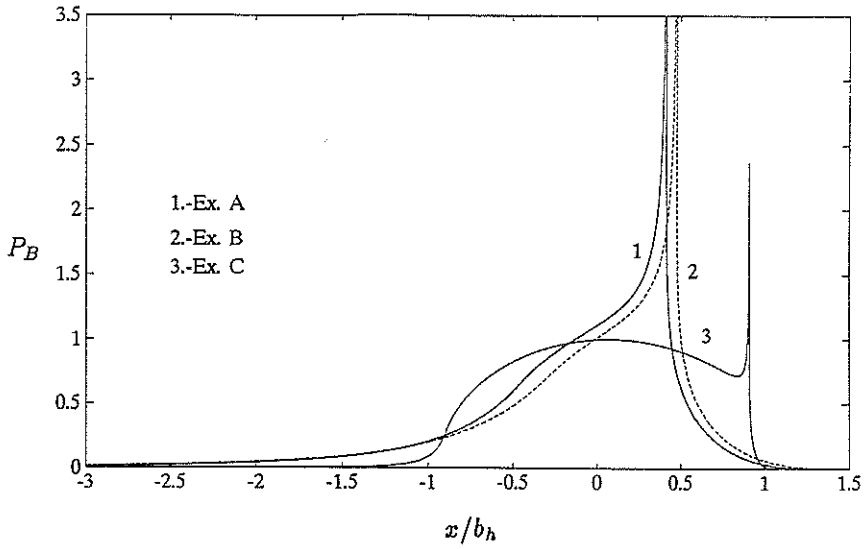

Figure 4.12: Present scheme pressures, Bissett and Glander examples A,B and C

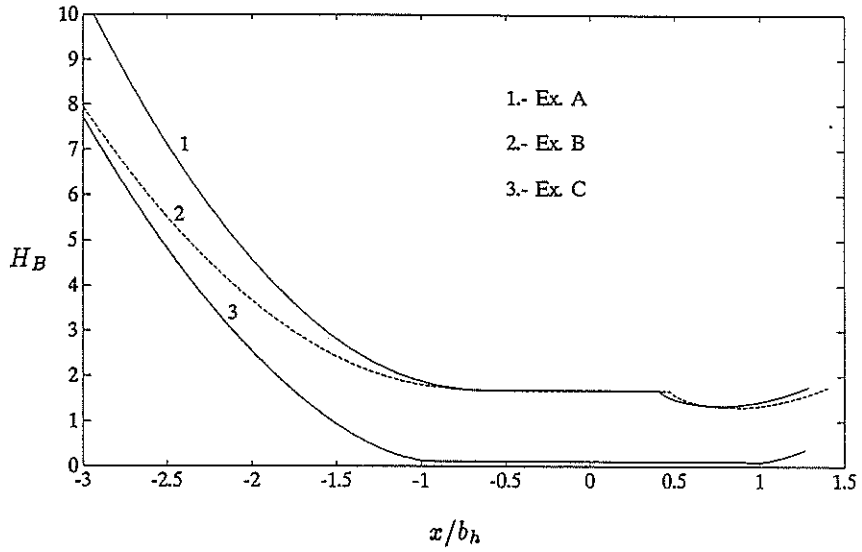

Figure 4.13: Present scheme shapes, Bissett and Glander examples A,B and C

Example	B_f	L_1/a	H^*	h_{min}/h^*	K_1	K	$\hat{q}_f$	$\hat{W}$	P_h
D. + H. 2	-0.152	1.571	0.130	0.763	10	25.359	0.0997	1.846	1.084
D. + H. 3	-0.187	1.571	1.300	0.770	8	0.822	0.1249	2.791	1.333
B. + G. A	-0.565	2.529	5.800	0.794	2.700	0.031	0.3673	5.403	1.855
B. + G. B	-0.566	2.724	6.500	0.781	2.700	0.031	0.3693	6.099	1.970
B. + G. C	same as D. + H. 2								

Table 4.1: Complete solutions. Parameters from the present scheme

					num.	eq. 4.33	
Example	ΔM	$(\hat{M})_R^R$	$(\hat{M}_h)_R$	$(\hat{M}_1)_R^L$	$(\hat{M}_{1h})_L$	$(\hat{M}_{1h})_L$	$(\hat{M}_h)_L$
D. + H. 2	0.0412	0.0424	0.0836	0.0683	3.7480	3.2729	0.0734
D. + H. 3	0.2350	0.1063	0.3413	0.1675	4.1474	3.6777	0.2144
B. + G. A	0.3780	0.5392	0.9172	0.8238	4.6197	4.5824	0.6858
B. + G. B	0.4250	0.5746	0.9996	0.8732	5.0770	4.7117	0.9405
B. + G. C	same as D. + H. 2						

Table 4.2: Stress intensity factors

Present Theory					Dowson and Higginson (D. + H.)			
Example	$\mathcal{S}$	$\mathcal{P}$	c/b_h	$(H_D)_{min}$	$\mathcal{S}$	$\mathcal{P}$	c/b_h	$(H_D)_{min}$
2	4.026	10.840	0.913	0.320×10^{-5}	4.200	10.930	≈ 0.9	0.395×10^{-5}
3	7.591	10.664	0.655	0.205×10^{-4}	7.470	10.930	≈ 0.6	0.200×10^{-4}
Present Theory					Bissett and Glander (B. + G.)			
Example	$\mathcal{S}$	$\mathcal{P}$	c/b_h	H_B^*	$\mathcal{S}$	$\mathcal{P}$	c/b_h	H_B^*
A	5.483	5.008	0.414	1.686	5.980	5.046	0.301	1.86
B	5.835	5.320	0.477	1.674	5.980	5.352	0.365	1.666
C	4.027	10.840	0.913	0.111	4.041	10.000	0.866	0.130

Table 4.3: Output data comparisons

The parameters $\mathcal{S}$ and $\mathcal{P}$ are the dimensionless velocity and load, and they are defined as:

$$\mathcal{S} = \alpha E' \left[\frac{\eta_o \bar{u}}{E'(2R)}\right]^{1/4} = \left[\frac{2}{3}\frac{K_1^4}{K}\right]^{1/4} \tag{4.55}$$

$$\mathcal{P} = \alpha p_h = K_1 P_h \tag{4.56}$$

Note that $\mathcal{P} = g_2$ and $\mathcal{S} = 2^{-1/4} g_4$; where g_2 and g_4 are the dimensionless parameters used by Johnson [40] 1970.

4.5 Maps of EHL Solutions

Fig. 4.14 shows calculated central film thicknesses and for comparison collected results from other authors are also included; with the following references: Archard [2] 1961; Cheng [12] 1972; Dowson and Higginson [21] 1977; Myers [59] 1991, Chittenden et al. [14] 1986. Now following Kapitza [45] 1955, the central film thickness is defined as:

$$H_k^* = \frac{h^*}{(2R)^{1/3}(\alpha\eta_o\bar{u})^{2/3}}$$

which is a convenient dimensionless parameter. The axes $\mathcal{P}$ and $\mathcal{S}$, are defined by equations 4.56 and 4.55.

In the introduction of the present scheme in Chapter 3 one of the main assumptions was discussed: the pressure spike is considered singular; therefore it is not possible to calculate its height. However, several authors (e.g Bissett and Glander [6] 1988, Venner et al. [79] 1990) claim that with enough resolution in the mesh, it is possible to see the smoothness of the spike and its finite height. What is clear, is that as the values of the dimensionless speed and load are varied, the pressure spike becomes either smoother or closer to a singularity (see results in e.g. Venner [75] 1991 and Myers [59] 1990). Fig. 4.16 shows a collection of results from several authors showing the spike height as function of the two parameters $\mathcal{S}$ and $\mathcal{P}$. Where the further references are: Pan and Hamrock [50] 1990 and Venner et al. [79] 1990. From Fig. 4.16 it is easy to see that compressible solutions give lower spike heights than equivalent incompressible ones.

It is known that the present scheme is more accurate for pressure distributions which show nearly singular spikes, where the inlet zone is short (e.g. $\mathcal{P} > 7$ and $\mathcal{S} > 2$). Fig. 4.15 shows solutions for the spike location from the same authors as before but some results with the present scheme have been also included.

The variable $DM = (M_h)_R - M_R^R$ is a good measure of the singularity strength of the pressure spike, since DM is the coefficient of the square root term in the central area pressures of equation 4.22 (left hand side of the spike) and it is also the coefficient for the square root term of the elastic slopes on the right hand side of the spike, equation 4.23. Therefore if $DM = 0$ the pressure distribution near the spike on the central region side must behave only as a logarithmic singularity and eventually as a nearly logarithmic non-singular function.

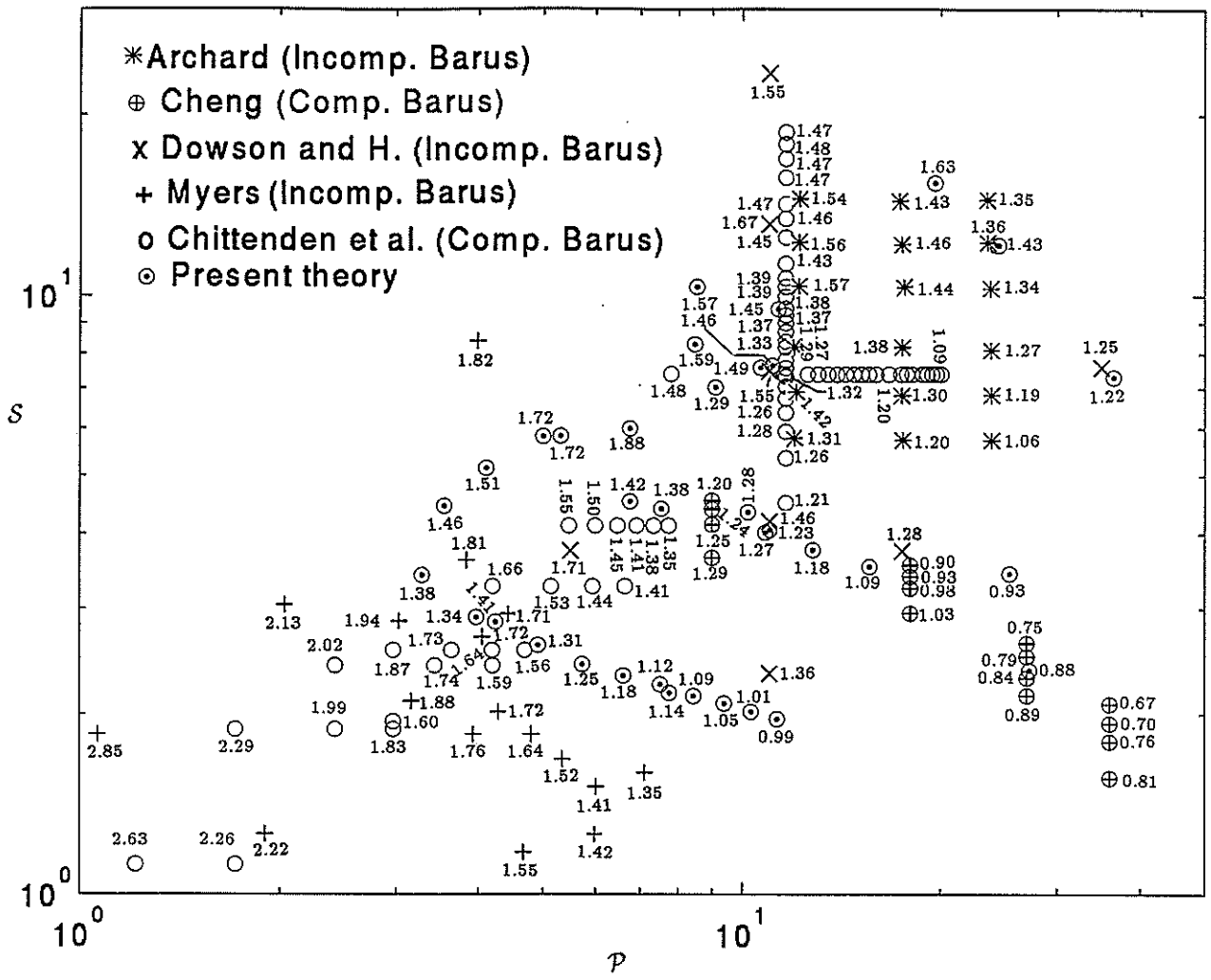

Figure 4.14: Solutions for the central Kapitza H_k^* film thickness, collected from several authors

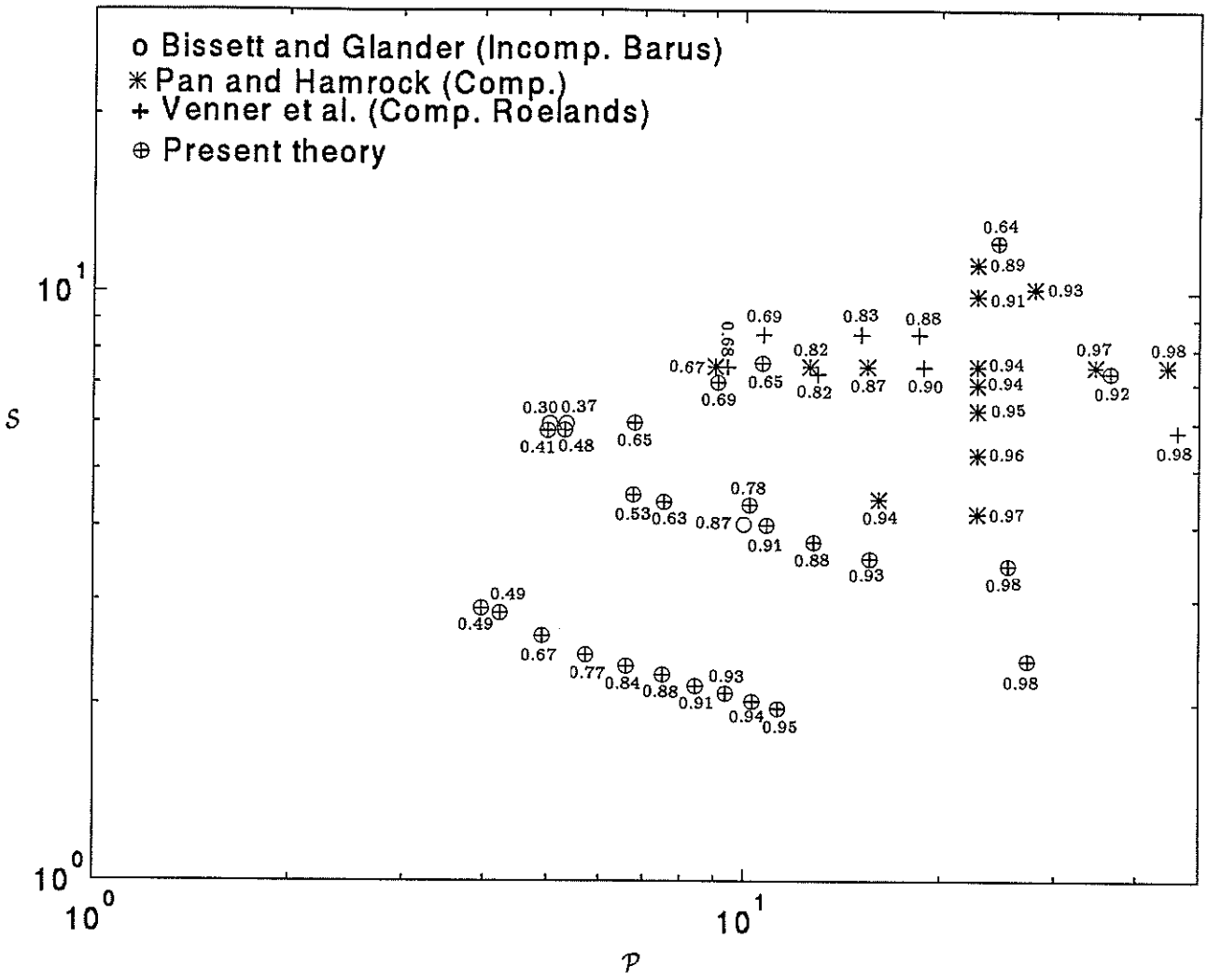

Figure 4.15: Solutions for the pressure spike location c/b_h, from several authors

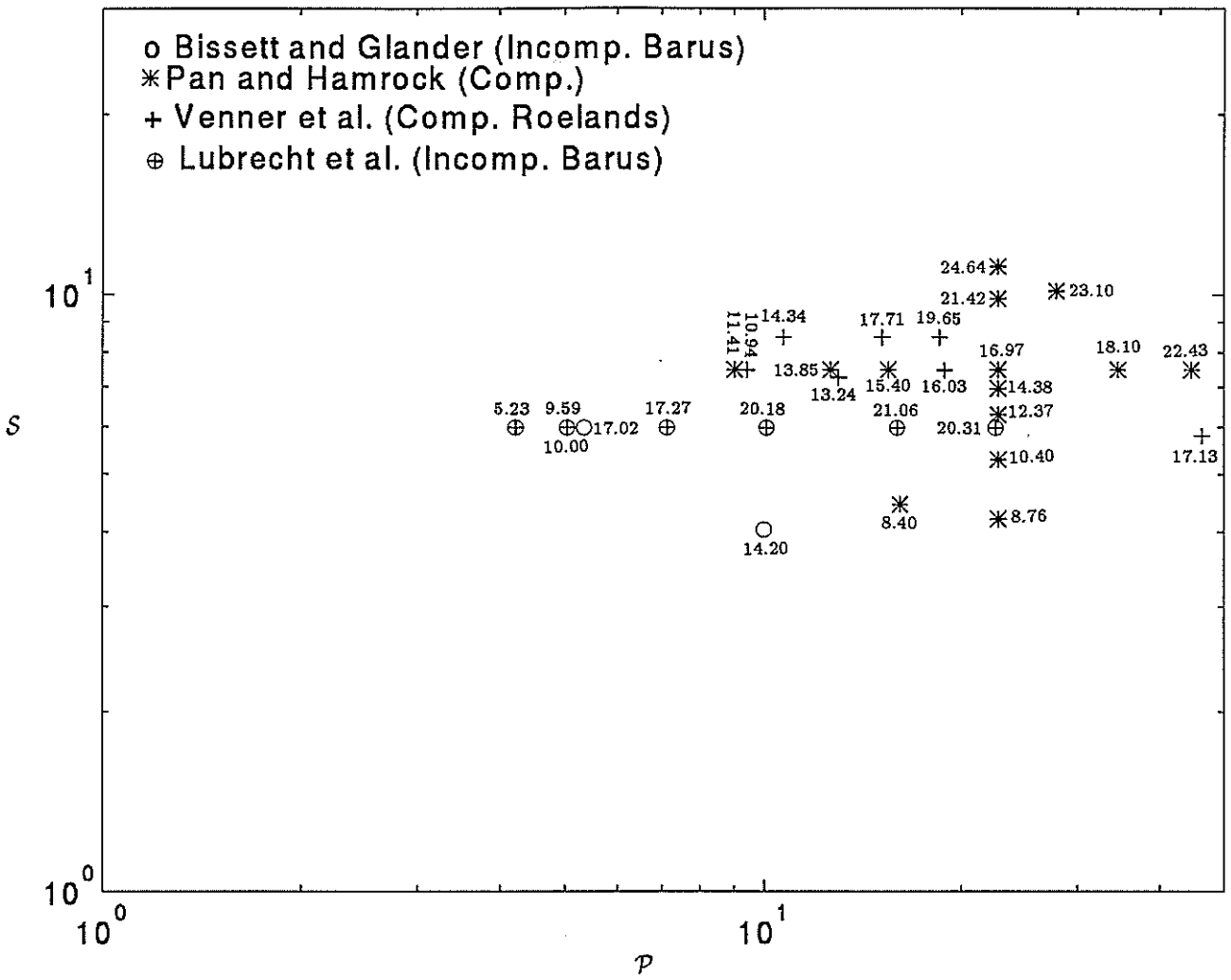

Figure 4.16: Solutions for the pressure spike height αp, from several authors

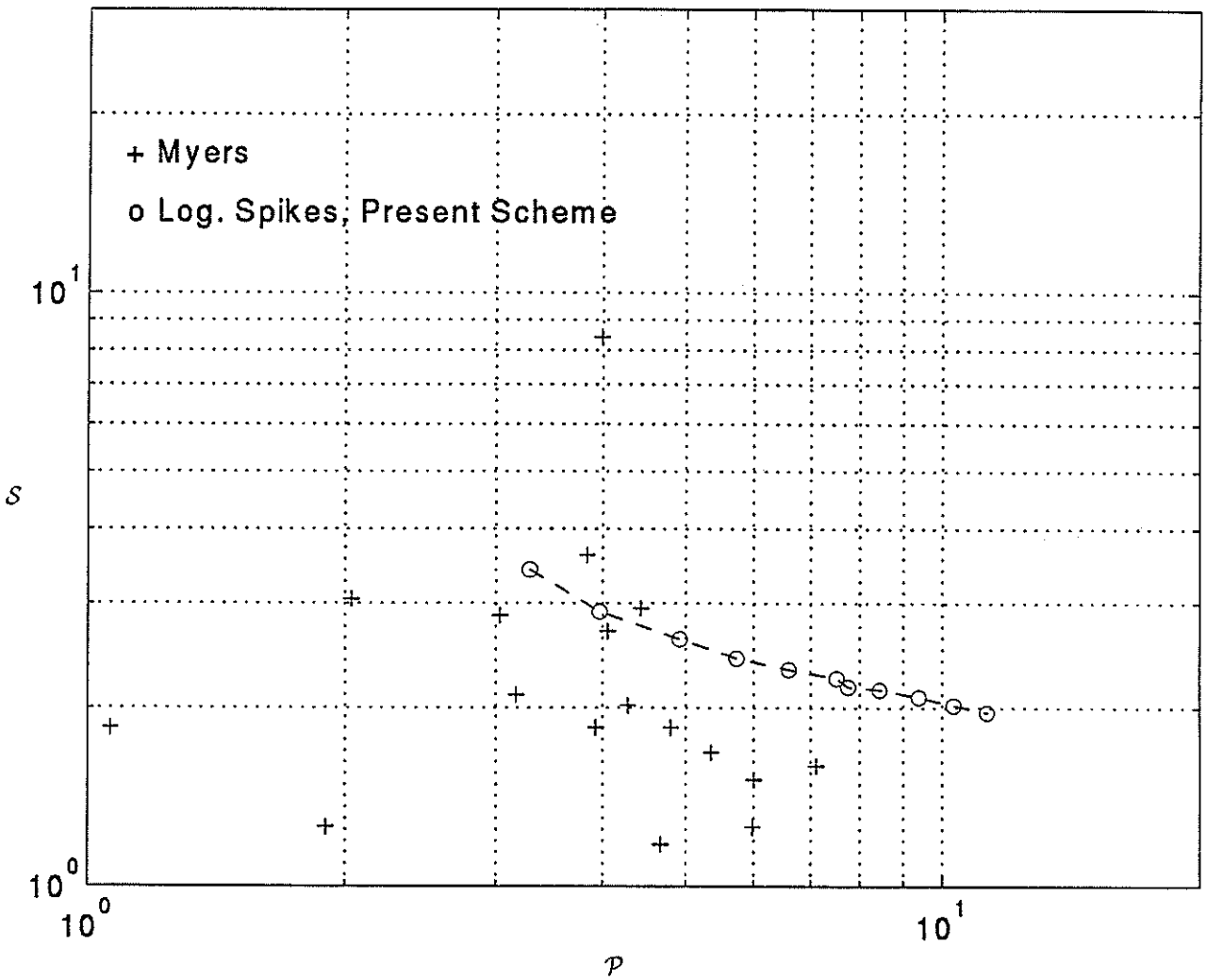

Figure 4.17: Solutions obtained with $\Delta M = 0$

Fig. 4.17 shows the solutions found by the present scheme with $\Delta M = 0$, so that there are purely logarithmic (i.e. rather weak) singularities. Above this line of solutions (for large values of $\mathcal{P}$ and $\mathcal{S}$) it is impossible to make $DM = 0$ and it seems likely that the square root component will increase. Below the line the spike will be finite and smooth until eventually, for low values of $\mathcal{P}$ and $\mathcal{S}$, it vanishes. The figure shows points representing the solutions obtained by Myers [59] 1991, using a method which can only be applied to cases with a finite and smooth spike, or no spike at all: note that, with one unexplained exception, all these points lie below, or very close to, the critical line. Johnson [40] points out that spikes can be expected for $g_4 > 2.2$ ($\mathcal{S} > 1.85$) and his conclusion is based on data with $\mathcal{P} \approx 10$; it agrees well with the first point of the log curve of Fig. 4.17.

Fig. 4.18 summarizes the trend of the singularity strength for the pressure spike.

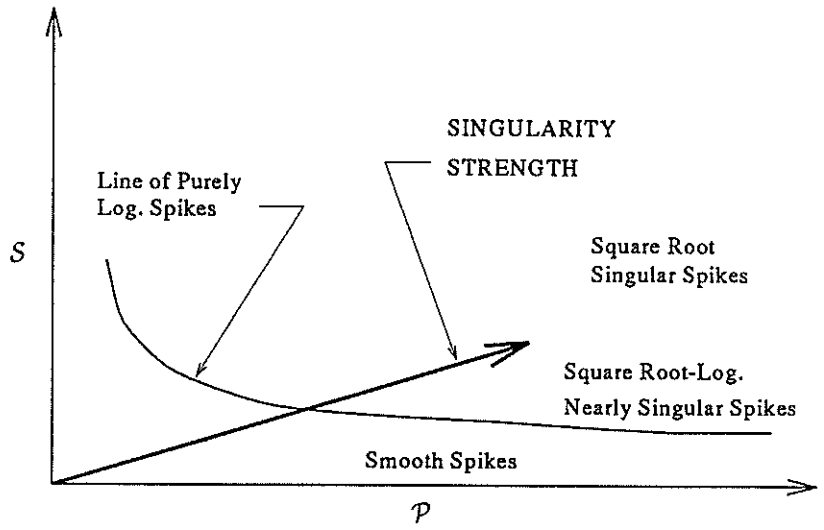

Figure 4.18: Observed trend of the singularity strength in the pressures spike

4.6 Compressibility

The limitations for the applicability of linear fracture mechanics on the solution of truncated Hertzian contacts have been pointed out in Section 3.1 where it is clear that the 'contact' zone after the application of the external tractions must remain parallel. When in EHL the analysis considers compressibility, it is known (e.g. Dowson and Higginson [21]) that one of the effects is precisely that the central region shape is no longer parallel

but slightly curved. However, if the curvature is not large enough (say less than 10 % of h^*) the application of the fracture mechanics equations would not be appreciably affected. Therefore it is useful to obtain a criterion to relate the amount of curvature in the central region under given conditions of load, so that the possibility of the application of the present EHL scheme can be assessed.

In order to have parallel film thickness ($h = h^*$) in the central region with constant lubricant velocity, the lubricant density has to be constant, since the constant mass flow is:

$$Q_m = \dot{\rho}\bar{u}h^*$$

For standard values of β and γ the Dowson and Higginson equation of density (e.g. Chapter 2) can be written as:

$$\bar{\rho} = \frac{\rho}{\rho_o} = 1 + \frac{0.6p}{1.7p + 1} \tag{4.57}$$

where p is given in GPa .

As a measure of parallelism of the channel it is possible to define a ratio of densities as:

$$r = \frac{\bar{\rho}_{min}}{\bar{\rho}_{max}} \tag{4.58}$$

where the density $\bar{\rho}_{max}$ is located at the pressures spike, then with $p_{max} = \infty$ from equation 4.57: $\bar{\rho}_{max} = 1.353$, however, it is not realistic to regard the surroundings of the spike as part of the parallel zone (see Fig. 4.19). It is more accurate to take the first maximum of pressure p_a^* (the maximum of the equivalent dry contact pressures to produce a flat of length a) which in dimensional form is:

$$p_{max} = p_a^* = \frac{\mathcal{P}}{\alpha P_h} \tag{4.59}$$

Now p_{min} is unknown but one can assume that at the end of the inlet zone the pressure is a fraction C_q of p_a^*, therefore:

$$p_{min} = C_q p_{max} \tag{4.60}$$

then by substituting equations 4.59 and 4.60 into equation 4.57, equation 4.58 can be written as:

$$r = \frac{p_a^*(1.7 + 2.3C_q + 3.91C_q p_a^*) + 1}{p_a^*(2.3 + 1.7C_q + 3.91C_q p_a^*) + 1} \tag{4.61}$$

A standard value of α is 17 GPa, so equation 4.59 is reduced to:

$$p_a^* = \frac{\mathcal{P}}{17P_h} \tag{4.62}$$

with P_h given by equation 4.51.

It is also possible to find the value of p_a^*, say $\bar{p}_a$ which produces a minimum in r. So by differentiating equation 4.61: $dr/dp_a^* = 0$, one obtains:

$$\bar{p}_a = \sqrt{\frac{0.6}{2.346C_q}} \tag{4.63}$$

Examples:

a).- $C_q = 0.3$, from equation 4.63: $\bar{p}_a = 0.9233$ GPa and substituting into equation 4.61: $r_{min} = 0.9156$.

b).- $C_q = 0.5$, from equation 4.63: $\bar{p}_a = 0.7152$ GPa and substituting into equation 4.61: $r_{min} = 0.9495$.

c).- $C_q = 0.7$, from equation 4.63: $\bar{p}_a = 0.6044$ GPa and substituting into equation 4.61: $r_{min} = 0.9735$.

It is clear than even for small values of C_q (e.g. $C_q = 0.3$) the minimum density ratio r is still near 1 ($r_{min} = 0.91$), it is 9 % of difference. Therefore it is likely that in most of practical EHL compressible contacts the error due to the parallel film assumption is small and the present theory can be applied.

4.6.1 Analysis of Flow in Compressible EHL

The Reynolds equation, as showed in Chapter 2, is based on a balance of mass throughout the channel. This condition has always to be satisfied. Consider an EHL contact which is divided in three zones (e.g. Fig. 4.19): inlet, ending at point '1', central zone from '1' to '2' and outlet starting at point '2'.

The mass flow at the point 1 is given by:

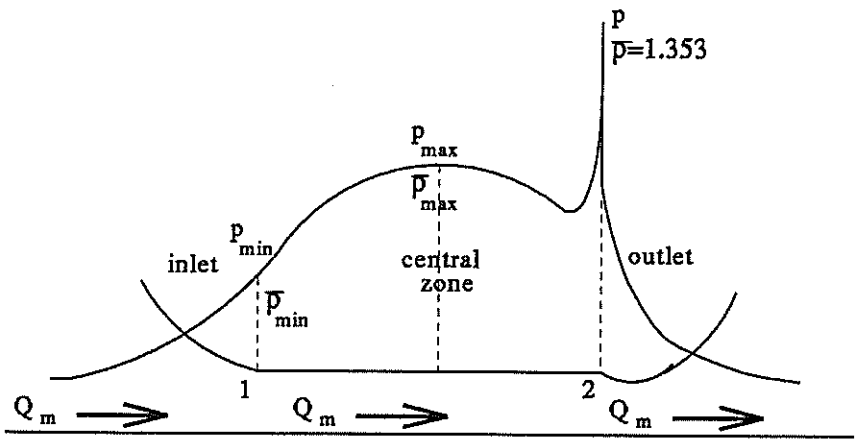

Figure 4.19: Balance of flow in a EHL contact

$$(Q_m)_1 = \rho \bar{u} (h^*)_1 \tag{4.64}$$

and for the point 2:

$$(Q_m)_2 = \rho \bar{u} (h^*)_2 \tag{4.65}$$

equating flows:

$$Q_m = (Q_m)_1 = (Q_m)_2$$

from which:

$$(h^*)_1 = \frac{\rho_2}{\rho_1} (h^*)_2 \tag{4.66}$$

or in dimensionless form:

$$(H^*)_1 = \frac{\rho_2}{\rho_1} (H^*)_2 \tag{4.67}$$

In conclusion, equation 4.66 relates the 'central' film thickness calculated for the inlet with the one from the outlet, in compressible lubricants. This condition must be included in the present scheme.

4.6.2 The Exit Condition for Compressible Fluids

When dealing with incompressible lubricants the parameter L_1 was defined as the value of x for which the outlet pressures become zero and $h = h^*$ (it is $v_f = 0$). This parameter is important in the integration of the Reynolds equation for the outlet and in the calculation of stress intensity factors and slopes. However, for compressible lubricants the conditions to calculate this length are affected by the densities: the pressure becomes zero when $\rho_o h = \rho^* h^*$.

Consider now the Reynolds equation for compressible lubricants:

$$\frac{dq}{dx} = 12\eta_o \bar{u} \frac{v_f + h^*(1 - \bar{\rho}^*/\bar{\rho})}{(h^* + v_f)^3} \tag{4.68}$$

which in dimensionless form is:

$$\frac{d\hat{q}}{dX} = \left[\frac{1}{K}\right] \frac{V_f + H^*(1 - \bar{\rho}^*/\bar{\rho})}{(H^* + V_f)^3} \tag{4.69}$$

from equation 4.68 it is clear that the Reynolds boundary condition: $\frac{dp}{dx} = 0$ and $p = 0$ at $x = L_1$ will be satisfied when:

$$v_f = -h^*(1 - \bar{\rho}^*/\bar{\rho}) \tag{4.70}$$

since $v_f = h - h^*$, therefore the condition becomes:

$$\bar{\rho} h = \bar{\rho}^* h^*$$

or:

$$\rho_o h = \rho^* h^* \tag{4.71}$$

Finally in dimensionless form equation 4.70 is written as:

$$V_f = H^*(\bar{\rho}^* - 1) \tag{4.72}$$

at $X = L_1/a$.

It is no longer: $V_f = 0$ at $X = L_1/a$. In the inlet $L_2 \to \infty$ and the condition makes no difference.

4.6.3 Compressible Complete Solutions

The same procedure described in Fig. 4.2 has been applied for compressible fluids but now including the conditions of equations 4.67 and 4.72 plus the compressible Reynolds equation (equation 4.69).

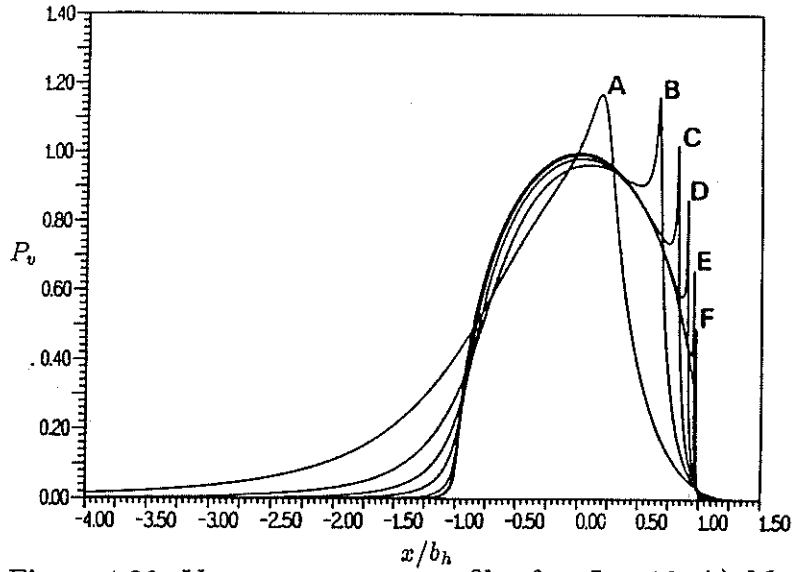

Figure 4.20: Venner pressures profiles for: $L = 10$, A) $M = 2$, B) $M = 5$, C) $M = 10$, D) $M = 20$, E) $M = 50$, and F) $M = 100$

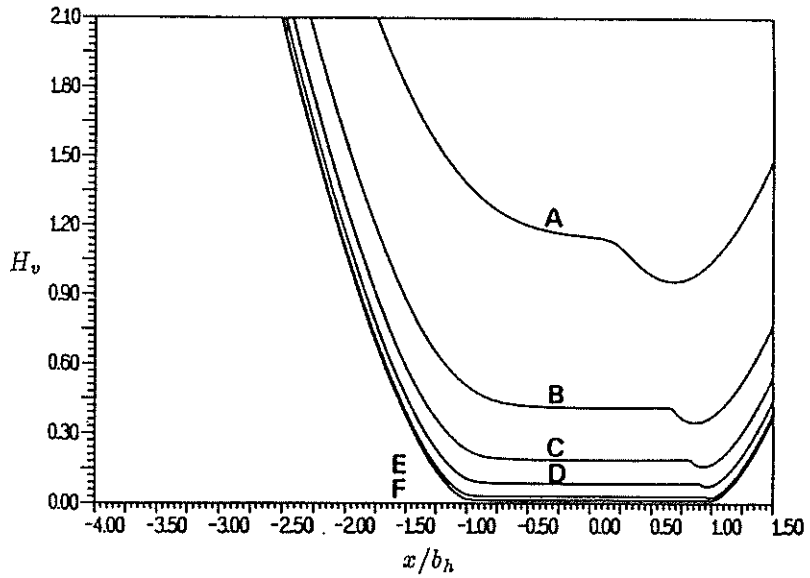

Figure 4.21: Venner film shapes for: $L = 10$, A) $M = 2$, B) $M = 5$, C) $M = 10$, D) $M = 20$, E) $M = 50$, and F) $M = 100$

Two examples of compressible lubricant with the Barus' law of viscosity are solved and

compared with the results of Venner [75] 1991; obtained by using the Roelands equation instead.

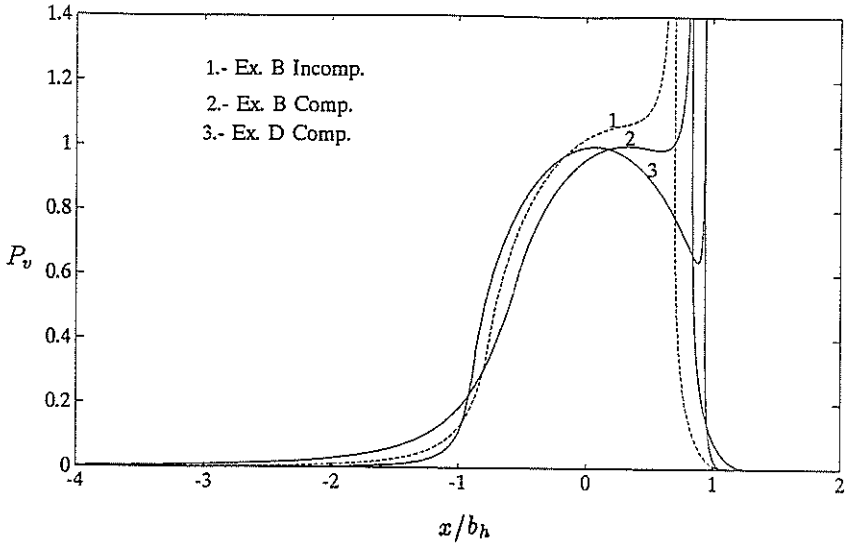

Figure 4.22: Present scheme pressure profile for: $L = 10$, B) $M = 5$, and D) $M = 20$

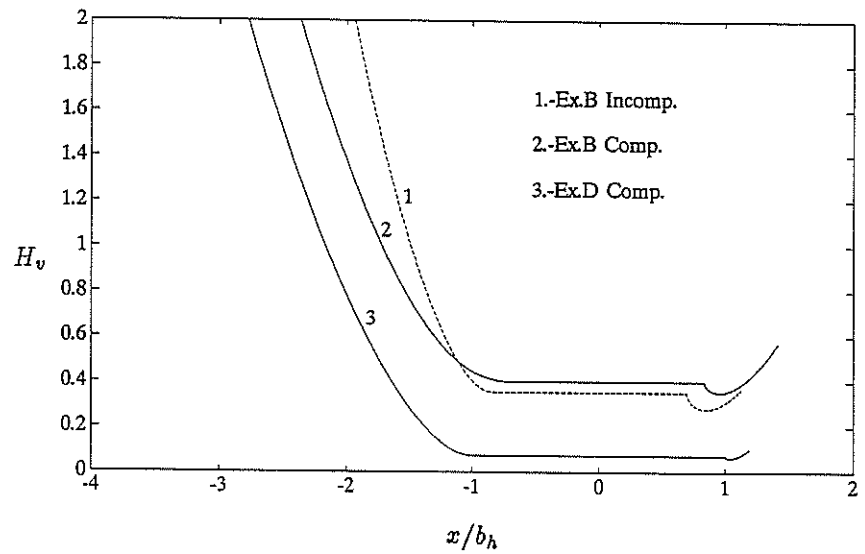

Figure 4.23: Present scheme film shapes for: $L = 10$, B) $M = 5$, and D) $M = 20$

The pressure distributions and shapes reported by the reference are shown in Figs. 4.20 and 4.21.

Where the dimensionless parameters used by Venner are:

$$M = W(2U)^{-1/2} = \sqrt{6}\hat{W}K^{1/2}$$

$$L = G(2U)^{1/4} = (\frac{8}{3})^{1/4}\frac{K_1}{K^{1/4}}$$

and his pressure and film thickness are defined as:

$$P_v = p/p_h; \quad H_v = \frac{hR}{b_h^2}$$

The results with the present scheme for examples B and D plus the incompressible solution of example B are given in Figs. 4.22 and 4.23, with further data in Tables 4.4, 4.5 and 4.6.

Example	B_f	L_1/a	$(H^*)_2$	$(H^*)_1$	h_{min}/h^*	K_1	K	$\hat{q}_f$	$\hat{W}$	P_h
B comp.	-0.235	1.398	1.300	1.507	0.884	6.7	0.536	0.1491	2.546	1.273
D comp.	-0.092	1.104	0.165	0.192	0.869	17.0	23.893	0.0588	1.791	1.068
B incomp.	-0.214	1.528	1.200	1.528	0.793	7.0	0.653	0.1428	2.662	1.302

Table 4.4: Complete solutions. Parameters from the present scheme

					num.	eq. 4.33	
Example	ΔM	$(\hat{M})_R^R$	$(\hat{M}_h)_R$	$(\hat{M}_1)_R^L$	$(\hat{M}_{1h})_L$	$(\hat{M}_{1h})_L$	$(\hat{M}_h)_L$
B comp.	0.1300	0.1044	0.2344	0.1644	3.4920	3.5098	0.2988
D comp.	0.0410	0.0211	0.0621	0.0337	3.0000	3.2391	0.0676
B incomp.	0.1920	0.1171	0.3091	0.1847	5.1000	3.6270	0.2130

Table 4.5: Stress intensity factors

	Present Theory				Venner			
Example	$\mathcal{S}$	$\mathcal{P}$	c/b_h	$(H_v^*)_2$	$\mathcal{S}$	$\mathcal{P}$	c/b_h	H_v^*
B comp.	7.075	8.530	0.836	0.401	7.071	8.920	≈ 0.700	≈ 0.420
D comp.	6.948	18.152	0.941	0.072	7.071	19.947	≈ 0.930	≈ 0.080
B incomp.	7.035	9.113	0.694	0.420	—	—	—	—

Table 4.6: Output data comparisons

It is clear from Figs. 4.22 and 4.23 and Table 4.6 that the agreement of the present scheme is slightly better for the Venner's example D where the load is higher. Also in

Fig. 4.22 the effect of compressibility in EHL can be seen, since the spike has been shifted to the right hand side of the contact and the central film thickness reduced. If the solution had been obtained with a conventional numerical scheme, the reduction of the spike height would have been observed also. From Table 4.6 it can be seen that the present scheme gives slightly lower central film thicknesses than the Venner's values and locates the spike slightly more to the right side.

4.7 The Roelands Viscosity Law

In Chapter 2 it was pointed out that for high pressures the viscosities predicted by the Barus' law become much larger than the experimental values observed. It was also pointed out that a more accurate relation is given by the Roelands' equation. In Fig. 4.24 the two equations have been plotted for values of the dimensionless pressure P. The disagreement is clear for large pressures.

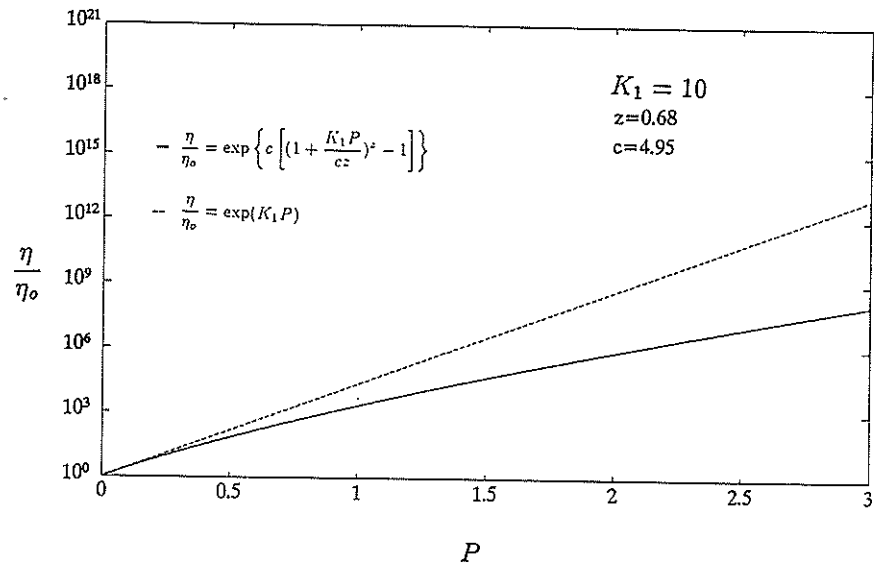

Figure 4.24: Comparison of viscosities between the Barus and Roelands' equations

Despite this difference, the results for film thickness and pressure in EHL are little affected, since for high pressures the viscosity is already too large and its reciprocal almost vanishes in the Reynolds equation.

However, more recent results from literature frequently are obtained involving the Roelands' equation rather than the Barus' law and it is convenient to modify the present scheme to deal with it.

In the present section the modifications are described and again comparisons with the Venner examples are made.

4.7.1 The Reduced Pressure Equation

The Roelands relationship was introduced in Section 2.2 from which:

$$\frac{\eta(p)}{\eta_o} = \exp\left\{c\left[(1+\frac{p}{p_o^*})^z - 1\right]\right\} \tag{4.73}$$

where: $c = 9.67 + \ln\eta_o$; z is constant depending on the lubricant (here z will be taken as 0.68) and $p_o^* = 1.98 \times 10^8$ Pa.

Substituting equation 4.73 in the reduced pressure equation 3.31 and differentiating it, so:

$$\frac{dq}{dx} = \exp\left\{-c\left[(1+p/p_o^*)^z - 1\right]\right\}\frac{dp}{dx} \tag{4.74}$$

integrating:

$$q(p) = \int_{p=0}^{p} \exp\left\{-c\left[(1+p/p_o^*)^z - 1\right]\right\}\, dp \tag{4.75}$$

The Barus equivalent of equation 4.75 (i.e. equation 3.34) was possible to integrate analytically, but in this case it is not possible.

In dimensionless form, equation 4.75 becomes:

$$\hat{q}(P) = \int_{P=0}^{P} \exp\left\{-c\left[(1+\frac{K_1 P}{cz})^z - 1\right]\right\}\, dP \tag{4.76}$$

where K_1 has the same definition ($K_1 = \alpha p_a^*$).

4.7.2 Outlet Integration of the Reynolds Equation

The Reynolds equation 3.33 is still valid, and in dimensionless form it is:

$$\frac{d\hat{q}}{dX} = \left[\frac{1}{K}\right]\frac{V_f}{(H^* + V_f)^3} \tag{4.77}$$

with K defined as before:

$$K = \frac{E'a^4}{192\eta_o \bar{u} R^3}$$

The first boundary condition is: At $X = 1$, $\hat{q} = \hat{q}(1)$, so:

$$\hat{q}(X) = \hat{q}(1) + \frac{1}{K} I(X) \tag{4.78}$$

where:

$$I(X) = \int_{X=1}^{X} \frac{V_f}{(H^* + V_f)^3}\, dX \tag{4.79}$$

And from equation 4.76:

$$\hat{q}(1) = \frac{1}{\bar{K}_1} = \lim_{P \to \infty} \int_{P=0}^{P} \exp\left\{-c\left[(1 + \frac{K_1 P}{cz})^z - 1\right]\right\}\, dP \tag{4.80}$$

where $\bar{K}_1$ is defined as the equivalent constant K_1 for the Reynolds-Roelands equation. From equations 4.78 and 4.80:

$$\hat{q}(X) = \frac{1}{\bar{K}_1} + \frac{1}{K} I(X) \tag{4.81}$$

The second boundary condition is: At $X = L_1/a$, $P = 0$. And from equation 4.78:

$$0 = \frac{1}{\bar{K}_1} + \frac{1}{K} I(L_1/a) \tag{4.82}$$

where:

$$I(L_1/a) = \int_{X=1}^{L_1/a} \frac{V_f}{(H^* + V_f)^3}\, dX \tag{4.83}$$

and:

$$K = -\bar{K}_1 I(L_1/a) \tag{4.84}$$

Finally by substituting equation 4.84 into 4.81 it is possible to obtain:

$$\hat{q}(X) = \frac{1}{\bar{K}_1}\left[1 - \frac{I(X)}{I(L_1/a)}\right] \tag{4.85}$$

Equations 4.84 and 4.81 show that the main difference with the equations coming from the Barus' law (equations 3.43 and 3.46) is that K_1 has now been replaced by $\bar{K}_1$.

4.7.3 Calculation of $\bar{K}_1$

The constant $\bar{K}_1$ is defined in equation 4.80, which for general cases has to be solved numerically.

Put:

$$t = c\left[(1 + \frac{K_1 P}{cz})^z - 1\right]$$

so, equation 4.80 becomes:

$$\hat{q}(1) = \frac{1}{\bar{K}_1} = \lim_{P\to\infty} \frac{1}{K_1} \int_{t=0}^{t} e^{-t} \left(\frac{t}{c} + 1\right)^{\frac{1}{z}-1} \, dt \tag{4.86}$$

it is to say:

$$\hat{q}(1) = \frac{1}{\bar{K}_1} = \frac{1}{K_1} \int_{t=0}^{\infty} e^{-t} \left(\frac{t}{c} + 1\right)^{\frac{1}{z}-1} \, dt \tag{4.87}$$

equation 4.87 can be solved by using Gaussian quadrature (e.g. Handbook of Mathematical Functions [1]):

$$\int_0^\infty e^{-t} f(t) \, dt = \sum_{i=1}^{n} w_i f(t_i)$$

which gives good results with $n \geq 8$.

Equation 4.80 is solved only once in the computational sequence for every example, since the value of K_1 remains unchanged.

4.7.4 Analytical Solution for $\hat{q}(X)$

For the particular case when $z = 2/3$ there is an analytical solution for equation 4.80; the equation can be written as:

$$\hat{q} = e^c \int_{P=0}^{P} \exp\left\{-c\left[1 + \frac{3K_1 P}{2c}\right]^{2/3} + c\right\} \, dP$$

defining:

$$u = \sqrt{c(1 + \frac{3K_1 P}{2c})^{2/3}}$$

then:

$$\hat{q}(u) = e^c \frac{2}{K_1\sqrt{c}} \int_{u=\sqrt{c}}^{u} u^2 e^{-u^2} \, du \tag{4.88}$$

integrating by parts equation 4.88:

$$\hat{q}(u) = \frac{-e^c}{K_1\sqrt{c}} \left\{ \epsilon\, e^{-\epsilon^2} - \sqrt{c}\, e^{-c} - \frac{\sqrt{\pi}}{2}[erf(\epsilon) - erf(\sqrt{c})] \right\} \tag{4.89}$$

where:

$$\epsilon = \sqrt{c}\,(1 + \frac{3K_1P}{2c})^{1/3}$$

and: $erf(\epsilon)$ is the error function which is approximately:

$$erf(\epsilon) \approx \frac{2}{\sqrt{\pi}} \sum_{i=0}^{n} \frac{(-1)^i \epsilon^{2i+1}}{i!\,(2i+1)} \tag{4.90}$$

where $n \geq 70$ for values of $2 \leq \epsilon \leq 5$ to obtain enough accuracy.

Example: $z = 2/3$, $c = 5.049$, $K_1 = 5$, $P = 7$, then: $\epsilon = 5.0568$, $erf(\epsilon) \approx erf(\infty) = 1$, and $erf(\sqrt{c}) \approx 0.9985$ (with $n = 85$).

From equation 4.89: $\hat{q}(P) = 0.21824920$. From equation 4.76 integrated by Simpson's rule: $\hat{q}(P) = 0.21824930$. And from equation 4.87 with $P = 7 \approx \infty$: $\hat{q}(P) = 0.21824936$. The agreement is very good !

4.7.5 Computational Procedure for the Outlet

The procedure is very similar to the one described in Section 3.4.2 except that now the integration of the calculation of pressures from the reduced pressures is made following several interpolations in order to relate $\hat{q}(X)$ with $P(X)$. The scheme is shown in Fig. 4.25.

4.7.6 Complete Solutions with the Roelands Viscosity Law

The inlet region is solved in the same way as before but now using the interpolation scheme described in Fig. 4.25. Notice the value of $\hat{q}_f$ for the inlet can now take values $\hat{q}_f \leq 1/\bar{K}_1$. The overall computational scheme of Fig. 4.2 is still applicable.

One example has been solved, the compressible Roelands example B given by Venner and already introduced in Section 4.6.3. Here the corresponding Roelands incompressible and compressible solutions are calculated and as a matter of comparison the Barus solutions are plotted. Figs. 4.26 and 4.27 show the pressures and shapes for the incompressible example B obtained with the present scheme, and Figs. 4.28 and 4.29 show the corresponding pressures and shapes for the compressible solutions of the same example.

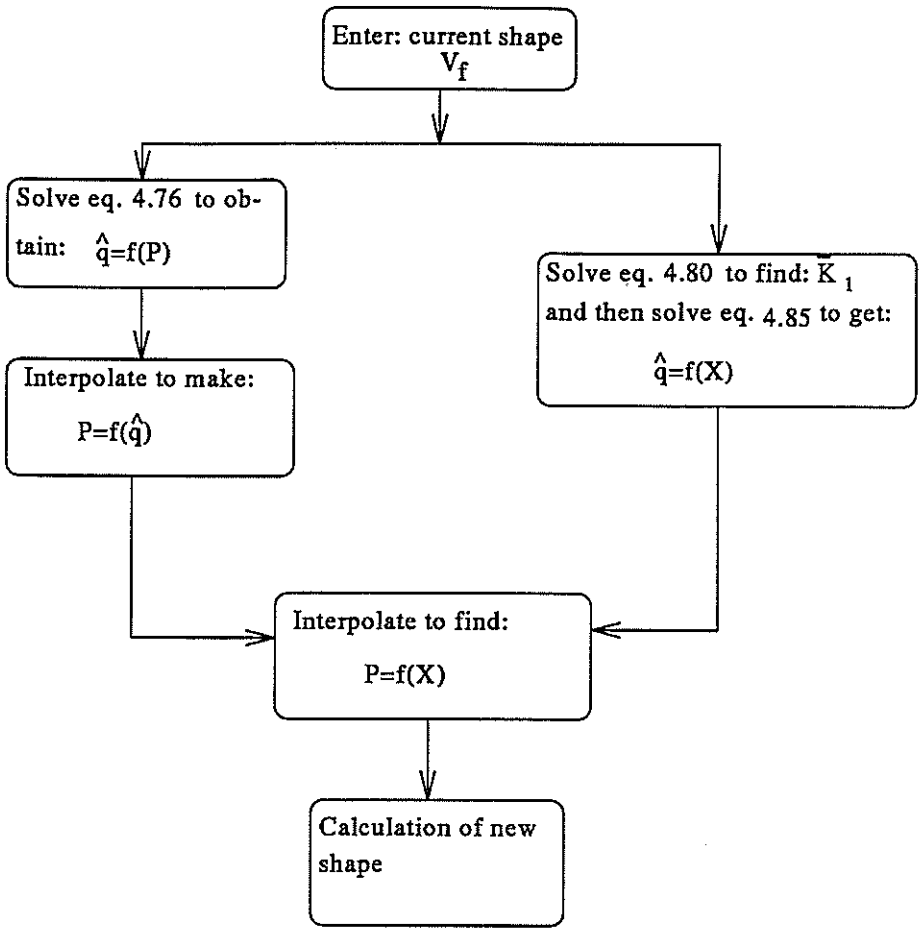

Figure 4.25: Integration of the Reynolds equation with the Roelands viscosity law included

Further data are given in Tables 4.7, 4.8 and 4.9. The solution can be compared with the Venner's results of Figs. 4.20 and 4.21 of Section 4.6.3.

By looking at Figs. 4.26 and 4.27 (incompressible fluids) it is possible to see that the effect of the Roelands viscosity law is small and it tends to locate the pressures spikes slightly more to the left hand side of the contact ($\approx$ 6 %) and the central film thickness is now slightly reduced ($\approx$ 7.5 %), this is the same qualitative effect expected from a reduction of load, since the viscosity has been reduced. However, for the compressible case the qualitative effects seem to be the opposite (e.g. Figs. 4.28 and 4.29), the spike has been shifted to the right hand side of the contact and the central film thickness reduced. This must be the effect of the compressibility rather than the change of viscosity law for this particular example. In any case, these remarks should be taken cautiously, since it is

very difficult to match precisely the parameters $\mathcal{S}$ and $\mathcal{P}$ with a comparable given solution (i.e. Table 4.9) due to the fact that in the present scheme they are output variables.

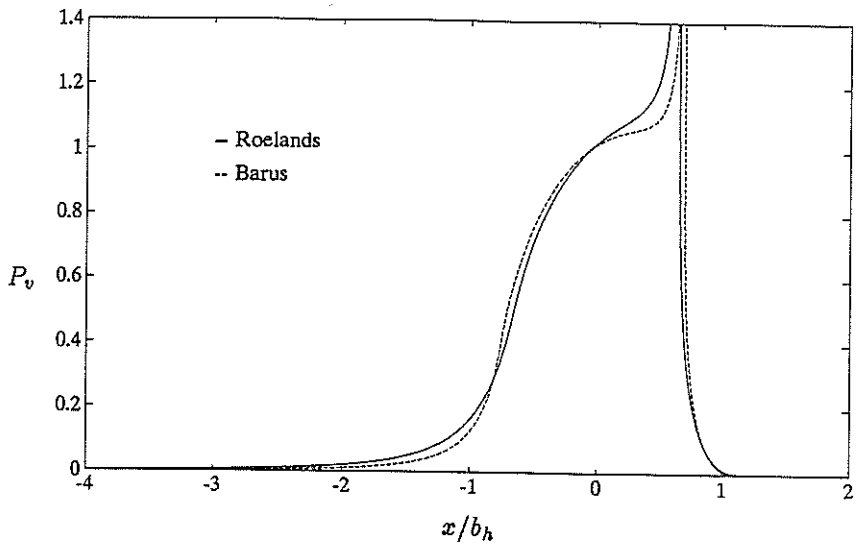

Figure 4.26: Present scheme pressure profile for: $L = 10$ and $M = 5$. Incompressible example B

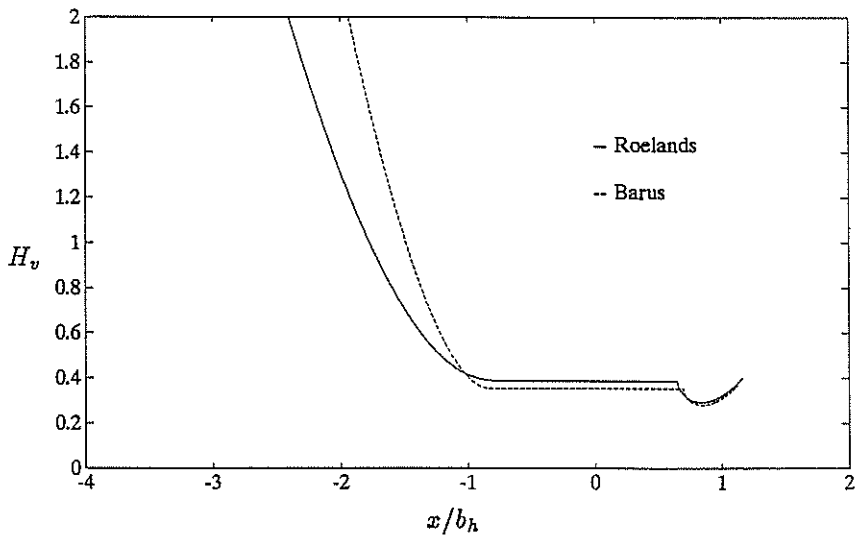

Figure 4.27: Present scheme film shapes for: $L = 10$ and $M = 5$. Incompressible example B

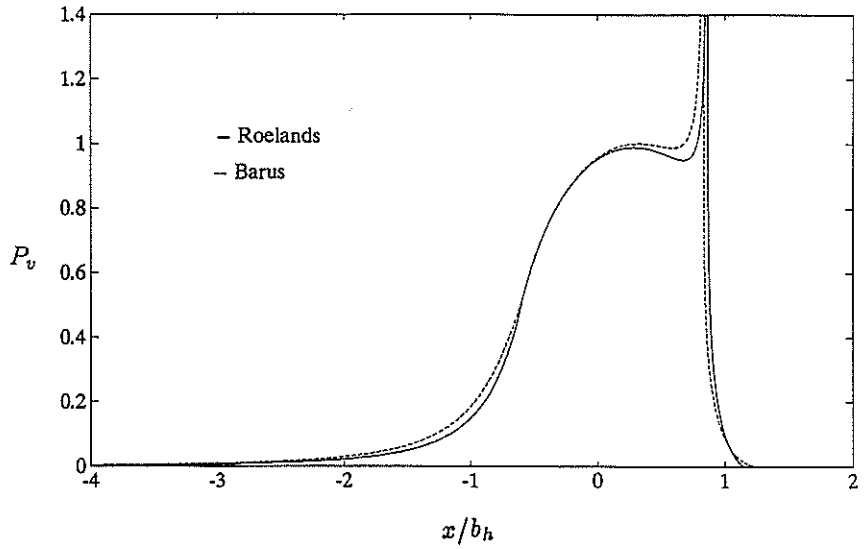

Figure 4.28: Present scheme pressure profile for: $L = 10$ and $M = 5$. Compressible example B

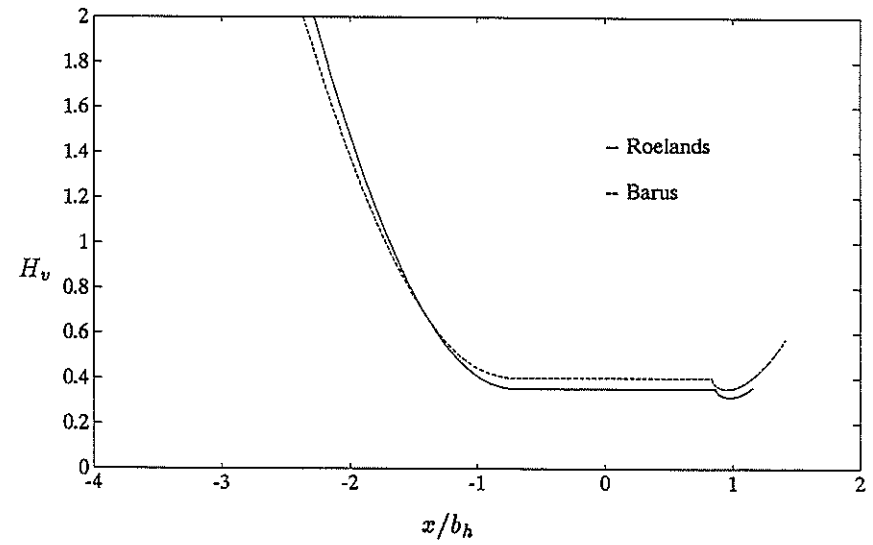

Figure 4.29: Present scheme film shapes for: $L = 10$ and $M = 5$. Compressible example B

Example	B_f	L_1/a	$(H^*)_2$	$(H^*)_1$	h_{min}/h^*	K_1	K	$\hat{q}_f$	$\hat{W}$	P_h
B comp. R.	-0.334	1.342	1.100	1.292	0.896	7.0	0.653	0.155	2.440	1.246
B comp. B.	-0.235	1.398	1.300	1.507	0.884	6.7	0.536	0.149	2.5461	1.273
B incomp. R.	-0.347	1.685	1.500	1.500	0.757	7.0	0.654	0.155	3.048	1.392
B incom. B.	-0.214	1.528	1.200	1.200	0.793	7.0	0.653	0.143	2.6624	1.302
where: R.= Roelands and B.= Barus										

Table 4.7: Complete solutions. Parameters from the present scheme

					num.	eq. 4.33	
Example	ΔM	$(\hat{M})_R^R$	$(\hat{M}_h)_R$	$(\hat{M}_1)_R^L$	$(\hat{M}_{1h})_L$	$(\hat{M}_{1h})_L$	$(\hat{M}_h)_L$
B comp. R.	0.1353	0.1203	0.2083	0.1885	3.4633	3.4687	0.2881
B comp. B.	0.1300	0.1044	0.2344	0.1644	3.4920	3.5097	0.2988
B incomp. R.	0.2217	0.1802	0.4019	0.2806	3.4654	3.7730	0.3053
B incomp. B.	0.1920	0.1171	0.3091	0.1847	5.1000	3.6271	0.2130
where: R.= Roelands and B.= Barus							

Table 4.8: Stress intensity factors

	Present Theory					Venner			
Example	$\mathcal{S}$	$\mathcal{P}$	c/b_h	$(H_v^*)_2$	K_1	$\mathcal{S}$	$\mathcal{P}$	c/b_h	H_v^*
B comp. R.	7.035	8.724	0.866	0.361	6.439	7.071	8.920	≈ 0.700	≈ 0.420
B comp. B.	7.075	8.530	0.836	0.401	—	—	—	—	—
B incomp. R.	7.034	9.746	0.649	0.387	6.439	—	—	—	—
B incomp. B.	7.035	9.113	0.694	0.354	—	—	—	—	—
where: R.= Roelands and B.= Barus									

Table 4.9: Output data comparisons

4.8 The Outlet in the Full Solution

4.8.1 The Outlet Pressures

In Section 3.5.2 it was shown that for incompressible fluids with the Barus viscosity law, and when the square root term in the elasticity equations is removed, the outlet

pressures are accurately described by the function:

$$P = B_f \left[\frac{L_1/a - X}{L_1/a - 1} \right] \ln \left(\frac{X - 1}{L_1/a - 1} \right)$$

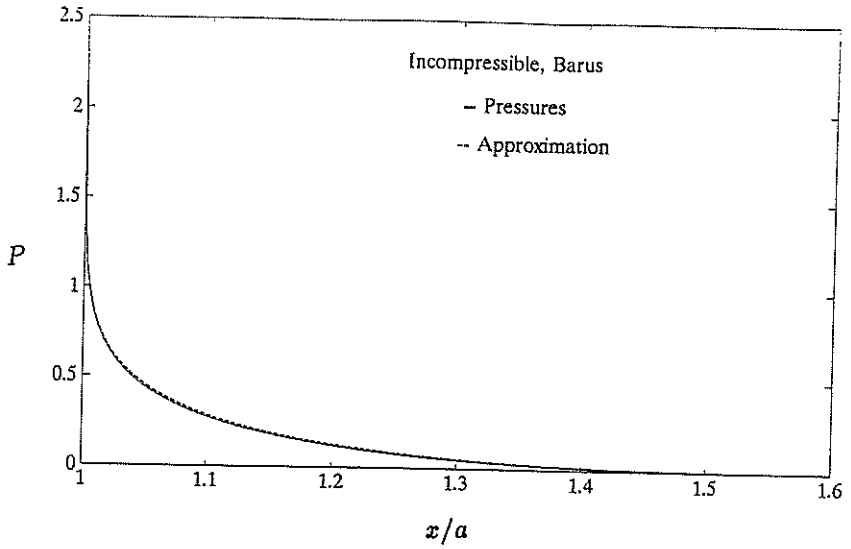

Figure 4.30: Outlet pressures from the complete solution for the B Barus incomp. example

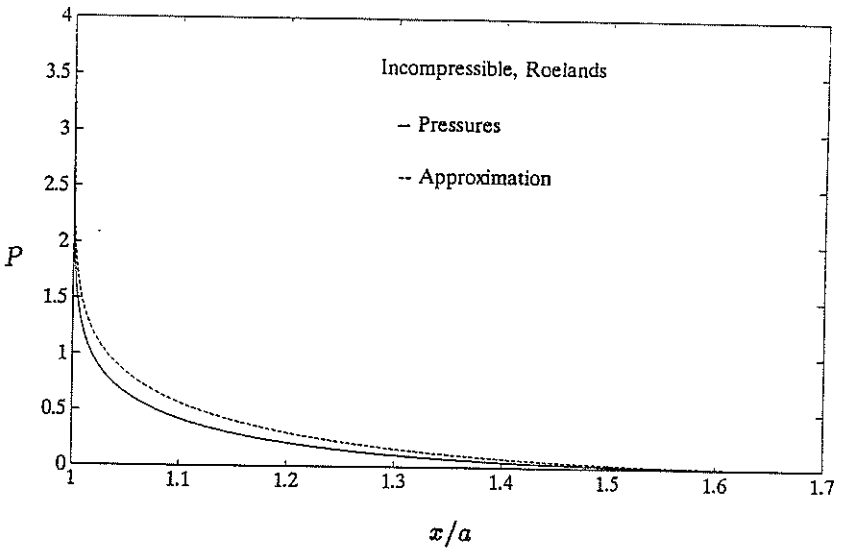

Figure 4.31: Outlet pressures from the complete solution for the B Roelands incomp. example

In a complete solution, since one is interested also in results away from the 'log. spikes' line of Fig. 4.17 then, the singular term cannot be removed and $DM \neq 0$. For $DM = 0$

both the outlet pressures p_R and the final internal stresses σ_f are logarithmic; otherwise, the internal stresses include a $x^{-1/2}$ term and it is important to know if the final pressures are still accurately described by the same function as in Section 3.5.2. Therefore, a similar curve fitting was carried out for several Roelands and Barus law outlet solutions, with and without compressibility. It was found that the above equation is still very accurate for outlet full Barus incompressible solutions, but less accurate for the other cases (obviously for compressible solutions the density should be considered). Fig. 4.30 shows the outlet pressures from the Venner B Barus incompressible example compared with the above equation (with the corresponding constants first obtained by satisfying the equation in two values of X). Fig. 4.31 shows the corresponding comparison for the Venner B Roelands incompressible example.

4.8.2 Relation B_f-K_1

In Section 3.5.3 an analysis was carried out to obtain the relationship between the outlet constant B_f and the constant K_1 for the case when the singular term is cancelled $\Delta M = 0$. However, if the singular term for the displacements is taken into account (i.e. $\Delta M \neq 0$) then the corresponding displacements as $X \rightarrow 1$ can be approximated according to equation 3.29 by:

$$V_s \approx -\Delta M \sqrt{2}\sqrt{X-1}$$

It is now convenient to approximate the non-singular component as $X \rightarrow 1$ by:

$$V_n \approx -D_2\sqrt{X-1}$$

Since at that location the Hertzian displacements are zero, the final shape is approximated only by:

$$V_f = V_s + V_n \approx -\sqrt{X-1}\left[\Delta M\sqrt{2} + D_2\right] \tag{4.91}$$

It was just shown in Section 4.8.1 that for Barus incompressible lubricants the approximation for the outlet pressure distribution (equation 3.55) is still valid, so the procedure described in Section 3.5.3 can be followed. Therefore the following relations can be obtained:

$$K_1 B_f = -\frac{3}{2} \tag{4.92}$$

$$(L_1/a-1)^{-3/2} = \frac{3K_1(\sqrt{2}|\Delta M| + D_2)}{2|K|(H^*)^3} \tag{4.93}$$

Equation 4.92 can be used to provide the initial guess of the outlet pressures in the iterative process. Its agreement (incompressible Barus examples) with numerical solutions is very good, as can be seen in the previous full solutions, Tables 4.1 and 4.4.

4.9 Conclusions

Using the basic ideas from Chapter 3 a complete scheme to solve full EHL line contacts has been described. The inlet and outlet regions are solved for pressures and shape separately (but interacting elastically) by iterating the Reynolds and fracture mechanics equations. When the solution is converged, the central pressures are calculated by first truncating the original Hertzian contact on both its edges and then replacing the removed Hertzian portions of the pressures by the inlet and outlet EHL pressures. The replacement of the pressures is done with the use of linear fracture mechanics theory so that the continuity and smooth pressures join for the inlet-central regions are included.

Originally the scheme is described for Newtonian incompressible fluids using the Barus law for viscosity; but later it is extended to account for Newtonian compressible and Roelands law fluids. Several solutions were obtained and comparisons with reported results were shown from which it is possible to outline the following conclusions:

a).- The agreement of film thickness and pressure distributions by the present theory with reported solutions in the literature is in general good, specially for cases which show nearly singular spikes, where the inlet region is small (e.g. $\mathcal{P} > 7$ and $\mathcal{S} > 2$). This is because for large inlets the removed portion of the inlet pressures to ensure smooth join increases. The location of the spike is then directly affected. However, it is difficult to measure the actual effect of this error since the spike location varies some times within a very wide range among different authors for the same example. This is the case of Bissett and Glander example A where by the present theory the spike is located at 0.414, Bissett and Glander locate it at 0.301, Venner at 0.2 and Okamura at 0.4 (see Bissett and Glander [6]).

b).- The known effects of lubricant compressibility in EHL solutions were observed: the spike moves towards the exit and the central film thickness slightly decreases.

c).- The use of the Roelands viscosity law instead of the Barus one has small effects on

pressure and shape. It was observed that for an incompressible fluid the spike location is slightly moved towards the inlet and the central film thickness is slightly increased.

d).- By solving a set of examples where the square root singular term was completely removed from the elasticity equations (fracture mechanics) it was possible to establish on a $\mathcal{P}$-$\mathcal{S}$ map the boundary for purely logarithmic pressure spikes. By observing the behaviour of the square root term coefficient in many other solutions it was possible to figure out the probable behaviour of the spike within the map. For high values of $\mathcal{P}$ and moderate values of $\mathcal{S}$ the spike is expected to behave as a square root singularity, however, for small values of these variables the spike is expected to behave as nearly logarithmic function and for even lower values the spike tends to disappear (as shown by the Myers solutions).

e).- For incompressible Barus fluids the outlet pressure distribution from a complete solution still behaves as:

$$p = B\left[\frac{L_1 - x}{L_1 - a}\right] \ln\left(\frac{x - a}{L_1 - a}\right)$$

where B and L_1 are the only two constants required. And now $B \approx -3/(2\alpha)$ and L_1 unknown a priori.

For Roelands incompressible solutions the above approximations are not so good.

f).- No problems of convergence have been found in the computational procedure and typically one solution converges within 2 or at most 3 complete cycles inlet-outlet.

CHAPTER FIVE

A MICRO-EHL ANALYSIS FOR LINE CONTACTS

In previous chapters the mechanism which generates the pressure distribution and film thickness in a EHL line contact with perfectly smooth surfaces has been studied. So far the attention has been addressed only to the macrogeometry of the contact. However, in recent years the concept of micro-elastohydrodynamic lubrication (micro-EHL) has been developed after which the elaborate mechanism of lubrication of microscopic asperities has been studied .

Since the rate of decrease of film thickness with increasing load is very slow, then from isothermal EHL theory it appears that there will always be a lubricant film of acceptable thickness between smooth surfaces. Therefore it is widely believed that failure of lubricated contacts is related to the roughness of the contributing bodies.

Sophisticated theoretical analyses allow for the effect of roughness, either by a relatively simple statistical averaging like Christensen and Tønder [16] 1971, Tønder [60] 1984 or by the widely followed 'flow factor' method introduced by Patir and Cheng [62] 1978. An average Reynolds equation is introduced with flow factors incorporating the effect of the fluid flow passing on rough surfaces. Although originally developed for hydrodynamic lubrication, this flow factor method has been used to take into account the effect of roughness in an EHL line contact situation, e.g. Patir and Cheng [62], Tripp and Hamrock [74] 1985, Sadeghi and Sui [70] 1989.

The biggest shortcoming of the flow factor method is to consider the surface roughness as rigid: when applied to EHL situations only the effect of elastic deformation on global geometry is taken into account.

Cheng, however, made one of the earliest calculations of the passage of an asperity through an EHL contact (Lee and Cheng [47] 1973), and found that it certainly did not pass unchanged: deformation takes place, which clearly throws doubt on models of 'partial' EHL contact in which the initial surface roughness is retained.

Recent advances in computational technique have enabled authors to study the behaviour of both transverse and longitudinal ridges or dents, or sinusoidal ripples, e.g. Kweh et al. [48] 1989, Lubrecht at al. [52] 1988, and with the inclusion of non-Newtonian and transient effects: Chang et al. [10] 1989, Chang and Webster [11] 1992. Full numerical solutions involving 'real' roughness in surfaces have been carried out assuming Newtonian behaviour, e.g. Kweh et al. [49] 1992 and Venner [75] 1991.

Despite all these sophisticated theoretical analyses, very little has been completely understood about the behaviour of roughness in EHL contacts and the subject is the object of numerous studies.

However, by considering an 'infinitely long EHL contact' instead of the finite 'Hertzian' region of a real EHL contact while retaining the characteristic mean pressure and viscosity, Greenwood and Johnson [30] 1992 developed a simple model to explain the behaviour of transverse roughness in EHL; their conclusion was based on the hypothesis that sinusoidal induced pressures, corresponding to a not-quite sinusoidal initial roughness, correctly represent a sinusoidal roughness: here this criterion will be confirmed. In this chapter a steady state 'exact' solution for an 'infinitely long EHL contact' will be proposed which enables any (1-D) initial roughness to be studied , and in particular demonstrates that only the low wave number components of real roughness persist, so that in some cases a rough surface becomes essentially plane.

5.1 Transverse Sinusoidal Roughness in Sliding EHL Contacts

In their analysis, Greenwood and Johnson considered the roughness to be sinusoidal ripples, perpendicular to the flow direction in pure sliding with the smooth surface moving with velocity u_1 and the rough surface stationary ($u_2 = 0$), and with small amplitude of roughness compared with its wavelength, so that lubrication was governed by the one-dimensional Reynolds' equation. They also relied on the findings of several authors (Goglia et al. [25] 1984, Kweh et al. [48] 1989, Venner [75] 1991) that both a single ridge and waviness virtually disappear under EHL conditions and are replaced by pressure rip-

ples. With a finite contact, the pressures are obtained numerically, but since in a wavy case the contact area has many ripples, Greenwood and Johnson just used the simple elastic solution for a half-space under sinusoidal pressure in order to find the deformation, as follows :

It is well known (e.g. Johnson [41] 1987) that the elastic deformation of a half-space surface due to a pressure:

$$p = p_o + p_1 \cos(2\pi x/\lambda) \tag{5.1}$$

is:

$$v = \frac{\lambda p_1 (1-\nu^2)}{E\pi} \cos(2\pi x/\lambda) \tag{5.2}$$

Since in a contact problem two surfaces are involved, and since the pressure which removes the roughness on one of them produces (if the two are the same material) a negative roughness of the same amplitude on the other, therefore the combined deformation is required:

$$v = \frac{2\lambda p_1}{\pi E'} \cos(2\pi x/\lambda) \tag{5.3}$$

Thus the amplitude of the pressure ripples needed to squash completely an initial sinusoidal roughness of amplitude z is:

$$p_1 = \frac{\pi E' z}{2\lambda} \tag{5.4}$$

In order to investigate the hydrodynamic mechanism in which those pressures are built, Greenwood and Johnson relied on the hypothesis that both the nominal film thickness h^* and the mean pressure p_o are known. So by substituting equation 5.4 into the 1-D Reynolds equation with the Barus' law for viscosity included and Newtonian fluid, they were able to obtain equations 5.5 and 5.6 :

$$k_1 = \frac{z h^{*^2} E'}{(\eta_{min} u_1 \lambda^2)\sqrt{\alpha p_1 + 1/4}} \tag{5.5}$$

$$a = k_1 h^* \tag{5.6}$$

where a is the amplitude of the deformed roughness . For $\alpha p_1 < 0.5$ the variation of the final shape is almost sinusoidal but, as αp_1 increases the film thickness remains almost constant except for local excursions on either side of the pressure minimum, they referred to this kind of film thickness variations as 'Reynolds' ripples.

When they applied the effect of compressibility in this analysis (using the Dowson and Higginson equation for density variation with pressure) they obtained equations 5.7, 5.8 and 5.9 :

$$p_1 = \frac{z}{\frac{2\lambda}{\pi E'} + \frac{(\gamma-\beta)h^*}{(1+\beta p_o)(1+\gamma p_o)}} \tag{5.7}$$

$$k_2 = \frac{(\gamma-\beta)p_1}{(1+\beta p_o)(1+\gamma p_o)} \tag{5.8}$$

$$a = k_2 h^* \tag{5.9}$$

where the final film thickness variation turned out to be sinusoidal since the compressibility effect is sinuidal always and bigger than the Reynolds ripples.

Clearly the Greenwood and Johnson statement is a simple and useful criterion to help to understand the behaviour of roughness in lubrication. But also clear is its main shortcoming: it can only deal with almost sinusoidal initial shapes and exactly sinusoidal final pressures.

In further sections the basic principles of this analysis will be extended to deal with any 1-D roughness and non-Newtonian fluids.

5.2 Real Roughness Approach

The basic assumptions of Greenwood and Johnson will be again used here, equally: the behaviour of the roughness in the Hertzian region of an EHL contact can be modelled by considering an infinitely large, nominally plane contact; the nominal film thickness is assumed to have been determined by conditions in the inlet, and the mean pressure will be assumed constant at a value related to the Hertz pressure. But now the Reynolds' equation for a compressible non-Newtonian lubricant (Conry et al. [17]) will be used:

$$h - (\rho^*/\rho)h^* = \left[\frac{Dh^3}{12\eta\overline{u}}\right]\frac{dp}{dx} \tag{5.10}$$

where D is a non-Newtonian correction factor, such that when $\tau_o \to \infty$, $D \to 1$ (Newtonian behaviour):

$$D = \frac{3t_v}{t_p}(\coth t_p - 1/t_p)\sqrt{s^2 + \left[\frac{\sinh t_p}{t_p t_v}\right]^2} \tag{5.11}$$

and:

$$s = \frac{u_2 - u_1}{\overline{u}}, \quad t_p = \frac{h}{2\tau_o}\frac{dp}{dx}, \quad t_v = \frac{\eta\overline{u}}{h\tau_o}$$

It will be assumed that the viscosity follows the Barus' law : $\eta = \eta_o e^{\alpha p}$ and the density obeys the Dowson and Higginson equation:

$$\rho = \frac{1 + \gamma p}{1 + \beta p}$$

where : $\gamma = 2.266 \times 10^{-9} m^2/N$ and $\beta = 1.683 \times 10^{-9} m^2/N$.

For known pressures p, the film thickness h can easily be found from equation 5.10. Since the equation is only a cubic in h, an explicit solution is available: but for a step-by-step solution iterating is more convenient. Although the overall EHL geometry of the contact is not considered, the elastic deformation of the roughness will be allowed to occur.

For this infinitely long contact, the pressures can be represented by a Fourier integral, or in practice, by a discrete Fourier transform:

$$p(x) = p_o + \sum_{n=1}^{N-1} B_n \sin(\frac{2\pi x n}{\lambda}) + \sum_{n=1}^{N} A_n \cos(\frac{2\pi x n}{\lambda}) \tag{5.12}$$

the deflection of a half-space by a sinusoidal pressure $p_1 \cos(2\pi x/\lambda)$ is given by equation 5.3 (combined deflection of the two bodies), therefore the deflection due to $p(x)$ is:

$$v(x) = v_o + \frac{2\lambda}{\pi E'}\left\{\sum_{n=1}^{N-1}\frac{B_n}{n}\sin(\frac{2\pi x n}{\lambda}) + \sum_{n=1}^{N}\frac{A_n}{n}\cos(\frac{2\pi x n}{\lambda})\right\} \tag{5.13}$$

and the number of points taken along x is defined as $M = 2N$. Finally the film thickness is:

$$h(x) = h^* + z(x) + v(x) \tag{5.14}$$

where $z(x)$ is the initial, undeformed roughness and h^* is the constant nominal film thickness, Fig. 5.1 .

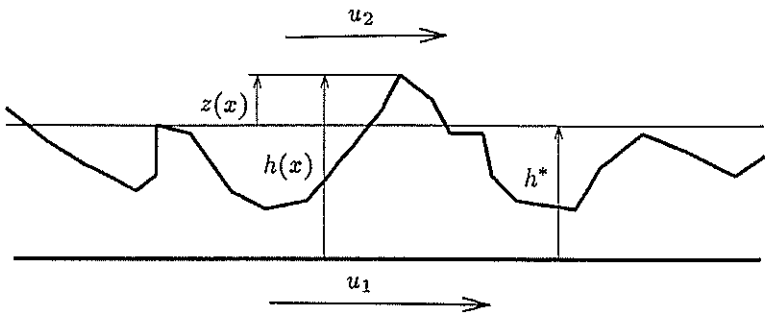

Figure 5.1: Infinitely long lubricated contact

The work of Rice [67] 1944 suggests a convenient simulation of a typical engineering surface :

$$z(x) = \sum_{n=1}^{n_{max}} z_n \cos(2n\pi x/\lambda + \varepsilon_n) \tag{5.15}$$

where ε_n are random phases ($0 \leq \varepsilon_n < 2\pi$). For this surface the autocorrelation function is:

$$E\{z(x)z(x+\zeta)\} = \frac{1}{2}\sum_{n=1}^{n_{max}} z_n^2 \cos(2\pi n\zeta/\lambda) \tag{5.16}$$

The RMS roughness σ is then given by:

$$\sigma^2 = \frac{1}{2}\sum_{n=1}^{n_{max}} z_n^2 \tag{5.17}$$

5.3 Solution

The solution of equations 5.10, 5.12, and 5.14 can be carried out by several approaches which are chosen according to the degree of numerical instability found in the particular case. High frequencies and high amplitudes of the initial roughness are specially harmful for the convergence process. However, in this section only the two most used approaches will be described.

5.3.1 The Direct Approach

To solve step-by step the involved equations, one takes the Fourier expansion of the initial roughness $z(x)$ and tries $h(x) = h^*$ as an initial guess, i.e. $v(x) = -z(x)$.

Equations 5.12 and 5.13 give the corresponding pressures; equation 5.10 determines $h(x)$ and finally equation 5.14 gives a new $v(x)$ (diagram of Fig. 5.2). It proves that this scheme is unstable for higher wave numbers: but application of Aitken's method of extrapolation to successive set of iterates (i.e. Hamming [35]) improves the convergence.

5.3.2 The Density Equation Approach

In cases of higher amplitudes of initial roughness and short wave lengths, despite the use of Aitken's extrapolation, instabilities may persist; for those cases the above sequence can be modified.

Defining :

$$f = h^3\left(\frac{D}{12\bar{u}\eta}\frac{dp}{dx}\right) \tag{5.18}$$

equation 5.10 becomes:

$$h - [\rho(p_o)/\rho]\, h_G = f \tag{5.19}$$

where:

$$h_G = \frac{h(p_{max})\rho(p_{max})}{\rho(p_o)} \tag{5.20}$$

now from equation 5.14

$$v(x) = \frac{\rho(p_o)}{\rho} h_G - h^* - z(x) + f \tag{5.21}$$

finally from the density-pressure equation:

$$\frac{\rho(p_o)}{\rho} = \left[\frac{1+\gamma\ p_o}{1+\beta\ p_o}\right]\frac{1+\beta\ p}{1+\gamma\ p} \tag{5.22}$$

consequentially it is easy to find that:

$$\frac{\rho(p_o)}{\rho} = 1 - (p - p_o)C + \frac{\gamma\, C(p - p_o)^2}{1 + \gamma\, p} \tag{5.23}$$

where:

$$C = \frac{\gamma - \beta}{(1 + \beta p_o)(1 + \gamma p_o)} \tag{5.24}$$

substituting equation 5.23 into equation 5.21 one obtains:

$$v(x) + h_G(p - p_o)C = (h_G - h^*) + h_G\gamma\, C\frac{(p - p_o)^2}{1 + \gamma\, p} + f - z(x) \tag{5.25}$$

Since v_o is arbitrary one may ignore the constant terms. Thus from equations 5.12 and 5.13 and applying FFT to the right hand side of equation 5.25:

$$\frac{2\lambda}{\pi E'}\sum_{n=1}^{N}\frac{p_n}{n}\exp(\frac{2\pi nxi}{\lambda}) + h_G C\sum_{n=1}^{N} p_n \exp(\frac{2\pi nxi}{\lambda}) = \sum_{n=1}^{N} q_n \exp(\frac{2\pi nxi}{\lambda}) \tag{5.26}$$

where q_n are the Fourier coefficients of the function in the right hand side of equation 5.25. And the Fourier coefficients for the pressures are giving by:

$$p_n = q_n(\frac{2\lambda}{\pi n E'} + C h_G)^{-1} \tag{5.27}$$

Equation 5.25 may be solved iteratively by using estimates of the pressure to find the right hand side and hence values of q_n: equation 5.27 then gives improved values of the pressure (diagram of Fig. 5.3).

For incompressible fluids : $\gamma = \beta$ and therefore $C = 0$.

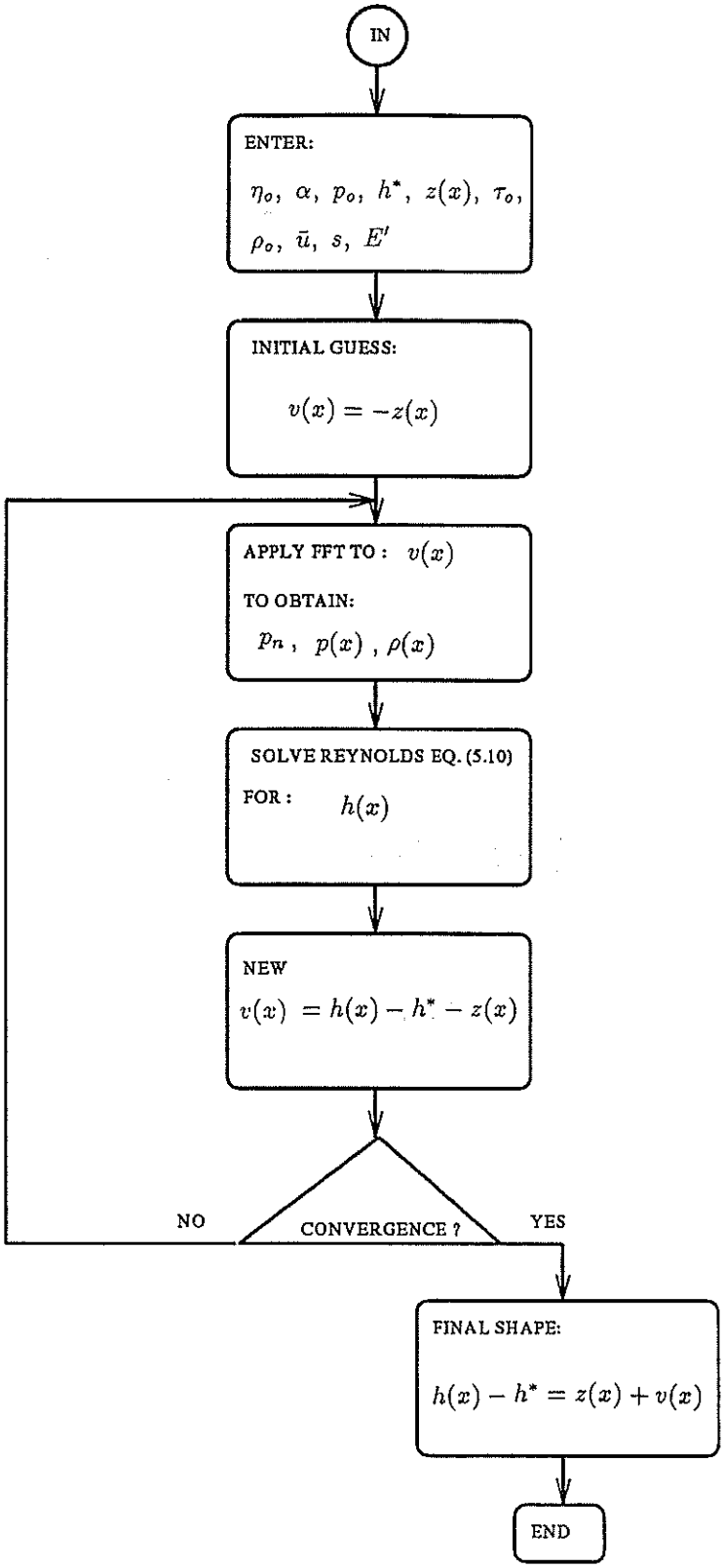

Figure 5.2: Direct approach

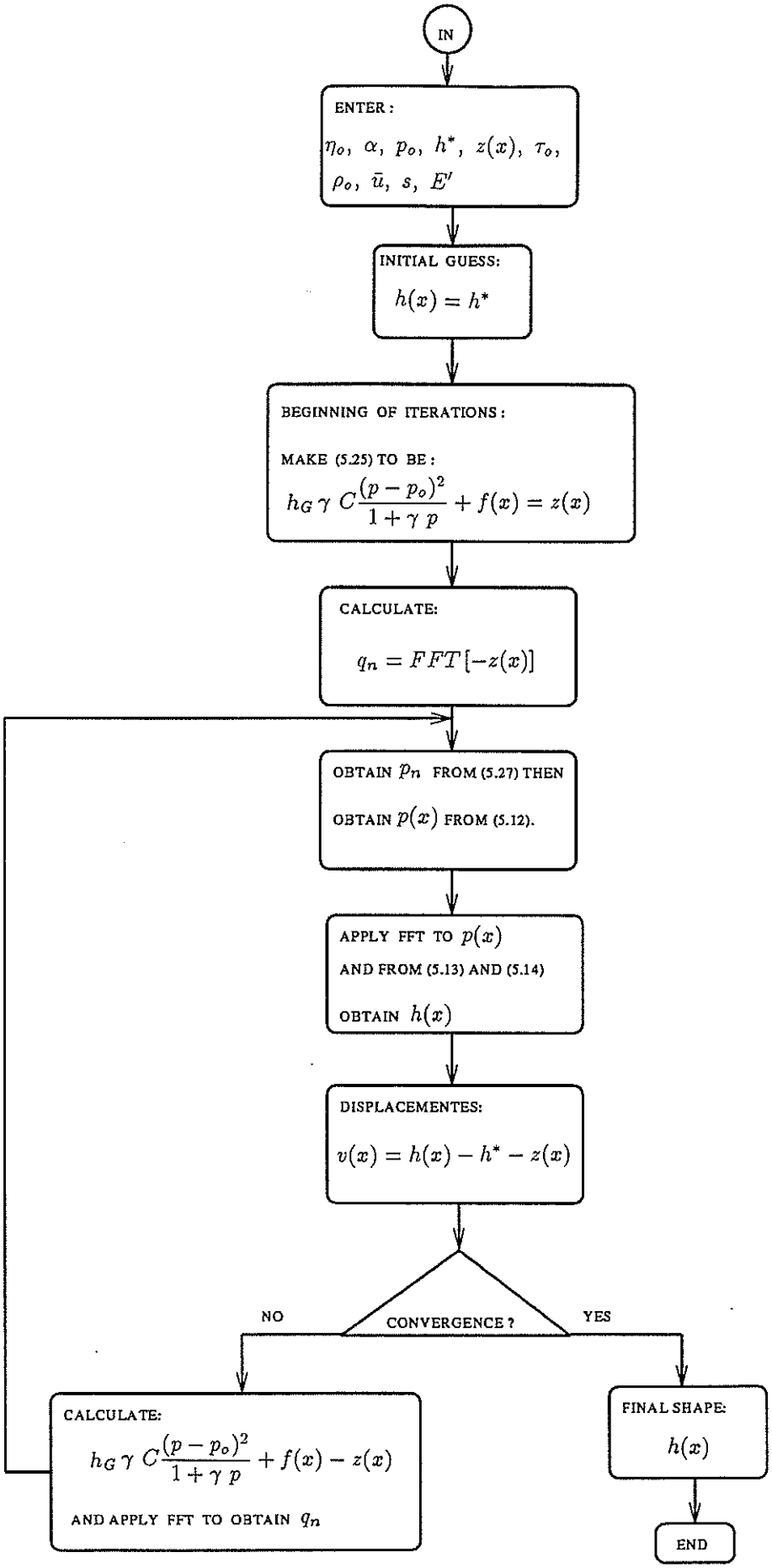

Figure 5.3: Density equation approach

5.4 Convergence

It was pointed out, in previous sections, that high values of amplitude and wave number in the original roughness $z(x)$ may lead to numerical instabilities in the convergence process. The reason for the difficulties appear to be that when calculating pressures from displacements, the pressure coefficients are multiplied by the wave number: $p_n = \frac{\pi E' v_n}{2\lambda} n$ thus increasing the numerical error for high values of n. The situation gets worse if the initial amplitudes of shape are large, since this will make p_n larger and therefore the minimum value of $p(x)$ would be closer to zero, where the analysis fails.

An inverse scheme which obtains displacements from pressures necessitates the calculation of both pressures and pressure gradients from the Reynolds-Eyring equation (5.10). This involves the problem of finding the pressure at the beginning of the analysed interval, which turns out to be a very unstable process as well.

It has also been observed that instability problems appear mainly in non-Newtonian cases. The Newtonian equivalents are in general very stable. So, rewriting the Reynolds-Eyring equation by substituting equation 5.11 into equation 5.10:

$$1 - \frac{h^*}{h}(\rho^*/\rho) = \frac{1}{2}\sqrt{s^2 + (\frac{\sinh(t_p)}{t_p t_v})^2}\ \ (\coth(t_p) - 1/t_p) \tag{5.28}$$

defining:

$$R = \sqrt{(\frac{s}{2})^2 + (\frac{\sinh t_p}{2t_p t_v})^2}$$

therefore:

$$h = \frac{h^*(\rho^*/\rho)}{R(\frac{1}{t_p} - \coth t_p) + 1} \tag{5.29}$$

writing:

$$\frac{1}{t_p} = \frac{h^*}{h t_p^*}$$

where:

$$t_p^* = \frac{h^*}{2\tau_o}\frac{dp}{dx}$$

and substituting into 5.29 :

$$h = \frac{h^*}{1 - R\coth t_p}\left[\frac{\rho^*}{\rho} - \frac{R}{t_p^*}\right] \tag{5.30}$$

Expression 5.30 shows that $h \to \infty$ as $R\coth t_p \to 1$; and this may happen for large values of t_p, t_v and pure sliding conditions ($s = \pm 2$) since for such cases $R \to 1$, and also $\coth t_p \to 1$. When the viscosity is high t_v is normally high ($t_v >> 40$), and when $\frac{dp}{dx}$ is large, also t_p is large; it is typical of short wave length and high amplitude in the initial roughness, precisely the more numerically unstable cases.

Continuing the analysis but now for a Newtonian fluid, the corresponding Reynolds equation is known to be:

$$h - (\rho^*/\rho)h^* = \frac{h^3}{12\eta\bar{u}}\frac{dp}{dx} \tag{5.31}$$

which does not show the nearly zero denominator for large values of $\frac{dp}{dx}$ and numerical problems due to it are unlike to occur.

5.4.1 Analysis of Numerical Error in the Process

It is convenient to perform an error analysis of the iterative sequence in order to develop a convergence criterion. Appendix B shows the deduction of the error equations for a single iteration, equations 5.32 and 5.33; where r is the amplification factor of the numerical error per iteration in the direct approach.

a).- Incompressible fluid:

$$r = (\frac{\pi h^*}{\lambda})^2 \frac{E'}{2\tau_o t_p^* \,(1 - R\coth t_p)}\left[1 - \frac{R}{t_p^*}\right](n^2) \tag{5.32}$$

b).- Compressible fluid:

$$r = \frac{h^*}{1 - R\coth t_p}\left[\frac{\pi C E'}{2\lambda}(n)\right] \tag{5.33}$$

In both cases $\mid r \mid < 1$ to ensure convergence in the process. Since $r = f(\frac{dp}{dx}, h)$ it will vary with x, however, in most of the cases with pure sliding $R \approx 1$ and for critical situations ($r = r_{max}$): $t_p = t_{p\ max}$ and $\coth t_p \approx \coth t_{p\ max}$.

In equations 5.32 and 5.33 r becomes uncontrollable as $R\coth t_p \to 1$ but for incompressible fluids it happens faster since the error is proportional to the square of the wave

number (n^2), whilst for compressible ones the error is proportional only to the first power of the wave number (n). So incompressible cases are expected to be more numerically unstable and they certainly are.

5.5 Non-Dimensionalisation of Equations

A convenient non-dimensionalisation of the equations involved in this analysis would have to be independent of the Hertzian contact length and of the rollers radii, since it is concerned only with an infinitely long contact.

So writing:

$H = h/h^*,\ P = \alpha p,\ X = x/L,\ \bar{\rho} = \rho/\rho_o,\ V = v/h^*,\ Z = z/h^*$

$$K = \frac{(h^*)^2 e^{-\alpha p_o}}{12\bar{u}\eta_o \alpha L}$$

$$C_3 = \alpha h^* E'/L$$

$$C_1 = \frac{h^*}{2\tau_o \alpha L}$$

L is the length studied in the Fourier analysis (i.e. the wave length of the fundamental component).

Clearly for a Newtonian fluid the two EHL independent variables are : K and C_3, while for a non-Newtonian fluid the three independent variables are C_1, K and C_3.

Then, the Reynolds-Eyring equation 5.10 becomes:

$$K\bar{\rho}H^3 D(e^{-P_1})\frac{dP}{dX} = \bar{\rho}H - \bar{\rho}^* H^* \tag{5.34}$$

where $P_1 = \alpha(p - p_o)$, D is still given by equation 5.11 but :

$$t_v = \frac{C_1\ e^{P_1}}{6KH} \tag{5.35}$$

$$t_p = C_1 H \frac{dP}{dX} \tag{5.36}$$

The discrete Fourier representations of $p(x)$ and $v(x)$ are:

$$P(X) = P_o + \sum_{n=1}^{N} P_n \exp(2\pi n i X) \tag{5.37}$$

$$V(X) = V_o + \sum_{n=1}^{N} V_n \exp(2\pi n i X) \tag{5.38}$$

where:

$$V_n = \frac{2}{\pi n C_3} P_n$$

The error equation for an incompressible fluid is:

$$r = \frac{\pi^2 C_1 \, C_3}{t_p^* \, (1 - R \coth t_p)} \left[1 - \frac{R}{t_p^*}\right] (n)^2 \tag{5.39}$$

and for a compressible fluid:

$$r = \frac{1}{1 - R \coth t_p} \left[\frac{C_3 \pi C_o}{2} (n)\right] \tag{5.40}$$

where:

$$C_o = C/\alpha$$

5.6 Results

In this chapter two sets of data are used to obtain the examples presented, the data are given in Table 5.1 and Table 5.2 . Data set 1 corresponds to a sinusoidal surface of amplitude z_{max} and it is used to make comparisons among Newtonian, non-Newtonian, compressible and incompressible cases. Data set 2 corresponds to a real roughness surface with maximum amplitude (z_{max}) and it is used to obtain solutions for compressible Newtonian and compressible Eyring fluids.

Set no.	τ_o	p_o	E'	$\bar{u}$	h^*	z_{max}	L	α	η_o
	Mpa	GPa	GPa	m/s	μ m	μ m	mm	GPa^{-1}	Pa s
1	10	1.0	227	25	0.7125	0.7125	2.4	14.8	0.0179
2	10	1.0	227	25	0.304	0.062	5.7	9.6	0.0024

Table 5.1: Sets of dimensional data

Set no.	P_o	C_1	K	C_3	Z_{max}
1	14.8	0.001	9.9441×10^{-10}	0.997381	1.0
2	9.6	2.77×10^{-4}	1.584×10^{-7}	0.11635	0.203

Table 5.2: Sets of dimensionless data

a).- Sinusoidal Roughness:

With data set 1 from Tables 5.1 and 5.2, four solutions have been obtained to enable comparisons between Newtonian and non-Newtonian (Eyring) cases, as well as between compressible and incompressible ones for an initial sinusoidal roughness in pure sliding. For these examples it was taken $L = 2\lambda$, divided in 64 points.

The amplitude of the initial roughness is more or less of the same size as the gap (central film thickness) which is supposed to pass through, but the elastic deformation which occurs makes this possible. For the present example roughness is very much flattened in all the cases but the Newtonian incompressible one is specially remarkable, Fig. 5.7.

By comparing Fig. 5.4 with Fig. 5.6 and Fig. 5.5 with Fig. 5.7, one can see that the roughness amplitude reduction is less with non-Newtonian lubricant than the corresponding Newtonian case, while in contrast the amplitude of the final pressure ripples are very similar indeed at least for the present example (this will be more extensively investigated in Chapter 6).

With a Newtonian compressible fluid, Fig. 5.6, the shape is in phase with its initial shape and exactly 180° out of phase with the pressure (and therefore with the displacements). The compressible non-Newtonian case Fig. 5.4, shows a final shape shifted in phase respect to its initial one.

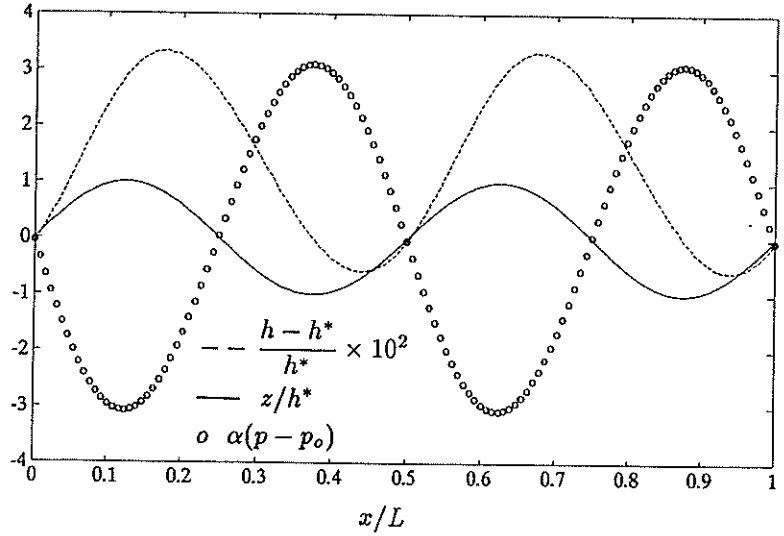

Figure 5.4: Data set 1, non-Newtonian compressible

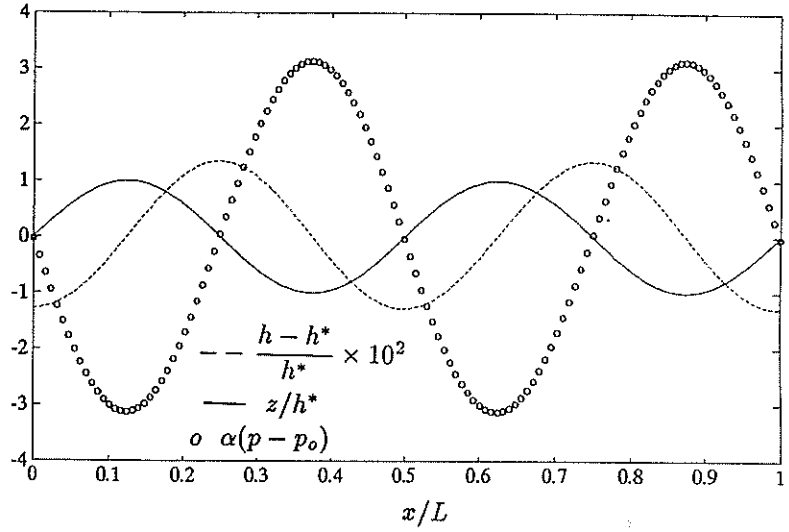

Figure 5.5: Data set 1, non-Newtonian incompressible

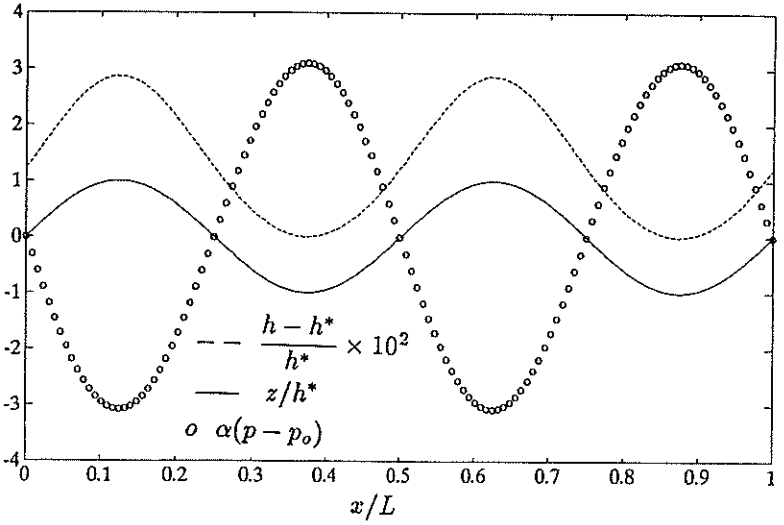

Figure 5.6: Data set 1, Newtonian compressible

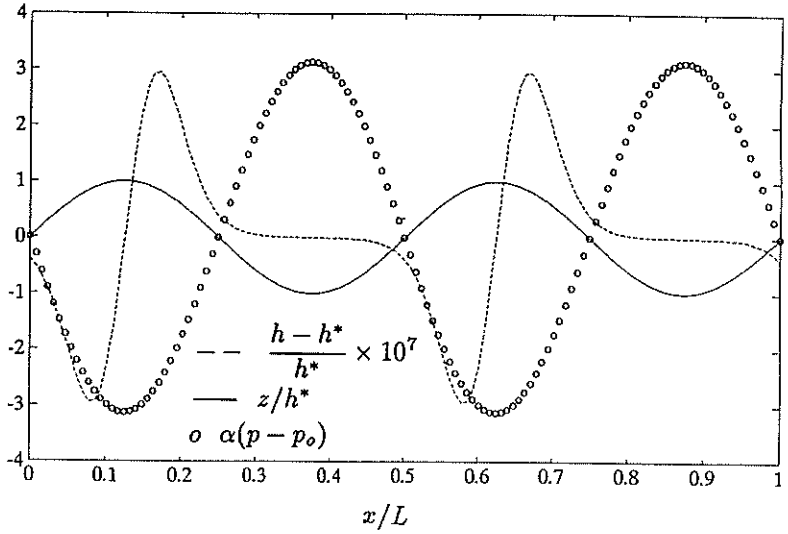

Figure 5.7: Data set 1, Newtonian incompressible

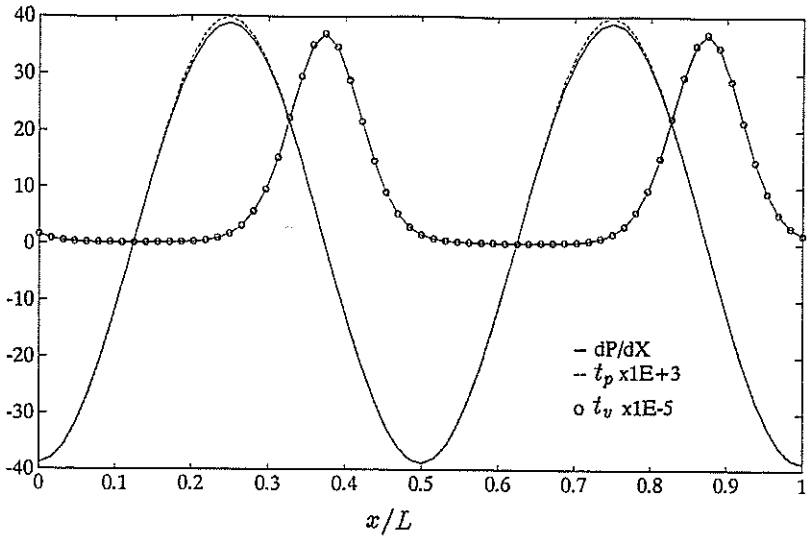

Figure 5.8: Data set 1, non-Newtonian compressible, $\frac{dP}{dX}$, t_p and t_v

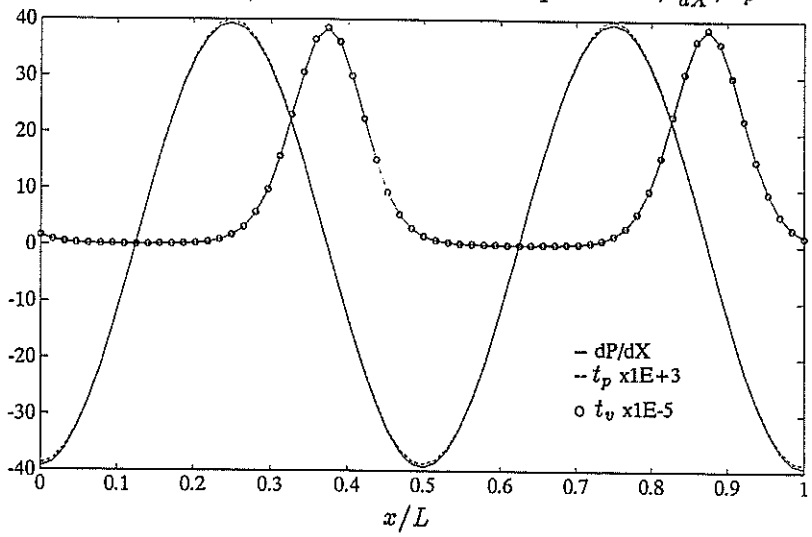

Figure 5.9: Data set 1, non-Newtonian incompressible, $\frac{dP}{dX}$, t_p and t_v

The Newtonian cases can be compared with the results predicted by Greenwood and Johnson's equations 5.4 to 5.9. According to them, for the incompressible lubricant the final amplitude of shape is $a/h^* = 2.97 \times 10^{-7}$ and the amplitude of the pressure ripples $P_1 = 3.1333$ while from the results of Fig. 5.7 is: $a/h^* \approx 3 \times 10^{-7}$ and $P_1 \approx 3.0$. For the compressible lubricant, according to Greenwood and Johnson $a/h^* = 1.436 \times 10^{-2}$ and $P_1 = 3.089$, while from Fig. 5.6 $a/h^* \approx 1.5 \times 10^{-2}$ and $P_1 = 3.0$. Both cases show a good agreement with Greenwood and Johnson's approximate result.

For the non-Newtonian examples the pressure gradients, t_p and t_v are important parameters in the convergence process, and they are plotted in, Fig. 5.8 and Fig. 5.9. It is possible to see that the difference between compressible and incompressible results is almost non-existent, the reason is that for this particular set of data the pressures turned

out to be very similar indeed. From these plots and equations 5.39 and 5.40 the error factors r are calculated: compressible $r = 4.34 \times 10^{-12}$ and incompressible $r = 0.246$. In both cases r is less than 1 for $n = 1$ with $t_p^* = 0.04$ and R=1. Note that in the incompressible case, for $n > 4$ the factor $r > 1$ but since the example is a sinusoidal case, the amplitudes of the high frequency pressure components are very small and therefore the numerical error does not show up.

b).- Real Roughness:

Data set 2 is used for this example, the initial roughness shown in Figs. 5.10 and 5.18 has been obtained by applying equation 5.15 with $n_{max} = 100$ and 1024 points along the abscissa x. Both the Newtonian and non-Newtonian solutions have been obtained for a compressible lubricant.

For the Eyring fluid, Fig. 5.10, shows a comparison between the undeformed and deformed roughness. The change is large, resulting in an almost flat deformed surface, as is also true for the Newtonian case Fig. 5.18. However, an amplification of the final shapes, Figs. 5.11 and 5.19 shows that the high frequency amplitudes still remain. This is made even clearer in Fig. 5.17 where the values of the squared Fourier coefficients for the shapes have been plotted versus the wave number. Again the low frequency amplitudes are very much deformed, but the higher frequencies are relatively little changed. Another feature shown in Fig. 5.17 is that the coefficients line for the deformed shape is slightly curved at high n for all non-Newtonian cases. In contrast Newtonian examples always show a completely horizontal pattern. Note that the coefficients lines suggest that a roughness component with a wave number exceeding 100 (n_{max} value used to create the artificial initial roughness) would be magnified: certainly when such components are included, the iteration accumulates numerical error and fails.

Fig. 5.12 shows the pressure variations for the Eyring example. A comparison with the Newtonian pressures Fig. 5.20 suggest that in both cases the pressures are similar but certainly they are not the same, as is clear from the different pressure gradients shown in Figs. 5.14 and 5.21.

For the non-Newtonian fluid the parameters t_p and t_v are shown in Figs. 5.15 and 5.16. For this real roughness case the wave length of the fundamental component has been taken to be $L = 5.7$mm , a large value for practical cases. A more realistic number would be perhaps $\frac{1}{5}L$, and Fig. 5.13 shows the undeformed and deformed roughness for

this length.

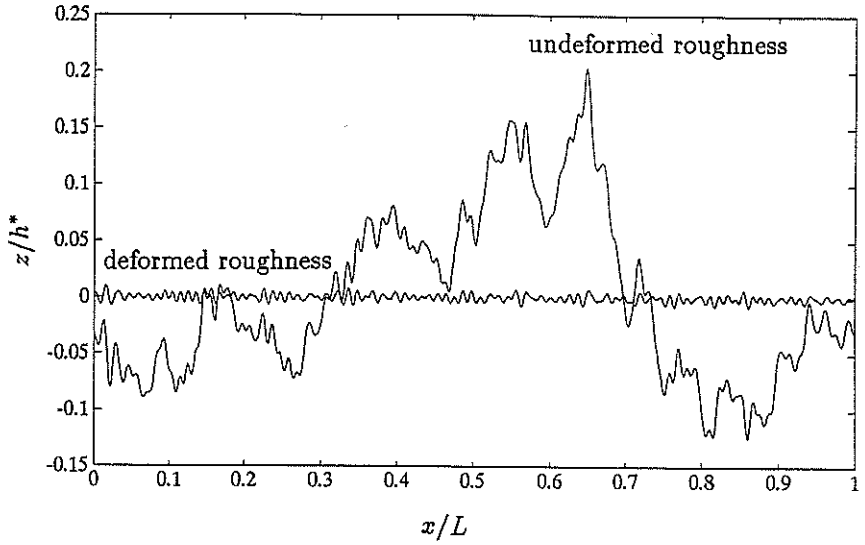

Figure 5.10: Data set 2, non-Newtonian compressible, deformed and undeformed roughness

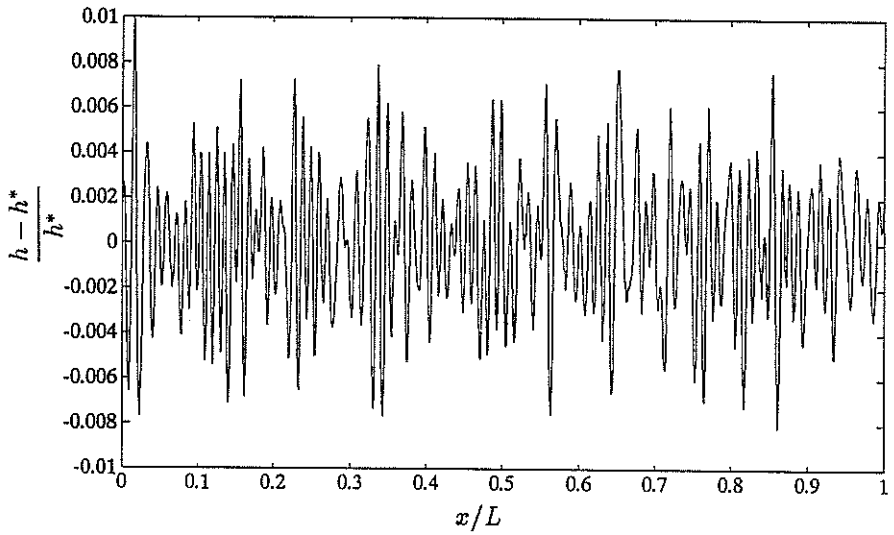

Figure 5.11: Data set 2, non-Newtonian compressible, deformed roughness

The error factor for the non-Newtonian (compressible) case is: $r = 1.711 \times 10^{-3}(n)$ with $t_p^* = 0.0139$ and $R = 1$ so, even if $n = 500$, r is still very small. The convergence is ensured in this example.

Basically the general remark already made for the sinusoidal roughness example is still valid in real roughness: the roughness amplitude reduction is less with the non-Newtonian lubricant. The conditions which determine how much an initial transverse roughness is deformed are studied in Chapter 6.

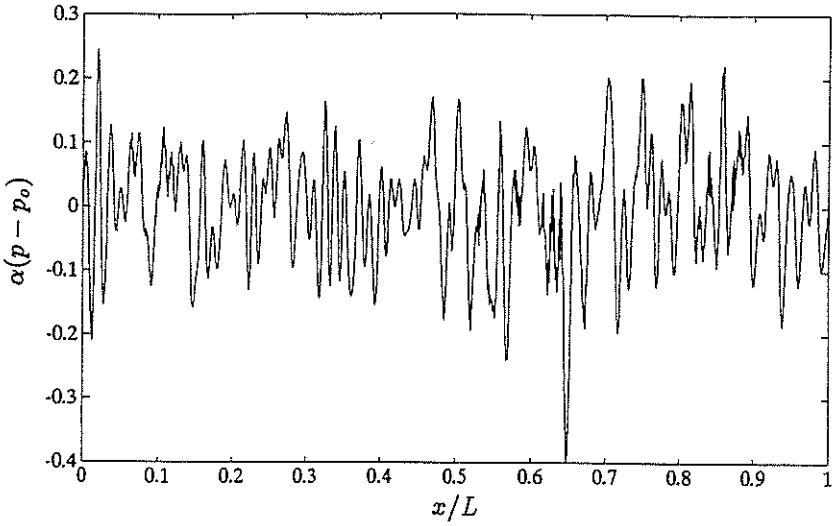

Figure 5.12: Data set 2, non-Newtonian compressible, final pressure variations

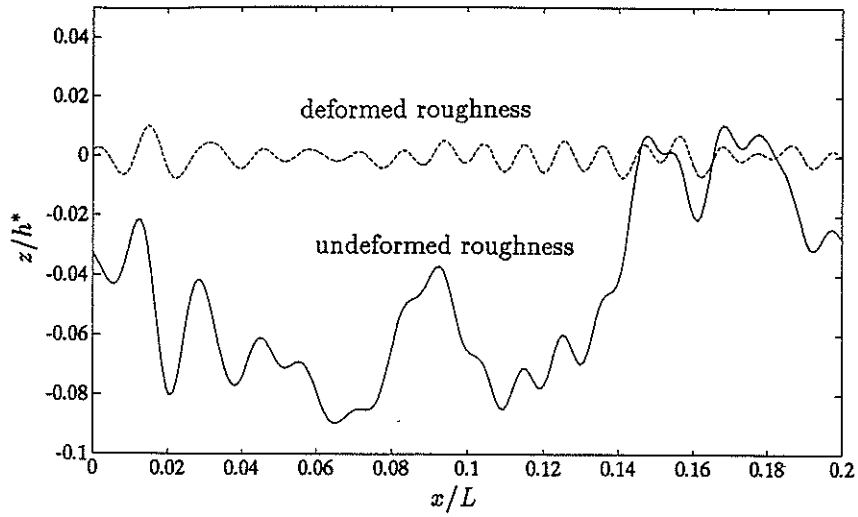

Figure 5.13: Data set 2, non-Newtonian compressible, deformed and undeformed roughness, amplified view

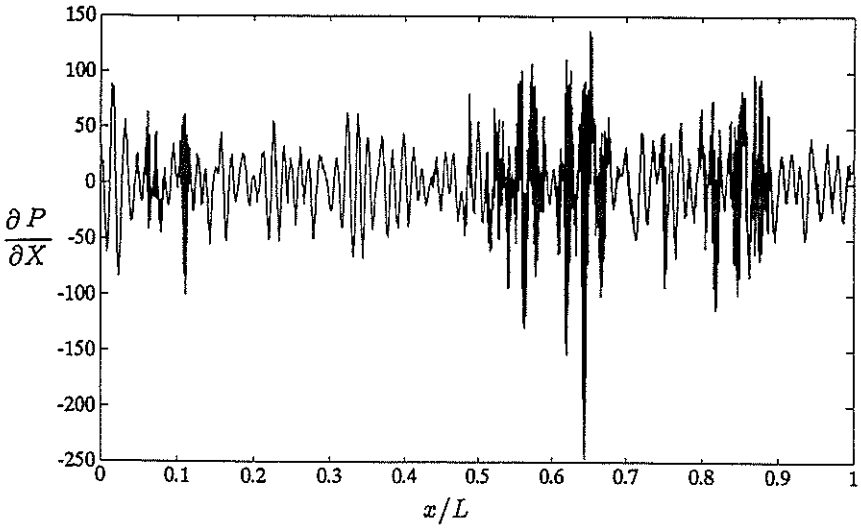

Figure 5.14: Data set 2, non-Newtonian compressible, pressure gradients

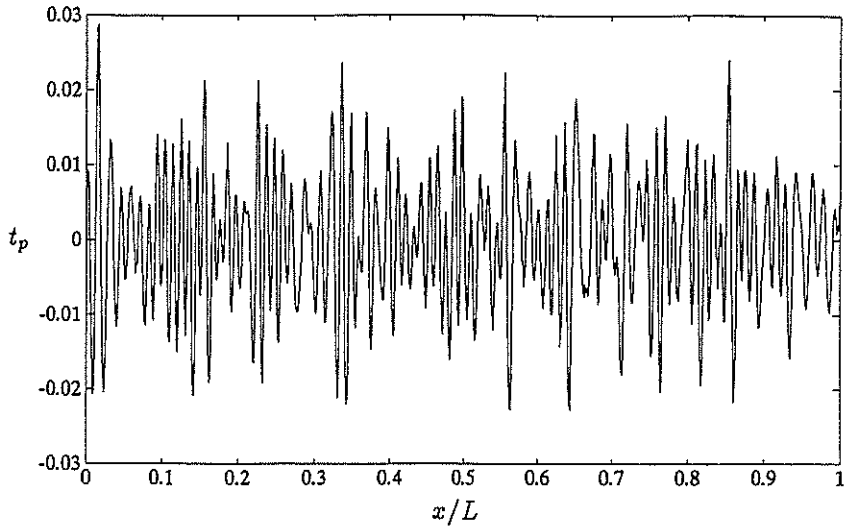

Figure 5.15: Data set 2, non-Newtonian compressible, t_p

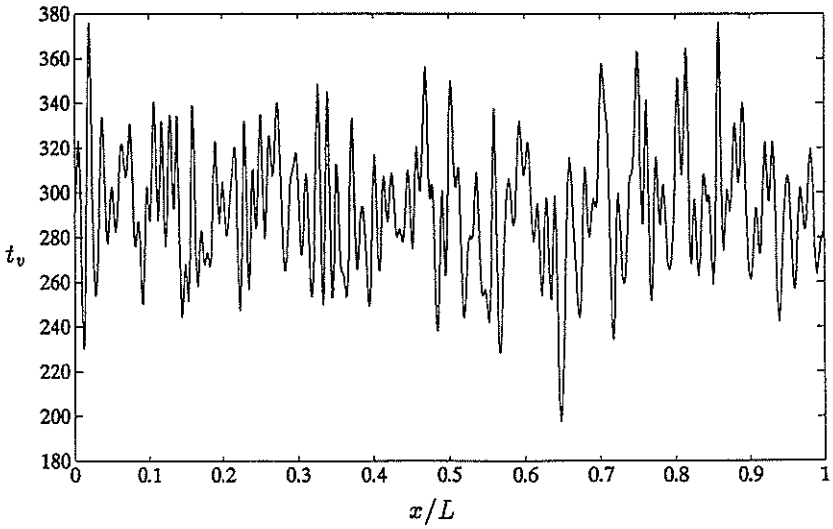

Figure 5.16: Data set 2, non-Newtonian compressible,t_v

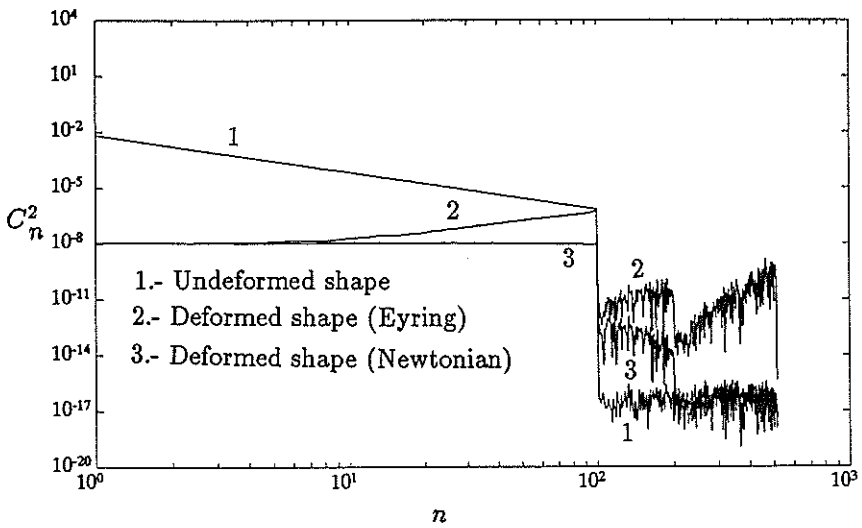

Figure 5.17: Square Fourier coefficients, compressible

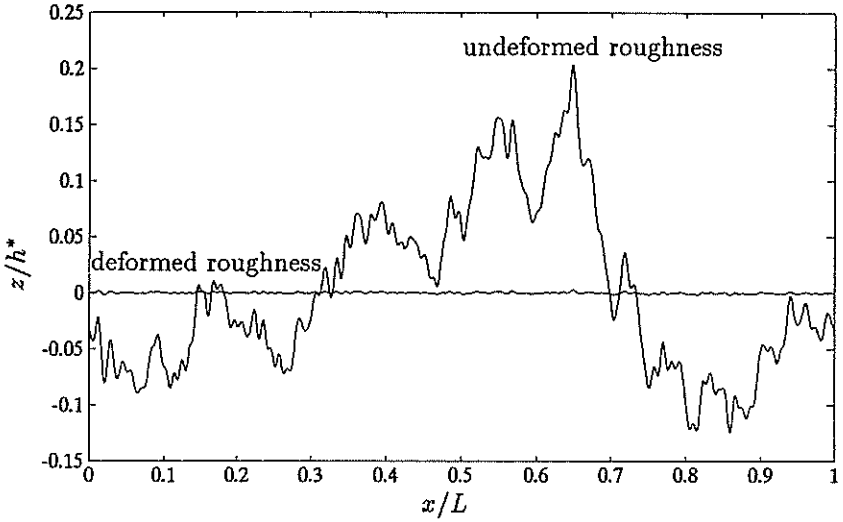

Figure 5.18: Data set 2, Newtonian compressible, undeformed and deformed roughness

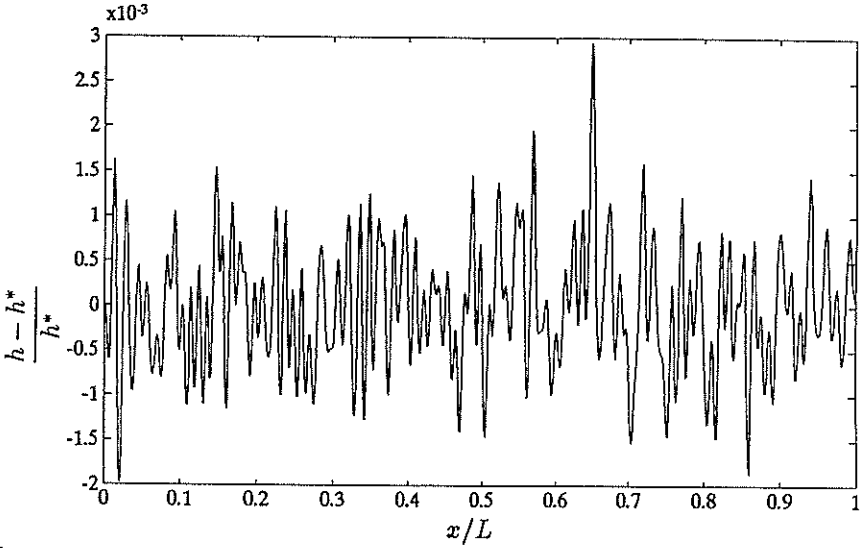

Figure 5.19: Data set 2, Newtonian compressible, deformed roughness

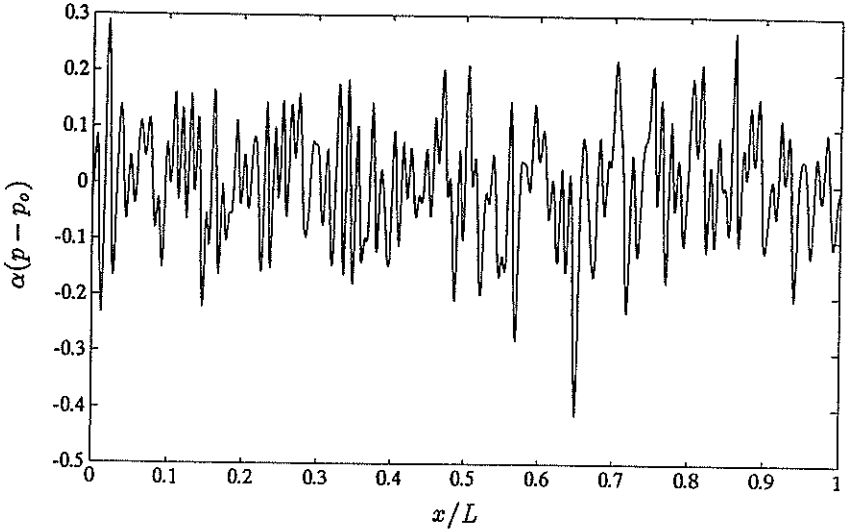

Figure 5.20: Data set 2, Newtonian compressible, final pressure variations

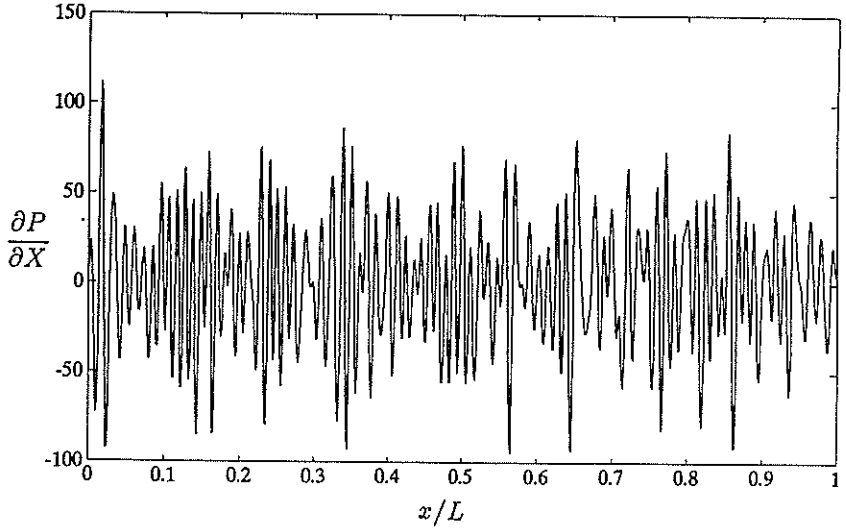

Figure 5.21: Data set 2, Newtonian compressible, final pressure gradients

5.7 Conclusions

A simple scheme to investigate the effects of 1-D real roughness and waviness in steady state EHL sliding contacts has been developed. Solutions have been obtained for wavy and real roughness surfaces and comparisons between Newtonian and non-Newtonian cases have been made as well as between compressible and incompressible ones from which the following conclusions can be obtained:

a).- The roughness amplitude reduction is less with a non-Newtonian lubricant.

b).- Newtonian cases show a final shape in phase with the original roughness and with a phase shift of 180° with respect to the pressures. In contrast, the final shape in non-Newtonian cases is out of phase with the initial roughness and with a shift of phase less than Newtonian results with respect to the pressures.

c).- For surfaces with real roughness the low frequency components are almost completely flattened after deformation which suggests that the basic assumption of 'partial' EHL models of retaining the original surface roughness could be suspect.

d).- The basic hypothesis of Greenwood and Johnson that sinusoidal induced pressures, corresponding to a not-quite sinusoidal initial roughness, correctly represent a sinusoidal roughness, has been confirmed, since the results from the present analysis agree very well with Greenwood and Johnson model.

CHAPTER SIX

ANALYSIS OF SHORT WAVE-LENGTH TRANSVERSE SINUSOIDAL ROUGHNESS IN MICRO-EHL

The numerical difficulties arising from the solution of short wave length roughness in EHL problems have been explained in Chapter 5. It was said that the methods of solution described may have convergence problems especially when the roughness wave length λ is short and the pressure gradients are high. However, it is important to be able to solve even short wave length problems in order to understand clearly the behaviour of the roughness in EHL.

In this chapter one analytical solution and one new numerical scheme have been developed to deal with the difficulties. Firstly by assuming the roughness and pressure ripples to be sinusoidal and small, an analytical approach is developed to solve the linearised Reynolds-Eyring equation under heavily loaded conditions. This solution is also used as a first guess for one of the iterative schemes of Chapter 5 in order to solve unstable examples.

Secondly a numerical scheme, the Two Point Boundary Value Problem (TPBVP) approach, is first used to solve a linearised Reynolds-Eyring equation and the method then extended to solve the full equation. The method is rather suitable for short λ and low amplitudes with only non-Newtonian fluids. However, it becomes unstable when the pressure variations are large.

With the help of these two schemes a criterion to describe the behaviour of the roughness deformation as a function of the ratio $\lambda/\bar{h}$ is given. It is shown that for small ratios ($\lambda/\bar{h} < 100$) under elastic deformation and with the Eyring stress being $\tau_o \approx 5 \times 10^6$ Pa

the original roughness is preserved.

Before describing the schemes and the relevant results, it is convenient to introduce two numerical examples of short wave-length transverse sinusoidal roughness which will be referred throughout the chapter.

6.1 Short Wave-Length Examples

The first example has been obtained from L. Chang (private communication), 1992 and which will be referred in the future as Chang's example number 1:

$E' = 2.20 \times 10^{11}$ Pa	$b = 167 \times 10^{-6}$ m
$\nu = 0.3$	$\bar{u} = 4$ m/s
$\alpha = 1.59 \times 10^{-8}\ Pa^{-1}$	$h^* = 0.65 \times 10^{-6}$ m
$\tau_o = 5 \times 10^6$ Pa	$p_o = 0.77 \times 10^9$ Pa
$\eta_o = 0.04$ Pa s	$\lambda = 50.00 \times 10^{-6}$ m
$R = 0.0119$ m	$z_1 = 0.104 \times 10^{-6}$ m

The compressible solutions are shown in Fig. 6.1 and Fig. 6.2:

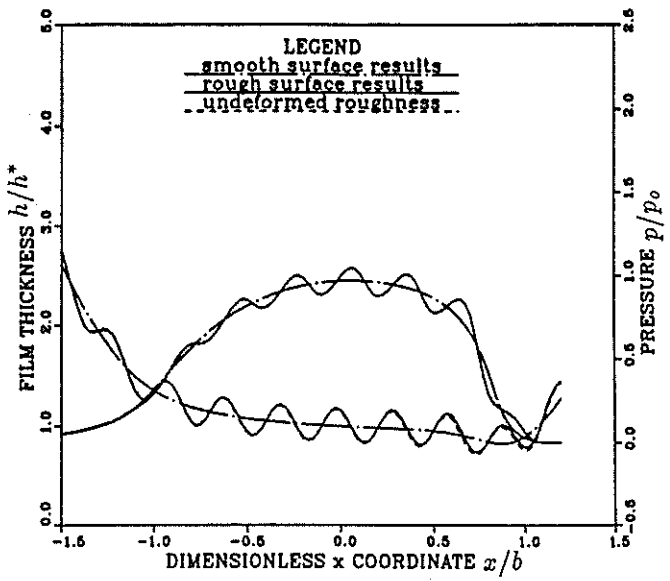

Figure 6.1: Chang's example 1, Non-Newtonian Lubricant

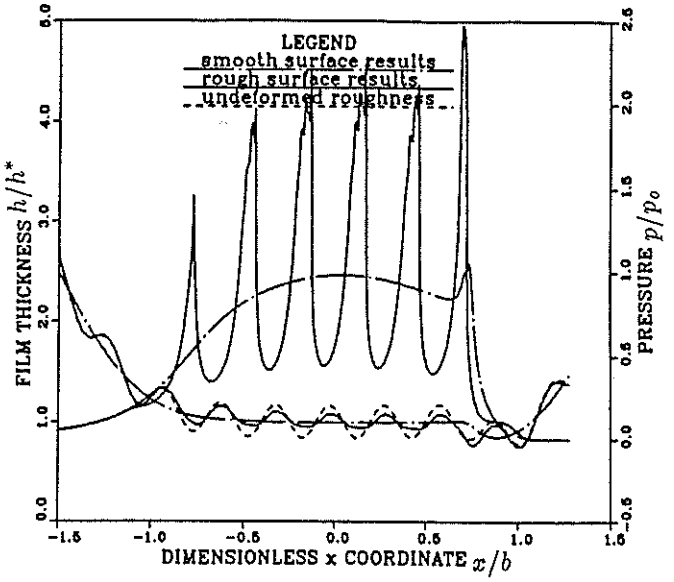

Figure 6.2: Chang's example 1, Newtonian lubricant

The second example has been obtained from L. Chang et al. [11] 1992 and in future will be referred as Chang's example number 2:

$$h^* = 0.60 \times 10^{-6} \text{ m} \qquad p_o = 1.1 \times 10^9 \text{ Pa}$$
$$\lambda = 71.70 \times 10^{-6} \text{ m} \qquad z_1 = 0.15 \times 10^{-6} \text{ m}$$

with all the other data as in example 1.

The compressible solutions are shown in Fig. 6.3 and Fig. 6.4:

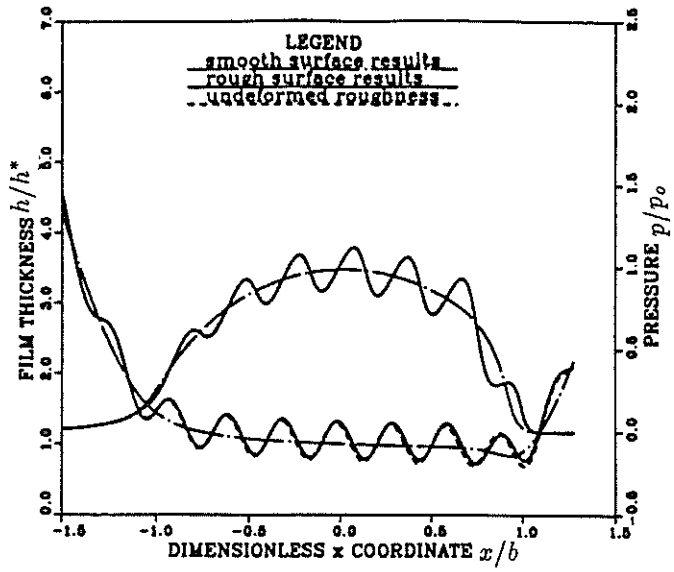

Figure 6.3: Chang's example 2, Non-Newtonian lubricant

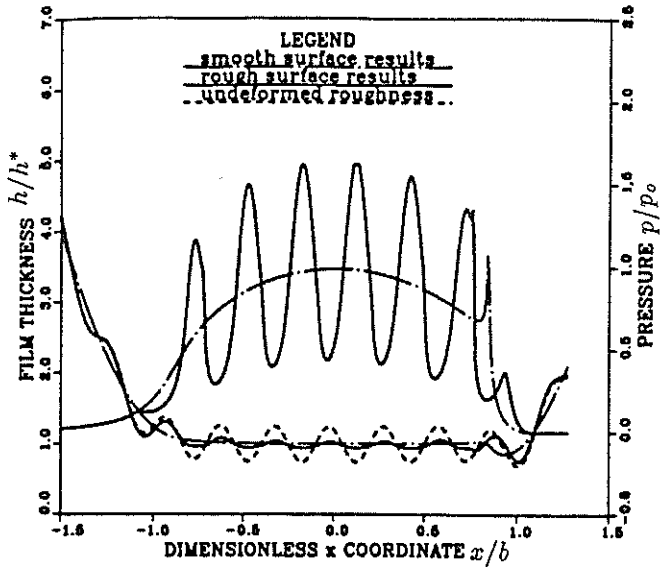

Figure 6.4: Chang's example 2, Newtonian lubricant

The main difference between the two examples is that for the second one the wave-length and the amplitude of the initial roughness have been slightly increased, resulting in smaller nominal film thickness and larger maximum Hertz pressure. In all the cases the solution of these examples with the schemes of Chapter 5 proved to be very unstable.

For both non-Newtonian solutions there is a remarkably small change in the shapes due to deformation and a correspondingly small amplitude of the pressure variations, despite the fact that the input data are not extremely different from the largely deformable examples of Chapter 5, except for the wave-length. However, Chang's Newtonian solutions show more deformable shapes and larger pressure ripples. Notice that Fig. 6.2 shows already some numerical instabilities for the pressures, so the lack of symmetry of the ripples may be just a consequence of it.

6.2 A Linearised Reynolds-Eyring Equation and its Analytical Solution

6.2.1 Linearised Reynolds-Eyring Equation

The Reynolds-Eyring equation for a compressible fluid was first introduced in Chapter 2:

$$h - (\rho^*/\rho)h^* = \frac{Dh^3}{12\eta\bar{u}}\frac{dp}{dx} \tag{6.1}$$

$$D = \frac{3t_v}{t_p}\sqrt{s^2 + (\frac{\sinh t_p}{t_p t_v})^2}\,(\coth t_p - 1/t_p) \tag{6.2}$$

Here equations 6.1 and 6.2 will be reduced in complexity assuming situations where the pressure and film thickness variations are small and the mean pressure is high (thus, viscosities too). For such cases $t_v \rightarrow \infty$ and the radical in equation 6.2 becomes $|s|$ and if t_p is not too big, then $\coth t_p - 1/t_p \approx t_p/3$ so, $D \approx |s|\, t_v = \frac{|s|\eta\bar{u}}{h\tau_o}$, finally equation 6.1 will be approximated by:

$$\frac{dp}{dx} = \frac{12\tau_o}{h\,|s|}(1 - \frac{\rho^* h^*}{\rho h}) \tag{6.3}$$

which may be compared with the Reynolds equation for Newtonian fluid ($D = 1$):

$$\frac{dp}{dx} = \frac{12\eta\bar{u}}{h^2}(1 - \frac{\rho^* h^*}{\rho h}) \tag{6.4}$$

notice that $\tau_o/\,|s|$ replaces $(\eta\bar{u})/h$. And in pure sliding situation: $s = \pm 2$ and $\bar{u} = u_1/2$.

In a general form, it is possible to write equations 6.3 and 6.4 as :

$$\frac{dp}{dx} = \frac{\bar{B}}{h}(1 - \frac{\rho^* h^*}{\rho h}) \tag{6.5}$$

where $\bar{B} = (12\eta\bar{u})/h$ for a Newtonian fluid and $\bar{B} = (12\tau_o)/\,|s|$ for an Eyring fluid. However, it must be pointed out while that this equation is a good approximation for Eyring fluids, for Newtonian lubricants $1/\bar{B}$ becomes very close to zero due to the high viscosity and the equation is valid only when the pressure variations are small.

Using the Dowson and Higginson equation for the density ratio :

$$\frac{\rho^*}{\rho} = \frac{\bar{\rho}^*}{\bar{\rho}} = \frac{1 + \beta_1(p - p_o)}{1 + \gamma_1(p - p_o)} \tag{6.6}$$

where:

$$\beta_1 = \frac{\beta}{1 + \beta p^*} \quad , \quad \gamma_1 = \frac{\gamma}{1 + \gamma p^*}$$

In order to make p^* a known value it is convenient to take $p^* = p_o$, so that ρ^* becomes ρ_m which is the density under the mean pressure, therefore h^* is redefined as h_G , just as in equation 5.20. Then equation 6.5 can be written as:

$$1 - [\frac{\mu}{H}]\frac{1 + \beta_o \Delta P}{1 + \gamma_o \Delta P} = HB\frac{dP}{d\theta} \tag{6.7}$$

where: $H = h/\bar{h}$, $\mu = h_G/\bar{h}$, $\Delta P = \alpha(p - p_o)$, $\theta = (2\pi x)/\lambda$, $B = (2\pi\bar{h})/(\bar{B}\lambda\alpha)$ and:

$$\beta_o = \frac{\beta}{\alpha(1+\beta p_o)}$$
$$\gamma_o = \frac{\gamma}{\alpha(1+\gamma\ p_o)} \tag{6.8}$$

Taking the average values of h and η to calculate $\bar{B}$, for Newtonian fluids:

$$B = \frac{\pi \bar{h}^2}{6\bar{u}\lambda\eta_o\alpha} e^{-\alpha p_o} \tag{6.9}$$

for Eyring fluids:

$$B = \frac{|s|\,\bar{h}\pi}{6\tau_o\lambda\alpha} \tag{6.10}$$

In dimensionless form, equation 6.9 and equation 6.10 become: Newtonian:

$$B = 2\pi K \tag{6.11}$$

Eyring:

$$B = \frac{\pi}{3} C_1 |s| \tag{6.12}$$

6.2.2 First Order Solution

Assuming a sinusoidal final shape and small pressure variations:

$$H = 1 + H_1 \cos\theta$$

and by series:

$$\frac{1}{H} \approx 1 - H_1 \cos\theta$$

and also by series:

$$\frac{1+\beta_o\Delta P}{1+\gamma_o\Delta P} \approx 1 - (\gamma_o - \beta_o)\Delta P$$

substituting into 6.7 :

$$1 - \mu[1 - H_1\cos\theta][1 - (\gamma_o - \beta_o)\Delta P] = B(1 + H_1\cos\theta)\frac{dp}{d\theta}$$

neglecting $H_1 \cos\theta \frac{dp}{d\theta}$ and $\Delta P H_1 \cos\theta$:

$$1 - \mu[1 - H_1\cos\theta - (\gamma_o - \beta_o)\Delta P] = B\frac{dp}{d\theta}$$

Writing:

$$C_o = \gamma_o - \beta_o = \frac{\gamma - \beta}{\alpha(1 + \beta p_o)(1 + \gamma p_o)} \tag{6.13}$$

then:

$$B\frac{dP}{d\theta} - C_o \mu \Delta P = 1 - \mu + H_1 \mu \cos\theta \tag{6.14}$$

A cyclic solution requires $\mu = 1$ (first order approximation) :

$$B\frac{dp}{d\theta} - C_o \Delta P = H_1 \cos\theta \tag{6.15}$$

Assuming :

$$\Delta P = P_b \sin\theta + P_a \cos\theta \tag{6.16}$$

by substituting 6.16 into 6.15 and solving:

$$\begin{aligned} P_b &= \tfrac{H_1 B}{B^2 + C_o^2} \\ P_a &= \tfrac{-H_1 C_o}{B^2 + C_o^2} \end{aligned} \tag{6.17}$$

and:

$$\Delta P = \frac{H_1}{\sqrt{B^2 + C_o^2}} \sin(\theta - \psi) \tag{6.18}$$

where: $\tan\psi = \frac{-P_a}{P_b} = C_o/B$.

To obtain the displacements from the pressures:

$$V = \frac{v}{\bar{h}} = V_b \sin\theta + V_a \cos\theta \tag{6.19}$$

where:

$$\begin{aligned} V_b &= AP_b \\ V_a &= AP_a \end{aligned} \tag{6.20}$$

and:

$$A = \frac{2\lambda}{\pi\alpha\bar{h}E'} = 2/C_3 \tag{6.21}$$

then since :

$$H(\theta) = 1 + Z_1 \cos(\theta - \phi) + V_b \sin\theta + V_a \cos\theta$$

the amplitude and phase angle of the original roughness with respect to the final shape is:

$$Z_1 = \sqrt{(H_1 - V_a)^2 + V_b^2}$$
$$\phi = \tan^{-1}\left(\frac{-V_b}{H_1 - V_a}\right) \tag{6.22}$$

It is now possible to relate the final amplitude of shape to the initial one by substituting equations 6.17 into equations 6.20 and then substituting these into equation 6.22 to obtain:

$$\frac{H_1}{Z_1} = \frac{\sqrt{B^2 + C_o^2}}{\sqrt{(C_o + A)^2 + B^2}} \tag{6.23}$$

Equation 6.23 represents the solution for the amplitude of the sinusoidal film thickness H_1 as a function of the amplitude of the sinusoidal original roughness Z_1. The pressures are given by equations 6.16, 6.17 and 6.18 and the displacements by equations 6.19, 6.20 and 6.21, finally the phase angle of the original roughness respect to the final shape is given in equations 6.22.

As an example of the application of this approximation Chang's example 2 has been solved and the solutions are shown in Figures 6.5 and 6.6, using the same scales as Chang.

In the non-Newtonian solution, by comparing Fig. 6.5 with Fig. 6.3 it is possible to see the good agreement of the analytical scheme with Chang's solution. It is also remarkable the small deformation occurred for this case. For the Newtonian case, comparing Fig. 6.6 with Fig. 6.4 also a good agreement of the solutions is observed.

Finally, it is important to point out that in this scheme two main approximations are made: taking B constant and linearizing the densities in the first order solution. For non-Newtonian fluids, B is in general very small, therefore one can avoid the further linearisation by using the scheme described in the following section.

6.2.3 The Analytical Solution as an Initial Guess for the Iterative Process

In Chapter 5 numerical instabilities remained unsolved for wavy roughness examples with very short wave length. One very useful application of the analytical scheme is to produce a very realistic first guess of the solution for the iterative schemes of Chapter 5, in this way the convergence rate is increased and numerical instabilities reduced.

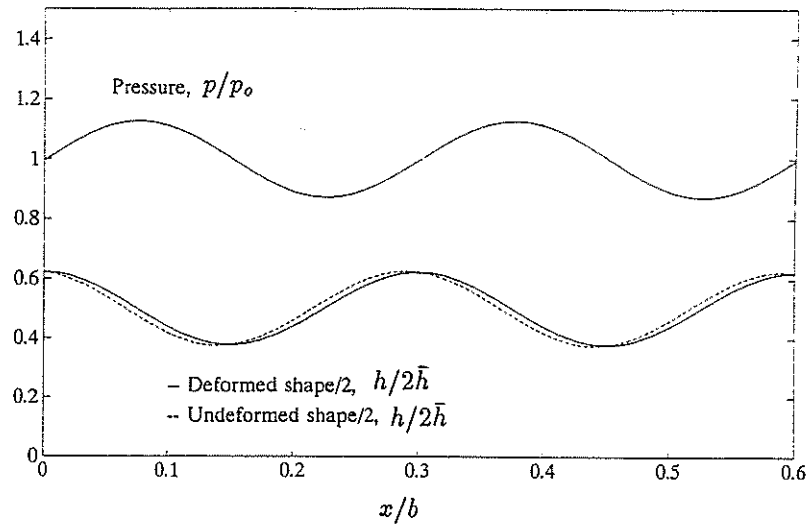

Figure 6.5: Chang's ex. 2 Non-Newtonian, linear solution

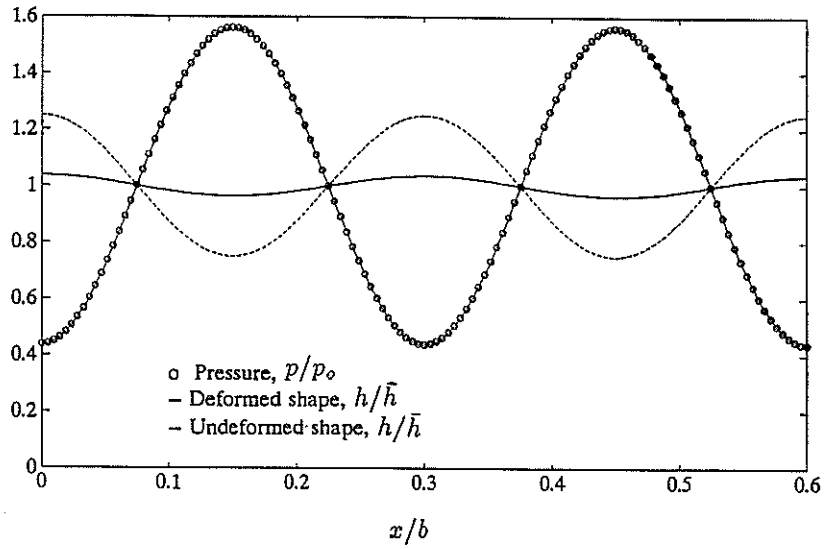

Figure 6.6: Chang's ex. 2 Newtonian, linear solution

Taking the Newtonian example of Fig. 6.4 of Chang's example 2, and calculating the initial guess for displacements using the analytical scheme, then correcting it with the direct approach, a converged solution is quickly obtained in Fig. 6.7 . Fig. 6.8 shows a comparison of the analytical pressure variations and the corrected ones after the iterative scheme was applied and Fig. 6.9 shows the corresponding comparison of displacements. It is easy to see that there is great similarity between the iterative and analytical pressures of Fig 6.8, in both cases the amplitudes are almost the same. Perhaps the only noticeable difference is that with the analytical solution the pressures are approximated to a perfect sinusoidal, whereas in the iterative results it is possible to see that the pressures are not

perfectly sinusoidal.

Fig. 6.7 agrees very well with the Chang's results of Fig. 6.4 in both pressures and final shape.

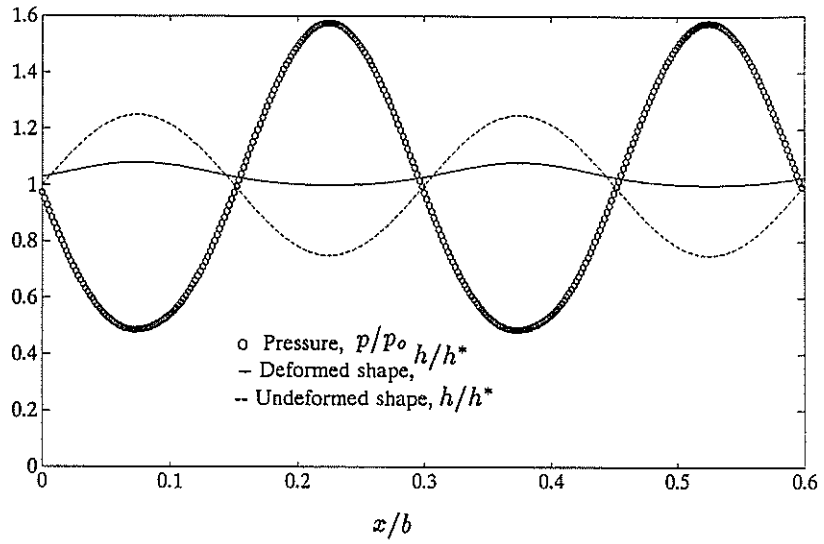

Figure 6.7: Chang's ex. 2, Newtonian. Direct scheme with initial guess from the analytical solution

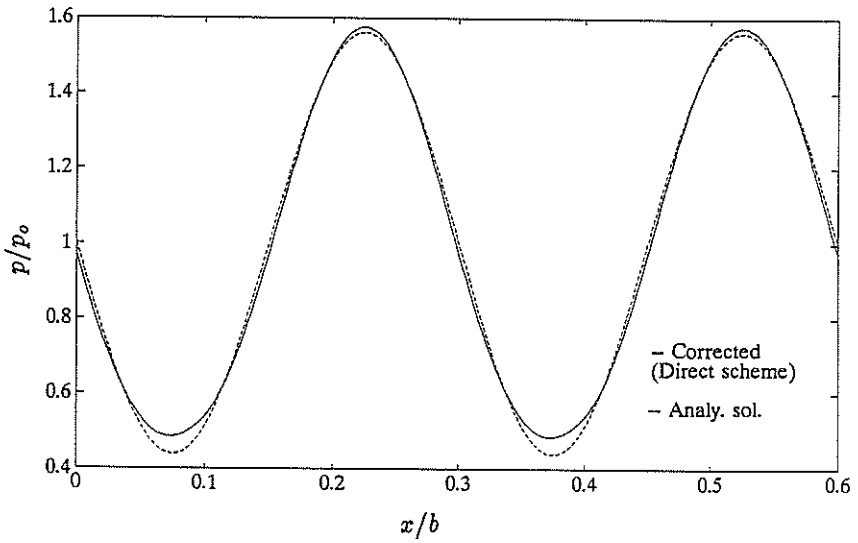

Figure 6.8: Comparison of analytical and corrected pressures

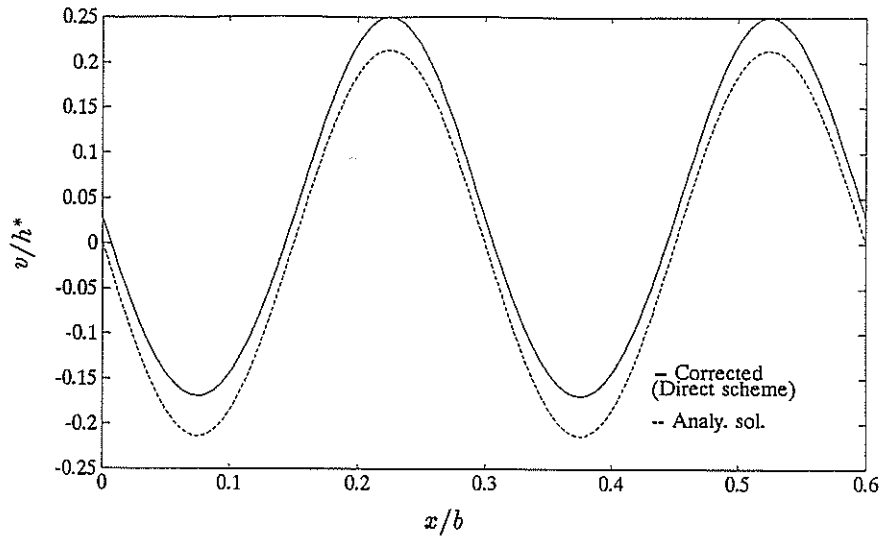

Figure 6.9: Comparison of analytical and corrected displacements

6.3 The Two Point Boundary Value Problem Scheme (TPBVP)

Equation 6.7 is a linear ordinary differential equation and it also can be solved for P for example using a Runge-Kutta method. Since it is known that the film thickness is a cyclic function, then a cyclic pressure distribution is expected, but the value of the pressures at the beginning of the x interval is unknown and has to be calculated from the boundary problem itself, that is to say the boundary values are explicitly unknown. This problem is an special case of 'two point boundary value problems'.

The process of solving equation 6.7 can be started by first assuming an initial guess for $H(x)$, then the initial value of μ can be assumed to be 1 and the value of the pressures at the edges of x can be approximated by the first order solution, equations 6.16 and 6.17 such that :

$$P(x = 0) = P_a + P_o$$

then equation 6.7 can be solved by Runge-Kutta. A function F is defined as :

$$F = P(\theta = 0) - P(\theta = 2\pi)$$

and applying a root finder algorithm (e.g. Newton-Raphson) the right value of μ which ensures $F = 0$ (cyclic pressures) can be found and hence the corresponding pressures.

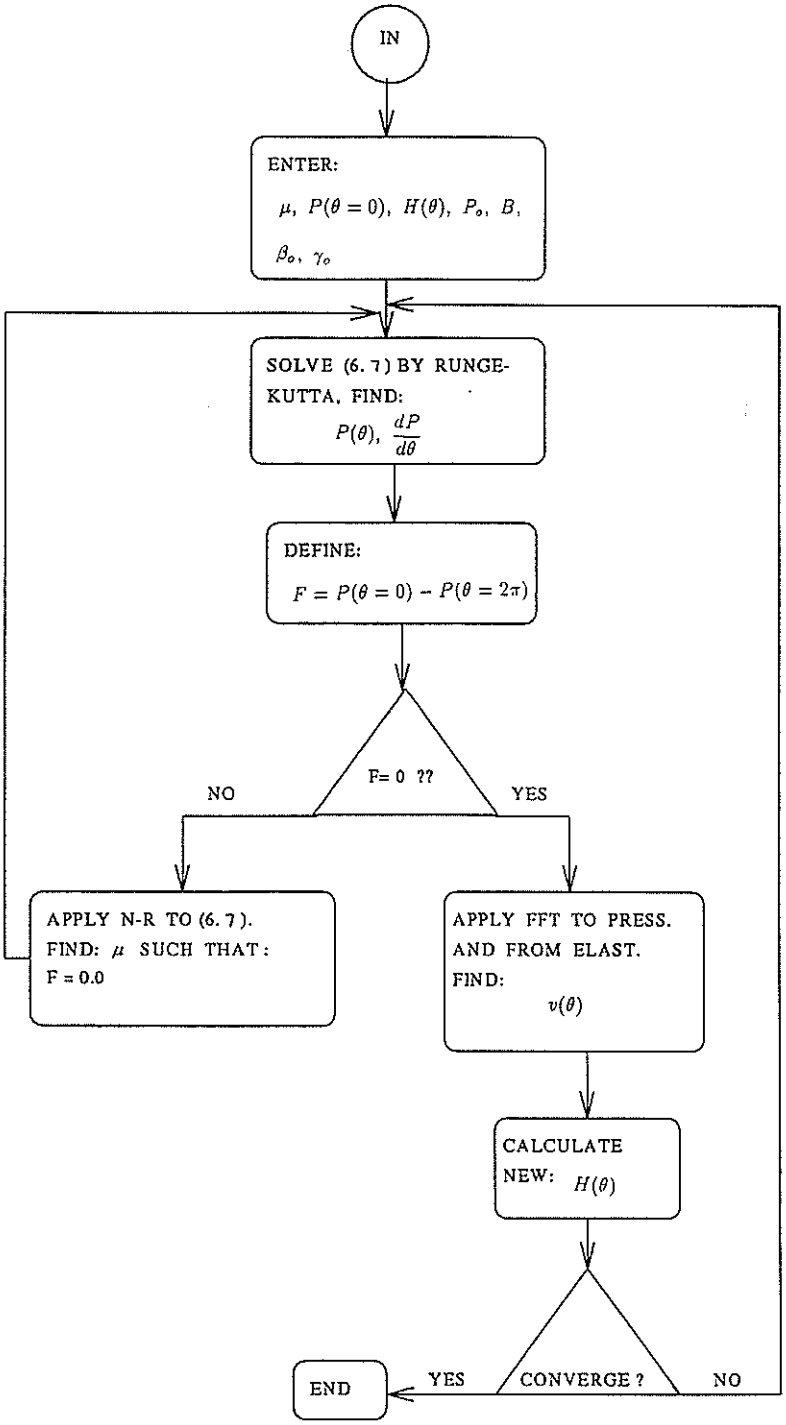

Figure 6.10: Two points boundary problem approach

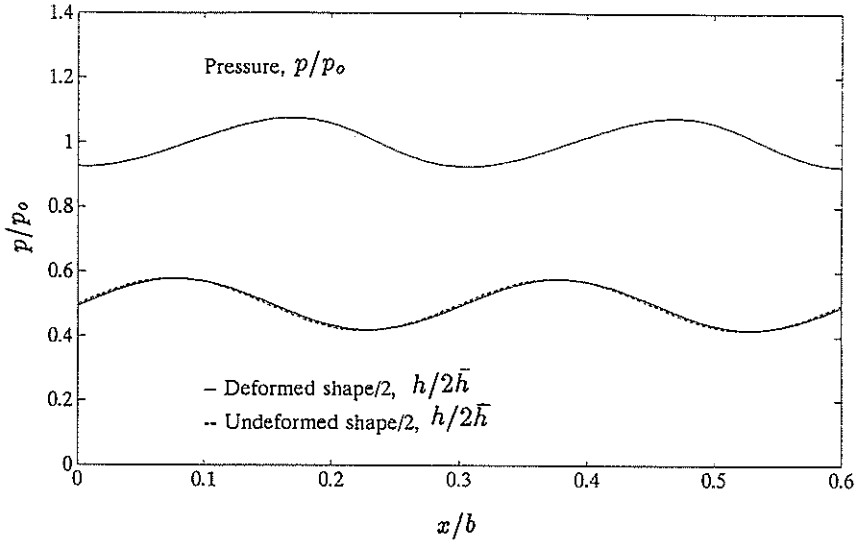

Figure 6.11: Chang's Ex. 1, Non-Newtonian, TPBVP Solution, $\mu = 0.99821$

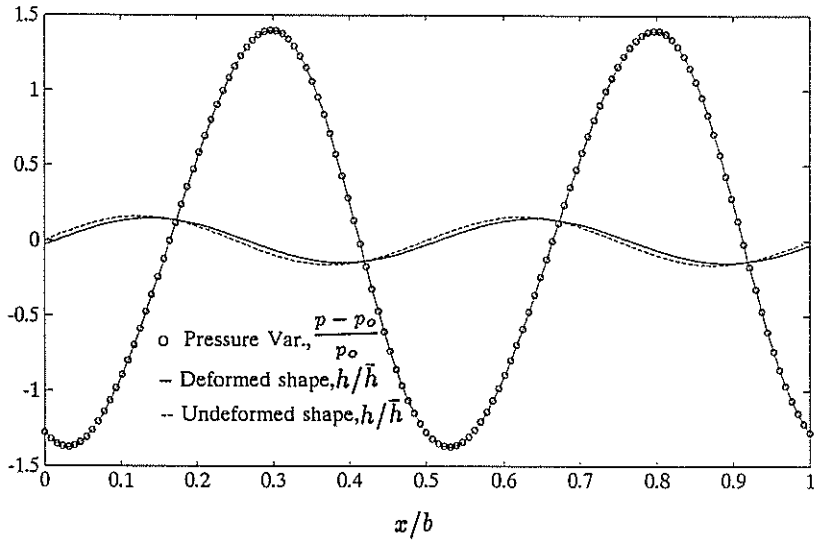

Figure 6.12: Non-Newtonian, TPBVP Solution, $\lambda = 83.1518 \times 10^{-6}$ m, $\mu = 1.00346$

After finding the pressures the displacements and film thickness can be calculated from elasticity. The process is described in Fig. 6.10 and the solution for Non-Newtonian fluid of Chang's example 1 (Section 6.1) is shown in Fig. 6.11. Notice that this scheme is only suitable for non-Newtonian fluids where the constant B in equation 6.7 is appreciably non-zero.

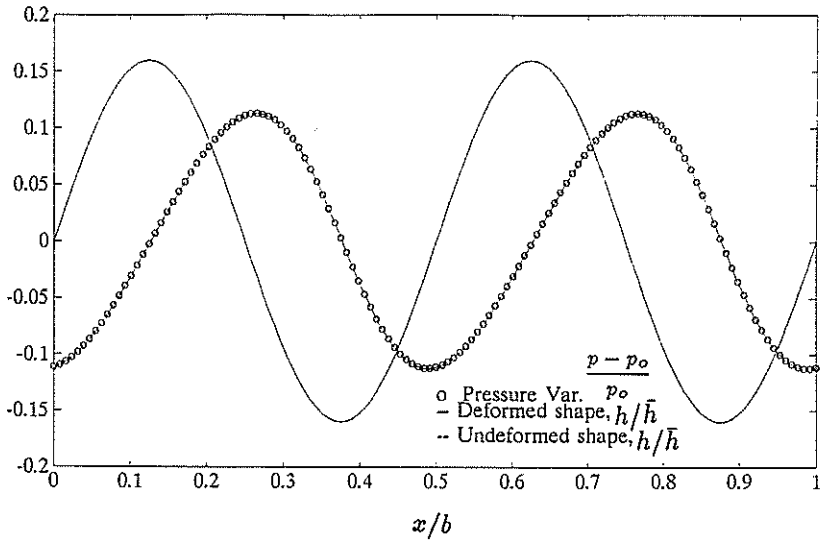

Figure 6.13: Non-Newtonian, TPBVP Solution, $\lambda = 5.966 \times 10^{-6}$ m, $\mu = 0.97827$

Two more examples are shown below where the basic data have been taken again from Chang's example 1 but the wave length of the initial roughness has been changed. In Fig. 6.12 the roughness wave length has been increased to $\lambda = 83.151 \times 10^{-6}$ m, whilst in Fig. 6.13 it has been reduced to $\lambda = 5.966 \times 10^{-6}$ m, with no visible deformation !.

There are two points to notice in this TPBVP scheme. One is that if one continues to increase the amplitude of initial roughness there is a value at which the root finder for μ (Newton-Raphson) becomes unstable and the whole process fails. And the other is that as the wave length of the initial roughness is increased the amplitude of the pressure ripples also increases and at some point again the root finder fails.

6.3.1 An Extension of the TPBVP Scheme for the Full Reynolds-Eyring Equation

The full Reynolds-Eyring equation can be written as:

$$qh\frac{dp}{dx} = 1 - \frac{\rho^* h^*}{\rho h} \tag{6.24}$$

where :

$$q = \frac{hD}{12\eta\bar{u}} \tag{6.25}$$

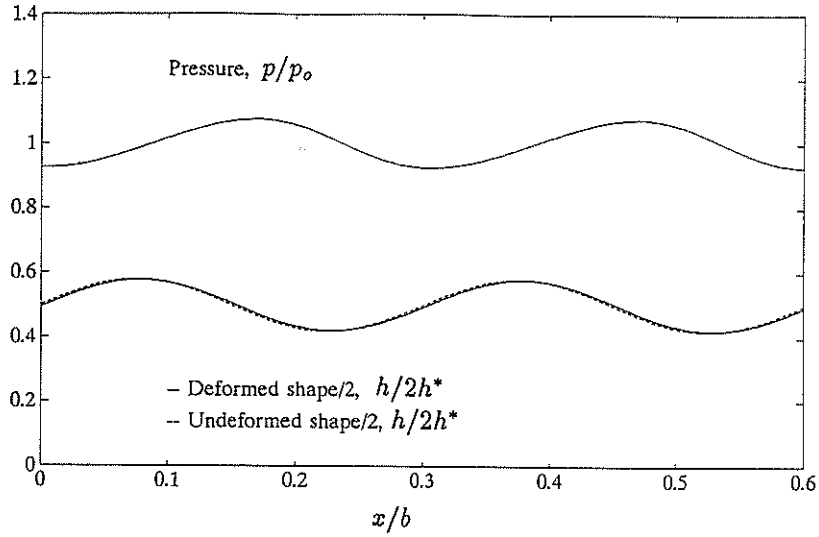

Figure 6.14: Chang's Ex. 1, non-Newtonian, full equation TPBVP solution, $\mu = 0.99847$

According to 6.2.1 the linearised equation for an Eyring fluid implies:

$$q \approx \frac{|s|}{12\tau_o}$$

and defining :

$$g = \frac{12\tau_o}{|s|}\frac{hD}{12\eta\bar{u}}$$

it is possible to rewrite equation 6.24 as:

$$BgH\frac{dP}{d\theta} = 1 - \frac{\mu}{H}\frac{1+\beta_o\Delta P}{1+\gamma_o\Delta P} \tag{6.26}$$

so that when $g = 1$ equation 6.26 becomes 6.7, with B still given by 6.10.

By non-dimensionalizing:

$$g = \frac{6K}{C_1}\frac{D\ e^{-(P-P_o)}}{|s|} \tag{6.27}$$

Equation 6.26 can be solved following the procedure described in Section 6.3, calculating g for every value of x. With this scheme Chang's example 1 was solved for the Non-Newtonian case, and the solution is shown in Fig. 6.14. By comparing Fig. 6.14 and Fig. 6.11 it can be seen that there is no appreciable difference in the results.

6.4 Analysis of Deformation for Sinusoidal Roughness

Fig. 6.12 and Fig. 6.13 clearly show that increasing the roughness wave length while keeping the other parameters fixed gives as a result more deformation. The sinusoidal roughness examples of Chapter 5 show that in both cases, Newtonian and Eyring fluids, the initial roughness almost vanishes after deformation.

The Chang's examples show that in the Non-Newtonian solutions, the original roughness is almost completely preserved (Fig. 6.1 and Fig. 6.3), with very little deformation occurring and small pressure ripples. The enormous difference in final shapes between the Eyring examples from Chapter 5 and the Non-Newtonian Chang's examples which have no extremely different input data except for the wave length, arouses some questions about the importance of the wave length of the initial roughness in determining the final shape. In this section the attention is focused on the influence of λ, or more precisely $\lambda/\bar{h}$, in the behaviour of transverse roughness in EHL.

In order to study the dependence of the solution on wave length, the data input of the Chang's example 2 were used except that the wave length was varied. The analytical solution of Section 6.2.2 has been applied to obtain solutions for compressible Eyring and Newtonian fluids. As a matter of comparison, the corresponding solutions using the Collocation Method of Appendix C and the incompressible results have been also obtained. The results are shown in Figs. 6.15 to 6.20, where λ_c is the wave length used by Chang in the example 2. The amplitudes of the pressure ripples P_1, are plotted in Fig. 6.15 and Fig. 6.16, the amplitudes of the elastic displacements V_1, are shown in Fig. 6.17 and Fig. 6.18. Finally the amplitudes of the final shapes are plotted in Fig. 6.19 and Fig. 6.20.

By looking at Fig. 6.19 and Fig. 6.20 it is clear that for both Newtonian and Eyring fluids the amplitude of the final shape decreases when λ increases, while for small values of λ the shape remains undeformed; for Newtonian fluids to keep the shape undeformed requires much shorter wave lengths than for Eyring fluids.

This effect cannot be understood by elasticity alone, since $v_1 = \frac{2\lambda}{\pi E'} p_1$, the elasticity equation suggests a linear variation between v and λ which according to Figs. 6.17 and 6.18 does not happen when hydrodynamics also are involved.

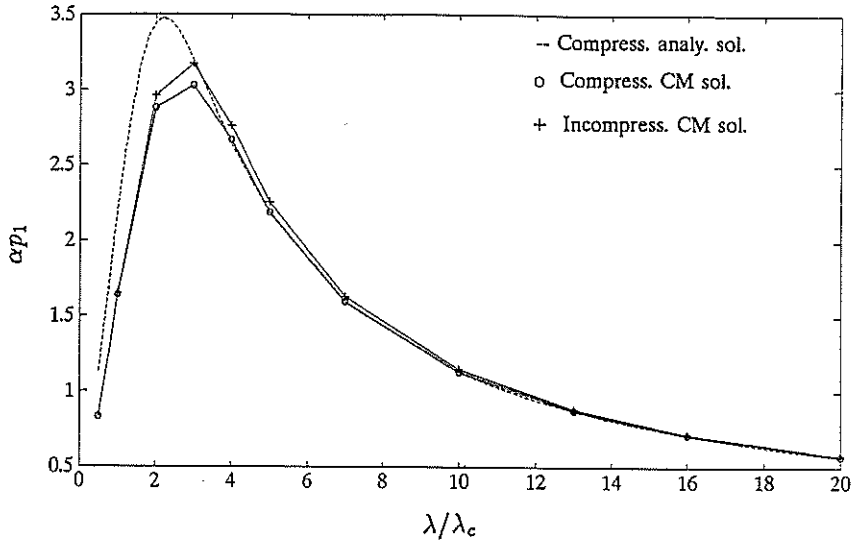

Figure 6.15: Non-Newtonian, amplitude of pressure ripples, $\lambda_c = 71.7 \times 10^{-6}$ m

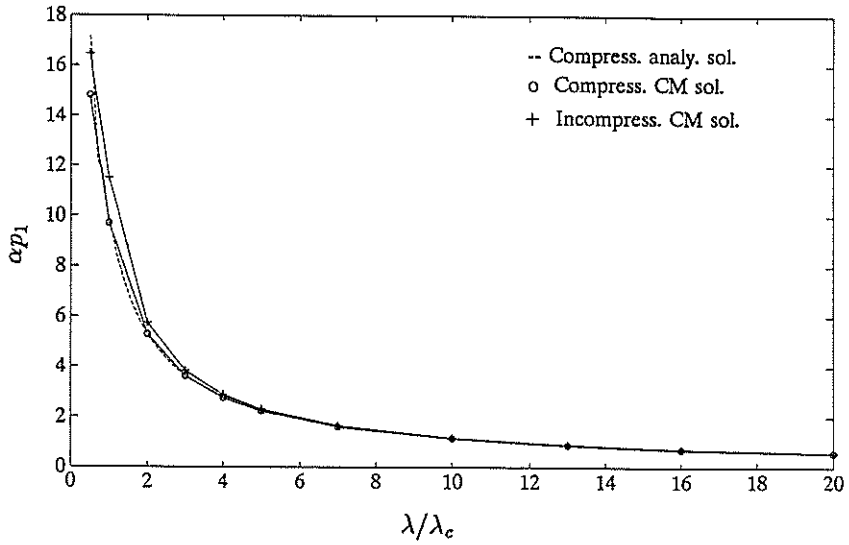

Figure 6.16: Newtonian, amplitude of pressure ripples, $\lambda_c = 71.7 \times 10^{-6}$ m

In general the linear theory and the collocation method of Appendix C agree well in predicting the final shape and pressures. However, when λ is very short and Newtonian fluid is considered there are differences in the results for the final shape and displacements, see Fig. 6.15. This differences could be attributed to the inaccuracy of the assumptions made in the analytical solution for large pressure ripples.

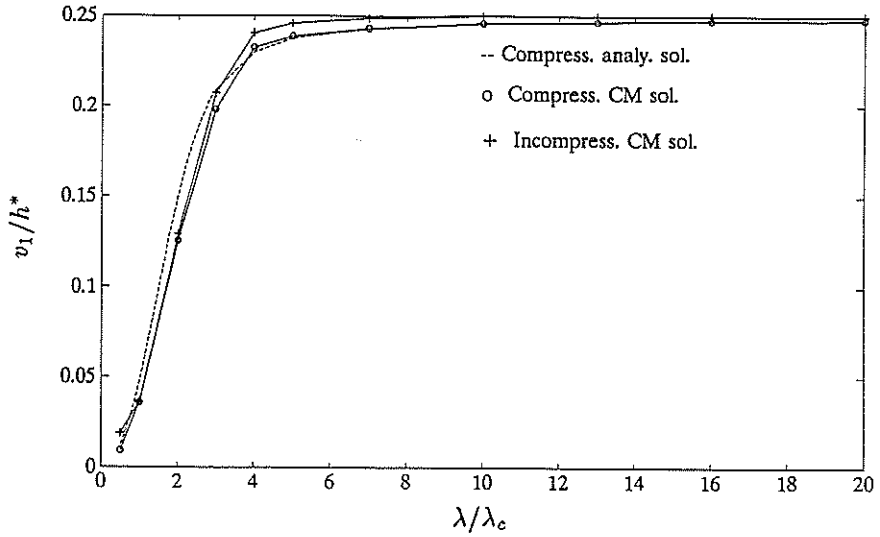

Figure 6.17: Non-Newtonian, amplitude of elastic displacements, $\lambda_c = 71.7 \times 10^{-6}$ m

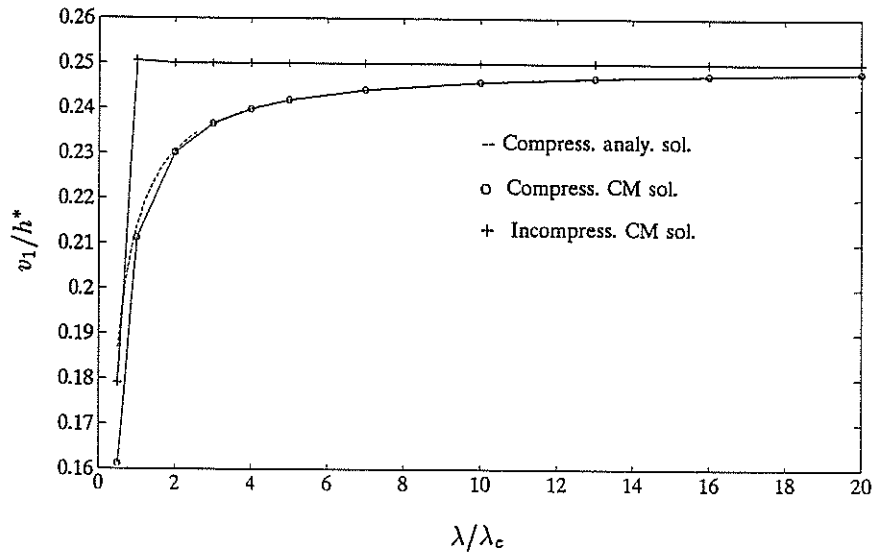

Figure 6.18: Newtonian, amplitude of elastic displacements, $\lambda_c = 71.7 \times 10^{-6}$ m

Figs. 6.15 and 6.16 show an important difference between Newtonian and non-Newtonian behaviour for the amplitude of the pressures ripples. While the non-Newtonian curves of Fig. 6.15 show a maximum value when $\lambda/\lambda_c \approx 3$; the corresponding Newtonian results of Fig. 6.16 show that the amplitude of the pressure ripples always increases when λ decreases.

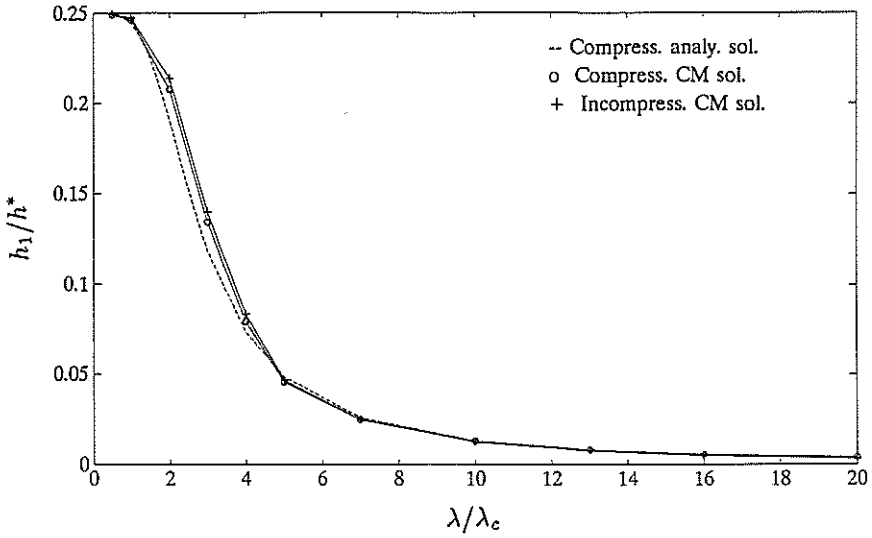

Figure 6.19: Non-Newtonian final shape amplitude, $\lambda_c = 71.7 \times 10^{-6}$ m

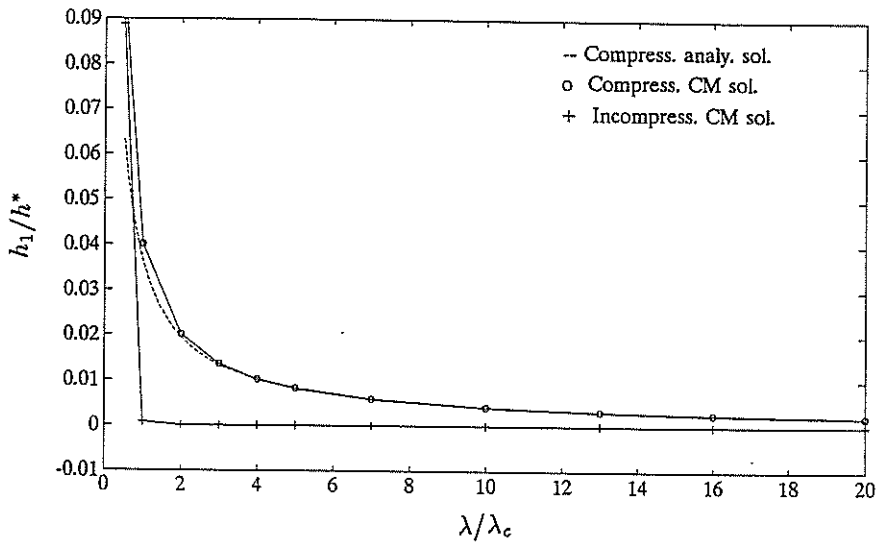

Figure 6.20: Newtonian, final shape amplitude, $\lambda_c = 71.7 \times 10^{-6}$ m

This effect is clearly due to the variation of viscosity with pressure . And in order to understand the reasons, consider equation 6.18. The pressure ripples amplitude can be approximated by:

$$\Delta P_1 = \frac{H_1}{\sqrt{B^2 + C_o^2}} \tag{6.28}$$

where the amplitude of the sinusoidal final shape H_1 is given by equation 6.23; now for Newtonian fluids and high viscosity (from equation 6.9) B must be very small, so taking $B = 0.0$, equation 6.23 becomes:

$$H_1 = \frac{Z_1 C_o}{C_o + A} \tag{6.29}$$

and equation 6.28 becomes:

$$\Delta P_1 = \frac{H_1}{C_o} \tag{6.30}$$

According to equation 6.21 when λ decreases, A also decreases and therefore (following equation 6.29) H_1 increases, thus from equation 6.30 ΔP increases as well. In an Eyring fluid B is not small and the behaviour is different.

Now using only the analytical solution (Section 6.2.1) the effect of varying the mean pressure and therefore the mean viscosity will be analysed. Three different levels of mean pressure ($P_o = 7.95$, $P_o = 17.49$, and $P_o = 31.8$) are used to obtain comparisons of Newtonian and Eyring solutions when the ratio $\lambda/\bar{h}$ is varied. Again the remaining data have been taken from the Chang's example 2.

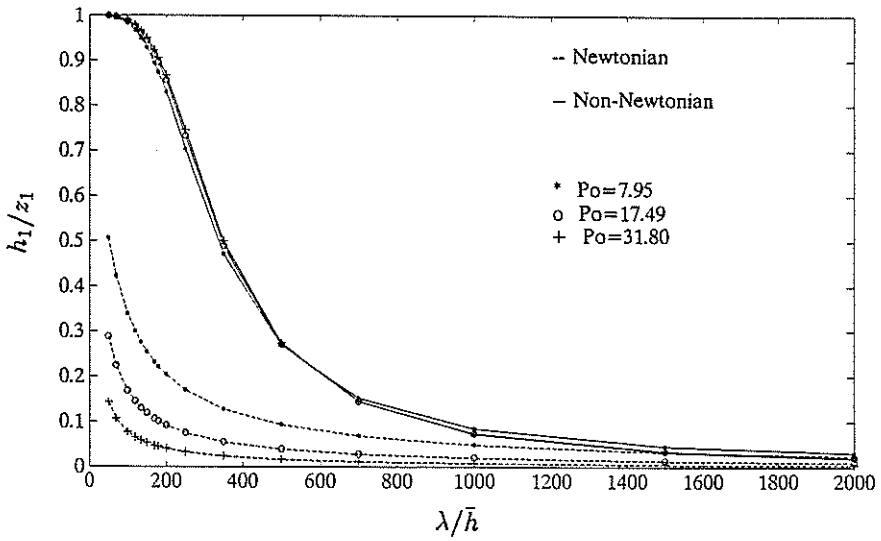

Figure 6.21: Final shape amplitudes for different P_o

Fig. 6.21 shows the ratio of the initial and final amplitude of shape as a function of the ratio $\lambda/\bar{h}$, and it suggests that the final shape in an Eyring fluid is barely affected by the value of the mean pressure for all values of $\lambda/\bar{h}$, as expected: in the linear theory (Section 6.2.1): the only effect of p_o in an Eyring fluid is a minor change in the

compressibility. However, for Newtonian fluids a change of p_o represents also a change of viscosity.

Fig. 6.23 shows the dimensionless pressure ripple amplitude and it is easy to see that for high values of $\lambda/\bar{h}$ the pressure ripples will have nearly the same amplitude for Newtonian and Eyring fluids, which was already pointed out in Chapter 5. For Fig. 6.23 C_p is defined as:

$$C_p = \frac{\gamma - \beta}{(1 + \beta p_{max})(1 + \gamma p_{min})}$$

The phase angle between initial and final shapes is plotted in Fig. 6.22 which shows that when $\lambda/\bar{h}$ is small the shift of phase is almost the same for the three different levels of P_o. Finally the pressure gradient is plotted in Fig. 6.24 from which similar conclusions to the pressures can be observed.

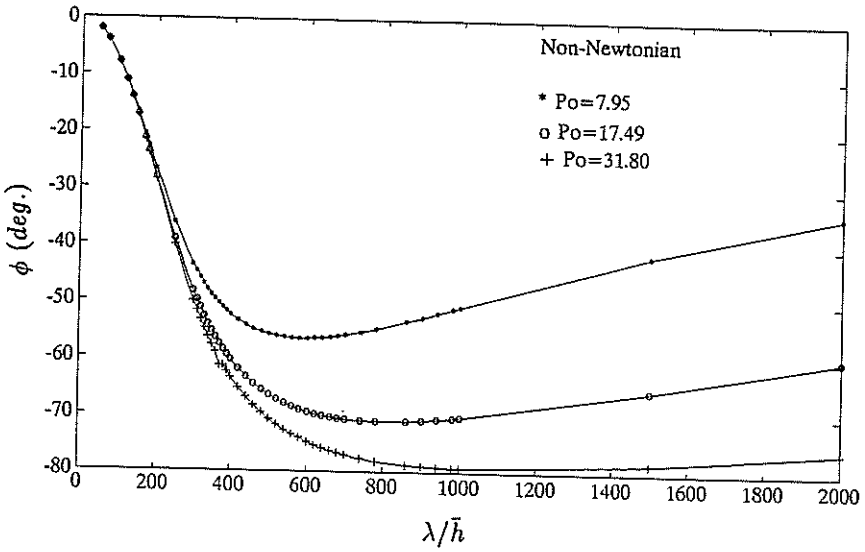

Figure 6.22: Phase angles between initial and final shape for different P_o

In order to extend the analysis to an assembly of wave lengths as in real roughness, one must replace in equations 6.9, 6.10 and 6.21 the wave length of the fundamental component λ by the wave length of the n harmonic $\lambda_n = \lambda/n$, since : $v_n = \frac{2\lambda}{n\pi E'} p_n$, thus :

$$B_n = nB \quad , \quad A_n = A/n$$

therefore equation 6.23 becomes:

$$\frac{(H_1)_n}{(Z_1)_n} = \frac{\sqrt{B_n^2 + C_o^2}}{\sqrt{(A_n + C_o)^2 + B_n^2}} \tag{6.31}$$

The effect of varying the wave number n is shown in Fig. 6.25 which uses the basic input data from Chang's example 2. The critical dependence of the final shape amplitude on the ratio $\lambda/\bar{h}$ is clear. From Fig. 6.25 it can be seen that the amplitudes of the original roughness components remain practically unchanged for all values of $\lambda/\bar{h}$.

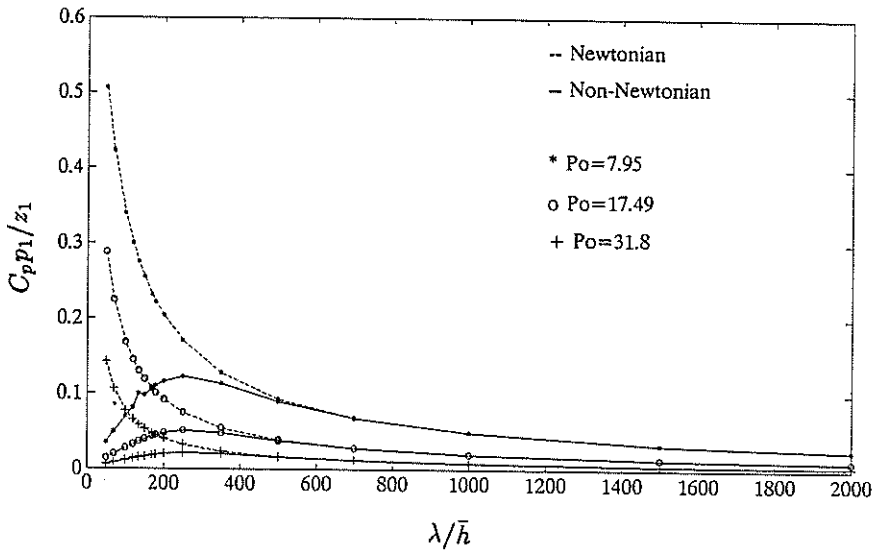

Figure 6.23: Pressure ripples amplitudes for different P_o

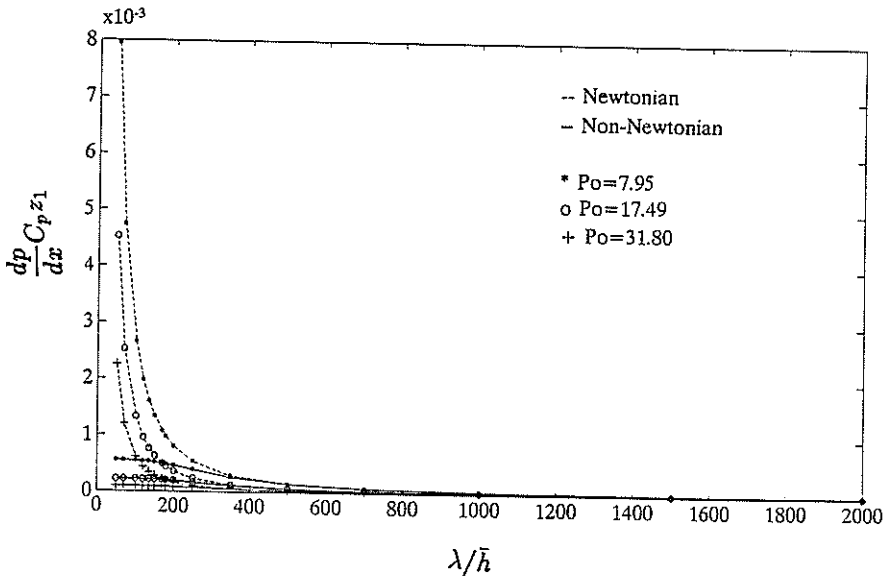

Figure 6.24: Pressure gradients amplitudes for different P_o

The roughness amplitude in the Chang's solution Fig. 6.3 is indeed unchanged; but this would no longer be the case if the wave length were increased by a factor 3. One can

show by studying equation 6.31 that, for plausible values of the parameters, the critical wave length for which the amplitude is reduced by a factor of 2 is given by the simple relation:

$$\frac{\lambda}{\bar{h}} > 1.6\sqrt{E'/\tau_o} \tag{6.32}$$

thus, for Chang's nominal film thickness (example 2) $\bar{h} = 0.6\ \mu m$, the critical wave length is $\lambda > 200\ \mu m$, in agreement with Fig. 6.25.

Equation 6.31 answers the question put in Chapter 5: it is now possible to understand why in a real roughness contact, the low frequencies of the initial roughness disappear and only the high frequencies remain after deformation.

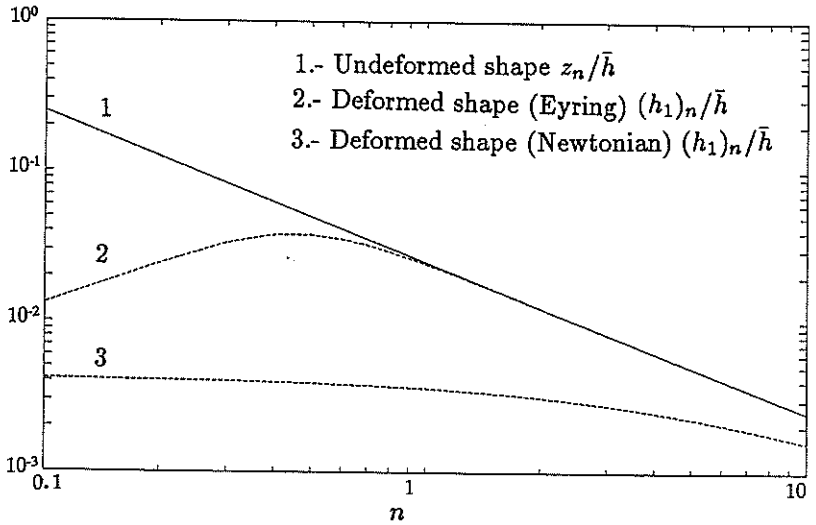

Figure 6.25: Variation of shape amplitude with the wave number

6.5 Conclusions

Two approaches have been described to investigate the behaviour of short wave length waviness in steady state EHL sliding contacts. The first one is an analytical solution of the linearised Reynolds-Eyring equation, which has proved to give good solutions for both Newtonian and Eyring fluids, however, its applicability is restricted by the linearisation assumption of high mean viscosity and small pressure ripples. Since it is an analytical solution there are no stability problems. The second approach is the Two Point Boundary Value Problem scheme (TPBVP) which can be used to solve both the full and linearised Reynolds-Eyring equations and its applicability is restricted to non-Newtonian fluids.

Using the TPBVP scheme a numerical example with short wave length was solved,

the wave length of the original roughness then was varied while keeping everything else fixed. It was observed that when increasing the wave length, the deformation of the initial roughness and the pressure ripples amplitude also increased, whereas when reducing the wave length it was possible to obtain no visible deformation in the final shape.

Applying the analytical scheme an important number of solutions have been produced by varying the roughness wave length for compressible Newtonian and Eyring fluids. Using the collocation method of Appendix C a comparison with the results of the analytical scheme was made and some results for incompressible fluids were also included. Amplitudes of the pressure ripples, the displacements and final shape have been plotted as well as the phase angle between initial and final shape; from which the following most important conclusions can be obtained:

a).- For Eyring fluids the deformation of the roughness is strongly dependent on the ratio $\lambda/\bar{h}$. For small values of this ratio ($\lambda/\bar{h} < 100$ with a fixed value of $\tau_o = 5 \times 10^6$ Pa), the original roughness is expected to persist.

b).- The amplitude of the pressure variations for Newtonian fluids increases when $\lambda/\bar{h}$ is decreased. But for Eyring fluids there is a maximum value of this amplitude after which it decreases when the ratio $\lambda/\bar{h}$ decreases. The maximum is more or less located at around $\lambda/\bar{h} = 200$ (for $\tau_o = 5 \times 10^6$ Pa).

c).- In Eyring fluids the variation of the mean pressure has little effect in the final shape whilst in Newtonian fluids when the mean pressure increases the deformation of the roughness is increased. This is due to the mean viscosity, when the mean pressure is large, then B of equation 6.9 is very small for Newtonian fluids.

d).- For Eyring fluids the phase angle between the initial and final shape decreases when $\lambda/\bar{h}$ decreases. For Newtonian fluids this angle is zero.

CHAPTER SEVEN

SUBSURFACE STRESSES IN MICRO-EHL

The fatigue life of machine elements is directly related to their internal stress distribution. The first analysis of deformation and stresses in contacting bodies was carried out by Hertz [38] in 1882. The internal stress distribution of dry contacts with wavy surfaces has been studied by Westergaard [81] 1939, Dundurs et al. [23] 1973, and Michau et al. [57] 1973. Real roughness in dry contacts was included only recently when the advances in computing and numerical techniques made it possible, e.g. Webster and Sayles [80] 1986, Merriman and Kannel [56] 1989.

Dowson et al. [22] 1962 were the first to calculate the overall stress distribution in smooth rolling EHL contacts. Goglia et al. [25] 1984 investigated the role of wavy surface irregularities on EHL sliding line contacts. Sadeghi [69] 1991 shows a comparison of the effects of three rheological models on the subsurface stresses of real roughness lubricated bodies in contact, his approach solves simultaneously the Reynolds and the elastic equations accounting for the whole EHL geometry.

In general, one important conclusion is obtained from all previous investigations mentioned above and dealing with roughness in elastic contacts: The stress fields show two high value zones:

a).- A maximum shear stress, analogous to the classical and well studied Hertzian shear stress, located well below the contact surface.

b).- A series of points of high stress distributed below the contact but very close to the surface and directly related to the asperities on the surfaces.

In this chapter the attention is focused on the subsurface stresses related to the surface roughness; and Hertzian (or almost Hertzian) stress distribution related to the full EHL

geometry are omitted. Therefore the analysis is concerned with small depths and the micro-EHL pressure distribution from any of the schemes of Chapters 5 and 6 can be used in the calculation of the subsurface stresses.

Once the pressures are known, the cartesian and principal stresses can be calculated by applying simple elasticity equations in a half-space assuming again the pressures to be an assembly of sinusoidal functions whose coefficients are obtained from a Fourier analysis.

Numerical examples are shown for wavy and real-roughness surfaces, displaying the stress distribution at different depths to analyse their variation.

Then the interest is addressed to the elastic shakedown theory which leads to the simple failure criterion: $\tau_{xz} \leq k$. The orthogonal shear stress τ_{xz} is tested to be a Gaussian variable for small depths, so the standard $2S$ and $3S$ confidence limits and the usual rules for assessing the expected largest value are applied.

7.1 Stresses Under Micro-EHL Pressures

Since the attention has been focussed only on the stresses related to the surface roughness, ignoring the influence of the EHL geometry, then it is possible to consider an elastic half-space under the plane strain criterion loaded on the surface by a known pressure distribution, which is the addition of the mean constant pressure p_o and the micro-EHL pressure variations related to the roughness, see Fig. 7.1.

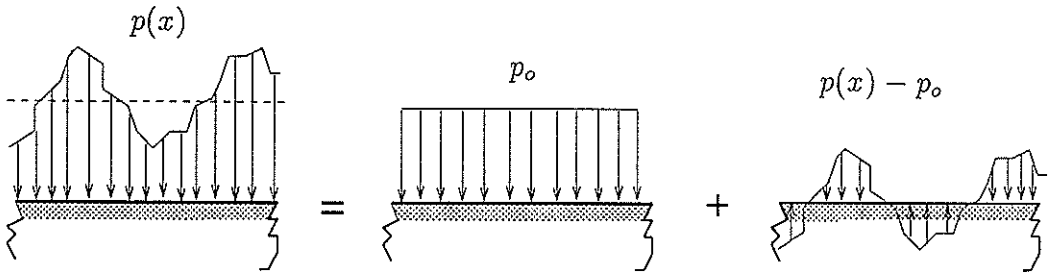

Figure 7.1: Elastic half-space loaded with micro-EHL pressures

The mean pressure will produce subsurface cartesian stresses, which are given by equations 7.1 (see Fig. 7.2):

$$\sigma_x = -\frac{p_o}{2\pi}[2(\theta_2 - \theta_1) - (\sin 2\theta_2 - \sin 2\theta_1)]$$

$$\sigma_z = -\frac{p_o}{2\pi}[2(\theta_2 - \theta_1) - (\sin 2\theta_2 - \sin 2\theta_1)] \tag{7.1}$$

$$\tau_{xz} = -\frac{p_o}{2\pi}[\cos 2\theta_1 - \cos 2\theta_2]$$

where:

$$\tan\theta_1 = \frac{x-a}{z} \quad , \quad \tan\theta_2 = \frac{x+a}{z}$$

z = depth below the surface.

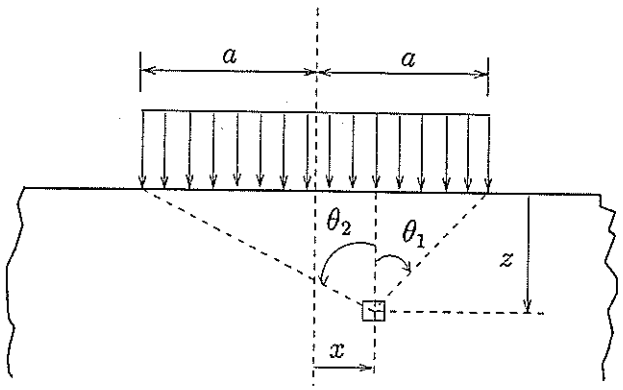

Figure 7.2: Constant strip of pressure on an elastic half-space

For small values of z and for $a \to \infty$ equations 7.1 become:

$$\begin{aligned} \sigma_x &\approx -p_o \\ \sigma_z &\approx -p_o \\ \tau_{xz} &\approx 0 \end{aligned} \tag{7.2}$$

The pressure variations can be considered as an assembly of sinusoidal functions with amplitudes given by their Fourier coefficients. And from elasticity, it is well known that the cartesian stresses due to a pressure: $p = p_n \cos s_n x$ are given by:

$$\sigma_x = -p_n(1 - s_n z)e^{-s_n z}\cos s_n x$$

$$\sigma_z = -p_n(1 + s_n z)e^{-s_n z}\cos s_n x \tag{7.3}$$

$$\tau_{xz} = -p_n(s_n z)e^{-s_n z}\sin s_n x$$

therefore, it is easy to find the cartesian stresses related to the pressure variations $p(x)-p_o$ by superposition of the contributions due to the separate Fourier terms.

After calculating the cartesian stresses, the principal stresses can be obtained in the usual way:

$$\begin{aligned} \sigma_1 &= \tfrac{\sigma_x+\sigma_z}{2} + \tau_c \\ \sigma_2 &= \tfrac{\sigma_x+\sigma_z}{2} - \tau_c \\ \sigma_3 &= \nu(\sigma_1+\sigma_2) \\ \tau_c &= \sqrt{(\tfrac{\sigma_x-\sigma_z}{2})^2 + \tau_{xz}^2} \end{aligned} \tag{7.4}$$

7.2 Variation of Stresses with the Depth

Two examples of micro-EHL pressures both compressible and non-Newtonian, are used to show the variation of stresses with the depth. The first example is the sinusoidal case for which pressures are shown in Fig. 5.4 and the second one is the real roughness case the pressures of which are shown in Fig. 5.12.

a).- Wavy pressure distribution (Fig. 5.4).

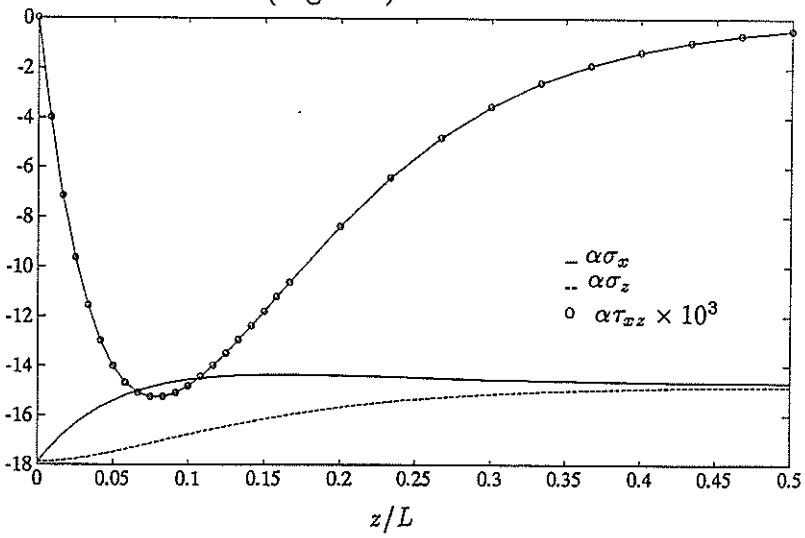

Figure 7.3: $\alpha\sigma_x$, $\alpha\sigma_z$, $\alpha\tau_{xz}$, at $x/L = 0.875$

Figs. 7.3 and 7.4 show the distribution of dimensionless cartesian and principal stresses for variable depth z/L underneath the pressure maxima. Figs. 7.5 and 7.6 show the same variables but plotted underneath the pressure minima.

For the dimensionless stresses $\alpha\sigma_x$, $\alpha\sigma_z$ and $\alpha\sigma_1$, $\alpha\sigma_2$, $\alpha\sigma_3$, the major changes occur at very small values of z/L, however, when $z/L \to \infty$ they will eventually vanish.

From Figs. 7.3 to 7.6 it can be concluded that the shear stresses τ_{xz} and τ_c show a maximum at some distance $z/L \approx 0.083$ below the surface, this would be typical for any other point along x/L. These maximum values will produce the high stresses zone which can be seen for τ_{xz} in Fig. 7.10. Since in failure theory what is important are the absolute values of the shear stress, this figure shows a 2-D plot of $(\alpha\tau_{xz})^2$.

Figs. 7.7, 7.8 and 7.9 show the stresses $\alpha\sigma_x$, $\alpha\sigma_z$ and $\alpha\tau_{xz}$ plotted along x/L for two fixed depths. The amplitude of the stresses decreases as the depth increases.

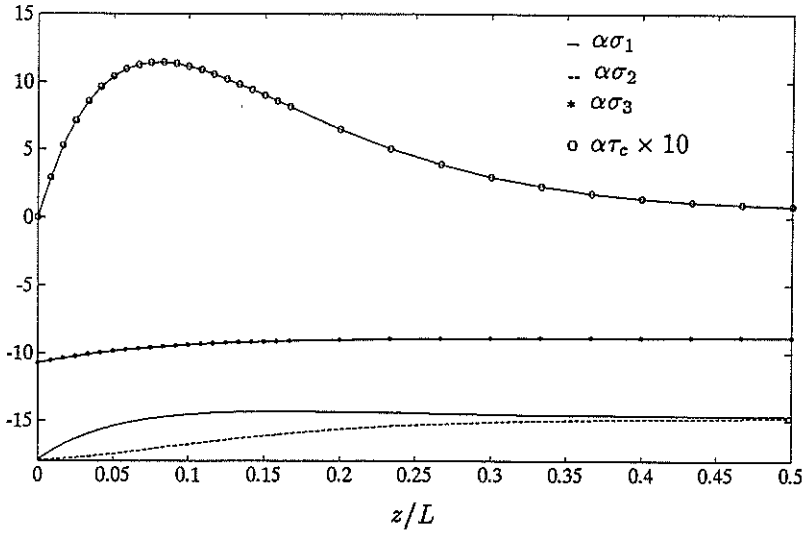

Figure 7.4: $\alpha\sigma_1$, $\alpha\sigma_2$, $\alpha\sigma_3$, $\alpha\tau_c$, at $x/L = 0.875$

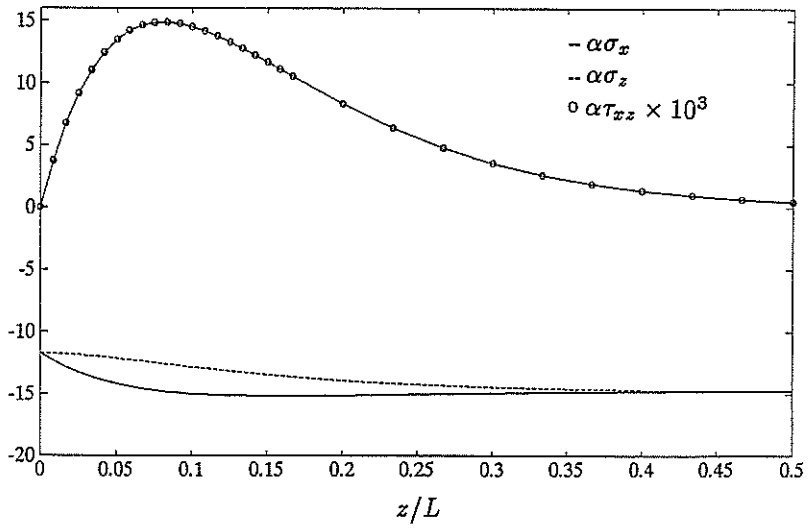

Figure 7.5: $\alpha\sigma_x$, $\alpha\sigma_z$, $\alpha\tau_{xz}$, at $x/L = 0.625$

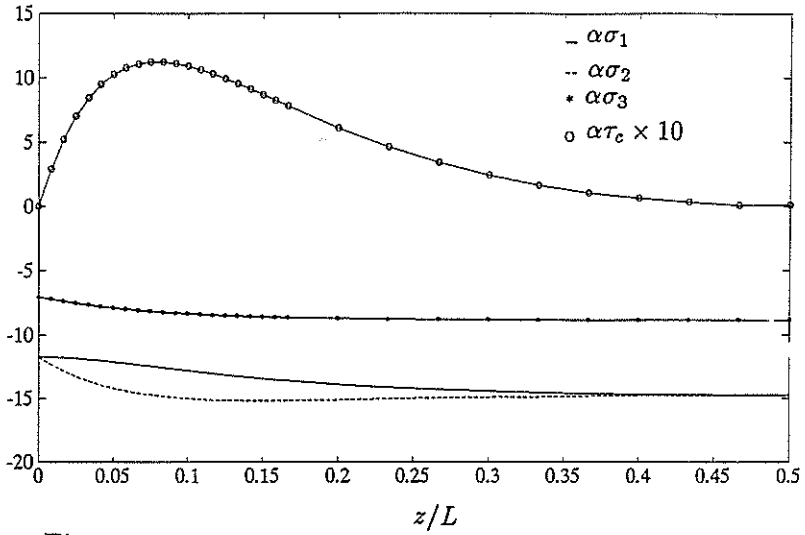

Figure 7.6: $\alpha\sigma_1$, $\alpha\sigma_2$, $\alpha\sigma_3$, $\alpha\tau_c$, at $x/L = 0.625$

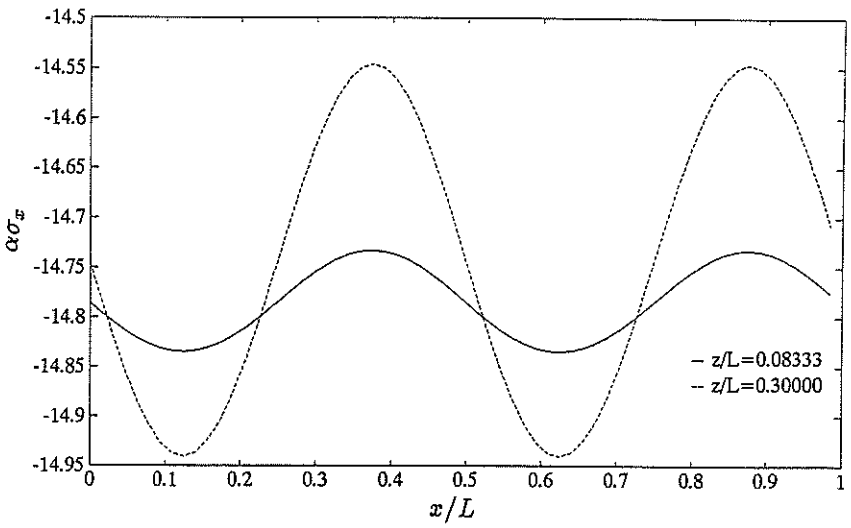

Figure 7.7: $\alpha\sigma_x$, vs. x/L, at $z/L = 0.0833$, and $z/L = 0.3$

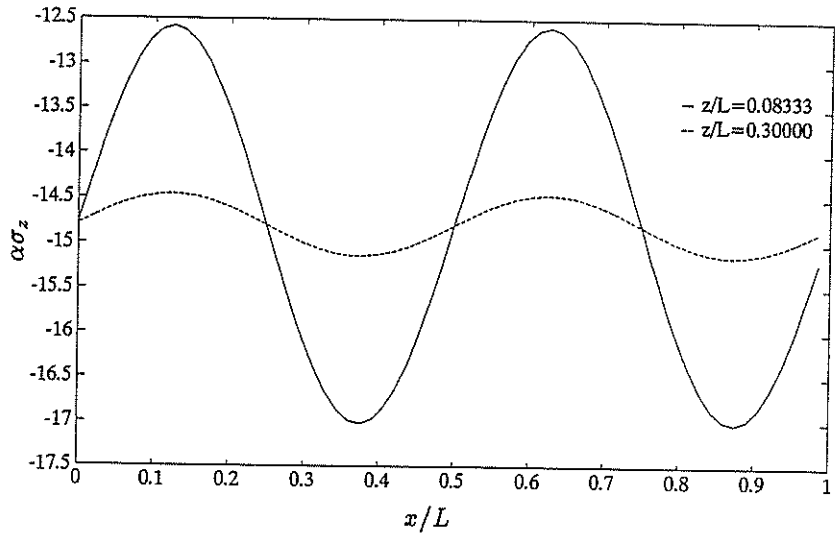

Figure 7.8: $\alpha\sigma_z$, vs. x/L, at $z/L = 0.0833$, and $z/L = 0.3$

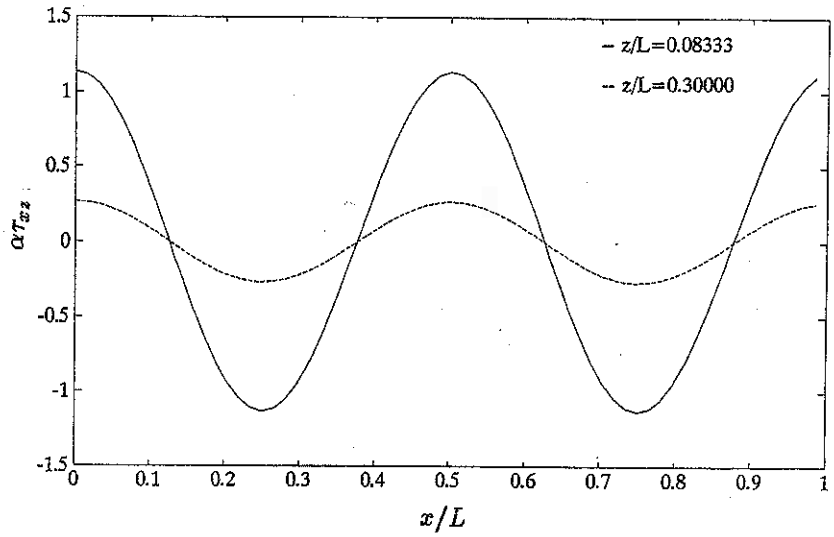

Figure 7.9: $\alpha\tau_{xz}$, vs. x/L, at $z/L = 0.0833$, and $z/L = 0.3$

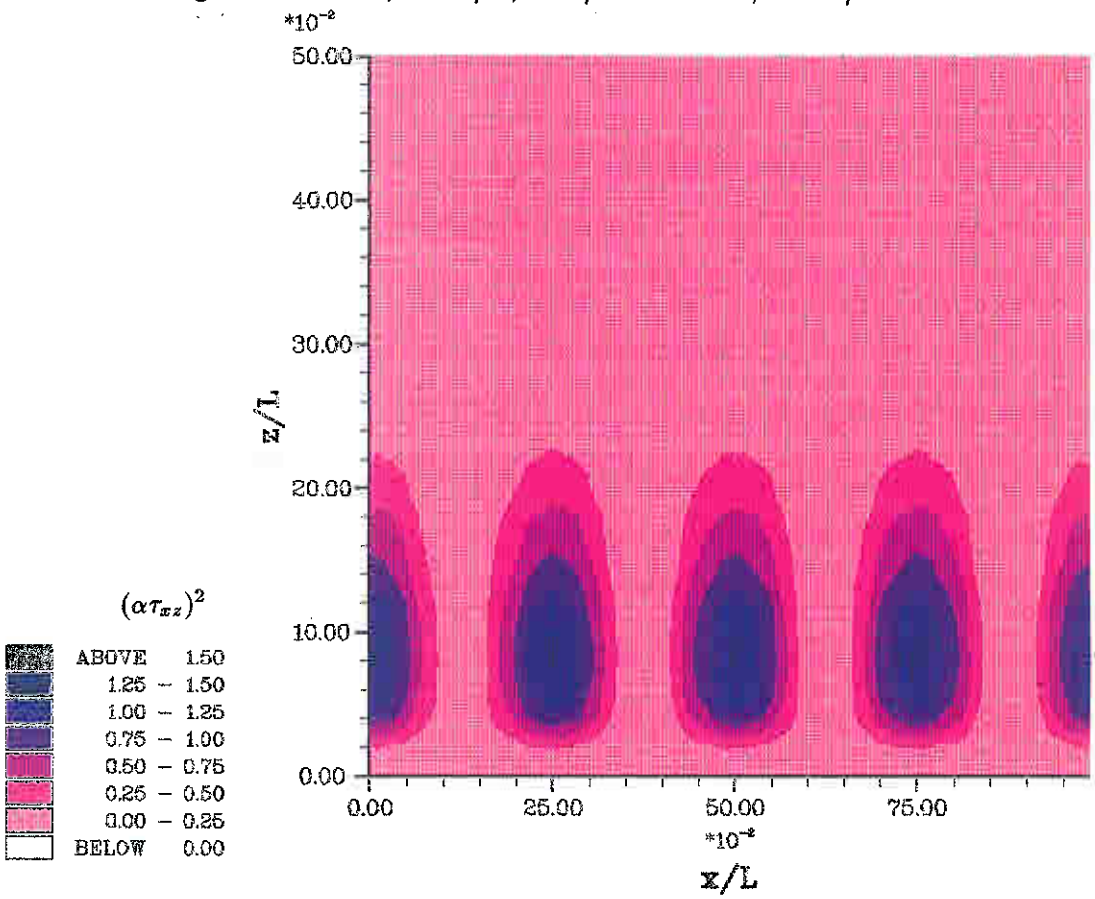

Figure 7.10: 2-D plot of $(\alpha\tau_{xz})^2$. Wavy pressures

b).- Subsurface stresses for a real roughness pressure distribution (Fig. 5.12).

Figs. 7.11 and 7.12 show the dimensionless stresses $\alpha\tau_{xz}$, $\alpha\sigma_x$ and $\alpha\sigma_z$ distribution for a fixed location $x/L = 0.35$ and variable depth z/L. Their behaviour is similar to the wavy pressure case (Figs. 7.3 and 7.5). Fig. 7.11 shows that the maximum value for the

shear stress τ_{xz} appears at $z/L \approx 0.0035$, it can be compared with the 2-D plot of $(\alpha\tau_{xz})^2$ Fig. 7.17 to find that the zone of high stresses is located more or less at the same depth.

In Figs. 7.13 and 7.14 the dimensionless stresses $\alpha\sigma_x$ and $\alpha\sigma_z$ (with standard deviation S and mean μ) have been plotted for $z/L = 0.0035$ (the high values zone for τ_{xz}).

Figs. 7.15 and 7.16 show again $\alpha\sigma_x$ and $\alpha\sigma_z$ but for a larger depth, $z/L = 0.02$. By comparing these figures with Figs. 7.13 and 7.14,the reduction of the standard deviation S and the disappearance of the high frequency components when the depth is increased is clear.

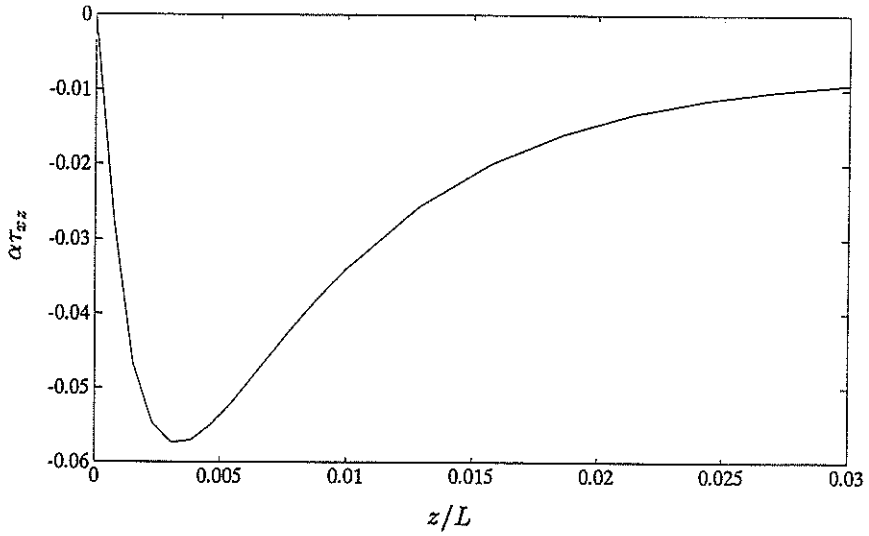

Figure 7.11: $\alpha\tau_{xz}$, at $x/L = 0.35$ as function of z/L

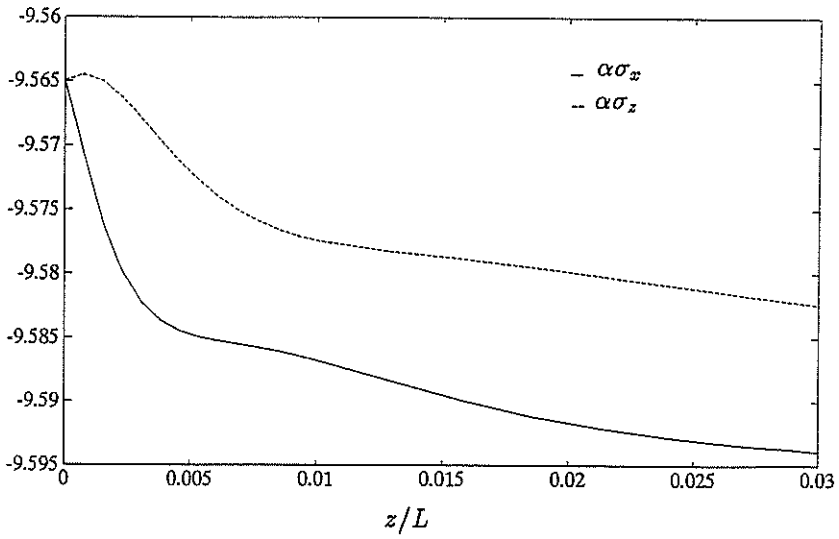

Figure 7.12: $\alpha\sigma_x$ and $\alpha\sigma_z$, at $x/L = 0.35$ as function of z/L

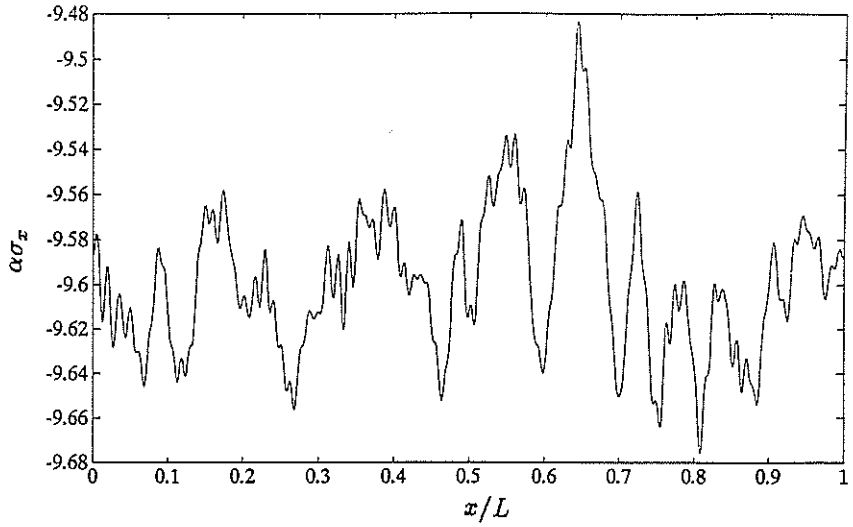

Figure 7.13: $\alpha\sigma_x$, at $z/L = 0.0035$ as function of x/L ($S = 0.0324$, $\mu = -9.599$)

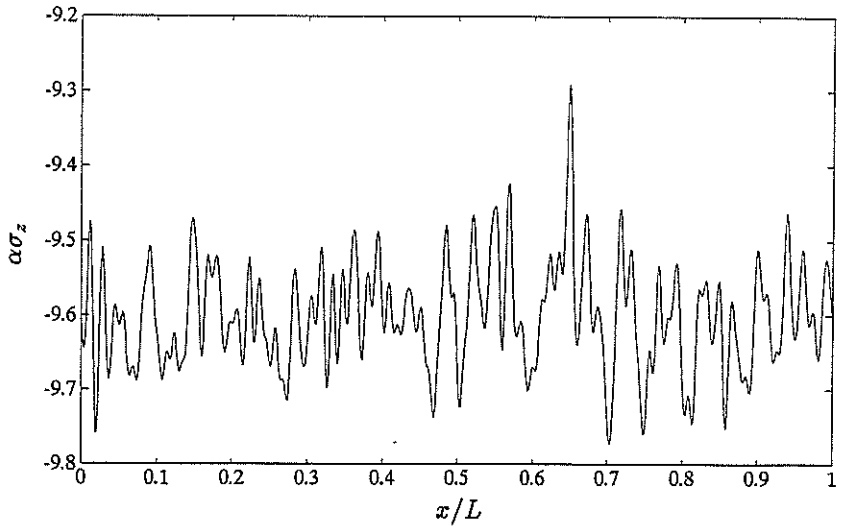

Figure 7.14: $\alpha\sigma_z$, at $z/L = 0.0035$ as function of x/L ($S = 0.0703$, $\mu = -9.60$)

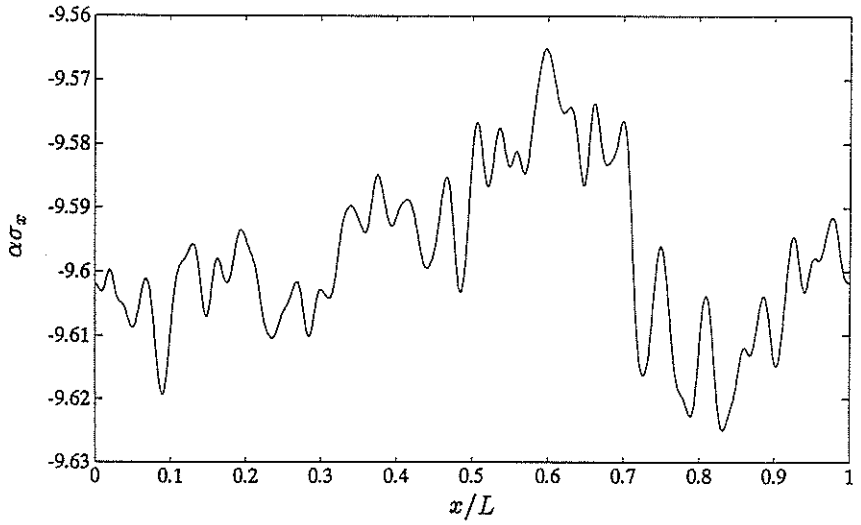

Figure 7.15: $\alpha\sigma_x$, at $z/L = 0.0200$ as function of x/L ($S = 0.013$, $\mu = -9.597$)

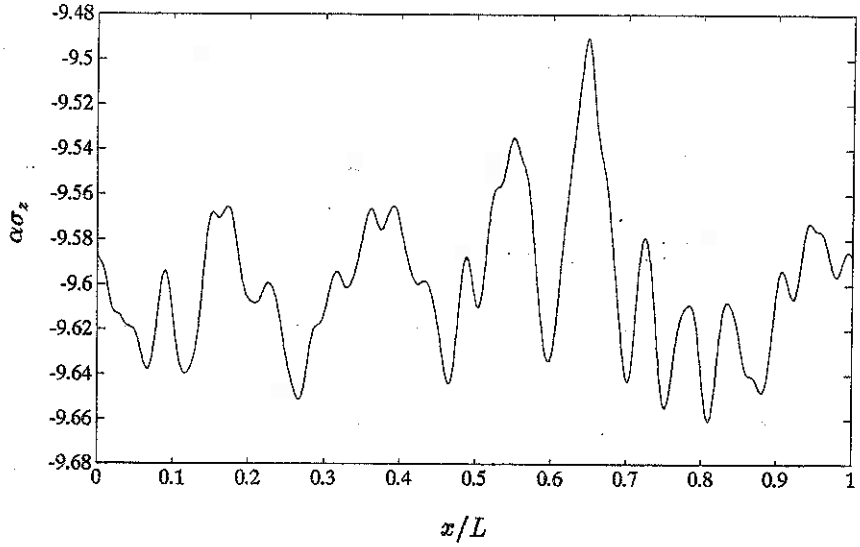

Figure 7.16: $\alpha\sigma_z$, at $z/L = 0.0200$ as function of x/L ($S = 0.0322$, $\mu = -9.60$)

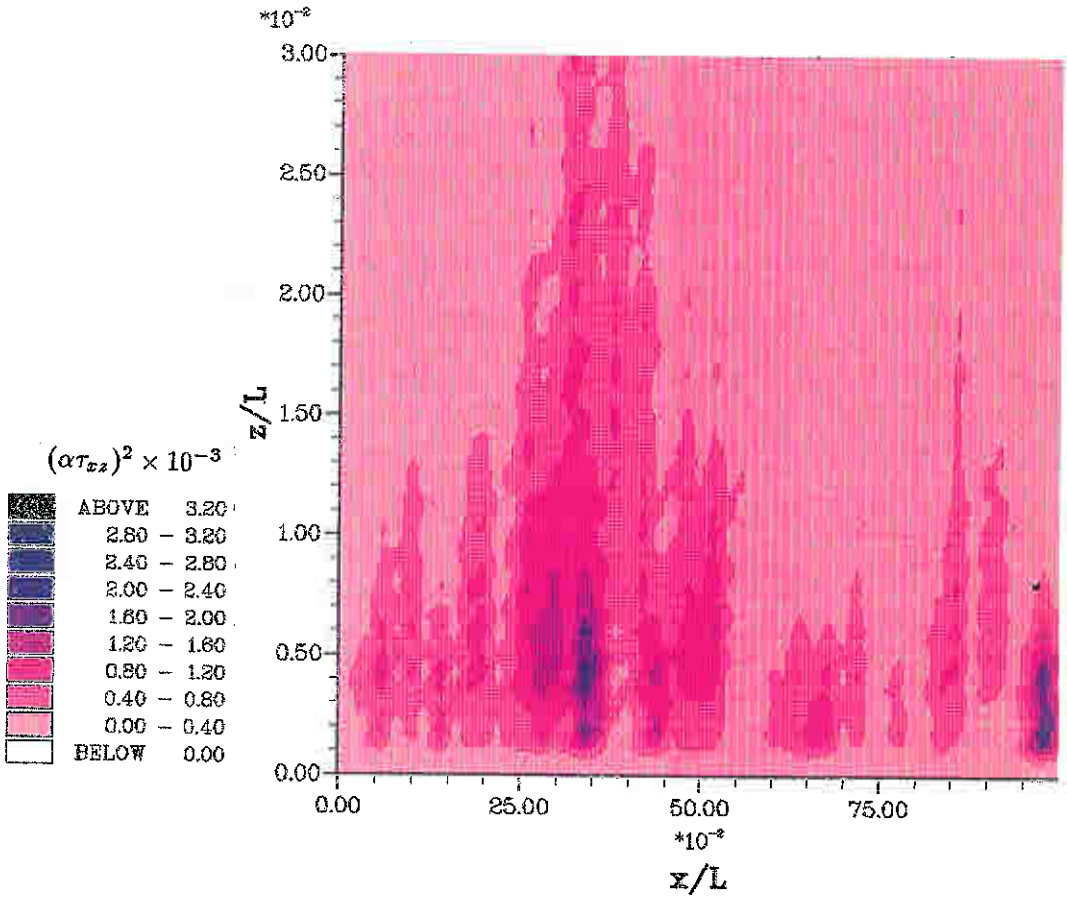

Figure 7.17: 2-D plot of $(\alpha\tau_{xz})^2$. Real roughness pressures

7.3 Elastic Shakedown Under Repeated Loading

In three-dimensional state of stresses, two standard criteria to assess whether plastic deformation is going to occur are due to Tresca and von Mises. The first one assumes the deformation to be elastic if:

$$max \left\{ \begin{array}{l} |\sigma_1 - \sigma_2| \\ |\sigma_2 - \sigma_3| \\ |\sigma_3 - \sigma_1| \end{array} \right\} < 2k \tag{7.5}$$

And von Mises criterion assumes elastic deformation if:

$$(\sigma_x - \sigma_y)^2 + (\sigma_y - \sigma_z)^2 + (\sigma_z - \sigma_x)^2 + 6(\tau_{xy}^2 + \tau_{yz}^2 + \tau_{xz}^2) < 6k^2 \tag{7.6}$$

where k is the yield stress in pure shear.

However, considering a practical application of contacts under repeated loading, e.g. roller bearings, the bodies in contact resist many repeated passages of the load. If the first pass produces some plastic deformation in some points of the bodies it also introduces residual stresses. When the load passes again the material will be subjected to the combined stress fields of the stresses due to the load and the residual ones left by the previous pass. In general the residual stresses are protective, thus they normally make it more difficult for yield to occur. In some cases after a few passes the residual stresses have been built up to such a degree that only elastic deformation is produced by subsequent passages of the load. This self protecting mechanism is known as *shakedown* under repeated loading.

To investigate whether in the case of an elastic cylinder, rolling freely on an elastic-perfectly-plastic half space shakedown occurs, it is convenient to follow Johnson [41] 1987. Notice that in dry contacts only the rolling condition produces negligible shear tractions, however, in lubrication even sliding produces negligible shear tractions.

According to Johnson the condition to avoid continously plastic deformation is:

$$\tau_{xz} \leq k \tag{7.7}$$

and the attention will be focused on the orthogonal shear stress τ_{xz}.

7.4 Normality Test for the Orthogonal Shear Stress

Looking at Figs. 7.13 to 7.16 where the cartesian stresses corresponding to the real pressures example are shown, it is clear that at any given depth they must be some sort of random variable.

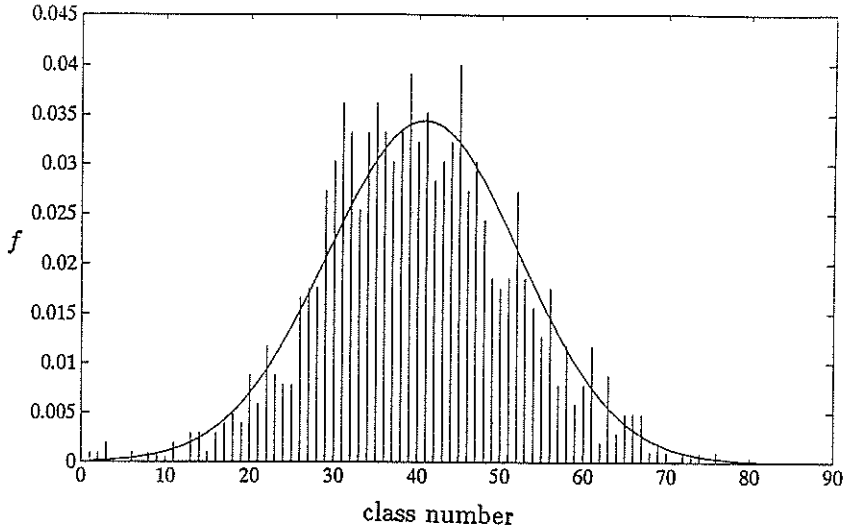

Figure 7.18: Histogram for $\alpha\tau_{xz}$, at $z/L = 0.001$, $sk = 0.07$, $ku = 3.24$

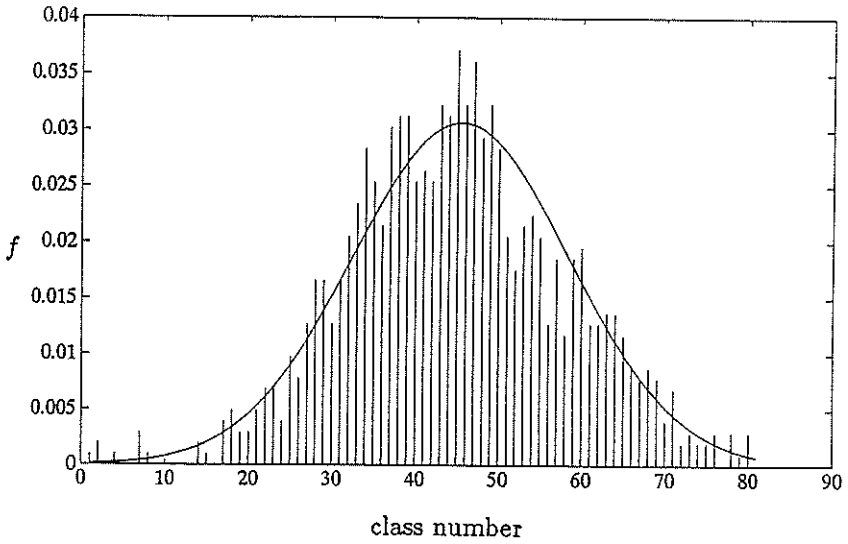

Figure 7.19: Histogram for $\alpha\tau_{xz}$, at $z/L = 0.0035$, $sk = 0.0208$, $ku = 3.085$

In Chapter 5 the micro-EHL pressure distribution for a real roughness contact was obtained from an assembly of an 'infinite' number of sinusoidal functions (as suggested by Fourier theory), so that by the Central Limit Theorem these pressures are expected to be a Gaussian variable and the stresses must also be Gaussian at least at small depths below the surface. Therefore it is interesting, specially for the case of τ_{xz}, to investigate whether it really behaves like a Gaussian variable in order to apply the standard rules for

assessing the largest expected value attained.

In order to test the 'Normality' of the variable τ_{xz} it is convenient to plot some of its histograms at different values of of the depth z and compare them with the Normal distribution curve scaled in such a way that its area equates the area of the histogram (area of the histogram = 1).

The scaled Normal density function would be:

$$f(x) = F_N \exp[-\frac{1}{2}(\frac{x-\mu}{S})^2] \tag{7.8}$$

where: F_N =is a coefficient selected to match the areas.

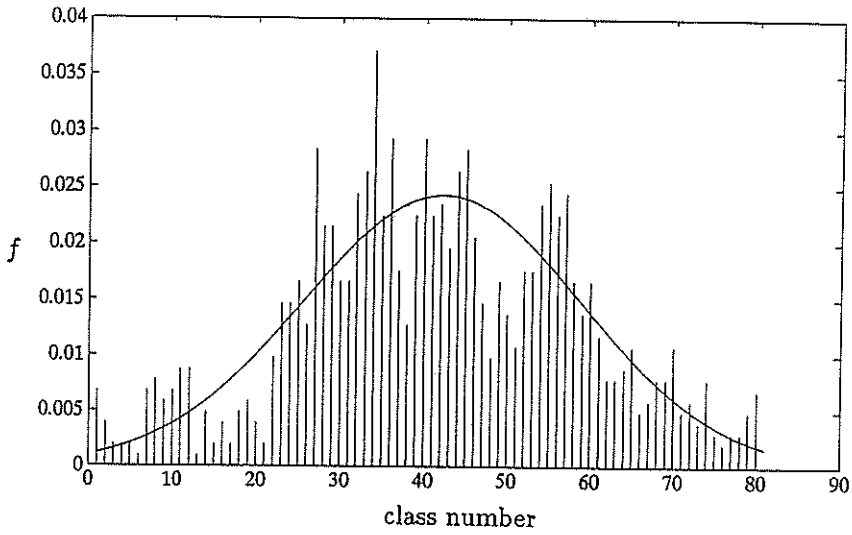

Figure 7.20: Histogram for $\alpha\tau_{xz}$, at $z/L = 0.02$, $sk = -.042$, $ku = 2.69$

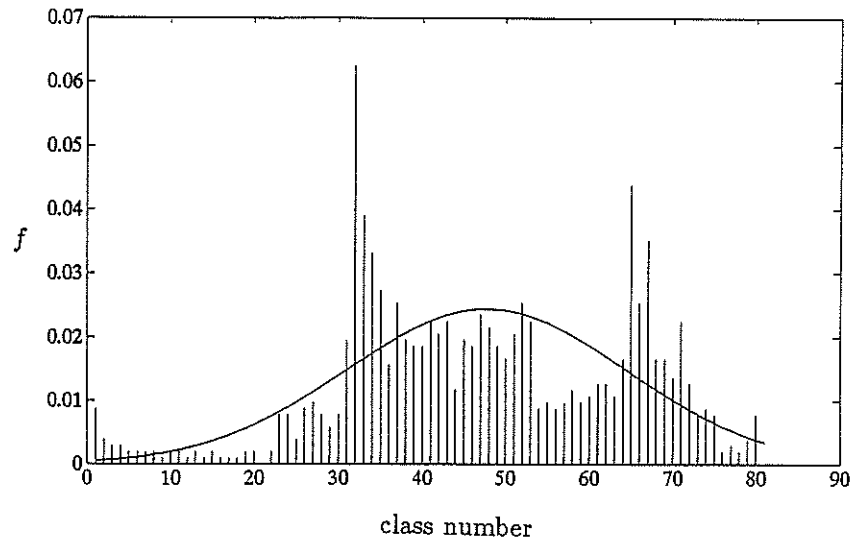

Figure 7.21: Histogram for $\alpha\tau_{xz}$, at $z/L = 0.04$, $sk = -0.237$, $ku = 2.69$

It is also convenient to calculate from the histogram parameters like the skewness (sk) and the kurtosis (ku) and compare them with the known values for the Normal distribution ($sk = 0$, $ku = 3$).

Figs. 7.18 to 7.21 show the histograms at different depths z/L for $\alpha\tau_{xz}$ of the same real pressure example. It is possible to see that in the two first cases (small z) Figs. 7.18 and 7.19 the variables $\alpha\tau_{xz}$ are quite Gaussian, their skewness and kurtosis are very close to the Gaussian values. However, when the depth increases (Figs. 7.20 and 7.21) the histograms began to be non-Normal, also the values of the skewness and kurtosis diverge from the Gaussian values.

This behaviour is explained since it has been seen that increasing z has the same effect as filtering the high frequency components of the stresses, so at the end, only low frequencies remain, therefore the histogram is 'one-sided'.

Similar tests were carried out to the remaining cartesian and principal stresses finding similar behaviour as $\alpha\tau_{xz}$; they are also Normal for small z.

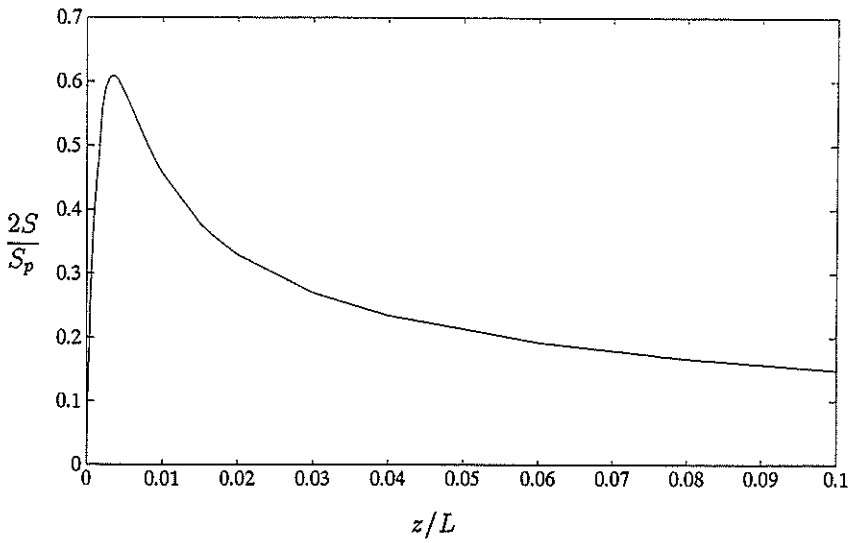

Figure 7.22: Standard deviation ratio ($2S/S_p$)of $\alpha\tau_{xz}$ vs. z/L

7.5 Largest Value Attained

Since it has been proved that for small values of the depth z, the orthogonal stress τ_{xz} is a Gaussian variable, then the standard $2S$ and $3S$ confidence limits (where S is the standard deviation of $\alpha\tau_{xz}$) can be used to asses the expected largest values under the shakedown criterion under repeated loading.

Figs. 7.23 and 7.24 show the plots of $\alpha\tau_{xz}$ at two depths below the surface for the same real pressures example. S_p is the standard deviation of the surface pressures αp, for this example $S_p = 0.089$.

Fig. 7.22 shows the variation of $2S/S_p$ with depth z/L and suggests that the maximum stress τ_{xz} will probably occur at $z/L = 0.0035$ with a 5 percent probability of the value $0.61S_p$ being exceeded.

Comparing Fig. 7.22 with the 2-D plot of Fig. 7.17 it is possible to observe a good agreement in the location of the zone of maximum stress.

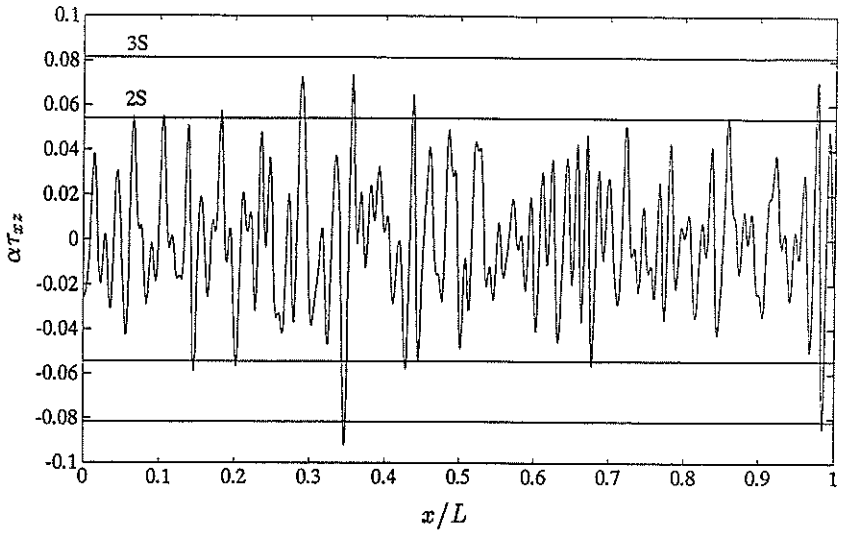

Figure 7.23: $\alpha\tau_{xz}$, at $z/L = 0.0035$, $S = 0.0271$

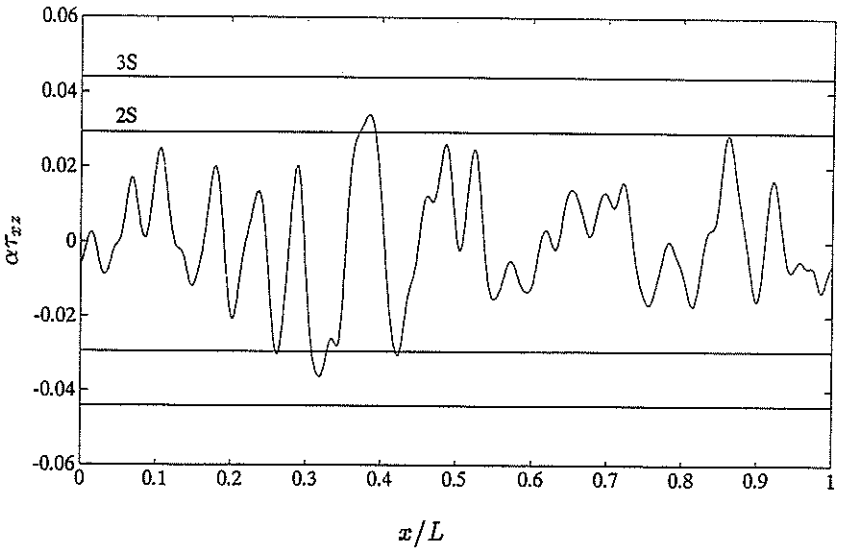

Figure 7.24: $\alpha\tau_{xz}$, at $z/L = 0.0200$, $S = 0.0147$

7.6 Conclusions

The subsurface stresses for a micro-EHL line contact with wavy and 'real' pressures have been calculated by assuming an elastic half-space and by ignoring the over-all EHL geometry. The scheme used is based on the idea of superimposing the stresses calculated for each of the sinusoidal components of the micro-EHL pressure in addition to the mean pressure.

The following conclusion can be obtained:

a).- For real roughness EHL contacts, the orthogonal subsurface shear stress at small depths was shown to be a Gaussian variable.

b).- Once having proved that the internal stresses under real roughness pressures are Gaussian variables, it is always possible to apply the standard $2S$ and $3S$ confidence limits to asses the maximum expected value. For instance, in Fig. 7.22, if $\alpha k = 0.61 S_p$, there is 5 percent of probability that τ_{xz} exceeds k and shakedown no longer occurs. Notice that the maximum stress is given statistically by a probability and by an approximate depth of location, rather than by a specific value and location x,z.

c).- The shear stresses always show a maximum value zone below but very close to the surface. This zone of high stresses is related only to the surface roughness.

d).- When the depth below the surface is increased and after the zone of maximum stresses the standard deviation of the stresses and the high frequency components are reduced.

CHAPTER EIGHT

TRANSIENT ANALYSIS OF SURFACE WAVINESS IN MICRO-EHL

In Chapters 5 and 6 some analyses concerned with the behaviour of transverse roughness in micro-EHL line contacts have been described. However, those analyses are only complete for the pure sliding situation in which the rough surface is stationary and the smooth surface is moving.

Unfortunately, in the real world most EHL contacts, e.g. gears, cams, roller bearings, etc. involve combinations of sliding and rolling and in any case the rough surfaces are not stationary. Therefore to complete the analysis, it is necessary to include the transient effects also. In this chapter a contribution on the understanding of the physical phenomenon of transient micro-EHL is made.

Transient micro-EHL investigations have been carried out only recently due to the complexity of computational and experimental resources required. Perhaps the first transient analysis of surface irregularities in EHL was made by Lee and Cheng [47] 1973, but the assumptions made limit very much their results. Later analyses (some of them including non-Newtonian fluids) have been made by Chang et al. [10] 1989, Xiaolan and Linqing [82] 1989, Lee and Hamrock [50] 1990.

Transient analyses of single asperities as well as of one wavy surface in EHL for a Newtonian fluid were made by Venner [75] 1991, Venner et al. [77] 1991 and Venner and Lubrecht [76] 1992. And the simulation of two-sided surface waviness has been carried out by Lubrecht and Venner [53] 1992. Experiments with surface irregularities in transient situations have been also carried out, e.g. Kaneta et al. [44] 1992.

However, the physical understanding of the behaviour of surface irregularities in EHL

is just beginning to emerge. Venner [75] 1991 states that in heavily loaded transient EHL contacts, since the viscosity is very high, the solution of the Reynolds equation reduces to $h \approx h(x - \bar{u}t)$, so consequently the film thickness irregularities caused by surface features e.g. indentation, bumps, waviness, etc. travel with the average velocity of the lubricant $\bar{u}$, regardless the velocity of which the surface feature itself moves. This has interesting consequences specially for sliding situations. For example, consider the case where the two surfaces are moving with different velocity and a dent or a bump located on the surface is moving with the lower velocity. In the Hertzian region of the contact, since $h \approx h(x - \bar{u}t)$, the changes in the film thickness induced by the feature upon its entrance to the Hertzian region will be propagated through the contact with the average velocity. This implies that the effects are propagated faster than the feature itself travels through the contact. Venner also concludes that the pressure disturbances travel with the velocity of the feature which generates them. So for the contrary case, where the feature moves with higher velocity than the average velocity of the lubricant, a delay in the film thickness respect to the pressures is observed.

In this chapter a theoretical investigation of the phenomenon is described bringing to light some interesting results. It is shown that the full transient solution of the micro-EHL problem is made of two parts: a) the moving steady state distribution of pressures and film thickness related to the squashing of the original roughness (particular integral), plus; b) a complementary function of film thickness which generates its own pressure distribution and which represents the film thickness modulation due to the roughness entering in the contact, so that its wavelength is directly related to the slide-roll ratio. Therefore the Venner's conclusions of film thickness disturbances travelling with $\bar{u}$ and pressure disturbances with u, become just a special case of a more general understanding of the phenomenon.

The importance of the inlet in determining the amplitude of the film and pressures modulations is now clear. Every time that a roughness ripple enters into the contact it produces a reduction and later an increase of the film thickness at that particular point, so the entering lubricant flow is modulated in the same way, producing disturbances of film and pressure which will be transported with the average velocity of the lubricant (according to the arguments of Venner). However, this is only one part of the phenomenon; these modulations are added to the deformed shape and corresponding pressures produced

by the steady state squashing of the roughness, and the result of this sum is the transient shape and pressure distributions. Therefore for special cases (Venner's examples) where the 'steady state' situation produces very much deformed shapes with large pressure ripples, the complete transient solution will appear having the film thickness produced by the inlet modulations (large amplitude) and moving with $\bar{u}$ together with the pressure ripples from the steady state solution (large amplitude) and moving with the velocity of the rough surface.

Once again, to facilitate the analysis the real contact with maximum Hertz pressure p_o is replaced by an infinitely long contact with known mean film thickness $\bar{h}$ and mean pressure taken to be equal to p_o. The Reynolds-Eyring equation is linearised and solved by using finite differences.

Firstly, the moving steady state solution will be obtained for both cases: one and two-sided surface sinusoidal roughness using Newtonian and Eyring fluids. This solution predicts satisfactorily the distribution of pressures and in the case of two-sided surface roughness also the deformation; but does not predict the current film thickness.

Secondly, the complementary function from the inlet is included in the case of one-sided sinusoidal roughness and the effects of varying the slide-roll ratio and the rheology of the lubricant in the full transient solution are shown. However, since the contact is considered to be infinitely long (the full EHL contact geometry is not considered), no natural way to include the inlet modulation of the film thickness exists, therefore the analysis requires an assumption about the amplitude of this modulation, from which the solution for the wavelength is then obtained.

8.1 The Physical Phenomenon

Moving roughness in EHL contacts produces modifications in the film thickness and pressures which are important to understand in order to model the situation. In these cases, the inlet of the contact plays a major role in the modulation of the amplitude and wavelength of the final shape.

Consider an EHL contact with the upper rough surface moving with velocity u_2 and the lower smooth surface moving with velocity u_1 as shown in Fig. 8.1. To deform the original roughness a pressure distribution has to build up, just as in the steady state and this pressure will travel with the velocity of the original roughness u_2 and will modify

the film thickness which will also travel at u_2. However, the roughness at the inlet of the contact is much less deformed than down stream (because of the lower pressures), and every time that a roughness ripple enters into the contact it will produce a variation in the film thickness at the inlet affecting the lubricant flow, and generating in this way a film thickness disturbance which will be transported down stream at the average velocity of the lubricant. Such film thickness disturbances will necessarily generate corresponding pressure disturbances also travelling at $\bar{u}$. Finally the film disturbances will be added to the moving steady state film thickness and the same will occur to the pressure disturbances, see Fig. 8.1.

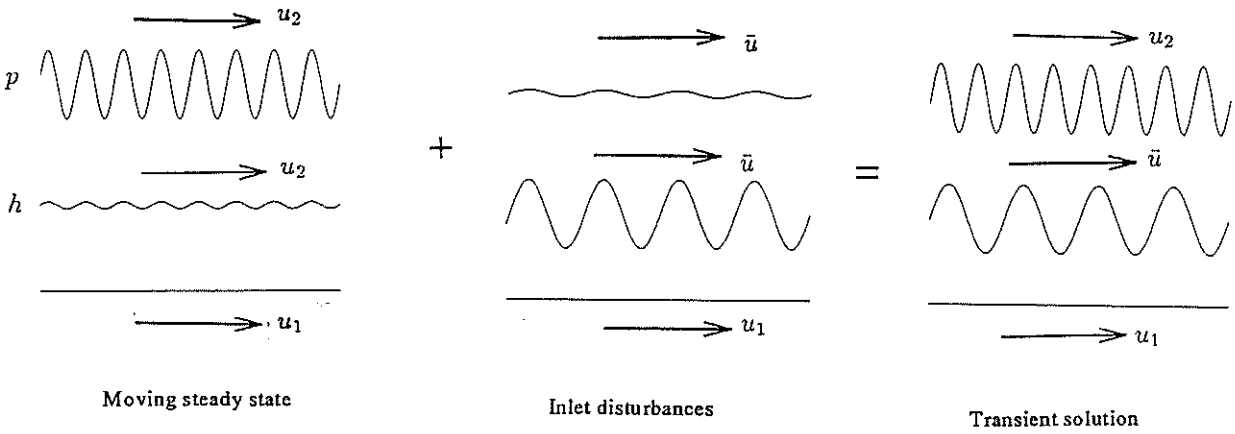

Figure 8.1: Final transient pressures and film thickness

Notice that in Fig. 8.1 the moving steady state solution associates small film ripples with large pressure ripples, because in general the original roughness is very much deformed, resulting in large pressure amplitudes; whilst the inlet disturbances associate large film ripples with small pressure ripples, because in general the incompletely deformed inlet roughness produces large amplitude shape and small pressure ripples. However, this situation may change in cases where even in the central zone the original roughness is little deformed (due to its short wavelength or to non-Newtonian behaviour of the fluid).

In many heavily loaded contacts with relatively long-wavelength roughness and Newtonian fluid, the initial shape is very much deformed by the 'steady state' pressure ripples which have a large amplitude. For these cases, in the transient situation only the inlet modulation would be visible and therefore the conclusion already made by some authors, e.g. Venner and Lubrecht [76] 1992 that final pressures travel at u_2 whilst film thickness travels at $\bar{u}$, is essentially correct. However, in cases where the initial roughness is not so

much deformed by the steady state pressures, so that the shape is of the same order as the inlet disturbances, the results are different.

What is also completely clear is that the wavelength of the inlet modulations of the film thickness and pressure will depend directly on the average velocity of the lubricant and therefore on the slide-roll ratio.

For pure rolling where there is no relative velocity between the two surfaces and $\bar{u} = u_2 = u_1$ the inlet disturbances will have the same wavelength as the initial roughness, and they may change the phase and the amplitude of the final shape but not its wavelength.

However, when the rough surface travels with higher velocity than the smooth one, then the film thickness and pressure modulations due to the inlet will have a shorter wavelength than the initial roughness. Finally, for the case when the rough surface travels with lower velocity than the smooth surface, the inlet disturbances will have larger wavelength than the initial roughness.

The geometry and velocity of the final shape and pressures will depend on the amplitude of both the inlet disturbances and the steady state shape and pressures.

8.2 The Transient Reynolds Equation

The Reynolds equation for line contacts including the squeeze term has been introduced in Section 2.1.5 for Newtonian fluids. However, a more general equation which includes Eyring fluids is equation 2.12:

$$\frac{\partial}{\partial x}\left(\frac{\rho h^3}{\eta} D \frac{\partial p}{\partial x}\right) = 12\bar{u}\frac{\partial(\rho h)}{\partial x} + 12\frac{\partial(\rho h)}{\partial t}$$

where D is the non-Newtonian correction factor defined in Section 2.1.7.

It is important to recognise the components of the film thickness when rough surfaces are in movement. For this new situation the film thickness $h(x,t)$ is given by the addition of the mean film thickness $\bar{h}$, the elastic displacements $v(x,t)$ and the moving initial roughness, see Fig. 8.2:

$$h(x,t) = \bar{h} + v(x,t) - z_2(x - u_2 t) - z_1(x - u_1 t) \tag{8.1}$$

and the film thickness is now a function of the location x and the time t. In equation 8.1,

$v(x,t)$ represents the combined elastic displacements of the two surfaces and is related to the 'steady state' pressure ripples.

Throughout this analysis the average film thickness $\bar{h}$ will be assumed constant in time. However, a more complex analysis should remove this assumption; for example consider a finite contact which in a particular instant of time carries the total load distributed in say, 5 positive and 4 negative pressure ripples, an instant later, the contact may carry the same load with 4 positive and 5 negative pressure ripples. This of course produces a variation of the mean pressure and therefore a variation of the mean film thickness.

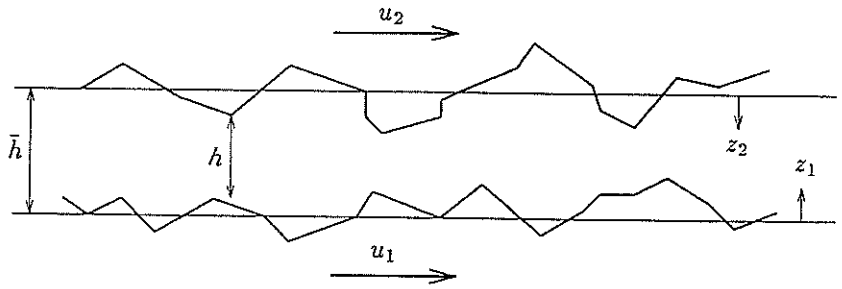

Figure 8.2: Film thickness in moving rough surfaces

8.2.1 Linearised Reynolds Equation

By writing $r = \rho h/\rho_o$ and $\hat{B} = \frac{rDh^2}{12\eta}$, equation 2.12 can be written as:

$$\frac{\partial r}{\partial t} = \frac{\partial}{\partial x}(\hat{B}\frac{\partial p}{\partial x}) - \bar{u}\frac{\partial r}{\partial x} \tag{8.2}$$

the linearisation is based on the assumption that the viscosity is high (high pressures) therefore $\hat{B}$ is small so that it can be considered to be constant and given by the mean values of its parameters: η_m, $\bar{h}$, r_m; D will have different values according to the rheology of the lubricant.

a).- Eyring Lubricant

When the pressure and film thickness variations are small and the mean pressure is high, it was shown in Section 6.2.1 that: $D \approx (|s|\eta\bar{u})/(h\tau_o)$, therefore $\hat{B}$ becomes:

$$\hat{B} = \frac{r_m\bar{h}\bar{u}|s|}{12\tau_o} \tag{8.3}$$

b).- Newtonian Lubricant

For Newtonian lubricants, the situation is different, $D = 1$ and:

$$\hat{B} = \frac{r_m \bar{h}^2}{12\eta_m} \tag{8.4}$$

It is important to point out that the Eyring linearisation is valid for moderately large pressure ripples but the Newtonian one only for rather small ripples. This is in fact useful since for Newtonian fluids $\hat{B}$ is very small ($\hat{B} \approx 0$) so it simplifies even more equation 8.4.

Finally, the linearised transient equation can be written as:

$$\frac{\partial r}{\partial t} + \bar{u}\frac{\partial r}{\partial x} = \hat{B}\frac{\partial^2 p}{\partial x^2} \tag{8.5}$$

A further simplification can be done in equation 8.5. The density ratio equation, following Section 6.2.2 can be linearised to give:

$$\frac{\bar{\rho}}{\bar{\rho}_m} \approx \alpha C_o \Delta p + 1$$

where C_o is given by:

$$C_o = \frac{\gamma - \beta}{\alpha(1 + \beta p_o)(1 + \gamma p_o)}$$

and $\bar{\rho}_m$ is the mean of the density ratio $\bar{\rho} = \rho/\rho_o$.

Therefore:

$$r = h\bar{\rho} \approx \bar{\rho}_m(h + h\alpha C_o \Delta p)$$

with small film thickness variations:

$$r \approx \bar{\rho}_m(h + \bar{h}\alpha C_o \Delta p)$$

therefore:

$$\frac{\partial^2 p}{\partial x^2} = \frac{1}{\bar{h} C_o \alpha \bar{\rho}_m}\left[\frac{\partial^2 r}{\partial x^2} - \bar{\rho}_m \frac{\partial^2 h}{\partial x^2}\right] \tag{8.6}$$

Substituting equation 8.1 with: $\hat{C} = 1/(\bar{h}\alpha C_o \bar{\rho}_m)$ and $v(x) = \hat{A}\Delta p$, where $\hat{A} = \frac{2\lambda}{\pi E'}$ gives:

$$\frac{\partial^2 p}{\partial x^2} = \frac{\hat{C}}{1 + \hat{C}\hat{A}\bar{\rho}_m}\left[\frac{\partial^2 r}{\partial x^2} - \bar{\rho}_m \frac{\partial^2 z_2}{\partial x^2} + \bar{\rho}_m \frac{\partial^2 z_1}{\partial x^2}\right] \tag{8.7}$$

Finally substituting equation 8.7 into equation 8.5:

$$\frac{\partial r}{\partial t} = C_T \left[\frac{\partial^2 r}{\partial x^2} - \bar{\rho}_m \frac{\partial^2 z_2}{\partial x^2} + \bar{\rho}_m \frac{\partial^2 z_1}{\partial x^2} \right] - \bar{u} \frac{\partial r}{\partial x} \tag{8.8}$$

where:

$$C_T = \frac{\hat{B}\hat{C}}{1 + \hat{C}\hat{A}\bar{\rho}_m}$$

Equation 8.8 is a form of equation 8.5 which can be solved by using finite differences.

8.3 Steady State Moving Solution

In this section two finite difference methods to solve equation 8.8 for r will be described. The schemes do not account for the inlet disturbances of real transient micro-EHL yet, but they form the basis of a more complete solution to follow.

8.3.1 Explicit Method

In this scheme the time derivatives will be discretized using forward differences and the space derivatives using central differences. The dashed variables (r', z_1', z_2', etc) will represent values at the present step of time, the undashed variables (r, z_1, z_2, etc) will represent values at the previous step of time.

The subscript j will represent the grid index in x direction. So:

$$\frac{\partial r}{\partial t} = \frac{r_j' - r_j}{\Delta t} \; ; \quad \frac{\partial^2 r}{\partial x^2} = \frac{r_{j+1} - 2r_j + r_{j-1}}{(\Delta x)^2}$$

$$\frac{\partial r}{\partial x} = \frac{r_{j+1} - r_{j-1}}{2\Delta x} \; ; \quad \frac{\partial^2 z}{\partial x^2} = \frac{z_{j+1} - 2z_j + z_{j-1}}{(\Delta x)^2}$$

substituting these equations into equation 8.8 and solving for r_j':

$$r_j' = \frac{\Delta t}{(\Delta x)^2} C_T \{ r_{j+1} - 2r_j + r_{j-1} - \bar{\rho}_m [(z_2)_{j+1} - 2(z_2)_j + (z_2)_{j-1}] +$$

$$\bar{\rho}_m [(z_1)_{j+1} - 2(z_1)_j + (z_1)_{j-1}] \} - \frac{\bar{u}\Delta t}{2\Delta x} (r_{j+1} - r_{j-1}) + r_j \tag{8.9}$$

Equation 8.9 is an explicit formula for r_j' and it is completely defined for each value of j, except for the edges.

Consider that in x there are $n-1$ grid cells and n points, then assuming sinusoidal roughness: $(z_1)_0 = (z_1)_{n-1}$; $(z_1)_{n+1} = (z_1)_2$, equally $(z_2)_0 = (z_1)_{n-1}$; $(z_2)_{n+1} = (z_2)_2$.

However, the behaviour of r is unknown, and there are at least two possibilities:

a).- Since the roughness is cyclic, one could expect that r will be also cyclic at any time, thus:

$$r_0 = r_{n-1} \;\; ; \;\; r_{n+1} = r_2 \tag{8.10}$$

b).- At the edges r is free so an extrapolation is useful. Newton's backward extrapolation formula gives good results:

$$\begin{aligned} r_0 &= \tfrac{9}{2}[r_1 - 2r_2 + r_3] - \tfrac{3}{2}[r_1 - 4r_2 + 3r_3] + r_3 \\ r_{n+1} &= \tfrac{9}{2}[r_n - 2r_{n-1} + r_{n-2}] - \tfrac{3}{2}[r_n - 4r_{n-1} + 3r_{n-2}] + r_{n-2} \end{aligned} \tag{8.11}$$

In practice, equations 8.10 and 8.11 give the same steady state moving solution for r, which suggests that in fact the steady state r for sinusoidal roughness is cyclic. However, equations 8.11 will be useful for the full transient scheme where r is no longer cyclic.

It is important to point out that for the case of equal two-sided surface sinusoidal roughness, the explicit method is not self-starting. If at $t = 0$ the shapes are in phase (since h = constant, thus $r_{j+1} = r_{j-1} = r_j$ and $(z_2)_j = (z_1)_j$, so $r'_j = r_j$) and some other method must be used for this situation.

In general for Newtonian fluids the explicit method is numerically stable when Δx and Δt are small enough. For non-Newtonian fluids the stability is very much reduced. However, its application remains valid for calculating the boundary conditions in the implicit method when r is not cyclic.

8.3.2 Implicit Method

A much more stable solution of equation 8.8 is provided by a general implicit method. Consider that $\frac{\partial r}{\partial t}$ behaves linearly between the consecutive times $t-\Delta t$ and t, also consider that $\frac{\partial r}{\partial t}$ at a certain time $(t - \Delta t) + \theta\Delta t$ inside this interval (where $0 \leq \theta \leq 1$) can be approximated to $\frac{r'-r}{\Delta t}$, therefore using linear interpolation it is possible to show that:

$$\frac{r' - r}{\Delta t} = \theta(\frac{\partial r}{\partial t})' + (1 - \theta)\frac{\partial r}{\partial t} \tag{8.12}$$

This general equation of finite differences can be particularized according to the value of θ to produce different well known schemes; see Table 8.1; (e.g. Reddy [65] 1984).

value of θ	scheme in time	convergence
0	forward differences	conditionally stable
1/2	Crank-Nicholson	unconditionally stable
2/3	Galerkin	unconditionally stable
1	backward differences	conditionally stable

Table 8.1: Various schemes for the general implicit method

Choosing properly the value of θ it is possible to improve the numerical stability of the solution in any particular case. The most stable schemes are Crank-Nicholson and Galerkin but θ can take any other value if required (here it was used $\theta = 2/3$). For $\theta = 0$, equation 8.12 is reduced to the explicit method (forward differences in time).

For the implicit method, the following difference equations will be used:

$$\frac{\partial^2 r}{\partial x^2} = \frac{r'_{j+1} - 2r'_j + r'_{j-1}}{(\Delta x)^2}$$

$$\frac{\partial r}{\partial x} = \frac{r'_{j+1} - r'_{j-1}}{2\Delta x} \; ; \quad \frac{\partial^2 z}{\partial x^2} = \frac{z'_{j+1} - 2z'_j + z'_{j-1}}{(\Delta x)^2}$$

substituting these equations into equation 8.8 and then substituting the result into equation 8.12:

$$\theta Q_1[r'_{j+1} - 2r'_j + r'_{j-1}] + \theta Q_1 \bar{\rho}_m[(z_2)'_{j+1} - 2(z_2)'_j + (z_2)'_{j-1}] + \theta Q_1 \bar{\rho}_m[(z_1)'_{j+1} - 2(z_1)'_j + (z_1)'_{j-1}]$$

$$-\theta Q_2[r'_{j+1} - r'_{j-1}] + (1-\theta)Q_1[r_{j+1} - 2r_j + r_{j-1}] + (1-\theta)Q_1 \bar{\rho}_m[(z_2)_{j+1} - 2(z_2)_j + (z_2)_{j-1}]$$

$$+ (1-\theta)Q_1 \bar{\rho}_m[(z_1)_{j+1} - 2(z_1)_j + (z_1)_{j-1}] - (1-\theta)Q_2[r_{j+1} - r_{j-1}] - r'_j + r_j = 0 \quad (8.13)$$

where:

$$Q_1 = \frac{C_T \Delta t}{(\Delta x)^2} \; ; \quad Q_2 = \frac{\bar{u}\ \Delta t}{2\ \Delta x}$$

Equation 8.13 has been obtained for a point j, in the same way taking $j = 2$ to $n-1$, gives a linear system of equations:

$$[A]\{r'\} = [B]\{r\} + [C]\{z'_2\} + [C]\{z'_1\} + [D]\{z_2\} + [D]\{z_1\} \quad (8.14)$$

where the symbol [ ] represents matrices and the symbol { } vectors. For example:

$$[A] = \begin{bmatrix} A_1 & A_2 & A_3 & 0 & 0 & \dots & 0 & 0 & 0 \\ 0 & A_1 & A_2 & A_3 & 0 & \dots & 0 & 0 & 0 \\ 0 & 0 & A_1 & A_2 & A_3 & \dots & 0 & 0 & 0 \\ \vdots & \vdots & \vdots & \vdots & \vdots & \dots & \vdots & \vdots & \vdots \\ 0 & 0 & 0 & 0 & 0 & \dots & A_1 & A_2 & A_3 \end{bmatrix}_{(n-2)\times n}$$

and:

$$\{r'\} = \begin{Bmatrix} r'_n \\ r'_{n-1} \\ \vdots \\ r'_1 \end{Bmatrix}_{n\times 1}$$

where: $A_1 = \theta(Q_1 - Q_2)$; $A_2 = -(2\theta Q_1 + 1)$; $A_3 = \theta(Q_1 + Q_2)$

similarly:

$$B_1 = (1-\theta)(Q_2 - Q_1) \; ; \quad B_2 = 2(1-\theta)Q_1 - 1 \; ; \quad B_3 = -(1-\theta)(Q_1 + Q_2)$$

$$C_1 = -\theta Q_1 \bar{\rho}_m \; ; \quad C_2 = 2\theta Q_1 \bar{\rho}_m \; ; \quad C_3 = -\theta Q_1 \bar{\rho}_m$$

$$D_1 = -(1-\theta)Q_2 \bar{\rho}_m \; ; \quad D_2 = 2(1-\theta)Q_2 \bar{\rho}_m \; ; \quad D_3 = -(1-\theta)Q_2 \bar{\rho}_m$$

The right hand side of equation 8.14 can be reduced to a known vector $\{G\}$ and the system can be written as:

$$[A]\{r'\} = \{G\} \tag{8.15}$$

where $\{r'\}$ is the unknown vector for the present time values of r.

In order to be able to solve the system 8.15 the boundary conditions have to be specified. For sinusoidal roughness, once again: $(z_1)_1 = (z_1)_n$ and $(z_2)_1 = (z_2)_n$.

Now for the boundary values in $\{r'\}$ it is possible to follow at least two ways:

a).- Method 1: The variable r is assumed to be cyclic, so:

$$r_n = r_1 \; ; \quad r'_n = r'_1$$

and

$$r_{n+1} = r_2 \; ; \quad r'_{n+1} = r'_2$$

therefore in the system 8.15 one more equation is needed for the point $j = n$, which becomes:

$$\{A_1 \;\; A_2 \;\; A_3\} \begin{Bmatrix} r'_2 \\ r'_n \\ r'_{n-1} \end{Bmatrix} = \begin{Bmatrix} G_2 \\ G_n \\ G_{n-1} \end{Bmatrix}$$

and the equation for the point $j = 2$ then can be written:

$$\{A_1 \;\; A_2 \;\; A_3\} \begin{Bmatrix} r'_3 \\ r'_2 \\ r'_n \end{Bmatrix} = \begin{Bmatrix} G_3 \\ G_2 \\ G_n \end{Bmatrix}$$

so the new system of equations is:

$$\begin{bmatrix} A_2 & A_3 & 0 & 0 & \dots & 0 & A_1 \\ A_1 & A_2 & A_3 & 0 & \dots & 0 & 0 \\ 0 & A_1 & A_2 & A_3 & \dots & 0 & 0 \\ \vdots & \vdots & \vdots & \vdots & \dots & \vdots & \vdots \\ A_3 & 0 & 0 & 0 & \dots & A_1 & A_2 \end{bmatrix}_{(n-1)\times(n-1)} \begin{Bmatrix} r'_n \\ r'_{n-1} \\ \vdots \\ \vdots \\ r'_2 \end{Bmatrix}_{(n-1)\times 1} = \begin{Bmatrix} G_n \\ G_{n-1} \\ \vdots \\ \vdots \\ G_2 \end{Bmatrix}_{(n-1)\times 1} \tag{8.16}$$

where:

$$G_j = f[(z_1)'_j,\ (z_2)'_j,\ (z_1)_j,\ (z_2)_j,\ r_j]$$

Since the matrix $[A]$ is tri-diagonal with additional elements in the upper right corner (A_1) and the lower left corner (A_3), the system can be solved efficiently by using a modified Thomas algorithm, e.g. Hirsch [39] 1988.

b).- Method 2: The boundary conditions of $\{r'\}$ are free and can be calculated by using the explicit method with the extrapolation condition (equations 8.11) for r_0 and r_{n+1}. Then the values of r'_n and r'_1 will be known and the system 8.15 is reduced to:

$$\begin{bmatrix} A_2 & A_3 & 0 & 0 & \dots & 0 & 0 \\ A_1 & A_2 & A_3 & 0 & \dots & 0 & 0 \\ 0 & A_1 & A_2 & A_3 & \dots & 0 & 0 \\ \vdots & \vdots & \vdots & \vdots & \dots & \vdots & \vdots \\ 0 & 0 & 0 & 0 & \dots & A_1 & A_2 \end{bmatrix}_{(n-2)\times(n-2)} \begin{Bmatrix} r'_{n-1} \\ r'_{n-2} \\ \vdots \\ \vdots \\ r'_2 \end{Bmatrix}_{(n-2)\times 1} = \begin{Bmatrix} G_{n-1} - A_1 r'_n \\ G_{n-2} \\ \vdots \\ \vdots \\ G_2 - A_3 r'_1 \end{Bmatrix}_{(n-2)\times 1} \tag{8.17}$$

and it can be solved by using the unmodified Thomas algorithm for tri-diagonal systems.

For the moving steady state solution the answer obtained by using (a) is the same as the one from (b), which shows that the steady state r is indeed cyclic. However, (b) will be useful in the full transient solution when r is no longer cyclic.

8.3.3 The Solution for H and P

Once the solution for the variable r has been found, the analysis can be completed with the calculation of the film thickness and pressures. In this section the procedure to do this is described.

It was shown in Section 8.2.1 that from the linearised density ratio equation:

$$r = h\bar{\rho} \approx h\bar{\rho}_m[1 + C_o\alpha(p - p_o)] \tag{8.18}$$

therefore by substituting equation 8.1 into 8.18 with $v = \hat{A}\Delta p$:

$$r \approx [(\Delta p)^2(\alpha\hat{A}C_o) + \Delta p(\alpha C_o\bar{h} + \hat{A} + z_2\alpha C_o - z_1\alpha C_o) + z_2 - z_1 + \bar{h}] \tag{8.19}$$

and solving 8.19 for Δp:

$$\Delta p = \frac{-b + \sqrt{b^2 - 4ac}}{2a} \tag{8.20}$$

where:

$$b = \alpha C_o\bar{\rho}_m(\bar{h} + \frac{\hat{A}}{\alpha C_o} + z_2 - z_1)$$

$$c = \bar{\rho}_m(z_2 - z_1 + \bar{h}) - r$$

$$a = \alpha\hat{A}C_o\bar{\rho}_m$$

From equation 8.20 the pressure variations can be obtained and from them the density ratios calculated:

$$\bar{\rho}/\bar{\rho}_m \approx 1 + C_o\alpha\Delta p \tag{8.21}$$

Finally, the film thickness can be obtained by:

$$h = \frac{r}{\bar{\rho}} \tag{8.22}$$

8.3.4 Two-Sided Surface Roughness Results

a).- Newtonian Fluids

In order to show the results obtained for the case of two-sided surface roughness with Newtonian fluid it will be convenient to use perhaps the only example so far available in the literature: Lubrecht and Venner [53] 1992, which describes two sinusoidal surfaces moving with different velocities:

$E' = 2.20 \times 10^{11}$ Pa	$b = 5 \times 10^{-4}$ m
$\alpha = 2.2 \times 10^{-8}\ Pa^{-1}$	$\bar{u} = 0.97$ m/s
$\eta_o = 40 \times 10^{-3}$ Pa s	$\bar{h} = 0.355 \times 10^{-6}$ m
$R = 1.41 \times 10^{-2}$ m	$\lambda = 1.25 \times 10^{-4}$ m
$p_o = 2.0 \times 10^{9}$ Pa	$(z_2)_{max} = (z_1)_{max} = 0.25 \times 10^{-6}$ m
$s = -1 \ \ (u_1 = 3u_2)$	

Their results for film thickness and pressures are shown in Figs. 8.3 to 8.7, where: $T = t\bar{u}/b$, $P = p/p_o$, $H = hR/b^2$, $Z = zR/b^2$, $X = x/b$.

An interesting feature of Figs. 8.3 to 8.6 is that despite the movement of the undeformed roughness , the deformed shapes keep their relative phase. Fig. 8.7 shows the Lubrecht and Venner variation of pressure and film thickness with time for a fixed location at $x/b = 0.25$.

Fig. 8.7 before $T = 4.25$ shows a transition period where the roughness are entering into the contact (running-in), since the simulation started at $T = 0$ with the smooth surfaces and since $u_1 = 3u_2$, the roughness of the lower surface enters before the upper one and causes a sharp increase in the central film thickness and the first oscillations in pressure and film thickness. But after $T = 4.25$ the situation is steady.

In comparison with the previous results, the film thickness and pressure distributions corresponding only to the moving steady state solution obtained by the implicit method with cyclic boundary conditions are shown in Figs. 8.8 to 8.12.

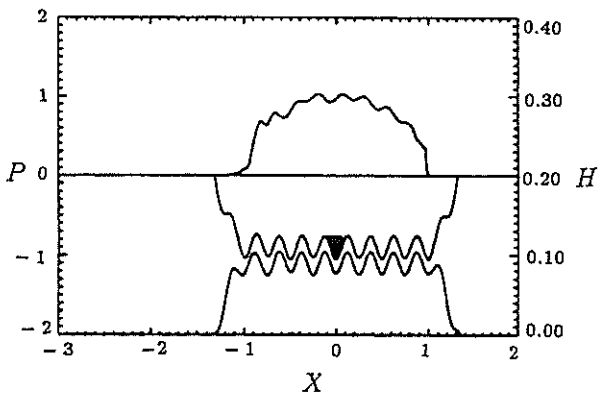

Figure 8.3: Pressures and film thickness for $T = 6.88$, from Lubrecht and Venner

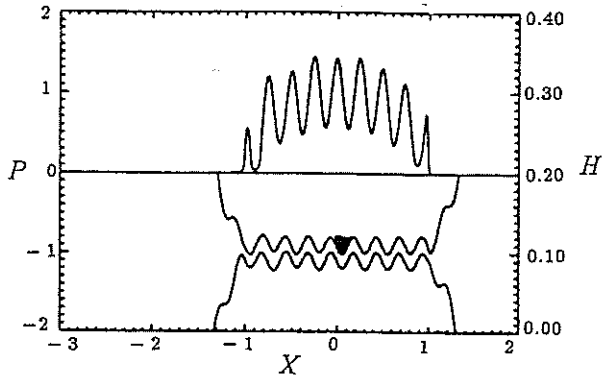

Figure 8.4: Pressures and film thickness for $T = 6.94$, from Lubrecht and Venner

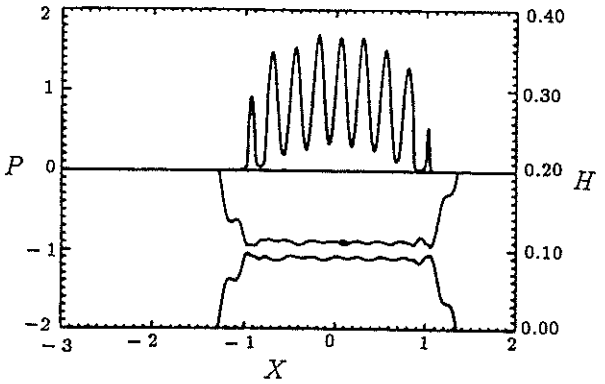

Figure 8.5: Pressures and film thickness for $T = 7.00$, from Lubrecht and Venner

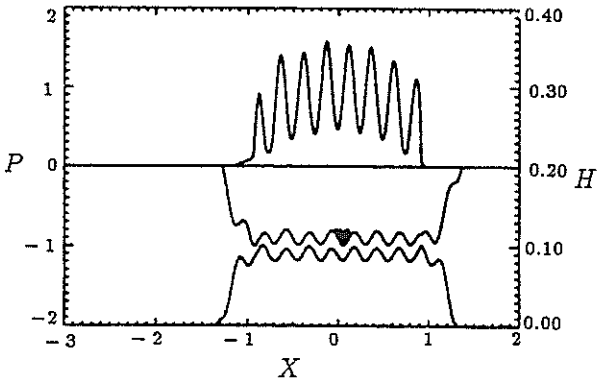

Figure 8.6: Pressures and film thickness for $T = 7.06$, from Lubrecht and Venner

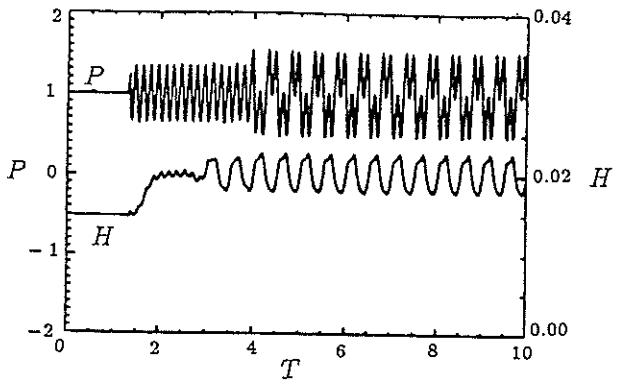

Figure 8.7: Pressures and film thickness for $x/b = 0.0$ as function of T, from Lubrecht and Venner

For the present analysis the simulation was started when both surfaces are in phase and the pressure variations are $P = 1$ (Fig. 8.8), just like Lubrecht and Venner Fig. 8.3. Now, Figs. 8.8 to 8.11 (for a better understanding) show two zones, from $x/b = -1$ to $x/b = 0$ represents the undeformed shapes, so the relative phase can be followed, and from $x/b = 0$ to $x/b = 1$ the deformed shapes and associated pressures are shown. Once again, despite the relative movement of the undeformed surfaces, the deformed ones still keep their original phase.

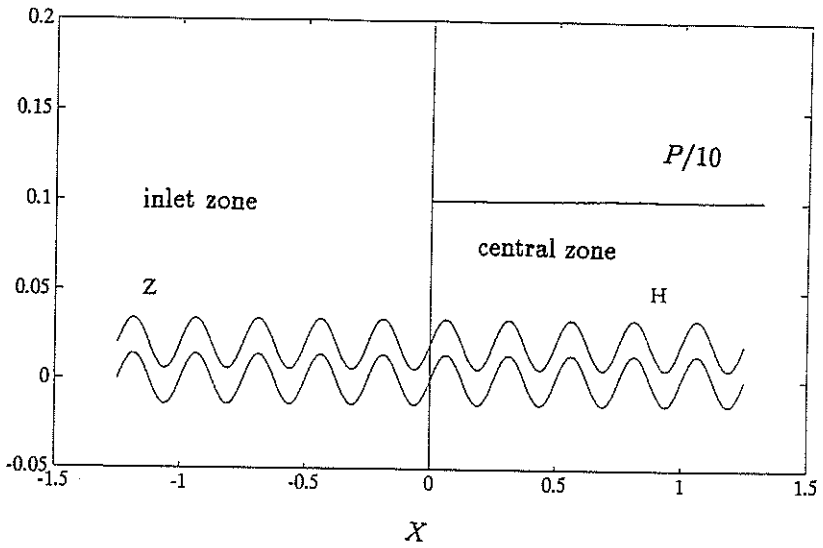

Figure 8.8: Pressures and film thickness for $T = 0.0$

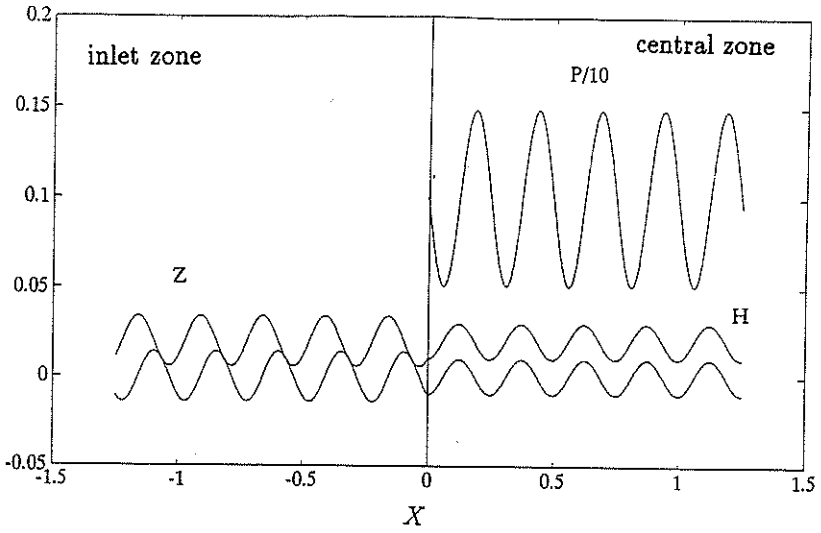

Figure 8.9: Pressures and film thickness for $T = 0.06$

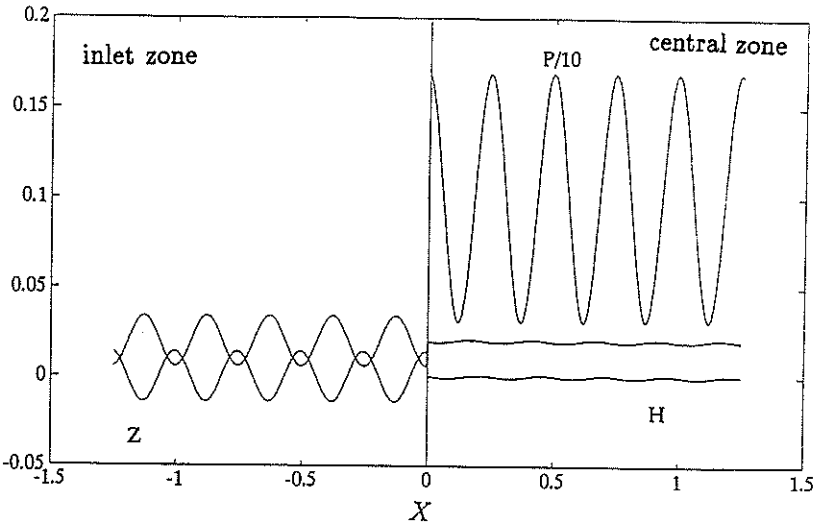

Figure 8.10: Pressures and film thickness for $T = 0.12$

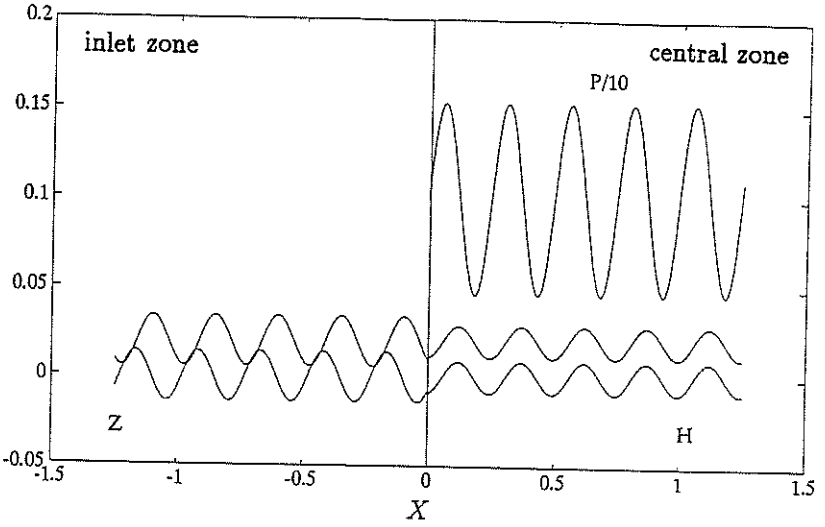

Figure 8.11: Pressures and film thickness for $T = 0.18$

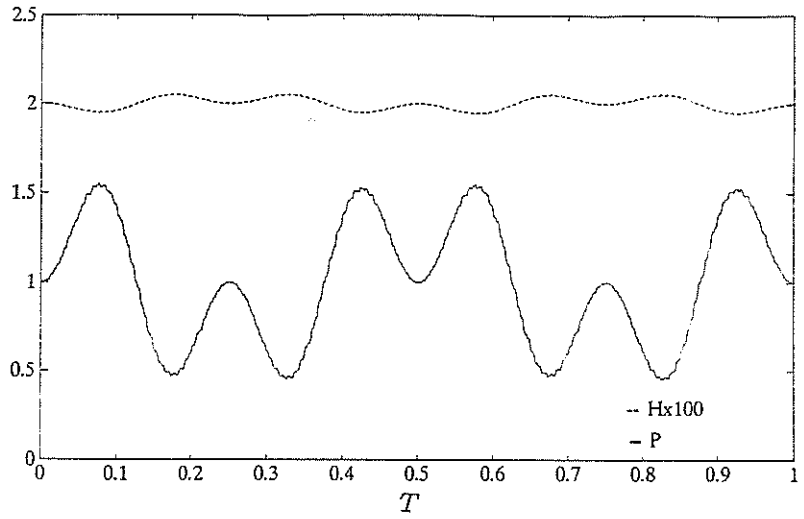

Figure 8.12: Pressures and film thickness for $x/b = -0.0625$ as function of T

The deformed shapes and pressures agree well with Lubrecht and Venner results Figs. 8.3 to 8.6 despite the incompleteness of the moving steady state solution.

Fig. 8.12 shows the film thickness and pressure distribution as a function of time T for a fixed point at $x/b = -.0625$ obtained with the implicit method. This figure may be compared with the Lubrecht and Venner results of Fig. 8.7 for times larger than $T = 4.25$. The pressures show very good agreement but the film thickness does not. In this comparison is clear that the inlet excitation cannot be neglected for the film thickness solution.

b).- Eyring Fluid

Using the implicit method and starting at $T = 0.0$ with the shapes in phase the following results were obtained for a compressible Eyring fluid ($\tau_o = 5 \times 10^6$ Pa).

Figs. 8.13 to 8.15 show smaller pressure ripples and less-deformed final shapes than their equivalent Newtonian cases Figs. 8.9 to 8.11. The deformed shapes do not keep their initial phase.

Fig. 8.16 shows a shift of phase between pressures and film thickness for the non-Newtonian fluid. This shift of phase is likely to be related to the steady state shift discussed in Chapter 5.

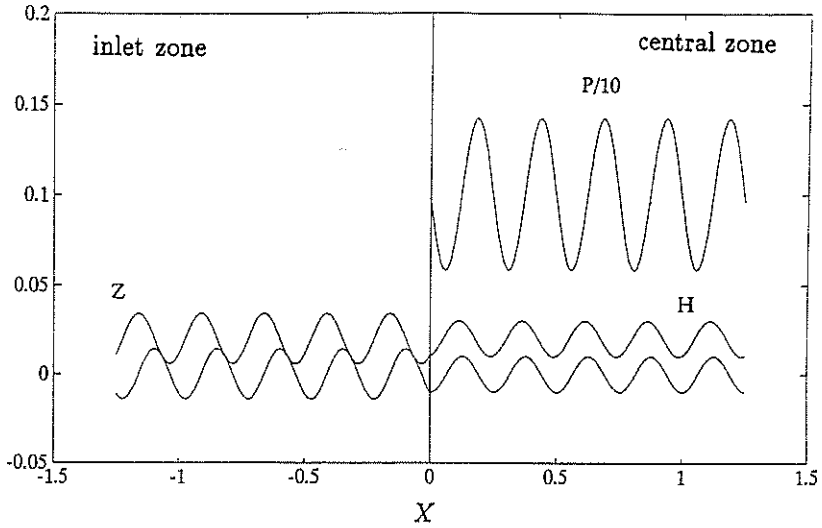

Figure 8.13: Pressures and film thickness for $T = 0.06$, Eyring fluid

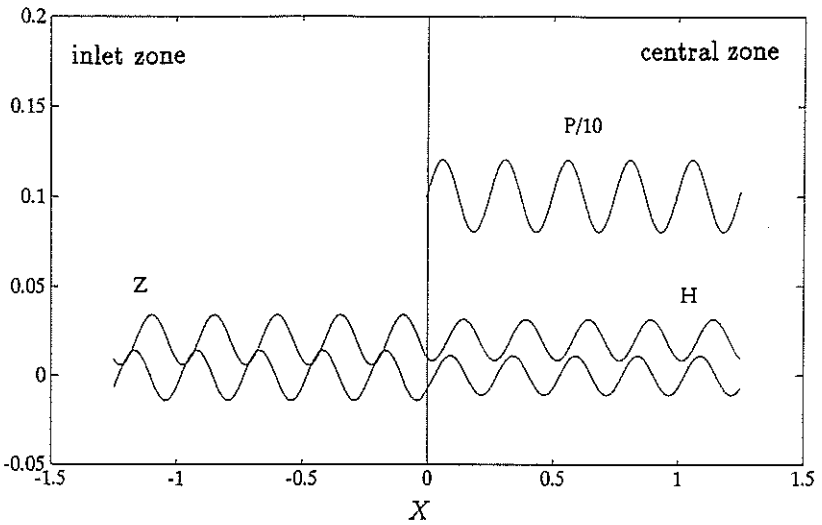

Figure 8.14: Pressures and film thickness for $T = 0.12$, Eyring fluid

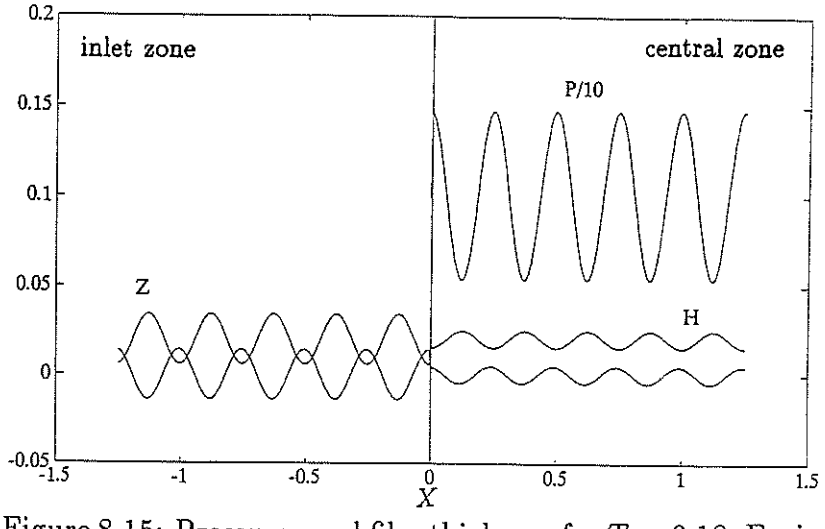

Figure 8.15: Pressures and film thickness for $T = 0.18$, Eyring fluid

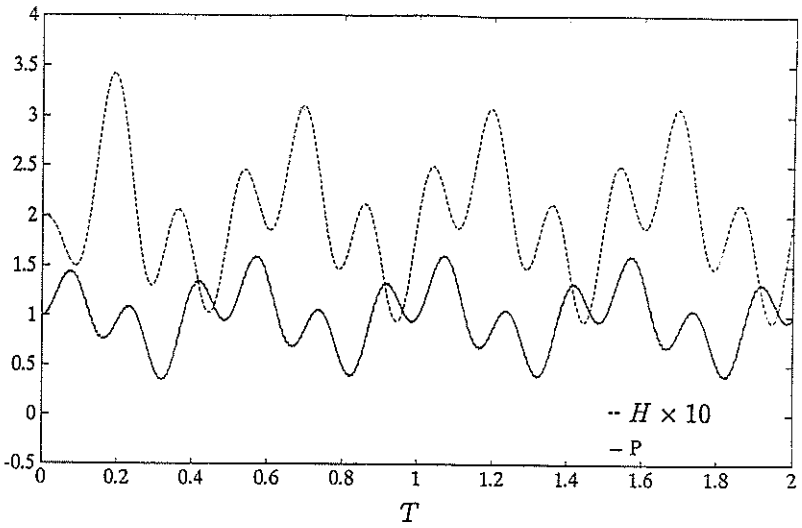

Figure 8.16: Pressures and film thickness for $x/b = 0.0625$, Eyring fluid

8.4 One-Sided Surface Roughness Results

In the condition of two-sided surface roughness it was relatively simple to invent some initial conditions for the simulation, since it was shown that after some running-in time the situation becomes steady and it was simpler to start the simulation with the two surfaces in phase.

However, for the case of one rough surface and the other smooth, there are at least two choices to start the simulation with; despite the fact that when the steady state condition is reached the result is the same.

a).- Steady state solution (s=-2) as initial condition:

This initial condition was chosen by Venner and Lubrecht [76] 1992 to solve the following example:

$$\bar{u} = 0.745 \text{ m/s}$$
$$\bar{h} = 0.30 \times 10^{-6} \text{ m}$$
$$\lambda = 2.5 \times 10^{-4} \text{ m}$$
$$(z_1)_{max} = 0.5 \times 10^{-6} \text{ m}$$

with the remaining parameters unchanged. Again $T = t\bar{u}/b$, $P = p/p_o$, $H = hR/b^2$, $Z = zR/b^2$, and $X = x/b$.

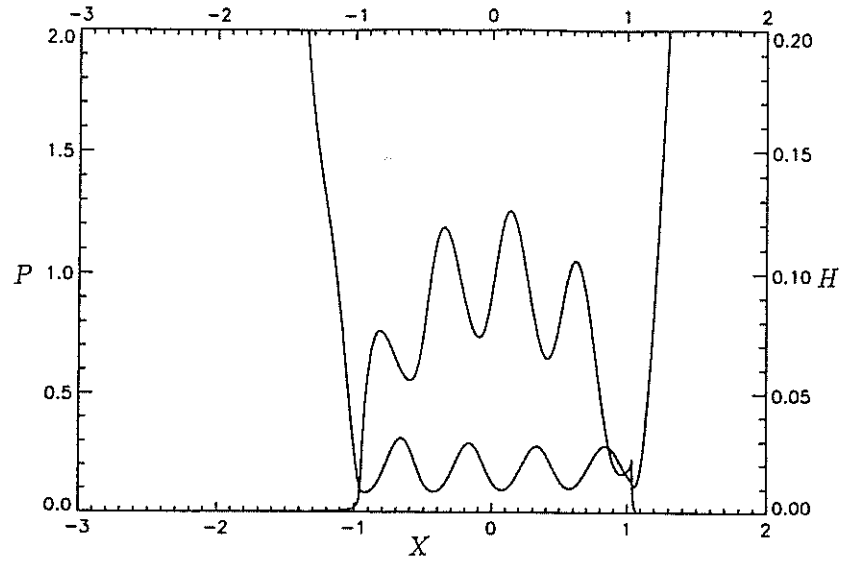

Figure 8.17: Pressures and film thickness for the case $s = 0$, from Venner and Lubrecht

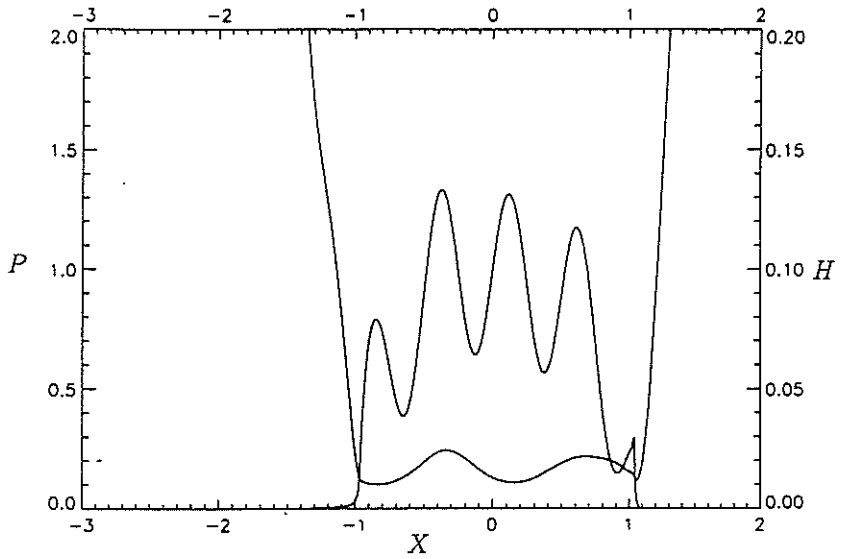

Figure 8.18: Pressures and film thickness for the case $s = -1$, from Venner and Lubrecht

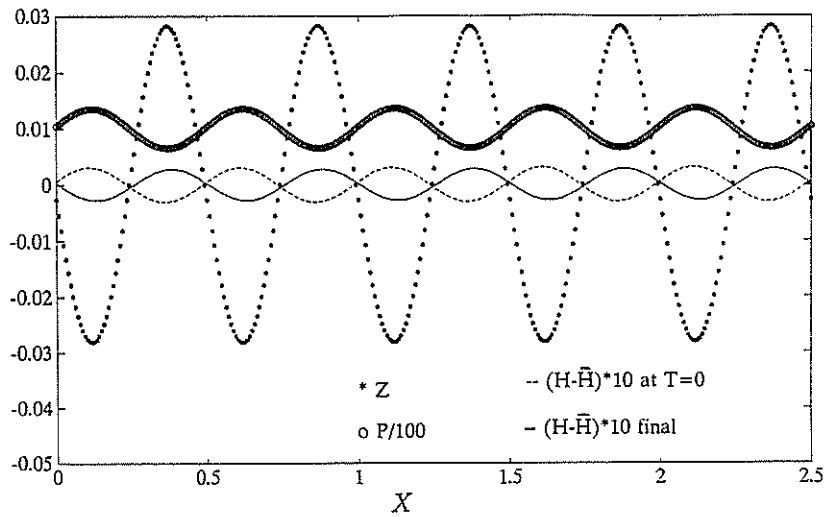

Figure 8.19: Pressures and film thickness for $T = 1.5$ and $s = -1$

Their results for two different slide-roll ratios ($s = 0$ and $s = -1$) and compressible Newtonian fluid are shown in Figs. 8.17 and 8.18, where the film thickness and pressures are shown.

Using for example the TPVBP method of Section 6.3 it is possible to obtain the steady state solution for the given example with $s = -2$ (pure sliding with the rough upper surface stationary). This solution now will be used as the initial condition with the implicit method and free boundary conditions to obtain the moving steady state solution of the Venner and Lubrecht example. The pressures and film thickness after a time $T = 1.5$ are given in Fig. 8.19.

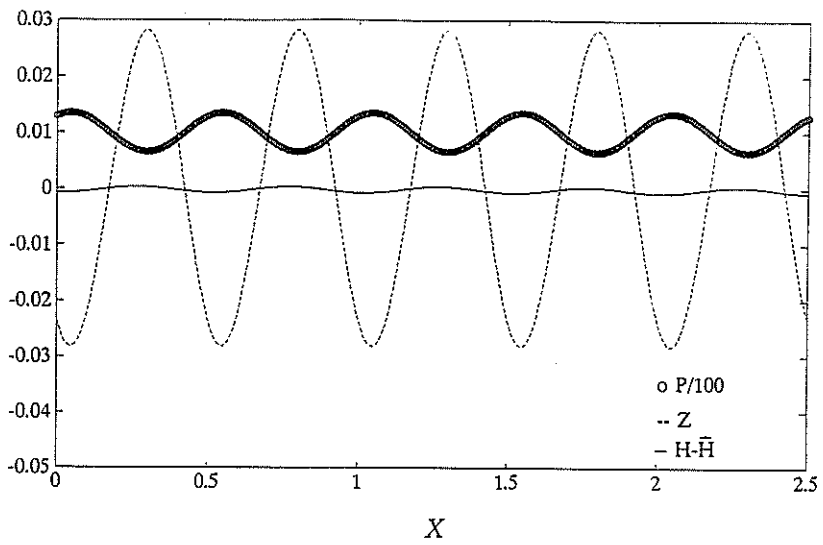

Figure 8.20: Steady State Pressures and film thickness for the case $s = 0$ at $T = 24.7$, starting with the undeformed shape

Fig. 8.19 shows clearly that after a certain time the steady state solution has been transported downstream without changing the amplitude or wavelength of the film thickness. This solution does not agree with the corresponding Venner and Lubrecht case of Fig. 8.18. So it is clear that there is some additional effect from the inlet which must be considered.

b).- Undeformed Shape as Initial Condition

It is interesting to observe the deformation process of the initial roughness in time without considering the effects of the inlet. This is perhaps the only way to see the effects of the squeeze term in the Reynolds equation under moving steady state conditions.

By taking the undeformed shape as the initial condition, after a time $T = 3500\Delta T$ where $\Delta T = 0.00705$, the Newtonian steady state solution is reached, see Fig. 8.20.

Fig. 8.21 shows the corresponding plot for pressures and film thickness as a function of time for the location $x/b = -.0625$. This makes clear the transitory state of the deformation and the build up of pressure.

8.5 The Full Transient Solution

So far solutions for one and two-sided sinusoidal surfaces have been obtained without accounting for the contact inlet effects. It was shown that the steady state moving solutions agreed well with Lubrecht and Venner results for the pressure distribution (and in the case of two-sided surface roughness for the final shape also) but the analysis cannot predict the amplitude and frequency of the film thickness.

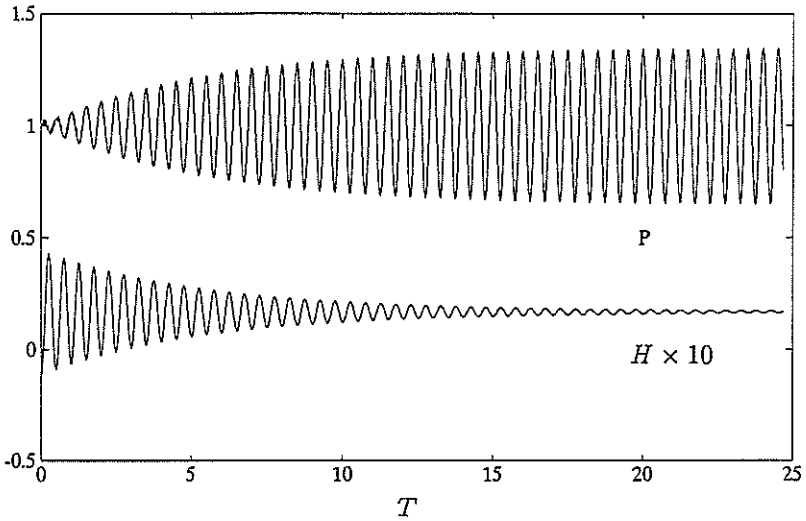

Figure 8.21: Transitory Pressures and film thickness for the case $s = 0$, starting with the undeformed shape

The full transient solution of a micro-EHL contact can be regarded as made of two separate solutions: the moving steady state solution and a complementary function accounting for the inlet modulation of pressures and film thickness which are transported down stream with the average velocity of the lubricant.

8.5.1 The Excitation Function

For the case of sinusoidal initial roughness it is reasonable to expect sinusoidal inlet disturbances of film and pressure, and therefore also sinusoidal disturbances are expected in the variable $r = h\bar{\rho}$ acting at the left hand side boundary (inlet) of the x interval ($j = 1$). An excitation function $r_1 = f(t)$ will be imposed with a frequency determined by the velocity of the wavy surface (u_2).

$$r_1' = r_m + r_b \sin[\frac{2\pi}{\lambda} u_2 t] \tag{8.23}$$

Cyclic boundary conditions can no longer be assumed in the implicit method, therefore for the right hand side boundary condition (r_n') the explicit solution will be used with the calculation of r_{n+1} by the extrapolation equations 8.11.

The constant r_m in equation 8.23 is the mean value of $\bar{\rho}h$ and it can be approximated to $r_m = \bar{\rho}_m \bar{h}$. Unfortunately it is impossible to know the amplitude of the excitation function r_b; this would require the consideration of the whole EHL contact geometry (like Venner and Lubrecht). Therefore an arbitrary value for r_b will have to be given and the solution obtained will predict only the wavelength of the film and pressures but not their amplitudes. However, at the inlet the roughness is considerably but incompletely deformed so one might expect $r_b \approx 0.5 r_m$ and in fact, it was found that with $r_b = 0.45 r_m$ (where $r_m = 2.6956 \times 10^{-5}$) it is possible to obtain approximately the amplitude for the film thickness reported by Venner and Lubrecht in their one-sided surface roughness pure rolling results, Fig 8.17

8.5.2 Newtonian Fluid Results

Figs. 8.22, 8.23, 8.25, 8.26 show the results using the implicit method for the transient solution including the complementary function of the Venner and Lubrecht example of Section 8.4 (with Newtonian compressible fluid). Fig. 8.22 represents the case of pure rolling and it shows that the film thickness and pressures from the steady state solution (initial condition) are being replaced by the inlet modification (for $1.5 \leq x/b$) which show film thickness and pressure with equal wavelength. The results agree well with Venner and Lubrecht Fig. 8.17.

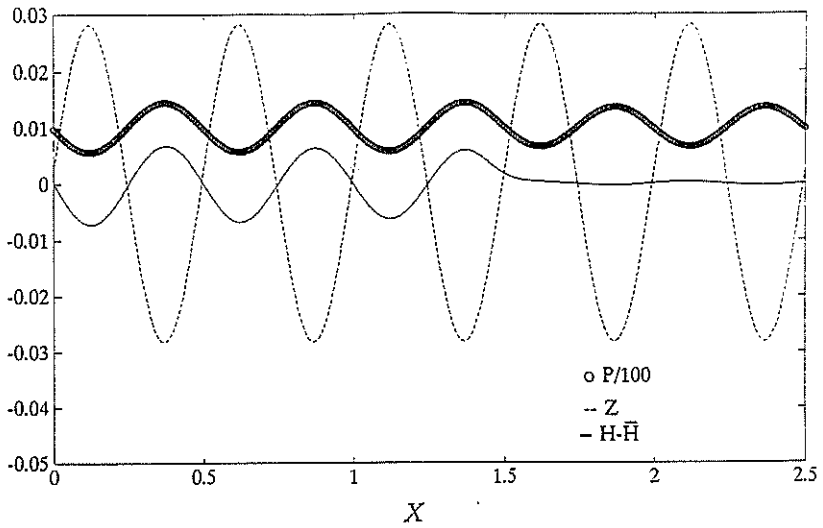

Figure 8.22: Complete pressures and film thickness for the case $s = 0$

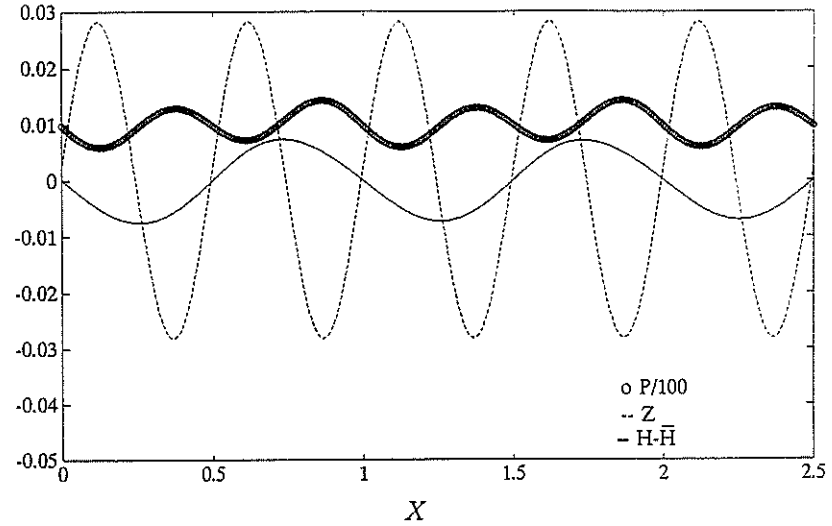

Figure 8.23: Complete pressures and film thickness for the case $s = -1$

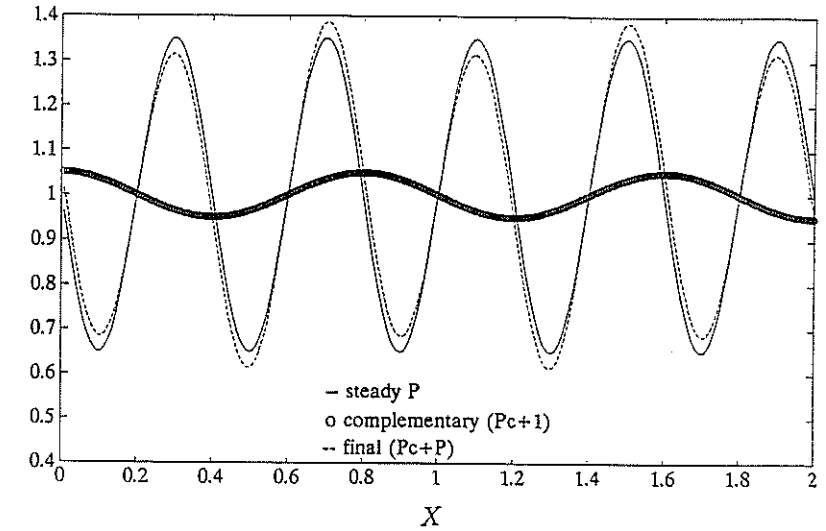

Figure 8.24: Components of the complete pressures for the case $s = -1$

Fig. 8.23 shows the film thickness and pressure for the roll-sliding case of $s = -1$ ($u_1 = 3u_2$) for a time when the initial shape has been fully replaced by the inlet modification. It is clear for this case where the velocity of the rough upper surface is only a third of the velocity of the lower surface that the inlet modulation will have a wavelength three times larger than the original roughness and pressure. This film modulation will also produce a pressure modulation of the same wavelength but small amplitude (if the amplitude and wavelength of the shape increases, the amplitude of the pressures decreases) and they will be added to the original pressures producing the pressure distribution shown if Fig. 8.23. This mechanism is better understood by looking at Fig. 8.24 where the pressure distribution of Fig. 8.23 is reproduced by adding together the pressures from the deformation of the original roughness and the pressures corresponding to the film modulation from the inlet (using the Greenwood and Johnson equations of Section 5.1). It can be seen that the steady state pressures are just slightly modified by the inlet modulation since its amplitude is small. In order to have a complete picture it would be necessary to add the 'Hertzian' pressures associated with a finite contact.

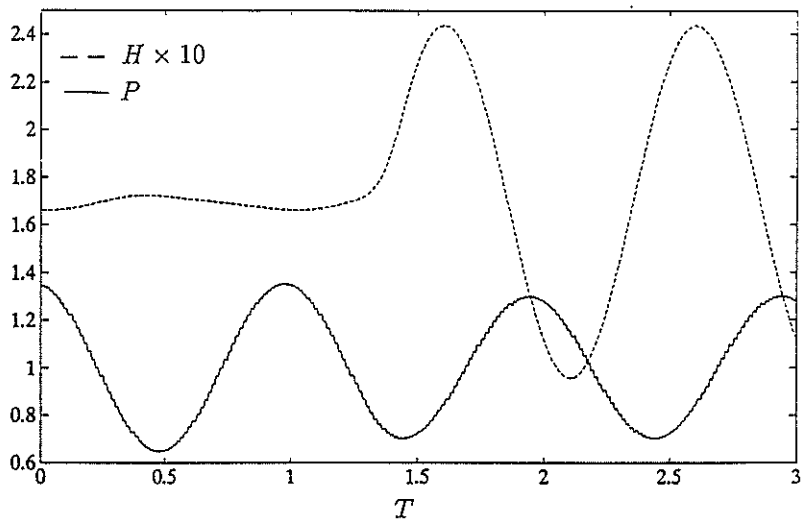

Figure 8.25: Complete pressures and film thickness for $x/b = 1.36$ and s=-1 as function of time

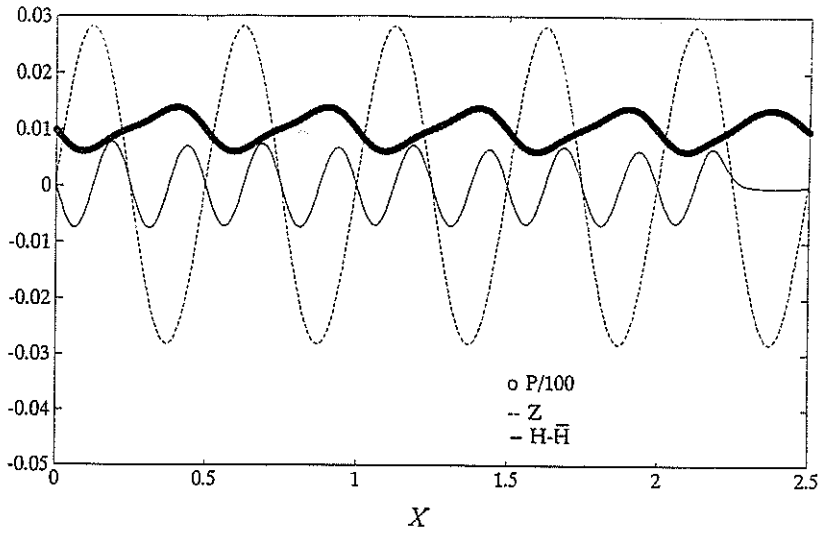

Figure 8.26: Complete pressures and film thickness for the case $s = 2$

In Fig. 8.25 it is easy to see that the location $x/b = 1.36$ is reached by the inlet modulation at $T = 1.3$.

Fig. 8.26 shows the film thickness and pressures for an instant when the inlet disturbances have nearly fully replaced the initial conditions in the case of pure sliding with the smooth lower surface stationary ($s = 2$). Since $u_2 = 2\bar{u}$, for this case the wavelength of the film modulation has been halved in comparison with the wavelength of the original roughness. The pressures have been only slightly distorted.

8.5.3 Non-Newtonian Results

The full transient solutions for the Venner and Lubrecht example of Section 8.4 but now with a compressible Eyring fluid are shown in Figs. 8.27 to 8.29. The pressures and film thickness for the case of pure rolling $s = 0$ are shown in Fig. 8.27 from which by comparison with its Newtonian equivalent Fig. 8.22 it is easy to see that there are no difference in amplitudes or wavelength since for this case there is no shear in the lubricant therefore the non-Newtonian effects are negligible.

Fig. 8.28 shows the film thickness distribution for three different values of the amplitude of the inlet excitation r_b ($0.1r_m$, $0.45r_m$, $1.5r_m$) for the case when $s = -1$ and the steady state solution has been only partially replaced. For $x/b > 1.7$ the steady state film shape still can be seen; it is also clear that for this case (non-Newtonian fluid) the original

roughness is much less deformed than for the Newtonian fluid, therefore the steady final deformed shape will be more visible after the inlet modulation is added. For the case of $r_b = 0.1r_m$, when the inlet modulation has small amplitude, the steady shape is only slightly modified in shape and wavelength. In the intermediate case of $r_b = 0.45r_m$ the final shape is clearly a mixture of the steady state shape and the complementary function and is not sinusoidal, its wavelength is evolving to become the disturbances wavelength. Finally for the case when $r_b = 1.5r_m$ the dominant wave is the complementary function.

Fig. 8.29 shows the corresponding pressures to the films of Fig. 8.28, where basically the original wavelength is preserved in all the cases, but the amplitudes are modified.

Fig. 8.30 shows the film thickness and pressures for a fixed location at $x/b = 0.68$ and $s = -1$ so it is comparable with its Newtonian equivalent Fig. 8.25. The main difference is the shift of phase between the pressures and the film thickness. This difference must be related to the steady state shift discussed in Chapter 5. Besides it, the different locations x/b are reached at different times.

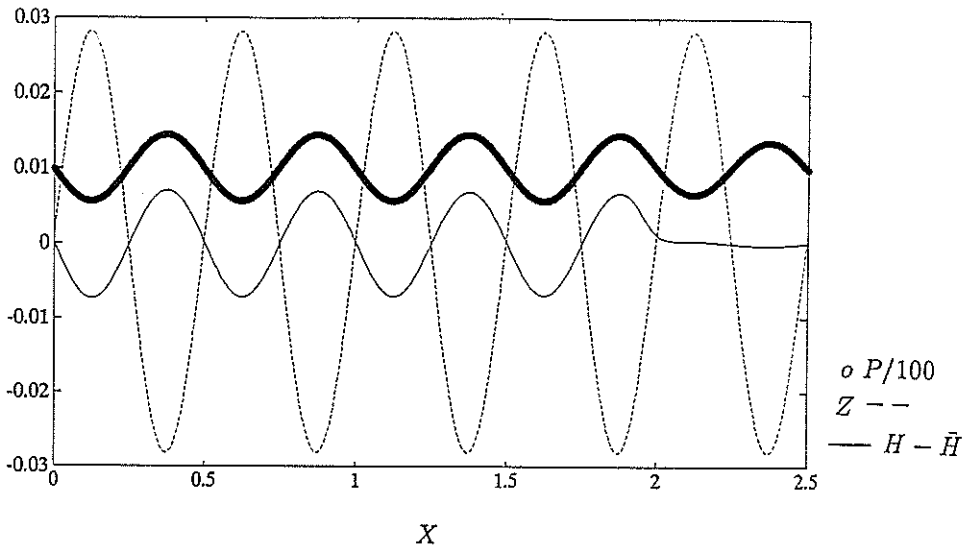

Figure 8.27: Complete pressures and film thickness for $s = 0$, Eyring fluid

1

[1]Note that in the LH side of Figs. 8.27 to 8.29 the complete transient shapes and pressures are shown, whist in the RH side the steady state solution still remains. This is of course only a theoretical exercise, in practical EHL only the two separate zones have physical meaning since the inlet disturbances almost instantaneously reach the exit of the contact.

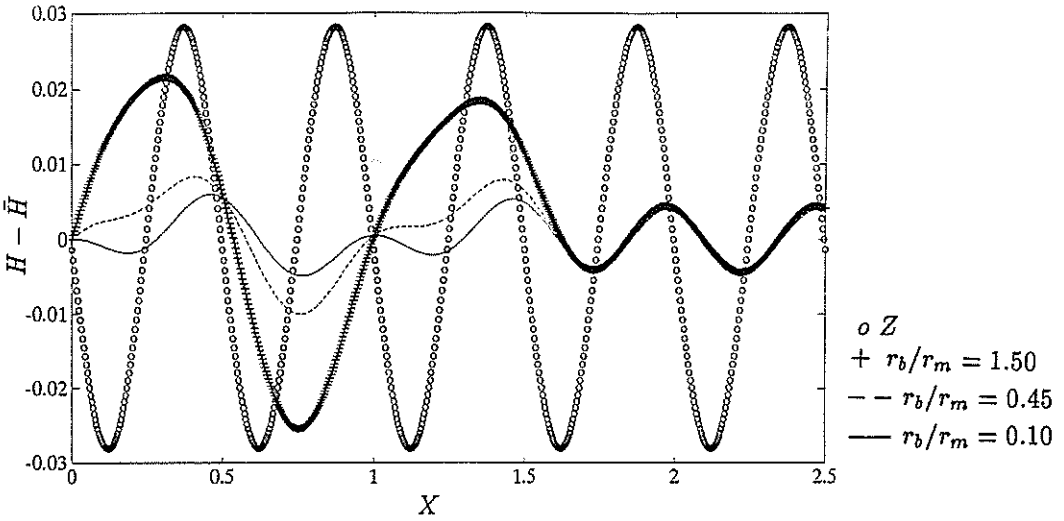

Figure 8.28: Complete film thicknesses for $s = -1$, Eyring fluid

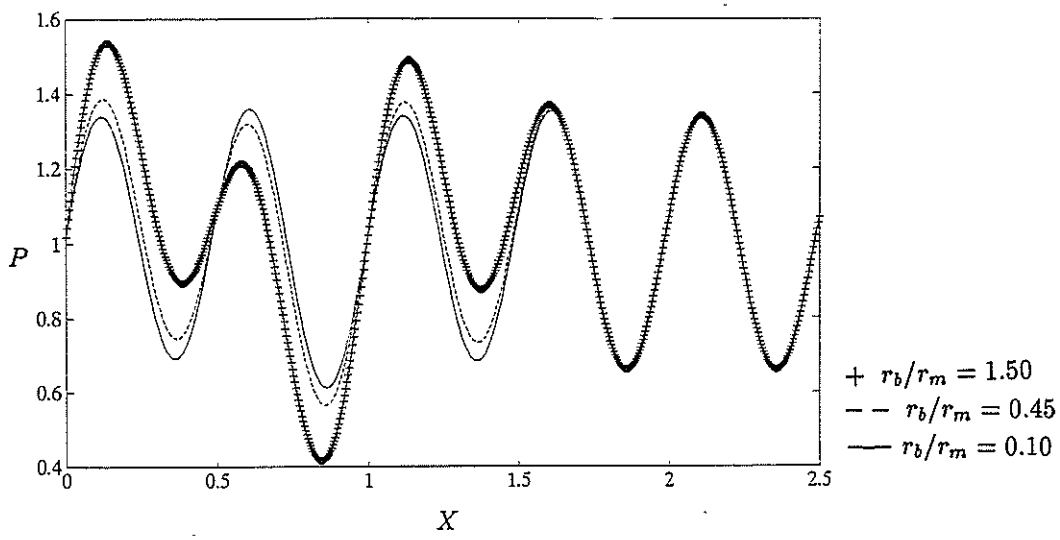

Figure 8.29: Complete pressures for $s = -1$, Eyring fluid

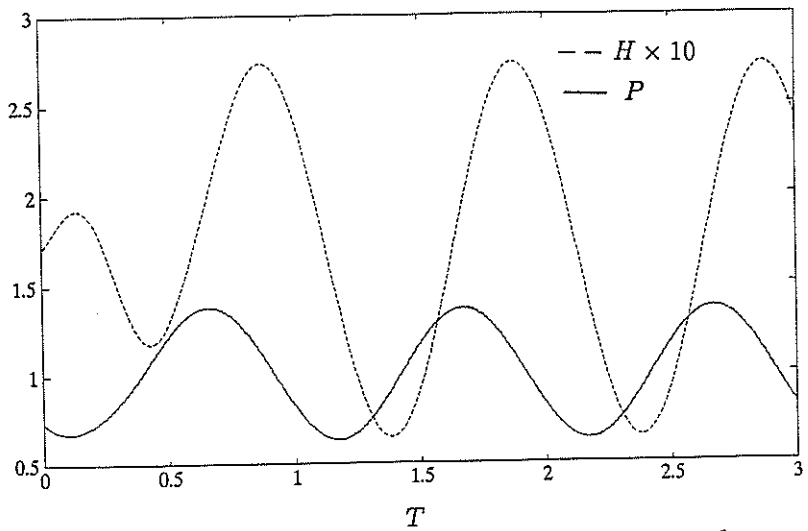

Figure 8.30: Complete pressures and film thickness for $x/b = 0.68$ and $s = -1$ as function of time

8.6 Numerical Damping of the Shape

In order to avoid numerical error in the solution of the transient Reynolds equation with complementary function included, care must be taken with the choice of ΔX and ΔT. Despite the stability of the implicit method, if the space grid and the time step are not small enough, the numerical error generated in the left hand side boundary will be transported down stream and added to the error there, and therefore the solution for r will be noticeably affected. The error will show up as a 'numerical damping' steadily reducing the amplitude of r and therefore H for larger values of X. Venner [75] 1991 and Venner and Lubrecht [78] 1992 have shown transient solutions of wavy surfaces where the film thickness appears to be gradually reduced in amplitude as it moves towards the exit of the contact. However, when Lubrecht and Venner increased the number of grid points (private communication) the same solutions showed a noticeable reduction in the damping. It is now believed that those solutions in fact show only numerical damping.

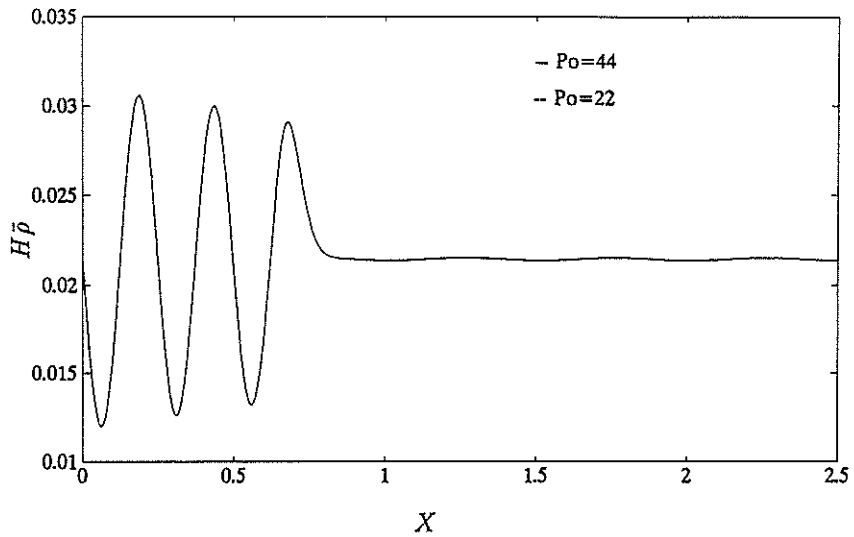

Figure 8.31: Variation of amplitude for $\bar{\rho}H$ for two mean loads and $s = 2$ ($\Delta X = 0.0078$, $\Delta T = 0.0025$)

The only possible explanation for a real physical damping in the film thickness amplitude as x increases is the variation of the viscosity along x, in which case the term $\partial p/\partial x$ of equation 8.2 is affected since $\hat{B}$ cannot be considered as constant, then amplitudes of r and therefore h calculated from a high viscosity zone will be different from those calculated from a low viscosity zone. Then in pure rolling where the pressures and shape

remain in phase, the shape would be one-sided reduced, while in sliding condition the reduction would be alternating. Notice that the linearisation of the Reynolds equation of Section 8.2.1 would not be possible, and its numerical solution would be much more complicated. In any case, the shapes showed by Venner and Lubrecht do not exhibit any of these features.

With the present linearized Reynolds equation it is possible to asses the influence of the viscosity term in the damping of the shape by changing the mean pressure p_o. Fig. 8.31 shows the solution for r of the Newtonian fluid example of Section 8.4 with $s = 2$ for two different mean pressures $P_o = 22.0$ and $P_o = 44.0$ giving almost exactly the same amplitude !. It is shown below, that the reduction of amplitude along x that they both show is only due to numerical problems; however, the important feature here is to show that in typical heavily loaded EHL contacts the reciprocal of the viscosity is so small that to regard or not its variation along x makes no difference in the solution (especially with Newtonian lubricants, $\hat{B} \approx 0$) and therefore there is no evidence of a real physical damping in the shape.

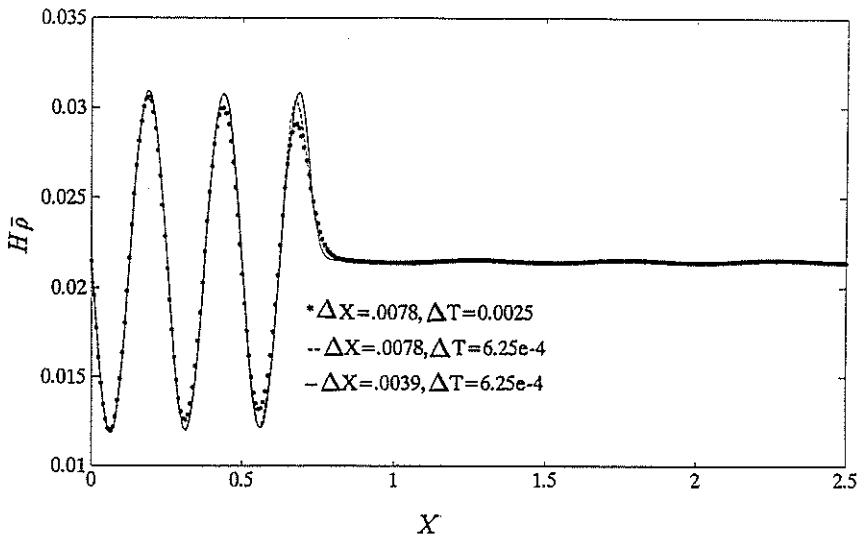

Figure 8.32: Numerical damping of $\bar{\rho}H$ for various ΔX and ΔT with $s = 2$

Considering again the Newtonian fluid example of Section 8.4, to give a solution without visible numerical error for the case $s = 0$ required $\Delta X = 0.0078$ and $\Delta T = 0.005$; for $s = -1$ it required $\Delta X = 0.0078$ and $\Delta T = 0.005$; and for $s = 2$ it needed $\Delta X = 0.0039$

and $\Delta T = 6.25 \times 10^{-4}$. There is a clear tendency of producing more numerical error for larger absolute values of s. This can be understood by considering the linearized Reynolds equation 8.8; the larger the absolute value of s the larger the constant C_T and therefore also the term involving derivatives of r, z_2 and z_1, so it is clear that this term is the source of the numerical error.

Fig. 8.32 shows the reduction of the numerical damping in the variable r when reducing ΔT and ΔX in the Newtonian example with $s = 2$ of Fig. 8.26.

8.7 Conclusions

A simple scheme to study the kinematic behaviour of sinusoidal roughness in EHL has been described. The approach once again assumes an infinitely long contact and solves a combined transient Reynolds-elasticity equation by finite differences for moving surfaces allowing for Newtonian and Eyring fluids.

It was shown that the full solution for pressures and film thickness is made of two parts : a) the moving steady state solution which is related only to the deformation of the original roughness and which produces pressure and film ripples travelling with the velocity of the rough surface u_2; b) a complementary function from the inlet modulation of film thickness and pressures which produces film and pressure disturbances travelling with the average velocity of the lubricant $\bar{u}$, so their wavelength depends directly on this velocity and therefore on the slide-roll ratio s. Since the complementary solution is completely produced by the inlet, with an infinitely long contact its amplitude is unknown and only solutions for the wavelength are given.

The following conclusions can be pointed out:

a).- The full kinematic solution of an EHL contact with rough surfaces is made of two components, see Fig. 8.24: the steady state solution for shape and pressure related to the deformation of the initial roughness and the inlet disturbances of film and pressure related to the entry into the contact of the less deformed roughness ripples. Therefore the final film and pressures will have geometry and velocity determined by a combination of these two components, i.e. Figs. 8.28 and 8.29.

b).- In one-sided surface roughness cases when the initial shape is very much deformed by the steady state pressures, and the inlet disturbances have a dominant amplitude in the solution then:

For pure rolling condition ($s = 0$) the final shape and pressures will keep the wavelength of the initial roughness regardless the rheology of the lubricant, i.e. Figs. 8.22 and 8.27.

For $s = -1$ (rough surface moving with half the velocity of the lubricant) the final shape has wavelength twice as long as the original roughness travelling at the average velocity, and pressures slightly different from the steady solution with the original roughness wavelength and velocity, regardless the lubricant rheology, i.e. Figs. 8.23 , 8.28 and 8.29.

For $s = 2$ (rough surface moving twice as fast as the average velocity of the lubricant) the final shape has wavelength half as long as the initial roughness wavelength, and the pressures are nearly the same as the steady solution with the original roughness wavelength and velocity, i.e. Fig. 8.26.

c).- By looking at some literature results (e.g. Venner and Lubrecht [76]) one can be very surprised when comparing the steady state solution with the transient one to find that the transient pressure ripples are almost the same as the steady state ones while the shapes are very different indeed; in general the transient shape shows larger amplitude of ripples as well as the difference in wavelengths. It would seem as if the transient shape is independent of the transient pressures!. This apparent disagreement is now understood with the consideration of having a transient solution made of two parts as explained in (a). So that in the referred cases the steady state solution presents very deformed shapes with large pressure ripples whilst the complementary solution due to the effect of the inlet shows large amplitude shapes with small pressure ripples; and when the two solutions are superimposed the steady state pressures are almost unchanged and so the transient shape. This phenomenon can be seen for pressures in Fig. 8.24.

d).- No real physical damping in the final shape was found. The damping exhibited in the Venner and Lubrecht solutions is now believed to be the result of numerical error.

e).- The main difference between Newtonian and Eyring fluid full solutions is the amplitude of shape and pressures from the steady state. Fig. 8.28 for $x/b > 1.6$ still shows the steady state shape which is being replaced by the inlet disturbances, so one can see that in comparison with an equivalent Newtonian case; Fig. 8.22 with the steady state shape visible for $x/b > 1.6$, the Eyring amplitude is much larger than the Newtonian one, so that for this case the Eyring steady shape is distorting the final shape.

Apart from this, there is a different shift of phase between pressures and final shape

in time, related to the steady state shift already discussed in Chapter 5.

f).- In the case of two-sided surface roughness, it was shown that the Newtonian moving steady solution agrees well with Lubrecht and Venner results for pressure and shape but not for film thickness. The inlet has to be considered to obtain a complete solution. The Eyring solutions show less deformed shapes and a shift of phase between shape and pressures in time in comparison with their Newtonian equivalents, i.e. Figs. 8.12 and 8.16. Newtonian deformed shapes always keep their initial relative shift of phase regardless the motion of the surfaces, whilst the Eyring deformed shapes vary their initial shape; this should also be related to the steady state shift discussed in Chapter 5.

CHAPTER NINE

CONCLUSIONS AND FUTURE RESEARCH

9.1 General Conclusions

In the present work some aspects of Elastohydrodynamic lubrication of smooth and rough surfaces in isothermal line contacts have been studied. With respect to smooth surfaces, a scheme which uses fracture mechanics theory has been suggested to solve separately the inlet, central and outlet regions of an EHL contact. The pressure spike is treated as a singularity so that there is no need to solve the Reynolds equation at the spike location, avoiding in this way the disadvantages of numerical instability of the full numerical solutions. The scheme is also extended to deal with lubricant compressibility and with the Roelands viscosity law. Outlet and complete EHL solutions are obtained, therefore the following conclusions can be outlined:

a).- The outlet pressure distribution is a closely logarithmic curve with two constants defining it completely.

b).- As an elastic consequence of (a) the exit bump joins the parallel film region with finite slope, not as in Greenwood's theory.

c).- The agreement of the results predicted by the present theory and results found in the literature from complete numerical solutions is in general good, especially for the cases when the spike is located closer to the exit. However, it was found that among different authors there is still great disagreement in some results related to the spike location.

d).- From the results obtained with the present scheme and from the observation of literature results it is possible to establish the behaviour of the pressure spike in a non-dimensional map $\mathcal{P} - \mathcal{S}$.

e).- The use of the Roelands viscosity law instead of the Barus law brings almost no

difference in the film and pressure results.

With respect to rough surfaces several schemes are shown for the solution of EHL contacts with Newtonian and non-Newtonian as well as compressible and incompressible lubricants. All of them are based on the idea that an EHL contact can be treated as an infinitely long contact with known mean film thickness and pressure. The roughness and associated pressures can then be considered to be an assembly of sinusoidal curves with the coefficients obtained from a Fourier analysis. Steady and transient effects are studied as well as 'real' and wavy roughness. Subsurface stresses related to the roughness are estimated and presented in form of probabilities rather than by specific value and location. And in summary the following conclusions are obtained:

1).- The roughness amplitude reduction after deformation is less with a non-Newtonian fluid, and the final shape shows a shift of phase with respect to the original one. In real roughness the high frequency components are retained after deformation.

2).- For Eyring fluids the deformation of the roughness is strongly dependent on the ratio $\lambda/\bar{h}$. For low values of this parameter the roughness will persist, even in heavily loaded situations. This conclusion gives a criterion of roughness deformation and explains why in (1) the high frequency components persist after deformation.

3).- In Eyring fluids varying the mean pressure has little effect on the final shape, whilst in Newtonian fluids when the mean pressure increases the deformation of the roughness is also increased. This is related to the mean viscosity and its effect on the Reynolds equation.

4).- The subsurface stresses under real-roughness pressures are shown to be Gaussian variables. This can be expected from the Central Limit Theorem since the stresses are an assembly of sinusoidal curves. Therefore the standard probability rules to asses the largest expected value can be applied. The results are given as a probability of exceeding certain limits rather than a specific value and location for the maximum stress.

5).- The transient EHL solution for film and pressures of rough surface contacts is shown to be made of two separate functions: the steady state pressure and shape distributions moving with the velocity of the rough surface, plus a film thickness and pressure complementary function moving with $\bar{u}$ and resulting from the modulation of the roughness of film and pressures in the inlet of the contact; this conclusion provides a more general understanding of the transient physical phenomenon.

6).- It is also shown that the gradual reduction of shape amplitude along the contact length (shape damping) previously reported in literature, is only a 'numerical feature' rather than a real physical damping.

9.2 Recommendations for Future Work

Elastohydrodynamic lubrication of smooth and rough surfaces offers an extensive field of research and the topics covered by the present work represent only a limited sample. However, the aim of the work was to perform general analyses with the minimum of complexity in the algorithms. Such a combination of objectives is particularly difficult to achieve in a field where the numerical instability is a major problem.

In relation with the work on smooth surfaces it is recommended to extend the applicability of the present theory to other regions of the $\mathcal{P}-\mathcal{S}$ map by implementing a less-error way to join the inlet and central pressures.

The greatest shortcoming of the present scheme is its limitation to predict the spike height, so a modification to enable the scheme to deal with finite spikes would be very useful. Even if fracture mechanics cannot be applied any longer for this situation.

Equally necessary modifications are the inclusion of the energy equation (to account for the effects of temperature) and the capability to deal with non-Newtonian fluids, so the effects of shear friction specially in sliding contacts could be studied.

With respect to rough surfaces EHL a study of single asperities and real roughness effects would be interesting to make especially in transient situations, however, the algorithms would require some important modifications. Now that the nature of the transient solution is better understood and the importance of the inlet in the determination of the modulations amplitude has been established, it would be necessary to modify the present algorithms to account for the inlet in some way. It is also recommended to extend the transient analysis to more real situations like the double sided roughness case.

Finally, in order to demonstrate the integration of the smooth and rough surfaces analysis described in the present work, it is necessary to perform a set of solutions where the macroscopic parameters as the mean film thickness and pressure are calculated using the EHL scheme and the microscopic effects as roughness deformation by using the micro-EHL schemes.

APPENDIX A

Numerical Solution of Stress Replacement Integrals

Most of the integrals showed in Chapters 3 and 4 related to the calculation of stress intensity factors, pressures and elastic slopes show singularities at either $x = a$ or $x = -a$, therefore care must be taken in their numerical solution. In this Appendix the used numerical schemes to carry out the integrals are described.

A.1 Stress Intensity Factors

a).- Calculation of M: The calculation of these stress intensity factors involves the evaluation of:

$$I = \int_{x_1=a}^{L} \frac{p(x_1)}{\sqrt{x_1^2 - a^2}}\, dx_1 \tag{A.1}$$

The singularity at $x_1 = a$ can be removed by the substitution: $t = \sqrt{x_1 - a}$; therefore equation A.1 becomes:

$$I = 2\int_{t=0}^{\sqrt{L-a}} \frac{p(t)}{\sqrt{t^2 + 2a}}\, dt \tag{A.2}$$

which can then be evaluated by Simpson's rule.

b).- Calculation of M_1: The calculation of M_1 involves the solution of two different sorts of integrals:

$$I_1 = \int_{x_1=a}^{L} \sqrt{\frac{X_1 - a}{X_1 + a}} p'(x_1)\, dx_1 \tag{A.3}$$

$$I_2 = \int_{x_1=a}^{L} \sqrt{\frac{X_1 + a}{X_1 - a}} p'(x_1)\, dx_1 \tag{A.4}$$

In each case, put $t = \sqrt{x_1 - a}$, then equations A.3 and A.4 become:

$$I_1 = 2 \int_{t=0}^{\sqrt{L-a}} \frac{t^2 p'(t)}{\sqrt{t^2 + 2a}}\, dt \tag{A.5}$$

$$I_2 = 2 \int_{t=0}^{\sqrt{L-a}} p'(t) \sqrt{t^2 + 2a}\, dt \tag{A.6}$$

A.2 Pressures

The equation for the pressures in the central region (i.e. equation 4.22) involves an integral of the type:

$$I = \int_{x_1=a}^{L} \frac{p(x_1)}{(x_1 - x)\sqrt{x_1^2 - a^2}}\, dx_1 \tag{A.7}$$

for $x < a$.

This integral for pressures is singular at $x_1 = a$ because $\sqrt{x_1^2 - a^2} = 0$ and at $x_1 = a$ also because the pressures become infinity. Unlike the equation for the deflection slopes, which also involves this integral, here always $x_1 > x$. Therefore a second singularity is avoided.

The integral of equation A.7 can be solved just like equation A.1. Put: $t = \sqrt{x_1 - a}$ and $s = \sqrt{x - a}$, so:

$$I = 2 \int_{t=0}^{\sqrt{L-a}} \frac{p(t)}{(t^2 - s^2)\sqrt{t^2 + 2a}} \tag{A.8}$$

for $x < a$.

A.3 Slopes

Equations 4.23 and 4.24 show two different integrals:

$$I_1 = \int_{x_1=a}^{L} \frac{p(x_1)}{(x_1 + x)\sqrt{x_1^2 - a^2}}\, dx_1 \tag{A.9}$$

$$I_2 = \int_{x_1=a}^{L} \frac{p(x_1)}{(x_1 - x)\sqrt{x_1^2 - a^2}}\, dx_1 \tag{A.10}$$

for $x > a$ and $x_1 > a$.

I_1 presents only the same singularity as the pressure integral equation A.7, so substituting again: $t = \sqrt{x_1 - a}$ and $s = \sqrt{x - a}$, equation A.9 becomes:

$$I_1 = 2\int_{t=0}^{\sqrt{L-a}} \frac{p(t)}{(t^2 + s^2)\sqrt{t_2 - 2a}}\, dt \tag{A.11}$$

However, the solution of equation A.10 is much more complicated, due to the strong singularity when $x_1 = x$, and the situation gets worse for the outlet, where the pressures are also singular.

For the solution of equation A.10 it is better to start by taking its simpler form given by equation A.8, then put:

$$g(t) = \frac{p(t)}{\sqrt{t^2 + 2a}}$$

then:

$$I_2 = 2\int_{t=0}^{\sqrt{L-a}} g(t)\frac{dt}{t^2 - s^2} \tag{A.12}$$

now, since:

$$\frac{1}{t^2 - s^2} = \frac{1}{2s}\left(\frac{1}{t - s} - \frac{1}{t + s}\right)$$

hence:

$$I_2 = \frac{1}{s}\int_{t=0}^{\sqrt{L-a}} g(t)\left(\frac{1}{t - s} - \frac{1}{t + s}\right)\, dt$$

and integrating by parts:

$$I_2 = \frac{1}{s}\left[g(t)\ln\left|\frac{t - s}{t + s}\right|\Bigg|_{t=0}^{\sqrt{L-a}} - \int_{t=0}^{\sqrt{L-a}} g'(t)\ln\left|\frac{t - s}{t + s}\right|\, dt\right]$$

where: $g'(t) = \frac{dg}{dt}$, and $\ln|-s/s| = 0$. And:

$$I_2 = \frac{1}{s}\left[g(\sqrt{L - a})\ln\left|\frac{\sqrt{L - a} - s}{\sqrt{L - a} + s}\right| - \int_{t=0}^{\sqrt{L-a}} g'(t)\ln\left|\frac{t - s}{t + s}\right|\, dt\right] \tag{A.13}$$

but in EHL $p(\sqrt{L-a}) = 0$ (end of the outlet and beginning of the inlet), so $g(\sqrt{L-a}) = 0$. Then:

$$I_2 = \frac{-1}{s} J \tag{A.14}$$

where:

$$J = \int_{t=0}^{\sqrt{L-a}} g'(t) \ln |\frac{t-s}{t+s}| \, dt \tag{A.15}$$

The integral A.15 can be solved by using a discrete numerical method developed by Johnson and Bentall [42] 1977, in which the 'pressures' (function $g(t)$) are divided into n regular elements, say triangles. Then the integration is carried out as a summation of n analytical integrals. Since the values of $g'(t)$ for a triangular element are known (i.e. Fig. A.1), therefore according to Johnson and Bentall the integral J is:

$$(J_t)_{i,j} = -\sum_{j=1}^{n} g_j [f(i+j) - f(j-i)] \tag{A.16}$$

where the index i corresponds to values of s ($s = ih$) and the index j corresponds to values of t ($t = jh$). For a complete triangular element:

$$f(k) = (k+1)\ln|k+1| - 2k\ln|k| + (k-1)\ln|k-1| \tag{A.17}$$

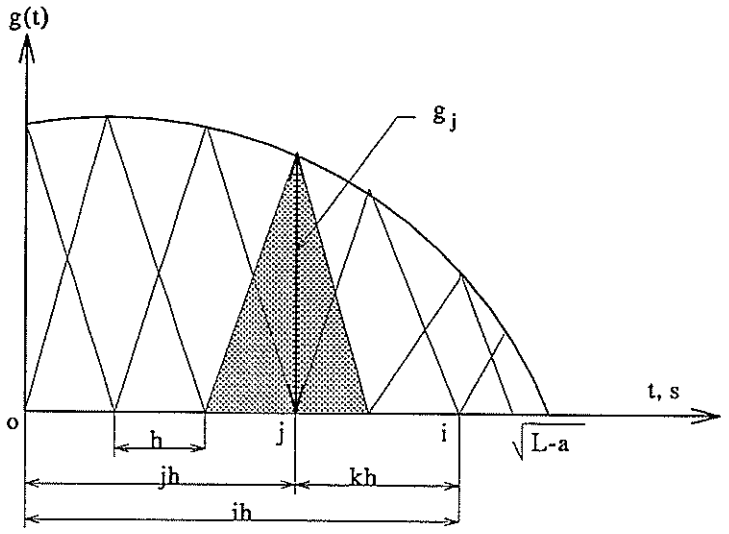

Figure A.1: Discretization with complete triangular elements

However, it is clear that for outlet EHL pressures, one cannot represent them accurately using only complete triangular elements, but two more types of element should be added: a half triangle and a logarithmic element, as shown in Fig. A.2:

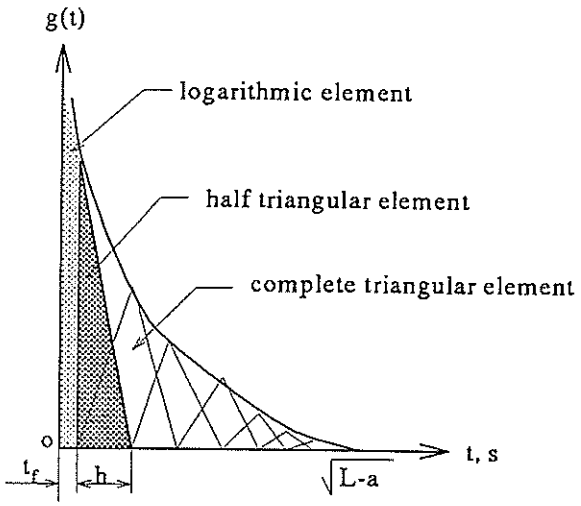

Figure A.2: Discretization using three types of elements

Half triangular element:

The slope is: $g'(t) = -g_j/h$, for $jh \leq t \leq (j+1)h$, then solving equation A.15:

$$(J_{ht})_{i,j} = -\int_{t=jh}^{(j+1)h} (\frac{g_j}{h}) \ln|\frac{hj - hi}{hj + hi}|\, dt = -g_j[f_{ht}(j+i) - f_{ht}(j-i)] \tag{A.18}$$

where:

$$f_{ht}(k) = (k+1)\ln|k+1| - k\ln|k| \tag{A.19}$$

Logarithmic element:

Put: $g(t) = B\ln|\frac{t^2}{L-a}|$, so from equations A.13 to A.15 the J integral of a logarithmic element of pressure (for $0 \leq t \leq t_f$) is:

$$J_{log} = B\ln|\frac{t^2}{L-a}|\ln|\frac{t_f - s}{t_f + s}| - (s)I_{2log} \tag{A.20}$$

where:

$$I_{2log} = \frac{B}{s}\int_{t=0}^{t_f} \ln|\frac{t^2}{L-a}|\,\frac{dt}{t^2 - s^2}$$

In this particular case it is simpler to solve directly I_{2log}; which by substituting $q = t/s$ becomes:

$$I_{2log} = 2B \int_{q=0}^{1} \left[\frac{1}{q - s/t_f} - \frac{1}{q + s/t_f} \right] \ln|q| \, dq \tag{A.21}$$

The integral A.21 can be numerically solved for all values of $s \neq t_f$ with a modified Gaussian quadrature, the method is fully described in the Handbook of Mathematical Functions [1] from where the solution of the integral:

$$\int_0^1 f(z) \ln(z) \, dz$$

is given by:

$$\sum_{k=1}^{m} w_k f(z_k)$$

where the coefficients w_i are given in the reference according to the chosen number m.

Full solution of I_2

Finally the solution of the integral of slopes I_2 of equation A.10 is given by:

$$(I_2)_{i,j} = \frac{1}{ih} \left\{ g_j[f_{ht}(j+i) - f_{ht}(j-i)] + \sum_{j=2}^{n} g_j[f(i+j) - f(j-i)] \right.$$

$$\left. -B \ln|\frac{t_f^2}{L-a}| \ln|\frac{t_f - ih}{t_f + ih}| + (ih) I_{2log} \right\} \tag{A.22}$$

with $f_{ht}(k)$ given by equation A.19, $f(k)$ by equation A.17 and I_{2log} by equation A.21.

APPENDIX B

Numerical Error in the Direct Approach

B.1 Incompressible Fluids

The convergence process in the direct approach goes in the following way:

$$\text{displacements} \rightarrow \text{pressures} \rightarrow \text{shape} \rightarrow \text{new displacements}$$

to go from displacements to pressures, the process is based on equation 5.13, from which:

$$\Delta p_n = \frac{\pi E'}{2\lambda} v_n(n) \tag{B.1}$$

and the Fourier coefficients of $\frac{dp}{dx}$ would be:

$$p'_n = v_n \frac{\pi^2 E'}{\lambda^2}(n)^2 \tag{B.2}$$

therefore the coefficients of t_p are:

$$(t_p)_n = \frac{h}{2\tau_0}\frac{\pi^2 E'}{\lambda^2}(n)^2 v_n$$

defining:

$$(t_p^*)_n = \frac{h^*}{h}(t_p)_n = \frac{h^*}{2\tau_o}\frac{\pi^2 E'}{\lambda^2}(n)^2 v_n \tag{B.3}$$

To calculate the Fourier coefficients of the film thickness, the equation B.3 is substituted into the Reynolds equation 5.30:

$$h_n = \frac{(h^*)^2}{2\tau_o}\frac{\pi^2 E'}{\lambda^2}\frac{[1 - \frac{R}{(t_p^*)_n}]v_n}{(t_p^*)_n(1 - R\coth t_p)}(n)^2$$

and writing:

$$r = (\frac{\pi h^*}{\lambda})^2 \frac{E'[1 - \frac{R}{(t_p^*)_n}](n)^2}{2\tau_o(t_p^*)_n(1 - R\coth t_p)} \tag{B.4}$$

thus:

$$h_n = rv_n \tag{B.5}$$

Finally the Fourier coefficients of the new displacements are given by subtracting the coefficients of the original roughness z_n from the coefficients h_n:

$$(v_f)_n = rv_n - z_n \tag{B.6}$$

In order to obtain convergence in the process, it is required that: $(v_f)_n = v_n$, therefore from equation B.6 :

$$v_n = \frac{-z_n}{1 - r}$$

and if there is any numerical error ϵ, then the coefficients become:

$$v_n = \frac{-z_n}{1 - r} + \epsilon \tag{B.7}$$

substituting B.7 into B.6 :

$$(v_f)_n = \frac{-z_n}{1 - r} + r\epsilon \tag{B.8}$$

Comparing equation B.8 and equation B.7 it is possible to see that the numerical error in one iteration of the process has increased to $r\epsilon$, therefore the error might become uncontrollable if:

$$|r| > 1 \tag{B.9}$$

and r can now be defined as the magnification factor of numerical error per iteration, for incompressible fluids it is given by equation B.4.

B.2 Compressible Fluids

Again the direct approach has the same sequence as for incompressible fluids. The pressure Fourier coefficients are still given by equation B.1. However, this time the compressibility ratio ρ^*/ρ will be different from 1 in the Reynolds equation 5.30.

Linearizing the density equation:

$$\frac{\rho^*}{\rho} \approx 1 - C(p - p_o) \tag{B.10}$$

where:

$$C = \frac{\gamma - \beta}{(1 + \beta p_o)(1 + \gamma p_o)}$$

by taking $R/(t_p^*) \approx 1$, equation 5.30 becomes:

$$h \approx \frac{h^*[-C\Delta p]}{1 - R\coth t_p} \tag{B.11}$$

Substituting equation B.1 in equation B.11, the Fourier coefficients for h can be obtained:

$$h_n = \frac{h^* C}{1 - R\coth t_p}\frac{\pi E'}{2\lambda}(n)v_n \tag{B.12}$$

The Fourier coefficients for the new displacements are obtained by subtracting the coefficients of the original roughness z_n from the h_n coefficients of equation B.12:

$$(v_f)_n = \frac{h^*}{1 - R\coth t_p}[\frac{C\pi E'}{2\lambda}(n)v_n] - z_n$$

and writing:

$$r = \frac{h^*}{1 - R\coth t_p}[\frac{C\pi E'}{2\lambda}(n)] \tag{B.13}$$

then:

$$(v_f)_n = rv_n - z_n \tag{B.14}$$

In order to have convergence in the process one requires that $(v_f)_n = v_n$, therefore from equation B.14 :

$$v_n = \frac{-1}{1-r}(z_n)$$

If there is any numerical error ϵ , then it becomes:

$$v_n = \frac{1}{r-1}(z_n) + \epsilon \tag{B.15}$$

and substituting equation B.15 into equation B.14:

$$(v_f)_n = \frac{1}{r-1}(z_n) + r\epsilon \tag{B.16}$$

By comparing equation B.16 with equation B.15, it is easy to see that in one iteration of the process the error has increased from ϵ to $r\epsilon$ and it might become uncontrollable if:

$$|r| > 1 \tag{B.17}$$

Once again r is the magnification factor of the numerical error per iteration and for compressible fluids it is given by equation B.13.

APPENDIX C

The Collocation Method (CM)

C.1 Description

The idea in this scheme is to avoid the long and numerically unstable process of iterating from pressures to shape or vice-versus. Here one must begin by using as the basic equation a combination of the Reynolds and elasticity equations and then solve it by approximating the pressures and displacements to an assembly of sinusoidal waves and satisfying the equation at some given values of x (points).

The analysis will be described for the general case of m points. And the basic equation to be used is 5.25 :

$$v(x) + h_G(p - p_o)C = h_G - h^* + h_G\gamma\, C\frac{(p-p_o)^2}{1+\gamma p} + f - z(x)$$

assuming that the pressure distribution, elastic displacements and initial roughness are additions of sinusoidal waves with amplitudes given by the Fourier coefficients, and writing: $\theta = \frac{2\pi x}{\lambda}$, then:

$$\begin{aligned} p(\theta) &= p_o + B_1 \sin\theta + A_1 \cos\theta + ... + B_n \sin n\theta + A_n \cos n\theta \\ v(\theta) &= \tfrac{2\lambda}{\pi E'}\left[B_1 \sin\theta + A_1 \cos\theta + ... + \tfrac{B_n}{n}\cos n\theta + \tfrac{A_n}{n}\sin n\theta\right] \\ z(\theta) &= b_1 \sin\theta + a_1 \cos\theta + ... + b_n \sin n\theta + a_n \cos n\theta \\ h(\theta) &= h^* + v(\theta) + z(\theta) \end{aligned} \tag{C.1}$$

where B_n and A_n are the Fourier coefficients for the pressures and b_n and a_n are the Fourier coefficients of the initial undeformed roughness, so:

$$B_n = \frac{\pi E'}{2\lambda} b_n \quad , \quad A_n = \frac{\pi E'}{2\lambda} a_n$$

Substituting equations C.1 into equation 5.25 for m different points along x, say θ_1, θ_2,...,θ_m, one obtains a non-linear algebraic system of equations:

$$\begin{aligned}
v(\theta_1) + h_G C[p(\theta_1 - p_o] - \tfrac{h_G \gamma\ C[p(\theta_1)-p_o]^2}{1+\gamma\ p(\theta_1)} - f(\theta_1) + z(\theta_1) = 0 \\
v(\theta_2) + h_G C[p(\theta_2 - p_o] - \tfrac{h_G \gamma\ C[p(\theta_2)-p_o]^2}{1+\gamma\ p(\theta_2)} - f(\theta_2) + z(\theta_2) = 0 \\
\vdots \qquad\qquad \vdots \qquad\qquad \vdots \\
v(\theta_m) + h_G C[p(\theta_m - p_o] - \tfrac{h_G \gamma\ C[p(\theta_m)-p_o]^2}{1+\gamma\ p(\theta_m)} - f(\theta_m) + z(\theta_m) = 0
\end{aligned} \tag{C.2}$$

Notice that for every equation there are $2n$ unknowns (A_n and B_n), so $m = 2n$ points are needed to solve the system. It can be solved by any root finder method, i.e. Newton-Raphson. And the initial guess for the pressure Fourier coefficients can be obtained by assuming the roughness to be totally flattened by the pressures.

After solving equations C.2 no further iterations are required, and the pressure coefficients are used directly to find the displacements and the final shape (by using equations C.1).

C.2 Effects of the Number and Location of the Points in the Solution

Since the method is 'exact' only at the values of x where the equations are fully satisfied the accuracy of the solution must improve when the number of points is increased, and some variation in the results scan be expected.

The location of the points affects not only the convergence rate of the solution, but also its accuracy. If the points are not equally distributed within the interval of analysis, then one must expect a more accurate solution in the region where the density of points is higher.

The effect of varying the number of points in this scheme is shown in Fig. C.1 and Fig. C.2 where the Chang example 1 (Section 6.1) has been solved and Chang's variables are used to display the solution.

Fig. C.1 shows the Newtonian solution where the pressures have been plotted for 2, 6 and 10 points equally distributed along the interval -0.7π to 0.3π, and the deformed shape shown represents the 10 points solution. It can be seen that the pressures slightly vary when the number of points is increased. In general, the CM solution for this example hardly agrees with Fig 6.2 (Chang's results) where the pressures appear non-symmetrical and with higher amplitude, besides, Chang's final shape is less deformed. However, notice

that Chang's own solution shows already some stability problems in the pressures and they may be the reason of the difference.

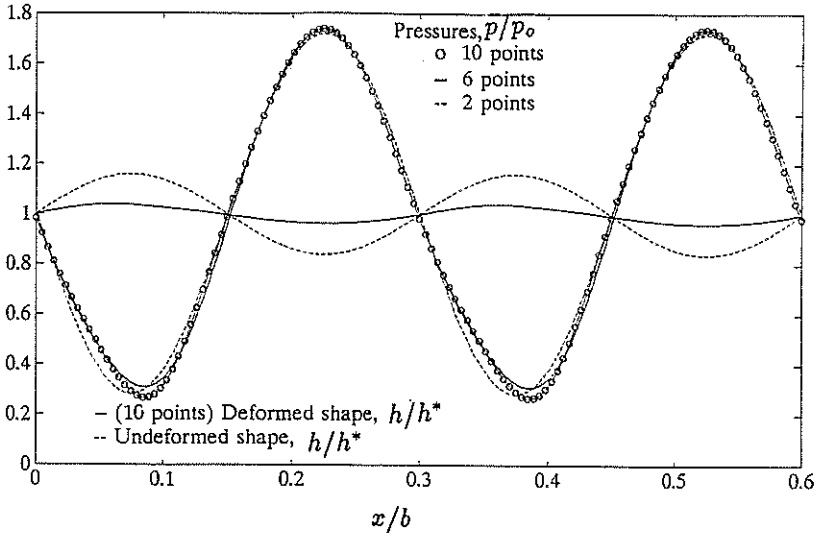

Figure C.1: Effect of the number of points, Newtonian lubricant

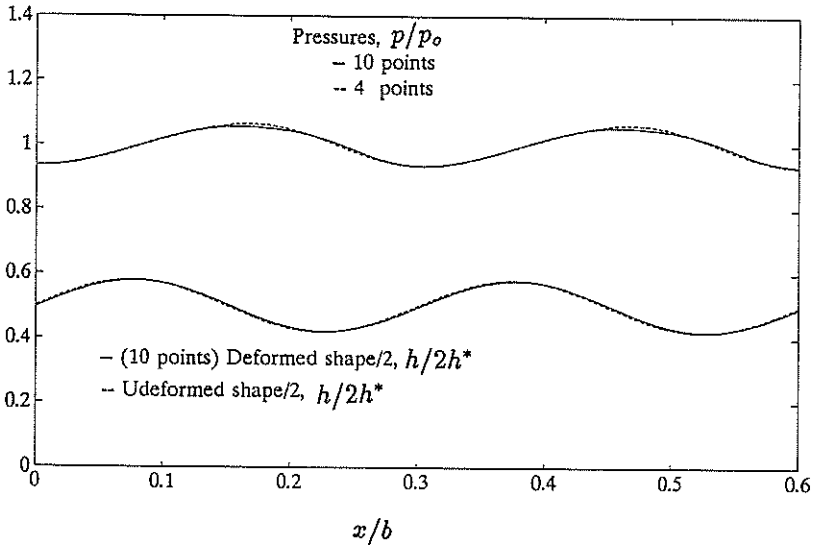

Figure C.2: Effect of the number of points, Eyring lubricant

Fig. C.2 shows the non-Newtonian solution where this time the pressures are plotted for 10, and 4 points equally distributed along the interval 0.0 to π, and the deformed shape shown represents the 10 point solution. Again the pressures barely vary when the number of points is increased. For this example, the results are in very good agreement with Chang's results (Fig. 6.1). It is also clear in this case that the pressures obtained by Chang (Fig. 6.1) look very stable. Notice the small amplitude of the pressure ripples and the small deformation occurred in the shape.

REFERENCES

[1] M. Abramowitz and I.A. Stegun. Handbook of mathematical functions. *Dover Publications, New York*, 1972.

[2] G.D. Archard, F. C. Gair, and W. Hirst. The elasto-hydrodynamic lubrication of rollers. *Proc. Roy. Soc. A*, volume 265, page 51, 1961.

[3] G.I. Barenblatt. The mathematical theory of equilibrium cracks in brittle fracture. *Advances in Applied Mech.*, volume 7, page 55, 1962.

[4] C. Barus. Isothermals, isopiestics and isometrics relative to viscosity. *Am. J. of Science*, volume 45, 1893.

[5] I.F. Bell. Elasto-hydrodynamic effects in lubrication. *M.Sc. Thesis, University of Manchester, U.K.*, 1961.

[6] E.J. Bissett and D.W. Glander. A highly accurate approach that resolves the pressure spike of elastohydrodynamic lubrication. *Trans. ASME, J. of Trib.*, volume 110, 1988.

[7] H. Blok. Correlation review of theoretical and experimental data on elasto-hydrodynamic lubrication. *Technische Hogeschol, Laboratorium voor Werktuigonderdelen, Delft, Holland*, 1959.

[8] A. Cameron. Basic lubrication theory. *Ellis Horwood Ltd*, 1981.

[9] A. Cameron. Righting a 40 years-old wrong. *Trib. Int. (comment)*, volume 18, 1985.

[10] L. Chang, C. Cusano, and T.F. Conry. Effects of lubricant rheology and kinematic conditions on micro-elastohydrodynamic lubrication. *Trans. ASME, J. of Trib.*, volume 111, 1989.

[11] L. Chang, M.N. Webster, and A. Jackson. On the pressure rippling and roughness deformation in elastohydrodynamic lubrication of rough surfaces. *Submitted to ASME J. of Trib.*, 1992.

[12] H.S. Cheng. Isothermal elastohydrodynamic theory for the full range of pressure-viscosity coefficient. *Trans. ASME J. Lub. Tech.*, page 35, 1972.

[13] R.J. Chittenden, D. Dowson, J.F. Dunn, and C.M. Taylor. A theoretical analysis of the isothermal elastohydrodynamic lubrication of concentrated contacts, parts 1 and 2. *Proc. R. Soc. Lond. A*, volume 397, page 271, 1985.

[14] R.J. Chittenden, D. Dowson, N.P. Sheldrake, and C.M. Taylor. The use of multi-level adaptative techniques for ehl line contacts. *Proc. of the 13th Leeds-Lyon Sim. on Trib.*, volume 2, page 183, 1986.

[15] H. Christensen. A simplified model of EHL of rollers. the central and exit solutions. *ASLE Trans.*, volume 22-4, page 323, 1979.

[16] H. Christensen and K. Tønder. The hydrodynamic lubrication of rough surfaces. *Trans. ASME J. Lub. Tech.*, volume 93-3, 1971.

[17] T.F. Conry, S. Wang, and C. Cusano. A Reynolds-Eyring equation for elastohydrodynamic lubrication in line contacts. *Trans. ASME, J. of Trib.*, volume 109, page 648, 1987.

[18] A.W. Crook. The lubrication of rollers, II. *Phil. Trans. A*, volume 254 A, page 29, 1963.

[19] A.W. Crook. The lubrication of rollers, IV, measurements of friction and effective viscosity. *Phil. Trans. A*, volume 255 A, page 281, 1963.

[20] D. Dowson and G.R. Higginson. A numerical solution to the elasto-hydrodynamic problem. *J. Mech. Engng. Sci.*, volume 1, page 6, 1959.

[21] D. Dowson and G.R. Higginson. Elasto-hydrodynamic lubrication. *Pergamon Press*, 1977.

[22] D. Dowson, G.R. Higginson, and B.A. Whitaker. Stress distribution in lubricated rolling contacts. *Proc. Inst. Mech. Engrs.*, 1962.

[23] J. Dundurs, K.C. Tsai, and L.A. Keer. Contact between elastic bodies with wavy surfaces. *J. Elasticity*, volume 3, No.2, page 109, 1973.

[24] H. Eyring. Viscosity, plasticity, and diffusion as examples of absolute reactions rates. *J. Chem. Phys.*, volume 4, page 283, 1936.

[25] P.R. Goglia, C. Cusano, and T.F. Conry. Effects of irregularities on the EHL of sliding line contacts, parts 1 and 2. *Trans. ASME, J. of Trib.*, volume 106, page 104, 1984.

[26] R. Gohar. Elastohydrodynamics. *Ellis Horwood Ltd*, 1988.

[27] R. Gohar and A. Cameron. Optical measurement of oil film thickness under EHD lubrication. *Nature*, volume 200, page 458, 1963.

[28] J.A. Greenwood. An extension of the Grubin theory of elastohydrodynamic lubrication. *J. Phys. D: Appl. Phys.*, volume 5, 1972.

[29] J.A. Greenwood and K.L. Johnson. Modified Hertzian contacts. *Eng. Depart. University of Cambridge, unpublished*, 1989.

[30] J.A. Greenwood and K.L. Johnson. The behaviour of transverse roughness in sliding elastohydrodynamic lubricated contacts. *Wear*, volume 153, page 107, 1992.

[31] A.N. Grubin. Investigation of the contact of machine components. *Kh, F. Ketova (ed.) Central Scientific research Institute for Technology and Mechanical Engineering, Moscow (DSIR translation No. 337)*, volume 30, 1893.

[32] R. W. Hall. Pressure spike in elastohydrodynamics - some elastic considerations. *Wear*, volume 131, page 151, 1989.

[33] R. W. Hall and M.D. Savage. Two-dimensional elastohydrodynamic lubrication, Part 1: the associated dry contact problem. *Proc Int. Mech. Engrs.*, volume 202, C5, page 347, 1988.

[34] G.M. Hamilton and S.L. Moore. Deformation and pressure in an elastohydrodynamic contact. *Proc. Roy. Soc. A322*, volume 313, page 335, 1971.

[35] R.W. Hamming. Numerical methods for scientists and engineers. *Dover Publications, New York*, 1973.

[36] B.J. Hamrock and D. Dowson. Isothermal elastohydrodynamic lubrication of point contacts, part 1 and part 2. *Trans. ASME, J. of Trib.*, volume 98, page 223, 1976.

[37] B.J. Hamrock and B.O. Jacobson. Elastohydrodynamic lubrication of line contacts. *ASLE Trans. 27*, volume 4, page 275, 1984.

[38] H. Hertz. Über die Berührung faster elastischer Körper (On the contact of elastic solids). *J. reine und angewandte Mathematik*, volume 92, page 156, 1882.

[39] C. Hirsch. Numerical computation of internal and external fluids. *Wiley and Sons*, volume 1, 1988.

[40] K.L Johnson. Regimes of elastohydrodynamic lubrication. *J. of Mech. Eng. Sc.*, volume 12, No.1, 1970.

[41] K.L. Johnson. Contact mechanics. *Cambridge University Press*, 1987.

[42] K.L Johnson and R.H. Bentall. A numerical method for finding elastic contact pressures. *Technical Report, University of Cambridge*, volume CUED/L-MECH/TRI 4, 1977.

[43] K.L Johnson and J.L. Tevaarwerk. Shear behaviour of EHD oil films. *Proc. Roy. Soc. London, Series A*, volume 356, page 215, 1977.

[44] M. Kaneta, T. Sakai, and H. Nishikawa. Optical interferometric observations of the effects of a bump on point contact EHL. *Trans. ASME, J. of Trib.*, volume 114, page 779, 1992.

[45] P.L. Kapitza. Hydrodynamic theory of lubrication during rolling. *Zhurnal Tekhnicheskoi Fiziki*, volume 25 (4), page 747, 1955.

[46] M.M. Kostreva. Pressures spikes and stability considerations in elastohydrodynamic lubrication models. *Trans. ASME, J. of Trib.*, volume 1984, 106.

[47] Lee Kwan and H.S. Cheng. Effects of surface asperity on elastohydrodynamic lubrication. *NASA report no. CR-2195*, 1973.

[48] C.C. Kweh, H.P. Evans, and R.W. Snidle. Micro-EHL of an elliptical contact with transverse and three-dimensional sinusoidal roughness. *Trans. ASME, J. of Trib.*, volume 111, page 577, 1989.

[49] C.C. Kweh, M.J. Patching, H.P. Evans, and R.W. Snidle. Simulation of elastohydrodynamic contacts between rough surfaces. *Trans. ASME, J. of Trib.*, volume 114, page 412, 1992.

[50] Rong-Tsong Lee and B.J. Hamrock. A circular non-Newtonian fluid model, parts 1 and 2. *Trans. ASME, J. of Trib.*, volume 112, page 486, 1990.

[51] A.A. Lubrecht. The numerical solution of the elastohydrodynamically lubricated line and point contact problem using multigrid techniques. *Ph.D. Thesis, University of Twente, Enschede*, volume ISBN 90-9001583-3, 1987.

[52] A.A Lubrecht, W.E. Ten Napel, and R. Bosma. Influence of longitudinal and transverse roughness on the EHL of circular contacts. *Trans. ASME, J. of Trib.*, volume 110, page 421, 1988.

[53] A.A Lubrecht and C.H. Venner. Aspects of two-sided surface waviness in an EHL line contact. *19th Leeds-Lyon Symposium on Tribology*, 1992.

[54] H.M. Martin. Lubrication of gear teeth. *Engineering, Lond.*, volume 102, page 199, 1916.

[55] A. Meldahl. Contribution to the theory of the lubrication of gears and the stressing of the lubricated flanks of gear teeth. *Am. J. of Science*, volume 45, 1941.

[56] T. Merriman and J. Kannel. Analyses of the role of surface roughness on contact stresses between elastic cylinders with and without soft surface coating. *Trans. ASME, J. of Trib.*, volume 111, page 87, 1989.

[57] B. Michau, D. Berthe, and M. Godet. Influence of pressure modulation in a line Hertzian contact on the internal stress-field. *Wear*, volume 28, page 187, 1974.

[58] M.Muskat and H.H. Evinger. The effect of the pressure variation of viscosity in lubrication of plane sliders. *J. of App. Phys.*, page 739, 1940.

[59] T.G. Myers. Chevyshev series methods for piezoviscous elastohydrodynamic lubrication. *PhD Thesis, University of Leeds*, 1990.

[60] K. Tønder. The hydrodynamic lubrication of rough surfaces based on a new perturbation approach. *Trans. ASME, J. of Trib.*, volume 106, page 440, 1984.

[61] H. Okamura. A contribution to the numerical analysis of isothermal elastohydrodynamic lubrication. *Proc. 9th Leeds-Lyon Symposium on Tribology, Leeds*, page 313, 1982.

[62] N. Patir and H.S. Cheng. Effect of surface roughness on the central film thickness in ehd contacts. *5th Leeds-Lyon Symposium on Tribology*, 1978.

[63] A.I. Petrusevich. Fundamental conclusions from the contact-hydrodynamic theory of lubrication. *Izo. Akad. Nauk SSSR (OTN)*, volume 2, page 209, 1951.

[64] J. Prakash and H. Christensen. A simplified model of EHL of rollers. the complete solution. *ASLE Trans.*, volume 24-3, page 362, 1981.

[65] J.N. Reddy. An introduction to the finite element method. *Mc. Graw-Hill*, 1984.

[66] O. Reynolds. On the theory of lubrication and its application to Mr. Beauchamp tower's experiments, including an experimental determination of the viscosity of olive oil. *Phil. Trans. R. Soc.*, volume 177, page 157, 1886.

[67] S.O. Rice. The mathematical analysis of random noise. *Bell Syst. Tech. J.*, volume 23, page 282, 1944.

[68] C.J.A. Roelands. Correlational aspects of the viscosity-temperature-pressure relationship of lubricating oils. *Ph.D. thesis, Technische Hobeschool Delft, The Netherlands*, 1966.

[69] F. Sadeghi. A comparison of the fluid models effect on the internal stresses of rough surfaces. *Trans. ASME, J. of Trib.*, volume 113, page 142, 1991.

[70] F. Sadeghi and P.C. Sui. Compressible elastohydrodynamic lubrication of rough surfaces. *Trans. ASME, J. of Trib.*, volume 111, page 56, 1989.

[71] R.A. Schapery. Theory of crack initiation and growth in viscoelastic media, parts i and ii. *Int. J. of Fract.*, volume 11, No.1, 1975.

[72] J. Shieh and B.J. Hamrock. Film collapse in EHL and micro-EHL. *Trans. ASME, J. of Trib.*, volume 113, page 372, 1991.

[73] B. Sternlicht, P. Lewis, and P. Flynn. Theory of lubrication and failure of rolling contacts. *Trans. Amer. Mech. Engrs. J. of Basic Engineering, 83 Series D*, volume 2, page 213, 1961.

[74] J.H. Tripp and B.J. Hamrock. Surface roughness effects in elastohydrodynamic contacts. *Proceedings 1984 Leeds Lyon Symposium on Trib.*, page 30, 1985.

[75] C.H. Venner. Multilevel solution of the EHL line and point contact problems. *Ph.D. Thesis, University of Twente, Enschede, The Netherlands*, volume 90-9003974-0, 1991.

[76] C.H. Venner and A.A. Lubrecht. Transient analysis of surface features in an EHL line contact in the case of sliding. *Submitted to ASME J. of Trib.*, 1992.

[77] C.H. Venner, A.A. Lubrecht, and W.E. ten Napel. Numerical simulation of overrolling of a surface feature in a EHL line contact. *Trans. ASME, J. of Trib.*, volume 113, 1991.

[78] C.H. Venner and W.E. ten Napel. Surface roughness effects in an EHL line contact. *Trans. ASME, J. of Trib.*, volume 114, page 616, 1992.

[79] C.H. Venner, W.E. ten Napel, and R. Bosma. Advanced multilevel solution of EHL line contact problems. *Trans. ASME, J. of Trib.*, volume 112, page 426, 1990.

[80] M.N. Webster and R.S. Sayles. A numerical model for the elastic frictionless contact of real rough surfaces. *Trans. ASME, J. of Trib.*, volume 108, page 314, 1986.

[81] H.M. Westergaard. Bearing pressures and cracks. *Trans. ASME, J. Appl. Mechs*, volume 6, page A49, 1939.

[82] Ai Xiaolan and Zheng Linqing. A general model for microelastohydrodynamic lubrication and its full numerical solution. *Trans. ASME, J. of Trib.*, volume 111, page 569, 1989.